New mechanisms controlling the positioning and activity of the ParAB*S* chromosome partition system

Dissertation

„kumulativ“

zur Erlangung des Grades eines

Doktor der Naturwissenschaften

(Dr. rer.nat.)

des Fachbereichs Biologie der Philipps-Universität Marburg

Vorgelegt von

Manuel Osorio Valeriano

aus Mexico City, Mexico

Marburg, Oktober 2020

Die Untersuchungen der vorliegenden Arbeit wurden von Oktober 2015 bis Dezember 2020 unter der Betreuung von Prof. Dr. Martin Thanbichler am Philipps Universität in Marburg durchgeführt.

Vom Fachbereich Biologie

Der Philipps-Universität Marburg als Dissertation

angenommen am: 15.12.2020

Erstgutachter: Prof. Dr. Martin Thanbichler

Zweitgutaschter: Prof. Dr. Lotte Sogaard-Andersen

Weitere Mitglieder der Prüfungskommission:

Prof. Dr. Victor Sourjik

Prof. Dr. Gert Bange

Prof. Dr. Peter Graumann

SUMMARY

DNA segregation is a central process in biology which ensures that every daughter cell receives the full complement of genetic information upon cell division. In bacteria, the most widespread mechanism to segregate DNA is the tripartite ParAB*S* system. It includes a DNA-binding protein named ParB, which interacts with centromere-like *parS* sequences typically located close to the origin of replication. After initial binding to *parS*, ParB spreads to adjacent DNA regions, giving rise to a large nucleoprotein complex known as the partition complex. It then interacts dynamically with the third component of the ParAB*S* system, the P-loop ATPase ParA, which directs the progressive movement of the partition complex towards opposite cell poles by a ratchet-like mechanism.

The ParABS system is often organized by polar landmarks that anchor the origin of replication at specific locations within the cell and sequester free ParA, likely enhancing the robustness of the segregation process. In this work, we identify the bactofilin cytoskeleton as a new organizer of the ParAB*S* DNA-segregation machinery in *Myxococcus xanthus*. We show that the ParB*S* partition complex associates with the pole-distal ends of the bactofilin filaments, whereas ParA binds along their entire length, recruited by the ParB-like protein PadC.

Structural studies of PadC revealed that the ParB/Srx domain of this protein functions as a nucleotide-binding domain that specifically interacts with the ribonucleotide CTP. CTP-binding keeps the ParB/Srx domain of PadC in a closed-dimer conformation that is necessary for the interaction with ParA. Remarkably, we show that CTP-binding is conserved in ParB. In this protein, the CTP-dependent dimerization of the N-terminal ParB/Srx domain is catalyzed by *parS*. In contrast to PadC, ParB exhibits CTPase activity. We show that CTP binding and hydrolysis are necessary for partition complex formation and function. Our results identify ParB homologues as a new class of nucleotide switches that use CTP instead of ATP or GTP and thus, open the possibility that CTP could regulate the function of other protein families.

In addition to its role in chromosome segregation, ParB participates in cell division in *Caulobacter crescentus* by recruiting the negative regulator of FtsZ polymerization, MipZ, to the cell poles, thereby limiting the assembly of the cytokinetic FtsZ ring to the midcell region. In this study, we show that the MipZ system is conserved in alphaproteobacteria. However, the mechanisms by which it regulates cell division might have adapted to the specific needs of the host organism.

ZUSAMMENFASSUNG

Die DNA Segregation ist ein zentraler biologischer Prozess, der sicherstellt, dass jede Tocherzelle, die aus einer Zellteilung hervorgeht, die vollständige genetische Erbinformation erhält. Der am weitesten verbreiteten DNA-Segregationsmechanismus in Bakterien stellt das ParAB*S*-System dar. Dieses System besteht aus einem DNA-Bindeprotein (ParB), welches an zentromerähnliche *parS*-Sequenzen in der Nähe des Replikationsursprungs bindet. Von dort breitet sich ParB über benachbarte DNA-Regionen aus und bildet so einen großen Nukleoproteinkomplex, der auch als Segregationskomplex bekannt ist. Dieser interagiert dynamisch mit der dritten Komponente des ParAB*S*-Systems, der P-Loop ATPase ParA, welche die gerichtete Bewegung des Segregationskomplexes zum gegenüberliegenden Zellpol über einen Ratschen-Mechanismus vermittelt.

Das ParAB*S*-System wird oftmals durch sogenannte polare Landmarken organisiert, die den Replikationsursprung an spezifischen Stellen innerhalb der Zelle verankern und freie ParA Moleküle „festhalten“. Dadurch wird sehr wahrscheinlich die Robustheit des Segregationsprozesses verstärkt. In der vorliegenden Arbeit identifizieren wir das Bactofilin-Zytoskelett von *Myxococcus xanthus* als neuartigen Organisator des ParAB*S*-DNA-Segregationsapparates. Wir zeigen, dass der ParB*S*-Teilungskomplex mit den vom Zellpol entfernten Enden der Bactofilin-Filamente assoziiert, wohingegen ParA-Moleküle mit Hilfe des Adapterproteins PadC entlang der gesamten Länge der Filamente binden.

Strukturelle Studien an PadC zeigten, dass seine ParB/Srx-Domäne als Nukleotidbindedomäne fungiert, die spezifisch mit dem Ribonukleotid CTP interagiert. Durch die Bindung von CTP wird die ParB/Srx-Domäne von PadC in einer geschlossenen Dimer-Konformation gehalten, welche für die Interaktion mit ParA nötig ist. Wir konnten wir zeigen, dass die Fähigkeit zur CTP-Bindung in ParB konserviert ist. In diesem Protein wird die CTP-abhängige Dimerisierung der N-terminalen ParB/Srx-Domäne durch *parS* katalysiert. Im Gegensatz zu PadC besitzt ParB CTPase-Aktivität. Wir zeigen, dass CTP-Bindung und -Hydrolyse für die Bildung und Funktion des Segregationskomplexes nötig sind. Unsere Ergebnisse identifizieren ParB-Homologe als eine neue Klasse von nukleotidabhängigen Schaltern, die CTP anstelle von ATP oder GTP nutzen. Es erscheint daher möglich, dass CTP auch die Funktion anderer Proteinfamilien regulieren könnte.

Zusätzlich zu seiner Rolle in der Chromosomensegregation erfüllt ParB in *Caulobacter crescentus* eine wichtige Funktion bei der Zellteilung, indem es MipZ, einen negativen Regulator der FtsZ-Polymerisation, zu den Zellpolen rekrutiert. Dadurch wird die Assemblierung des Zellteilungsapparats auf die Zellmitte beschränkt. In der vorliegenden Arbeit zeigen wir, dass das MipZ-System in Alphaproteobakterien konserviert ist, sein Wirkungsmechanismus aber an die spezifischen Anforderungen des jeweiligen Organismus adaptiert wurde.

CONTENTS

INTRODUCTION

DNA is regarded as the blueprint of life since it contains the information needed to build a living cell. In every cell cycle, cells must duplicate their genetic material and ensure the accurate transmission of the duplicated DNA to the daughter cells upon cell division. Errors in DNA segregation could lead to the loss of genetic information and thus, compromise cell viability.

DNA segregation in eukaryotes

In eukaryotes, the segregation of chromosomal DNA depends on a proteinaceous multi-subunit assembly formed by more than 100 different proteins, named the kinetochore (van Hooff *et al.*, 2017). This complex connects the sister chromatids to the spindle microtubules along which they then segregate in opposite directions into the daughter cells during cell division (Musacchio & Desai, 2017). The kinetochore assembles on a specialized chromatin locus, named the centromere. In contrast to the high degree of protein conservation among kinetochores from distant evolutionary lineages, centromeres consist of highly repetitive DNA sequences that vary widely in sequence and length, ranging from 125 base pairs in yeast to several million base pairs in humans (Bloom, 2014, Oliferenko, 2018). Centromeric heterochromatin is characterized by specific histone modifications, the presence of a centromere-specific histone H3 variant (CENP-A or Cse4), and the enrichment of topoisomerase II. Moreover, it associates with the Structural Maintenance of Chromosomes (SMC) proteins cohesin and condensin (Figure 1) (Ohzeki *et al.*, 2019).

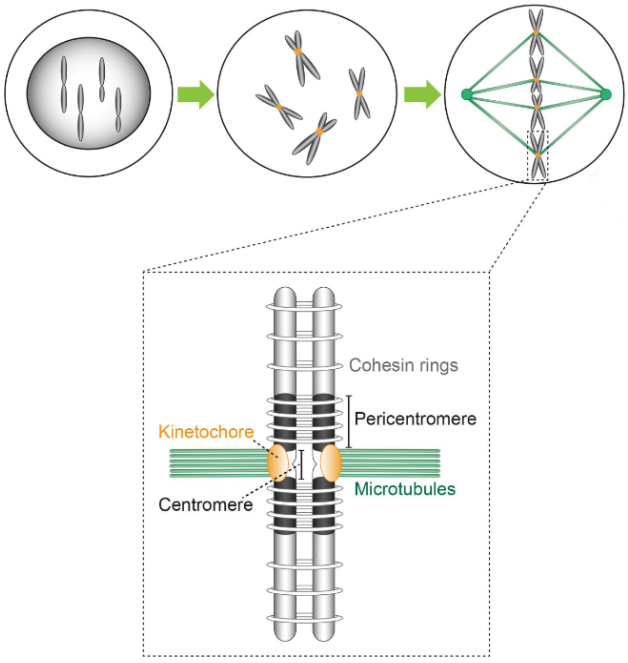

Figure 1. Chromosome segregation during eukaryotic cell division. Kinetochores (orange) assembled at the centromeric regions attach sister chromatids to the spindle microtubules (green) along which they then segregate in opposite directions into the two daughter cells. Modified from Smurova & De Wulf (2018).

Prokaryotic DNA segregation: the ParAB*S* system

DNA segregation in prokaryotes was first investigated in replicative low-copy-number plasmids. Dividing *Escherichia coli* cells contain only two copies of plasmid P1. Nevertheless, the production of cells lacking the plasmid is an extremely rare event (Austin *et al.*, 1981). This observation suggested the existence of a highly accurate partition mechanism that actively translocates the newly replicated genetic material to the daughter cells during cell division.

In 1982, seminal work from S. Austin and A. Abeles led to the identification of a 2,500 bp DNA region containing elements that are necessary and sufficient to promote the equipartition of replicative plasmids: a *cis*-acting element analogous to the eukaryotic centromere, named *parS*, and two open reading frames encoding the partition proteins ParA and ParB (Abeles *et al.*, 1985, Austin & Abeles, 1983a, Austin & Abeles, 1983b, Austin *et al.*, 1982). The latter is a DNA-binding protein that, upon interaction with *parS* sequences, spreads over adjacent DNA regions to form a nucleoprotein complex known as the partition complex. ParA is a P-loop ATPase that binds non-specifically to the nucleoid and transiently interacts with the partition complex, directing its progressive translocation to the opposite cell pole.

One decade later, the ParAB*S* DNA-segregation system was also shown to mediate the segregation of chromosomal DNA in bacteria (Ireton *et al.*, 1994, Sharpe & Errington, 1996, Mohl & Gober, 1997). A bioinformatic analysis identified putative ParAB*S* systems in nearly 70% of all bacterial genomes sequenced thus far (Livny *et al.*, 2007).

parS: the bacterial centromere

Centromere-like *parS* sites consist of 16 base pairs palindromic sequences typically located close to the origin of replication (Figure 2) (Pillet *et al.*, 2011, Davis & Austin, 1988, Abeles *et al.*, 1985). Although *parS* sites are highly conserved in sequence and relative position in the chromosome, their copy number varies considerably among species, ranging from 1 to more than 20 (Livny *et al.*, 2007, Iniesta, 2014, Harms *et al.*, 2013, Böhm *et al.*, 2020, Tran *et al.*, 2018, Lagage *et al.*, 2016, Breier & Grossman, 2007, Jecz *et al.*, 2015, Kawalek *et al.*, 2020). Interestingly, previous studies have shown that a single *parS* site is sufficient to support partition complex formation (Lagage *et al.*, 2016, Böhm *et al.*, 2020, Breier & Grossman, 2007, Jecz *et al.*, 2015). However, additional *parS* sites might enable robust ParB loading and facilitate ParB spreading over larger genomic distances. The placement of *parS* near the origin of replication appears to be essential for partition, as insertion of *parS* motifs outside a “permissive zone” of ~500 kb results in atypical segregation events and anucleate cells (Lagage *et al.*, 2016, Tran *et al.*, 2018, Böhm *et al.*, 2020).

A recent study reported the presence of hundreds of half-*parS* motifs scattered across the entire chromosome in *Pseudomonas aeruginosa* (Kawalek *et al.*, 2018). Interestingly, ParB associates with

these motifs. However, they do not support ParB spreading. Genome-wide interactions of ParB with hundreds of *parS* half-sites could have an impact on global chromosome topology, compaction and gene expression (Kawalek *et al.*, 2018, Kawalek *et al.*, 2020).

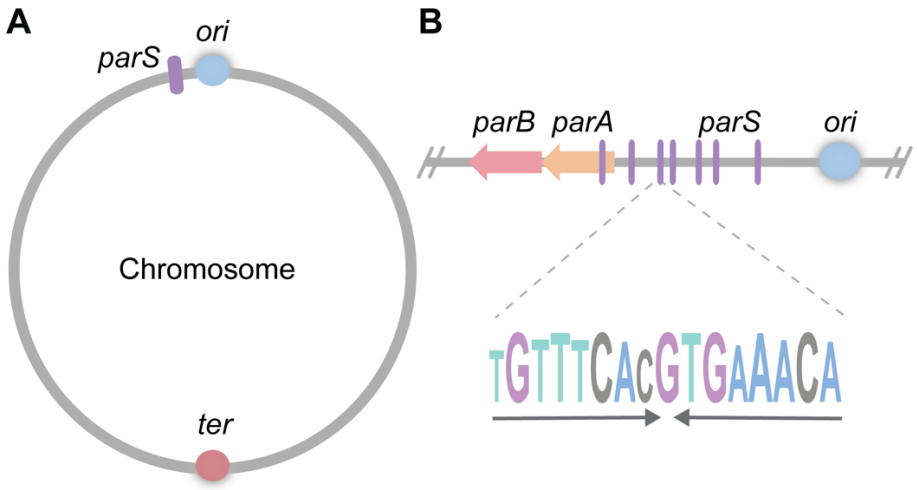

Figure 2. Genomic position of the ParAB*S* chromosome segregation components. A) *Caulobacter crescentus* chromosome showing the *ori* (blue) and *ter* (red) regions, parS sites are depicted in purple. **B)** Amplification of the origin-proximal genomic region (Tran *et al.*, 2018). Centromeric-like *parS* sites are typically located close to the *ori*, similarly, the *parAB* operon is encoded in the vicinity. A consensus *parS* palindromic sequence is depicted at the bottom. The size of the letters corresponds to the degree of conservation in different species.

ParB and the formation of the partition complex

ParB was initially identified as a DNA-binding protein that specifically interacts with *parS* sites (Davis & Austin, 1988). ParB binding to *parS* represents the first step in partition. After initial specific recognition of *parS* sites, ParB dimers spread to adjacent DNA regions, giving rise to a kinetochore-like partition complex that can extend over tens of thousands of base pairs (Tran *et al.*, 2018, Murray *et al.*, 2006, Jalal *et al.*, 2019).

Despite the low conservation at the amino acid sequence level, ParB proteins share a common domain organization, comprising a central DNA-binding domain (DBD) (Schumacher & Funnell, 2005, Sanchez *et al.*, 2013, Schumacher *et al.*, 2010, Chen *et al.*, 2015, Schumacher *et al.*, 2007) that is flanked by a C-terminal dimerization domain (CTD) (Fisher *et al.*, 2017, Schumacher *et al.*, 2007) and an N-terminal ParB/Srx domain (NTD) (Figure 3) (Chen *et al.*, 2015, Leonard *et al.*, 2004, Jalal *et al.*, 2019).

The DNA-binding domain of ParB mediates specific *parS* recognition though a helix-turn-helix (HTH) motif (Chen *et al.*, 2015, Schumacher *et al.*, 2010, Jalal *et al.*, 2020) (Figure 3). Furthermore, crystal structures of ParB proteins bound to *parS* revealed that additional residues located outside the HTH are also critical for *parS* interaction (Sanchez *et al.*, 2013, Chen *et al.*, 2015).

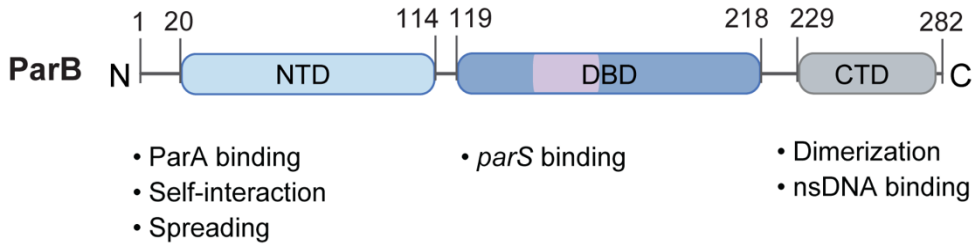

Figure 3. Domain organization of ParB. Schematic representation of the domain arrangement of *Bacillus subtilis* ParB (Spo0J). The N-terminal ParB/Srx domain (NTD) is followed by a central DNA-binding domain (DBD) containing a helix-turn-helix HTH motif (pink), this domain is connected by a short unstructured linker region to the C-terminal dimerization domain (CTD). This organization is conserved among the vast majority of centromere-binding ParB proteins. Functions assigned to each domain are listed at the bottom.

In agreement with previous biochemical studies that identified the C-terminal region of ParB as a dimerization domain (Lobocka & Yarmolinsky, 1996, Surtees & Funnell, 1999, Bartosik *et al.*, 2004, Leonard *et al.*, 2004), the structure of a C-terminal fragment (residues 227 to 282) from the *Bacillus subtilis* chromosomal ParB homologue corresponds to a well-defined dimer comprising two α-helices and two β-strands per monomer. The dimer interface consists of an intermolecular β-sheet and two domain-swapped C-terminal helices (Fisher *et al.*, 2017). Interestingly, the overall fold resembles, to some degree, to that reported for the corresponding regions of the plasmid P1 ParB and SopB proteins (Schumacher & Funnell, 2005, Schumacher *et al.*, 2007, Schumacher *et al.*, 2010).

The C-terminal dimerization domain of *B. subtilis* ParB displays non-specific (ns) DNA-binding activity that has been shown to condense DNA *in vitro*. These interactions are mediated by a positively charged, lysine-rich surface (Fisher *et al.*, 2017, Schumacher & Funnell, 2005, Schumacher *et al.*, 2007). However, this feature is not conserved in all ParB proteins. For instance, the *C. crescentus* ParB protein lacks the lysine-rich patch. Accordingly, it displays no or very weak nsDNA-binding activity and does not condense DNA *in vitro* (Jalal *et al.*, 2019). The nsDNA-binding of *C. crescentus* ParB can be artificially enhanced by introducing lysine residues at the C-terminal domain. Conversely, extensive mutation of lysine residues naturally present in ParB from *B. subtilis* abolishes nsDNA binding (Jalal *et al.*, 2019).

The N-terminal domain of ParB is structurally and evolutionarily related to the eukaryotic sulfiredoxin Srx (Jönsson *et al.*, 2008, Liu *et al.*, 2019, Basu & Koonin, 2005), which plays a role in peroxide-mediated signaling. It does so by reducing, and thus reactivating, hyperoxidized cysteine residues in the catalytic center of peroxiredoxins in an ATP-dependent manner (Jönsson *et al.*, 2008, Jönsson *et al.*, 2009, Liu *et al.*, 2019). Srx was proposed to be a rare case of a dramatic functional switch in evolution in which a *bona fide* enzyme evolved from a non-enzymatic DNA-binding ancestor. Alternatively, it was suggested that ParB could bind a so-far unidentified ligand (Basu & Koonin, 2005).

The ParB/Srx domain plays a central role in ParB function and has been identified as the interaction determinant for ParA (Radnedge *et al.*, 1998, Surtees & Funnell, 1999, Dmowski & Jagura-Burdzy, 2011, Volante & Alonso, 2015). Moreover, cross-linking experiments suggest that, in addition to the main dimerization determinant represented by the C-terminal domain, the N-terminal region of ParB could function as a second self-association interface (Surtees & Funnell, 1999, Kusiak *et al.*, 2011).

A sequence alignment of the N-terminal domains from chromosome and plasmid ParB homologues identified three conserved regions, called Box I, Box II, and Box III (also known as Region II) (Yamaichi & Niki, 2000, Bartosik *et al.*, 2004). Box II contains an invariant arginine patch that is essential for ParB spreading and partition complex formation (Figure 4) (Autret *et al.*, 2001, Graham *et al.*, 2014, Song *et al.*, 2017).

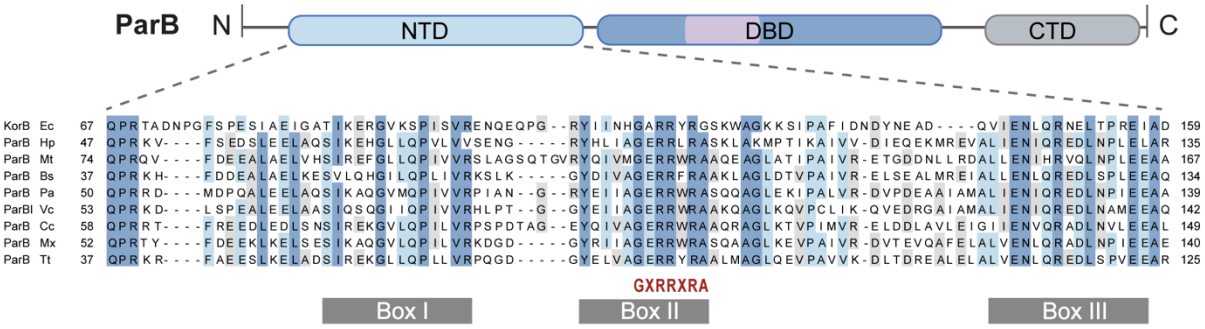

Figure 4. Conserved motifs in the N-terminal domain of ParB. Amino acid sequence alignment of the N-terminal domains of some well-studied plasmidic and chromosomal ParB homologues. The previously described conserved regions Box I, Box II and Box III (also known as Region II) (Yamaichi & Niki, 2000, Bartosik *et al.*, 2004) are indicated in dark gray, and the arginine rich motif is shown in red letters at the bottom. The UniProt accession numbers of the sequences used in the alignment are as follows: P07674 (KorB Ec, *Escherichia coli*); P26497 (ParB Bs, *Bacillus subtilis*); O25758 (ParB Hp, *Helicobacter pylori*); P9WIJ9 (ParB Mt, *Mycobacterium tuberculosis*); Q9HT12 (ParB Pa, *Pseudomonas aeruginosa*); Q9KNG7 (ParBI Vc, *Vibrio cholerae*); P0CAV8 (ParB Cc, *Caulobacter crescentus*); Q1CVJ4 (ParB Mx, *Myxococcus xanthus*); Q72H91 (ParB Tt, *Thermus thermophilus*). The numbers at the beginning and at the end of each line indicate the position of the first and last amino acid of the respective protein shown in the primary sequence. Modified from Osorio-Valeriano *et al.* (2019).

A recent crystal structure of ParB bound to *parS* shows a tetrameric nucleoprotein complex stabilized by interactions that involve the so-called arginine patch (Chen *et al.*, 2015). Interestingly, mutations in this motif abolish *parS*-independent DNA condensation *in vitro* (Graham *et al.*, 2014, Song *et al.*, 2017). It has been suggested that ParB oligomerization might contribute to partition complex formation by bridging ParB dimers bound to distant DNA regions.

An additional role for ParB in some species, is the recruitment of the SMC condensin complex, a protein family present in all domains of life (Cobbe & Heck, 2004). In bacteria, this complex forms a ring-like structure that promotes bulk chromosome segregation by actively compacting and aligning the two arms of sister chromatids. Similar to eukaryotes, the SMC complex is enriched in the centromeric regions in bacteria (Gruber & Errington, 2009). ParB spreading from *parS* sites is necessary for SMC

loading, but the mechanism by which ParB recruits SMC is not yet fully understood (Gruber & Errington, 2009, Sullivan *et al.*, 2009, Minnen *et al.*, 2011).

Models for partition complex formation.

Despite more than three decades of intensive research, the precise mechanism underlying the formation of the prokaryotic kinetochore-like partition complex remains elusive. However, at least three different models that recapitulate some of the properties observed *in vivo* and *in vitro* have been proposed.

One of the earliest models proposed a lateral 1D spreading of ParB by polymerization along the DNA from *parS* nucleation sites (Figure 5A) (Murray *et al.*, 2006, Rodionov *et al.*, 1999). This model was inferred based on the ability of ParB to silence genes flanking *parS,* especially when overexpressed (Lynch & Wang, 1995, Hanai *et al.*, 1996) and by the fact that ParB spreading can be inhibited in a polar manner by high-affinity DNA-binding sites recognized by other proteins known as 'roadblocks', located on the side of the *parS* sequences (Rodionov *et al.*, 1999, Murray *et al.*, 2006). However, experimental evidence demonstrated that the number of ParB dimers in the cell (~140 dimers per partition complex) is lower than would be needed to form a continuous filament spanning tens of kilobases (Graham *et al.*, 2014), challenging the 1D polymerization model.

An alternative model incorporates recent studies reporting the ability of ParB to condense DNA *in vitro* (Graham *et al.*, 2014, Taylor *et al.*, 2015). This model combines 1D spreading with 3D bridging interactions between ParB molecules bound to distant DNA regions (Graham *et al.*, 2014, Song *et al.*, 2017, Chen *et al.*, 2015), allowing a relatively small number of ParB molecules to cover large distances away from *parS* (Figure 5B) (Broedersz *et al.*, 2014). However, the physiological relevance of such DNA condensation activity remains to be assessed, especially because it occurs in a *parS*-independent manner (Graham *et al.*, 2014). Nevertheless, *parS* is essential for partition complex assembly *in vivo* (Böhm *et al., 2020,* Lagage *et al., 2016)*.

More recently, single-molecule imaging of the F-plasmid ParB homologue SopB led to a largely similar model, defining ParB networks as fluid structures that nucleate at *parS* using a 'nucleation and caging' mechanism (Sanchez *et al.*, 2015, Debaugny *et al.*, 2018). The authors found that nearly all ParB molecules are actively confined around *parS* (confinement region size of ~150 nm), presumably due to synergistic protein-protein and protein-DNA interactions (Figure 5C). However, despite recent advances in the understanding of the formation of the ParB*S* partition complex, the molecular mechanism underlying this process still remains elusive.

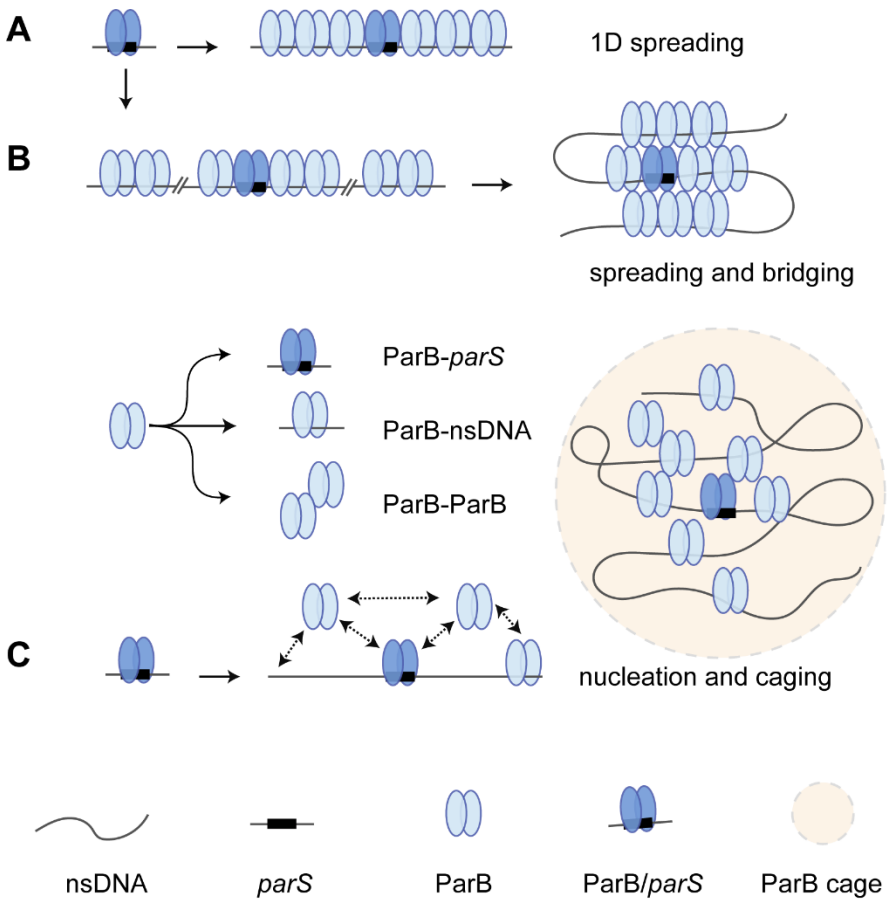

Figure 5. Different models for partition complex formation. Schematic representation of three different models for prokaryotic partition complex formation. **A**) In the 1D spreading model, ParB dimers propagate by nearest-neighbor interactions in 1D along the DNA, forming filaments that extend from *parS* nucleation sites to flanking DNA regions in both directions (Rodionov *et al.*, 1999). **B**) A second model combines the 1D spreading with 3D bridging interactions between ParB dimers located at distant DNA regions (Graham *et al.*, 2014, Broedersz *et al.*, 2014). **C**) In the nucleation and caging model, transient interactions between ParB molecules and with nsDNA provide a network of weaker interactions that prevent ParB diffusion far from *parS* nucleation sites (Sanchez *et al.*, 2015, Debaugny *et al.*, 2018). Modified from Sanchez *et al.* (2015).

ParA and its role in partition complex translocation

The third component of the ParAB*S* DNA-segregation system is the P-loop ATPase ParA. This group of proteins belong to a large superfamily of NTPases characterized by two conserved sequence signatures: a deviant Walker A motif (known as the phosphate-loop or P-loop) and a Walker B motif, which bind, respectively, the beta and gamma phosphate moieties of the bound NTP; as well as a Mg^{2+} cation (Leipe *et al.*, 2002). The energy from nucleotide hydrolysis is typically utilized to induce conformational changes that alter their affinities for binding partners, which constitutes the basis of their biological functions (Romero Romero *et al.*, 2018).

ParA cycles in a nucleotide-dependent manner between an apo or ADP-bound monomer and an ATP-bound dimer (Figure 6A). ATP-dependent dimerization of ParA promotes non-specific nucleoid DNA-binding via surface-exposed positively charged residues located at the dimer interface (Figure 5)

(Corrales-Guerrero *et al.*, 2020, Hester & Lutkenhaus, 2007, Leonard *et al.*, 2005, Vecchiarelli *et al.*, 2010b). ATP hydrolysis leads to dissociation of the ParA dimer and releases the monomers from the DNA. Nucleotide exchange allows the cycle to start again (Figure 6A).

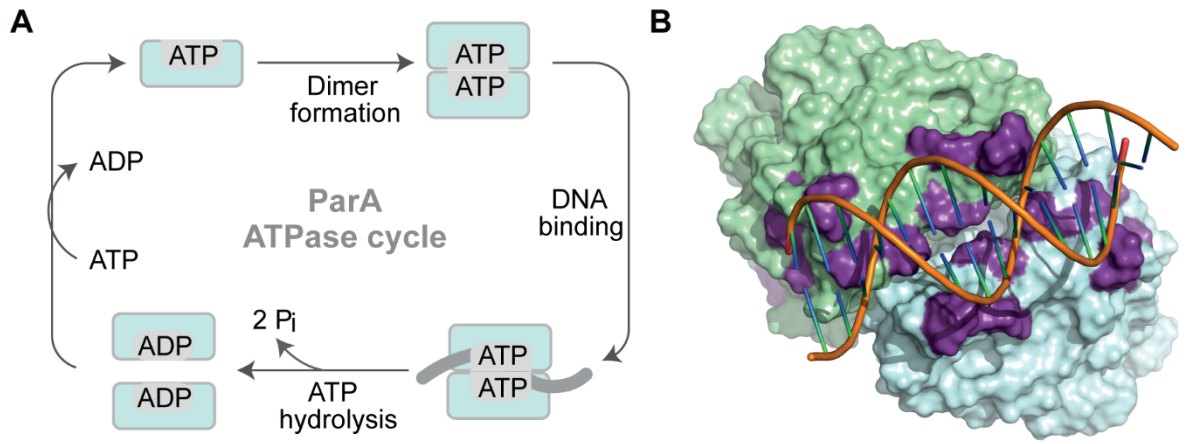

Figure 6. The ParA ATPase cycle. A) ParA ATPase cycle. ParA dimerizes upon binding of ATP; ParA dimers can bind non-specifically to DNA. Upon ATP hydrolysis, ParA monomerizes and dissociates from the DNA. Nucleotide exchange will allow the cycle to start again. **B**) Structural model of the ParA dimer from *C. crescentus* bound to nsDNA (Corrales-Guerrero *et al.*, 2020). One monomer is colored in light green and the second monomer in light blue, a short double-stranded DNA molecule (orange) is modeled on the ParA dimer. Amino acid residues shown to mediate DNA-binding are highlighted in purple. Modified from Lin *et al*. (2017) and Corrales-Guerrero *et al*. (2020).

ParA plays an essential role in DNA translocation by actively directing the progressive movement of the newly replicated *ori* region to the nascent daughter cell. Replication of the chromosomal *ori* region results in two physically separated copies of the ParB*S* complex. Generally, the ParB*S* complex closer to the old pole remains attached to polar anchors (see below), while the other one migrates towards the new pole, following a retracting gradient of ParA dimers associated with the nucleoid (Vecchiarelli *et al.*, 2010b, Ah-Seng *et al.*, 2009) (Figure 6).

It has been proposed that during translocation, the newly formed partition complex is transiently tethered to the nucleoid by the interaction with nucleoid-bound ParA dimers. This interaction results in the stimulation of the ParA ATPase activity and consequently ParA dissociates from the DNA (Watanabe *et al.*, 1992, Lim *et al.*, 2014, Vecchiarelli *et al.*, 2013, Hwang *et al.*, 2013). The reformation and rebinding of ParA dimers to the nucleoid are relatively slow processes, which creates a time delay between ParA monomers release and the formation of DNA-binding competent ParA dimers (Vecchiarelli *et al.*, 2010a, Hwang *et al.*, 2013, Vecchiarelli *et al.*, 2012). This delay contributes to the establishment of the ParA gradient by allowing ParA to diffuse throughout the cell and rebind to any region of the nucleoid with equal probability rather than rebinding in the physical proximity from where it dissociated.

The released ParB*S* complex is again captured by DNA-associated ParA-dimers bound in its the vicinity. Iteration of this cycle is thought to promote the directed movement of the segregating *ori* region along the ParA dimer gradient (Figure 7). It has been proposed that the forces that drive the segregation process are generated by the elastic dynamics of the chromosome itself in a DNA-relay mechanism (Lim *et al.*, 2014).

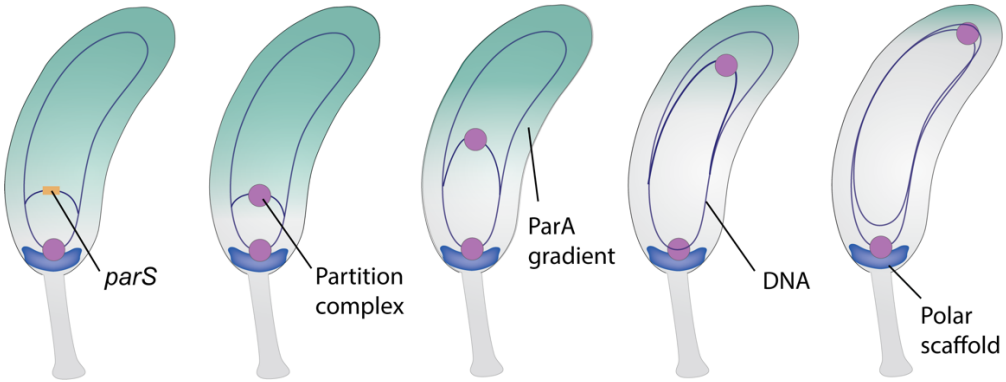

Figure 7. ParAB*S*-mediated DNA translocation. In many species, the ParB*S* partition complex is tethered by polar anchors. Upon replication of the *ori* region, binding of ParB dimers at *parS* sites followed by spreading to adjacent DNA regions, results in the formation of a second partition complex which is actively translocated following a retracting gradient of ParA dimers associated with the nucleoid. This gradient is progressively shortened by the ATPase-activating activity of ParB in a process driven by a ratchet-like mechanism.

Different polar landmarks organize the ParAB*S* segregation machinery

Many ParAB*S* systems function together with polar landmark proteins that anchor the ParB*S* partition complex to the cell pole and sequester ParA monomers (Figure 7). For instance, in *C. crescentus*, the pole-organizing protein PopZ tethers one ParB*S* complex to the stalked pole via direct interaction with ParB (Bowman *et al.*, 2008, Ebersbach *et al.*, 2008) and captures ParA monomers released from the nucleoid upon ATP hydrolysis. A second polarity factor, named TipN, recruits ParA to the opposite cell pole ensuring rapid directional translocation of the segregated ParB*S* complex (Schofield *et al.*, 2010, Ptacin *et al.*, 2010).

In Gram-positive bacteria, the *ori* region is typically anchored by the polar scaffolding protein DivIVA. In *Corynebacterium glutamicum*, *Streptococcus pneumoniae* and *Deinococcus radiodurans*, DivIVA interacts directly with ParB (Donovan *et al.*, 2012, Fadda *et al.*, 2007, Chaudhary *et al.*, 2019). By contrast, immobilization of the *ori* region in sporulating *B. subtilis*, is mediated by an additional protein named RacA, which specifically binds to palindromic DNA sequences located close to the origin of plication and physically connects the chromosome to DivIVA (Wu & Errington, 2003, Schumacher *et al.*, 2016, Ben-Yehuda *et al.*, 2003, van Baarle *et al.*, 2013).

Interestingly, DivIVA has also been implicated in ParA recruitment. In *Mycobacterium smegmatis* (Ginda *et al.*, 2013, Pióro *et al.*, 2019) DivIVA interacts directly with ParA, whereas in *Streptomyces*

coelicolor, this interaction is mediated by the cytoskeletal protein Scy (Ditkowski *et al.*, 2013). In *Vibrio cholerae*, the polar targeting of ParA is mediated by HubP, a multipurpose scaffolding protein that additionally localizes the chemotactic machinery in this bacterium (Yamaichi *et al.*, 2012).

In chapter II, we describe a new organizer of the ParAB*S* DNA-segregation machinery in *Myxococcus xanthus*. In this species, the ParB*S* complex and the DNA partitioning ATPase ParA are immobilized closed to the cell poles by bactofilins, a widespread class of nucleotide-independent cytoskeletal proteins. The ParB*S* partition complex is tethered to the pole-distal end of the bactofilin polymers, whereas ParA monomers are sequestered by a ParB-like protein named PadC, which associates along the entire length of the bactofilin filaments.

ParB, more than a DNA segregation protein

In addition to its role in chromosome segregation, ParB also regulates cell division in *C. crescentus* by controlling the placement of the FtsZ cytokinetic ring through the interaction with a second P-loop ATPase, named MipZ, which acts as a negative regulator of FtsZ polymerization (Thanbichler & Shapiro, 2006). The ParB*S* partition complex recruits MipZ monomers to the cell pole, and ATP-dependent dimerization allows MipZ to bind non-specifically to the nucleoid. Competition of ParB and the nucleoid for MipZ, together with the ATP cycle of this NTPase, result in the formation of a MipZ gradient with concentration maxima at the cell poles and a minimum at midcell (Thanbichler & Shapiro, 2006, Kiekebusch *et al.*, 2012). High concentrations of MipZ at the cell poles, prevent Z-ring assembly at these locations, thereby limiting cell division to the cell center (Kiekebusch *et al.*, 2012, Thanbichler & Shapiro, 2006).

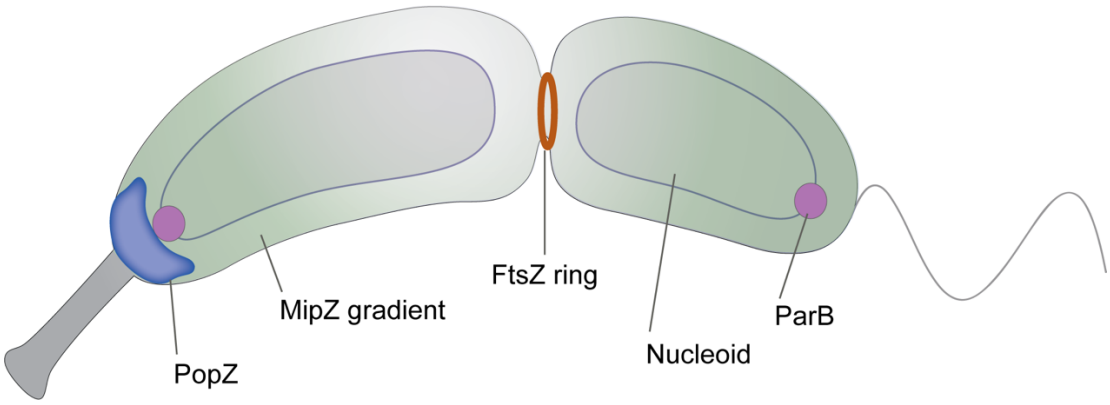

Figure 8. MipZ gradient-mediated positioning of the FtsZ cytokinetic ring in *C. crescentus*. Gradient-like distribution of MipZ over the nucleoid of a *C. crescentus* predivisional cell. MipZ dimers formed in the proximity of the ParB*S* partition complexes are retained in the polar regions of the cell through non-specific interaction with chromosomal DNA. The inhibitory effect of MipZ over FtsZ polymerization restricts Z-ring formation at midcell.

Apart from *C. crescentus*, the MipZ system has only been studied in the photosynthetic bacterium *Rhodobacter sphaeroides*. In this species, MipZ does not form a gradient, but it oscillates between the

cell poles in newly divided cells. Prior to cell division, MipZ forms a ring-like structure close to the FtsZ ring and likely regulates its polymerization (Dubarry *et al.*, 2019).

MipZ is widely distributed among alphaproteobacteria. However, the mechanisms by which it regulates cell division might have adapted to the different hosts. In chapter IV, we investigate the MipZ system in *Magnetospirillum gryphiswaldense*. We show that this bacterium possesses two MipZ homologues; one of them behaves like the *C. crescentus* protein, while the second displays a localization pattern reminiscent of the one of MipZ from *R sphearoides*.

Nucleotide-dependent molecular switches

Nucleotide-dependent switches alternate between two different states: a GTP (or ATP)-bound 'on' state and a GDP (or ADP)-bound 'off' state. The transition between these two states is driven by the nucleotide binding and hydrolysis activities (Bange & Sinning, 2013, Bourne *et al.*, 1990, Gasper *et al.*, 2009).

P-loop NTPases belong to a superclass of nucleotide-dependent molecular switches whose members regulate multiple cellular pathways in prokaryotes and eukaryotes. This superclass of GTPases and related ATPases can be divided into two classes: The first one is known as the translation factors (TRAFAC) class, which includes proteins involved in translation, signal transduction, and cell motility. The second, is named the signal recognition particle, MinD and BioD (SIMIBI) class, which includes the SRP54 and SRP receptor (SR) GTPases and MinD-like ATPases involved in protein localization, chromosome partitioning, and membrane transport (Leipe *et al.*, 2002, Shan, 2016).

Upon nucleotide binding, members of the SIMIBI class such as ParA or MipZ, form homo- or heterodimers that are biologically active. Dimerization also efficiently assembles the catalytic machinery of this proteins by complementation of the active site of one protomer with that of the other (Gasper *et al.*, 2009). All regulatory NTPases described so-far utilize purine nucleotides (ATP or GTP). Remarkably, in chapter III, we identify ParB as the first nucleotide switch that specifically binds and hydrolyzes the pyrimidine nucleotide CTP.

Nucleotide-binding binding promotes the self-association of the ParB N-terminal domain which in turn, reduces its affinity for *parS* sites. Mutations in ParB that impair nucleotide binding and hydrolysis interfere with partition complex formation and result in chromosome segregation defects. Our results open the possibility that CTP could regulate the function of other protein families and thus be a more general regulatory principle in biology.

REFERENCES

Abeles, A.L., Friedman, S.A., and Austin, S.J. (1985) Partition of unit-copy miniplasmids to daughter cells. III. The DNA sequence and functional organization of the P1 partition region. *J Mol Biol* **185**: 261-272.

Ah-Seng, Y., Lopez, F., Pasta, F., Lane, D., and Bouet, J.Y. (2009) Dual role of DNA in regulating ATP hydrolysis by the SopA partition protein. *J Biol Chem* **284**: 30067-30075.

Austin, S., and Abeles, A. (1983a) Partition of unit-copy miniplasmids to daughter cells. I. P1 and F miniplasmids contain discrete, interchangeable sequences sufficient to promote equipartition. *J Mol Biol* **169**: 353-372.

Austin, S., and Abeles, A. (1983b) Partition of unit-copy miniplasmids to daughter cells. II. The partition region of miniplasmid P1 encodes an essential protein and a centromere-like site at which it acts. *J Mol Biol* **169**: 373-387.

Austin, S., Hart, F., Abeles, A., and Sternberg, N. (1982) Genetic and physical map of a P1 miniplasmid. *J Bacteriol* **152**: 63-71.

Austin, S., Ziese, M., and Sternberg, N. (1981) A novel role for site-specific recombination in maintenance of bacterial replicons. *Cell* **25**: 729-736.

Autret, S., Nair, R., and Errington, J. (2001) Genetic analysis of the chromosome segregation protein Spo0J of Bacillus subtilis: evidence for separate domains involved in DNA binding and interactions with Soj protein. *Mol Microbiol* **41**: 743-755.

Bange, G., and Sinning, I. (2013) SIMIBI twins in protein targeting and localization. *Nat Struct Mol Biol* **20**: 776-780.

Bartosik, A.A., Lasocki, K., Mierzejewska, J., Thomas, C.M., and Jagura-Burdzy, G. (2004) ParB of Pseudomonas aeruginosa: interactions with its partner ParA and its target parS and specific effects on bacterial growth. *J Bacteriol* **186**: 6983-6998.

Basu, M.K., and Koonin, E.V. (2005) Evolution of eukaryotic cysteine sulfinic acid reductase, sulfiredoxin (Srx), from bacterial chromosome partitioning protein ParB. *Cell Cycle* **4**: 947-952.

Ben-Yehuda, S., Rudner, D.Z., and Losick, R. (2003) RacA, a bacterial protein that anchors chromosomes to the cell poles. *Science* **299**: 532-536.

Bloom, K.S. (2014) Centromeric heterochromatin: the primordial segregation machine. *Annu Rev Genet* **48**: 457-484.

Böhm, K., Giacomelli, G., Schmidt, A., Imhof, A., Koszul, R., Marbouty, M., and Bramkamp, M. (2020) Chromosome organization by a conserved condensin-ParB system in the actinobacterium Corynebacterium glutamicum. *Nat Commun* **11**: 1485.

Bourne, H.R., Sanders, D.A., and McCormick, F. (1990) The GTPase superfamily: a conserved switch for diverse cell functions. *Nature* **348**: 125-132.

Bowman, G.R., Comolli, L.R., Zhu, J., Eckart, M., Koenig, M., Downing, K.H., Moerner, W.E., Earnest, T., and Shapiro, L. (2008) A polymeric protein anchors the chromosomal origin/ParB complex at a bacterial cell pole. *Cell* **134**: 945-955.

Breier, A.M., and Grossman, A.D. (2007) Whole-genome analysis of the chromosome partitioning and sporulation protein Spo0J (ParB) reveals spreading and origin-distal sites on the Bacillus subtilis chromosome. *Mol Microbiol* **64**: 703-718.

Broedersz, C.P., Wang, X., Meir, Y., Loparo, J.J., Rudner, D.Z., and Wingreen, N.S. (2014) Condensation and localization of the partitioning protein ParB on the bacterial chromosome. *Proc Natl Acad Sci U S A* **111**: 8809-8814.

Chaudhary, R., Gupta, A., Kota, S., and Misra, H.S. (2019) N-terminal domain of DivIVA contributes to its dimerization and interaction with genome segregation proteins in a radioresistant bacterium Deinococcus radiodurans. *Int J Biol Macromol* **128**: 12-21.

Chen, B.W., Lin, M.H., Chu, C.H., Hsu, C.E., and Sun, Y.J. (2015) Insights into ParB spreading from the complex structure of Spo0J and parS. *Proc Natl Acad Sci U S A* **112**: 6613-6618.

Cobbe, N., and Heck, M.M. (2004) The evolution of SMC proteins: phylogenetic analysis and structural implications. *Mol Biol Evol* **21**: 332-347.

Corrales-Guerrero, L., He, B., Refes, Y., Panis, G., Bange, G., Viollier, P.H., Steinchen, W., and Thanbichler, M. (2020) Molecular architecture of the DNA-binding sites of the P-loop ATPases MipZ and ParA from Caulobacter crescentus. *Nucleic Acids Res* **48**: 4769-4779.

Davis, M.A., and Austin, S.J. (1988) Recognition of the P1 plasmid centromere analog involves binding of the ParB protein and is modified by a specific host factor. *EMBO J* **7**: 1881-1888.

Debaugny, R.E., Sanchez, A., Rech, J., Labourdette, D., Dorignac, J., Geniet, F., Palmeri, J., Parmeggiani, A., Boudsocq, F., Anton Leberre, V., Walter, J.C., and Bouet, J.Y. (2018) A conserved mechanism drives partition complex assembly on bacterial chromosomes and plasmids. *Mol Syst Biol* **14**: e8516.

Ditkowski, B., Holmes, N., Rydzak, J., Donczew, M., Bezulska, M., Ginda, K., Kedzierski, P., Zakrzewska-Czerwińska, J., Kelemen, G.H., and Jakimowicz, D. (2013) Dynamic interplay of ParA with the

polarity protein, Scy, coordinates the growth with chromosome segregation in Streptomyces coelicolor. *Open Biol* **3**: 130006.

Dmowski, M., and Jagura-Burdzy, G. (2011) Mapping of the interactions between partition proteins Delta and Omega of plasmid pSM19035 from Streptococcus pyogenes. *Microbiology* **157**: 1009-1020.

Donovan, C., Sieger, B., Krämer, R., and Bramkamp, M. (2012) A synthetic Escherichia coli system identifies a conserved origin tethering factor in Actinobacteria. *Mol Microbiol* **84**: 105-116.

Dubarry, N., Willis, C.R., Ball, G., Lesterlin, C., and Armitage, J.P. (2019) Imaging of the Segregation of the 2 Chromosomes and the Cell Division Proteins of. *mBio* **10**.

Ebersbach, G., Briegel, A., Jensen, G.J., and Jacobs-Wagner, C. (2008) A self-associating protein critical for chromosome attachment, division, and polar organization in caulobacter. *Cell* **134**: 956-968.

Fadda, D., Santona, A., D'Ulisse, V., Ghelardini, P., Ennas, M.G., Whalen, M.B., and Massidda, O. (2007) Streptococcus pneumoniae DivIVA: localization and interactions in a MinCD-free context. *J Bacteriol* **189**: 1288-1298.

Fisher, G.L., Pastrana, C.L., Higman, V.A., Koh, A., Taylor, J.A., Butterer, A., Craggs, T., Sobott, F., Murray, H., Crump, M.P., Moreno-Herrero, F., and Dillingham, M.S. (2017) The structural basis for dynamic DNA binding and bridging interactions which condense the bacterial centromere. *Elife* **6**.

Gasper, R., Meyer, S., Gotthardt, K., Sirajuddin, M., and Wittinghofer, A. (2009) It takes two to tango: regulation of G proteins by dimerization. *Nat Rev Mol Cell Biol* **10**: 423-429.

Ginda, K., Bezulska, M., Ziółkiewicz, M., Dziadek, J., Zakrzewska-Czerwińska, J., and Jakimowicz, D. (2013) ParA of Mycobacterium smegmatis co-ordinates chromosome segregation with the cell cycle and interacts with the polar growth determinant DivIVA. *Mol Microbiol* **87**: 998-1012.

Graham, T.G., Wang, X., Song, D., Etson, C.M., van Oijen, A.M., Rudner, D.Z., and Loparo, J.J. (2014) ParB spreading requires DNA bridging. *Genes Dev* **28**: 1228-1238.

Gruber, S., and Errington, J. (2009) Recruitment of condensin to replication origin regions by ParB/SpoOJ promotes chromosome segregation in B. subtilis. *Cell* **137**: 685-696.

Hanai, R., Liu, R., Benedetti, P., Caron, P.R., Lynch, A.S., and Wang, J.C. (1996) Molecular dissection of a protein SopB essential for Escherichia coli F plasmid partition. *J Biol Chem* **271**: 17469-17475.

Harms, A., Treuner-Lange, A., Schumacher, D., and Søgaard-Andersen, L. (2013) Tracking of chromosome and replisome dynamics in Myxococcus xanthus reveals a novel chromosome arrangement. *PLoS Genet* **9**: e1003802.

Hester, C.M., and Lutkenhaus, J. (2007) Soj (ParA) DNA binding is mediated by conserved arginines and is essential for plasmid segregation. *Proc Natl Acad Sci U S A* **104**: 20326-20331.

Hwang, L.C., Vecchiarelli, A.G., Han, Y.W., Mizuuchi, M., Harada, Y., Funnell, B.E., and Mizuuchi, K. (2013) ParA-mediated plasmid partition driven by protein pattern self-organization. *EMBO J* **32**: 1238-1249.

Iniesta, A.A. (2014) ParABS system in chromosome partitioning in the bacterium Myxococcus xanthus. *PLoS One* **9**: e86897.

Ireton, K., Gunther, N.W.t., and Grossman, A.D. (1994) spo0J is required for normal chromosome segregation as well as the initiation of sporulation in Bacillus subtilis. *J Bacteriol* **176**: 5320-5329.

Jalal, A.S.B., Pastrana, C.L., Tran, N.T., Stevenson, C.E., Lawson, D.M., Moreno-Herrero, F., and Le, T.B.K. (2019) Structural and biochemical analyses of *Caulobacter crescentus* ParB reveal the role of its N-terminal domain in chromosome segregation. *bioRxive*.

Jalal, A.S.B., Tran, N.T., Stevenson, C.E., Chan, E.W., Lo, R., Tan, X., Noy, A., Lawson, D.M., and Le, T.B.K. (2020) Diversification of DNA-Binding Specificity by Permissive and Specificity-Switching Mutations in the ParB/Noc Protein Family. *Cell Rep* **32**: 107928.

Jecz, P., Bartosik, A.A., Glabski, K., and Jagura-Burdzy, G. (2015) A single parS sequence from the cluster of four sites closest to oriC is necessary and sufficient for proper chromosome segregation in Pseudomonas aeruginosa. *PLoS One* **10**: e0120867.

Jönsson, T.J., Johnson, L.C., and Lowther, W.T. (2009) Protein engineering of the quaternary sulfiredoxin.peroxiredoxin enzyme.substrate complex reveals the molecular basis for cysteine sulfinic acid phosphorylation. *J Biol Chem* **284**: 33305-33310.

Jönsson, T.J., Murray, M.S., Johnson, L.C., and Lowther, W.T. (2008) Reduction of cysteine sulfinic acid in peroxiredoxin by sulfiredoxin proceeds directly through a sulfinic phosphoryl ester intermediate. *J Biol Chem* **283**: 23846-23851.

Kawalek, A., Bartosik, A.A., Glabski, K., and Jagura-Burdzy, G. (2018) Pseudomonas aeruginosa partitioning protein ParB acts as a nucleoid-associated protein binding to multiple copies of a parS-related motif. *Nucleic Acids Res* **46**: 4592-4606.

Kawalek, A., Wawrzyniak, P., Bartosik, A.A., and Jagura-Burdzy, G. (2020) Rules and Exceptions: The Role of Chromosomal ParB in DNA Segregation and Other Cellular Processes. *Microorganisms* **8**.

Kiekebusch, D., Michie, K.A., Essen, L.O., Löwe, J., and Thanbichler, M. (2012) Localized dimerization and nucleoid binding drive gradient formation by the bacterial cell division inhibitor MipZ. *Mol Cell* **46**: 245-259.

Kusiak, M., Gapczynska, A., Plochocka, D., Thomas, C.M., and Jagura-Burdzy, G. (2011) Binding and spreading of ParB on DNA determine its biological function in Pseudomonas aeruginosa. *J Bacteriol* **193**: 3342-3355.

Lagage, V., Boccard, F., and Vallet-Gely, I. (2016) Regional Control of Chromosome Segregation in Pseudomonas aeruginosa. *PLoS Genet* **12**: e1006428.

Leipe, D.D., Wolf, Y.I., Koonin, E.V., and Aravind, L. (2002) Classification and evolution of P-loop GTPases and related ATPases. *J Mol Biol* **317**: 41-72.

Leonard, T.A., Butler, P.J., and Lowe, J. (2005) Bacterial chromosome segregation: structure and DNA binding of the Soj dimer--a conserved biological switch. *EMBO J* **24**: 270-282.

Leonard, T.A., Butler, P.J., and Löwe, J. (2004) Structural analysis of the chromosome segregation protein Spo0J from Thermus thermophilus. *Mol Microbiol* **53**: 419-432.

Lim, H.C., Surovtsev, I.V., Beltran, B.G., Huang, F., Bewersdorf, J., and Jacobs-Wagner, C. (2014) Evidence for a DNA-relay mechanism in ParABS-mediated chromosome segregation. *Elife* **3**: e02758.

Liu, M., Wang, J., Li, X., Sylvanno, M.J., Li, M., Zhang, M., and Wang, M. (2019) The crystal structure of sulfiredoxin from Arabidopsis thaliana revealed a more robust antioxidant mechanism in plants. *Biochem Biophys Res Commun* **520**: 347-352.

Livny, J., Yamaichi, Y., and Waldor, M.K. (2007) Distribution of centromere-like parS sites in bacteria: insights from comparative genomics. *J Bacteriol* **189**: 8693-8703.

Lobocka, M., and Yarmolinsky, M. (1996) P1 plasmid partition: a mutational analysis of ParB. *J Mol Biol* **259**: 366-382.

Lynch, A.S., and Wang, J.C. (1995) SopB protein-mediated silencing of genes linked to the sopC locus of Escherichia coli F plasmid. *Proc Natl Acad Sci U S A* **92**: 1896-1900.

Minnen, A., Attaiech, L., Thon, M., Gruber, S., and Veening, J.W. (2011) SMC is recruited to oriC by ParB and promotes chromosome segregation in Streptococcus pneumoniae. *Mol Microbiol* **81**: 676-688.

Mohl, D.A., and Gober, J.W. (1997) Cell cycle-dependent polar localization of chromosome partitioning proteins in Caulobacter crescentus. *Cell* **88**: 675-684.

Murray, H., Ferreira, H., and Errington, J. (2006) The bacterial chromosome segregation protein Spo0J spreads along DNA from parS nucleation sites. *Mol Microbiol* **61**: 1352-1361.

Musacchio, A., and Desai, A. (2017) A Molecular View of Kinetochore Assembly and Function. *Biology (Basel)* **6**.

Ohzeki, J., Larionov, V., Earnshaw, W.C., and Masumoto, H. (2019) De novo formation and epigenetic maintenance of centromere chromatin. *Curr Opin Cell Biol* **58**: 15-25.

Oliferenko, S. (2018) Understanding eukaryotic chromosome segregation from a comparative biology perspective. *J Cell Sci* **131**.

Osorio-Valeriano, M., Altegoer, F., Steinchen, W., Urban, S., Liu, Y., Bange, G., and Thanbichler, M. (2019) ParB-type DNA Segregation Proteins Are CTP-Dependent Molecular Switches. *Cell* **179**: 1512-1524.e1515.

Pillet, F., Sanchez, A., Lane, D., Anton Leberre, V., and Bouet, J.Y. (2011) Centromere binding specificity in assembly of the F plasmid partition complex. *Nucleic Acids Res* **39**: 7477-7486.

Pióro, M., Małecki, T., Portas, M., Magierowska, I., Trojanowski, D., Sherratt, D., Zakrzewska-Czerwińska, J., Ginda, K., and Jakimowicz, D. (2019) Competition between DivIVA and the nucleoid for ParA binding promotes segrosome separation and modulates mycobacterial cell elongation. *Mol Microbiol* **111**: 204-220.

Ptacin, J.L., Lee, S.F., Garner, E.C., Toro, E., Eckart, M., Comolli, L.R., Moerner, W.E., and Shapiro, L. (2010) A spindle-like apparatus guides bacterial chromosome segregation. *Nat Cell Biol* **12**: 791-798.

Radnedge, L., Youngren, B., Davis, M., and Austin, S. (1998) Probing the structure of complex macromolecular interactions by homolog specificity scanning: the P1 and P7 plasmid partition systems. *EMBO J* **17**: 6076-6085.

Rodionov, O., Lobocka, M., and Yarmolinsky, M. (1999) Silencing of genes flanking the P1 plasmid centromere. *Science* **283**: 546-549.

Romero Romero, M.L., Yang, F., Lin, Y.R., Toth-Petroczy, A., Berezovsky, I.N., Goncearenco, A., Yang, W., Wellner, A., Kumar-Deshmukh, F., Sharon, M., Baker, D., Varani, G., and Tawfik, D.S. (2018) Simple yet functional phosphate-loop proteins. *Proc Natl Acad Sci U S A* **115**: E11943-E11950.

Sanchez, A., Cattoni, D.I., Walter, J.C., Rech, J., Parmeggiani, A., Nollmann, M., and Bouet, J.Y. (2015) Stochastic Self-Assembly of ParB Proteins Builds the Bacterial DNA Segregation Apparatus. *Cell Syst* **1**: 163-173.

Sanchez, A., Rech, J., Gasc, C., and Bouet, J.Y. (2013) Insight into centromere-binding properties of ParB proteins: a secondary binding motif is essential for bacterial genome maintenance. *Nucleic Acids Res* **41**: 3094-3103.

Schofield, W.B., Lim, H.C., and Jacobs-Wagner, C. (2010) Cell cycle coordination and regulation of bacterial chromosome segregation dynamics by polarly localized proteins. *EMBO J* **29**: 3068-3081.

Schumacher, M.A., and Funnell, B.E. (2005) Structures of ParB bound to DNA reveal mechanism of partition complex formation. *Nature* **438**: 516-519.

Schumacher, M.A., Lee, J., and Zeng, W. (2016) Molecular insights into DNA binding and anchoring by the Bacillus subtilis sporulation kinetochore-like RacA protein. *Nucleic Acids Res* **44**: 5438-5449.

Schumacher, M.A., Mansoor, A., and Funnell, B.E. (2007) Structure of a four-way bridged ParB-DNA complex provides insight into P1 segrosome assembly. *J Biol Chem* **282**: 10456-10464.

Schumacher, M.A., Piro, K.M., and Xu, W. (2010) Insight into F plasmid DNA segregation revealed by structures of SopB and SopB-DNA complexes. *Nucleic Acids Res* **38**: 4514-4526.

Shan, S.O. (2016) ATPase and GTPase Tangos Drive Intracellular Protein Transport. *Trends Biochem Sci* **41**: 1050-1060.

Sharpe, M.E., and Errington, J. (1996) The Bacillus subtilis soj-spo0J locus is required for a centromere-like function involved in prespore chromosome partitioning. *Mol Microbiol* **21**: 501-509.

Smurova, K., and De Wulf, P. (2018) Centromere and Pericentromere Transcription: Roles and Regulation … in Sickness and in Health. *Front Genet* **9**: 674.

Song, D., Rodrigues, K., Graham, T.G.W., and Loparo, J.J. (2017) A network of cis and trans interactions is required for ParB spreading. *Nucleic Acids Res* **45**: 7106-7117.

Sullivan, N.L., Marquis, K.A., and Rudner, D.Z. (2009) Recruitment of SMC by ParB-parS organizes the origin region and promotes efficient chromosome segregation. *Cell* **137**: 697-707.

Surtees, J.A., and Funnell, B.E. (1999) P1 ParB domain structure includes two independent multimerization domains. *J Bacteriol* **181**: 5898-5908.

Taylor, J.A., Pastrana, C.L., Butterer, A., Pernstich, C., Gwynn, E.J., Sobott, F., Moreno-Herrero, F., and Dillingham, M.S. (2015) Specific and non-specific interactions of ParB with DNA: implications for chromosome segregation. *Nucleic Acids Res* **43**: 719-731.

Thanbichler, M., and Shapiro, L. (2006) MipZ, a spatial regulator coordinating chromosome segregation with cell division in Caulobacter. *Cell* **126**: 147-162.

Tran, N.T., Stevenson, C.E., Som, N.F., Thanapipatsiri, A., Jalal, A.S.B., and Le, T.B.K. (2018) Permissive zones for the centromere-binding protein ParB on the Caulobacter crescentus chromosome. *Nucleic Acids Res* **46**: 1196-1209.

van Baarle, S., Celik, I.N., Kaval, K.G., Bramkamp, M., Hamoen, L.W., and Halbedel, S. (2013) Protein-protein interaction domains of Bacillus subtilis DivIVA. *J Bacteriol* **195**: 1012-1021.

van Hooff, J.J., Tromer, E., van Wijk, L.M., Snel, B., and Kops, G.J. (2017) Evolutionary dynamics of the kinetochore network in eukaryotes as revealed by comparative genomics. *EMBO Rep* **18**: 1559-1571.

Vecchiarelli, A.G., Han, Y.W., Tan, X., Mizuuchi, M., Ghirlando, R., Biertumpfel, C., Funnell, B.E., and Mizuuchi, K. (2010a) ATP control of dynamic P1 ParA-DNA interactions: a key role for the nucleoid in plasmid partition. *Mol Microbiol* **78**: 78-91.

Vecchiarelli, A.G., Han, Y.W., Tan, X., Mizuuchi, M., Ghirlando, R., Biertümpfel, C., Funnell, B.E., and Mizuuchi, K. (2010b) ATP control of dynamic P1 ParA-DNA interactions: a key role for the nucleoid in plasmid partition. *Mol Microbiol* **78**: 78-91.

Vecchiarelli, A.G., Hwang, L.C., and Mizuuchi, K. (2013) Cell-free study of F plasmid partition provides evidence for cargo transport by a diffusion-ratchet mechanism. *Proc Natl Acad Sci U S A* **110**: E1390-1397.

Vecchiarelli, A.G., Mizuuchi, K., and Funnell, B.E. (2012) Surfing biological surfaces: exploiting the nucleoid for partition and transport in bacteria. *Mol Microbiol* **86**: 513-523.

Volante, A., and Alonso, J.C. (2015) Molecular Anatomy of ParA-ParA and ParA-ParB Interactions during Plasmid Partitioning. *J Biol Chem* **290**: 18782-18795.

Watanabe, E., Wachi, M., Yamasaki, M., and Nagai, K. (1992) ATPase activity of SopA, a protein essential for active partitioning of F plasmid. *Mol Gen Genet* **234**: 346-352.

Wu, L.J., and Errington, J. (2003) RacA and the Soj-Spo0J system combine to effect polar chromosome segregation in sporulating Bacillus subtilis. *Mol Microbiol* **49**: 1463-1475.

Yamaichi, Y., Bruckner, R., Ringgaard, S., Möll, A., Cameron, D.E., Briegel, A., Jensen, G.J., Davis, B.M., and Waldor, M.K. (2012) A multidomain hub anchors the chromosome segregation and chemotactic machinery to the bacterial pole. *Genes Dev* **26**: 2348-2360.

Yamaichi, Y., and Niki, H. (2000) Active segregation by the Bacillus subtilis partitioning system in Escherichia coli. *Proc Natl Acad Sci U S A* **97**: 14656-14661.

Chapter II:

Bactofilin-mediated organization of the ParAB*S* chromosome segregation system in *Myxococcus xanthus*

Lin Lin,[1,2,§,#] Manuel Osorio Valeriano,[1,2,#] Andrea Harms,[3] Lotte Søgaard-Andersen,[3,4] and Martin Thanbichler [1,2,4,*]

This chapter is written in manuscript style and was published in *Nature Communications* in November 2017. My contribution to this work included designing and performing the biochemical interaction studies, analyzing the data obtained, elaborating the respective figure panels and writing the methods part for the corresponding experiments.

[1] Laboratory for Microbiology, Faculty of Biology, Philipps University, 35043 Marburg, Germany
[2] Max Planck Fellow Group "Bacterial Cell Biology", Max Planck Institute for Terrestrial Microbiology, 35043 Marburg, Germany
[3] Department of Ecophysiology, Max Planck Institute for Terrestrial Microbiology, 35043 Marburg, Germany
[4] LOEWE Center for Synthetic Microbiology, Hans-Meerwein-Straße, 35043 Marburg, Germany

[§] current address: Biozentrum, University of Basel, 4056 Basel, Switzerland

[#] These authors contributed equally to this work.
[*] Correspondence: thanbichler@uni-marburg.d

ABSTRACT

In bacteria, homologs of actin, tubulin, and intermediate filament proteins often act in concert with bacteria-specific scaffolding proteins to ensure the proper arrangement of cellular components. Among the bacteria-specific factors are the bactofilins, a widespread family of polymer-forming proteins whose biology is poorly investigated. Here, we study the three bactofilins BacNOP in the rod-shaped bacterium *Myxococcus xanthus*. We show that BacNOP co-assemble into elongated scaffolds that restrain the ParAB*S* chromosome segregation machinery to the subpolar regions of the cell. The centromere (*parS*)-binding protein ParB associates with the pole-distal ends of these structures, whereas the DNA partitioning ATPase ParA binds along their entire length, using the newly identified protein PadC (MXAN_4634) as an adapter. The integrity of these complexes is critical for proper nucleoid morphology and chromosome segregation. BacNOP thus mediate a novel mechanism of subcellular organization that recruits proteins to defined sites within the cytoplasm, far off the cell poles.

INTRODUCTION

The function of cells critically depends on the proper spatiotemporal organization of their components. In particular, many proteins need to be targeted to distinct subcellular positions to perform localized activities in vital processes such as DNA segregation, cell division, cell polarity, or cell growth. Eukaryotic cells often sort proteins into membrane-bounded organelles to confine their distribution and establish compartments with specialized functions. Bacteria, by contrast, usually lack this compartmentalization mechanism. Nevertheless, they have evolved strategies to organize their cytoplasm into functionally distinct domains, whose maintenance is essential for survival and fitness (Rudner & Losick, 2010, Shapiro *et al.*, 2009, Schlimpert *et al.*, 2012).

In rod-shaped bacteria, specialized subcellular domains are most commonly established at the cell poles. Interestingly, the molecular landmarks guiding the formation of polar domains vary significantly among different bacterial lineages (Lin & Thanbichler, 2013, Treuner-Lange & Søgaard-Andersen, 2014, Laloux & Jacobs-Wagner, 2014). Among the best-studied determinants are the scaffolding proteins DivIVA and PopZ. DivIVA is a coiled-coil protein that is highly conserved among Gram-positive bacteria. It assembles into lattice-like oligomeric structures *in vitro* (Stahlberg *et al.*, 2004, Oliva *et al.*, 2010) and specifically associates with negatively curved membranes at the cell poles and division septa (Ramamurthi & Losick, 2009, Eswaramoorthy *et al.*, 2011, Lenarcic *et al.*, 2009). Depending on the species, these assemblies interact, directly or indirectly, with different proteins to regulate cell division (Bramkamp *et al.*, 2008, Patrick & Kearns, 2008), chromosome segregation (Ben-Yehuda *et al.*, 2003, Wu & Errington, 2003, Ginda *et al.*, 2013, Donovan *et al.*, 2012, Ditkowski *et al.*, 2013), and/or cell wall biogenesis (Hempel *et al.*, 2008, Letek *et al.*, 2008, Sieger *et al.*, 2013). PopZ, on the other hand, is limited to Gram-negative alphaproteobacteria. Its homolog from *Caulobacter crescentus* was shown to form branched oligomers *in vitro* and to self-assemble into a dense matrix that is associated with the cell poles (Ebersbach *et al.*, 2008, Bowman *et al.*, 2008, Bowman *et al.*, 2013, Laloux & Jacobs-Wagner, 2013). Apart from mediating the polar localization of signaling proteins involved in cell cycle regulation, PopZ also plays a central role in chromosome segregation by controlling the localization and dynamics of the chromosome segregation machinery (Ebersbach *et al.*, 2008, Bowman *et al.*, 2008, Bowman *et al.*, 2010).

Both PopZ and, in part, DivIVA affect chromosome segregation by interacting with the ParAB*S* DNA partitioning system, a highly conserved module that mediates segregation of the chromosomal replication origin regions in a wide variety of bacteria (Gerdes *et al.*, 2010, Wang *et al.*, 2013). ParB is a DNA-binding protein that recognizes conserved sequence (*parS*) motifs clustered within the origin region (Mohl & Gober, 1997). In *C. crescentus*, the resulting ParB·*parS* complex interacts with the PopZ matrix, leading to its attachment to the cell poles (Bowman *et al.*, 2008, Ebersbach *et al.*, 2008). At the

onset of S-phase, the single origin region is released from the old pole and duplicated. Its two copies immediately re-associate with ParB and then move apart, with one of them reconnecting to PopZ at the old pole and one traversing the cell and attaching to a newly formed PopZ matrix at the opposite (new) cell pole (Mohl & Gober, 1997, Thanbichler & Shapiro, 2006, Toro *et al.*, 2008, Shebelut *et al.*, 2010, Bowman *et al.*, 2010). Origin movement is directed by ParA, a Walker-type ATPase that acts as a nucleotide-dependent molecular switch cycling between an ATP-bound, dimeric and an ADP-bound, monomeric state (Leonard *et al.*, 2005, Schofield *et al.*, 2010, Ptacin *et al.*, 2010). ParA dimers bind non-specifically to the nucleoid and, in addition, interact with the ParB·*parS* complexes, thereby tethering them to the nucleoid surface. ParB, in turn, stimulates the ATPase activity of interacting ParA dimers, inducing their disassembly. As a consequence, the ParB·*parS* complex is loosened from the nucleoid and able to reconnect with adjacent ParA dimers, thereby gradually moving across the nucleoid surface by a ratchet-like mechanism (Vecchiarelli *et al.*, 2013b, Hwang *et al.*, 2013, Leonard *et al.*, 2005, Schofield *et al.*, 2010, Ptacin *et al.*, 2010). Efficient translocation of the tethered complex was proposed to depend on the elastic properties of the chromosome (Lim *et al.*, 2014). Its directionality is determined by a gradient in the concentration of ParA dimers on the nucleoid that is highest in the vicinity of the new pole and gradually decreases towards the moving ParB·*parS* complex (Shebelut *et al.*, 2010, Schofield *et al.*, 2010, Ptacin *et al.*, 2010, Fogel & Waldor, 2006). In *C. crescentus*, formation of this gradient depends on the sequestration of free ParA monomers by PopZ and the landmark protein TipN (Schofield *et al.*, 2010, Ptacin *et al.*, 2010) and, potentially, on localized dimerization of ParA within the polar PopZ matrix (Ptacin *et al.*, 2014).

Several years ago, an additional group of cytoskeletal proteins, called bactofilins, has been identified in bacteria (Kühn *et al.*, 2010, Koch *et al.*, 2011). Bactofilins are widespread among both Gram-positive and Gram-negative bacteria, with many species containing several paralogous copies. They possess a unique β-helical structure (Shi *et al.*, 2015, Vasa *et al.*, 2015, Zuckerman *et al.*, 2015, Kassem *et al.*, 2016) and polymerize into polymeric bundles or sheets in the absence of nucleotide cofactors *in vitro* (Kühn *et al.*, 2010, Koch *et al.*, 2011). Previous studies suggest that these polymers can act in various cellular pathways. In *C. crescentus*, two bactofilin paralogs assemble into a polar scaffold that recruits a peptidoglycan synthase involved in pole morphogenesis (Kühn *et al.*, 2010). The human pathogen *Helicobacter pylori*, by contrast, employs a single bactofilin to maintain its characteristic helical cell shape (Sycuro *et al.*, 2010), whereas two of these proteins are required to ensure proper flagellar assembly in *B. subtilis* (El Andari *et al.*, 2015). Finally, four bactofilin paralogs have been identified in *Myxococcus xanthus*, a model bacterium that has been studied intensively for its ability to translocate on solid surfaces and to aggregate into multi-cellular fruiting bodies under conditions of nutrient deprivation. One of them, BacM, is important for cell shape maintenance (Koch *et al.*, 2011). Its paralog

BacP, by contrast, has been implicated in the subpolar localization of the Ras-like GTPase SofG, which mediates the proper sorting of two pole-associated ATPases responsible for the extension and retraction of the polar type IV pili (Bulyha *et al.*, 2013).

Apart from its motility machineries, *M. xanthus* has a variety of other intriguing cell biological features, including a very particular organization of its ParAB chromosome partitioning proteins. In this organism, the spatial organization and segregation dynamics of chromosomal DNA are reminiscent of those in *C. crescentus*, with newborn cells containing a single, fully replicated chromosome whose origin and terminus regions are oriented towards the old and new pole, respectively (Harms *et al.*, 2013). However, rather than being attached to the poles, the ParB·*parS* complexes localize to distinct sites within the cytoplasm at a distance of about 1 µm from the cell tips. ParA, on the other hand, forms elongated subpolar patches that bridge the gap between the adjacent pole and the origin-associated ParB protein (Harms *et al.*, 2013, Iniesta, 2014). The molecular mechanism mediating this unique arrangement of the chromosome segregation machinery has so far remained unknown. In this work, we show that the three bactofilins BacNOP of *M. xanthus* co-assemble into extended scaffolds that stretch the subpolar regions and serve to control the localization of both the ParB·*parS* complex and ParA within the cell. ParB associates with the pole-distal ends of these structures, whereas ParA binds along their entire length, recruited by the newly identified adapter protein PadC. The integrity of this complex is critical for faithful chromosome segregation, indicating a close connection between ParAB localization and function. These findings reveal an additional role for bactofilins in the organization of *M. xanthus* cells. Moreover, they provide evidence for a novel mechanism of subcellular organization in which a cytoskeletal element serves as a molecular ruler to position proteins and DNA at a defined distance from the cell poles.

RESULTS

BacNOP form elongated structures at the cell poles

The *M. xanthus* genome contains four bactofilin genes, named *bacP, bacO, bacN*, and *bacM*, respectively (Kühn *et al.*, 2010). Whereas *bacM* lies immediately downstream of the *parAB* operon, the *bacNOP* genes are located in a putative operon with two uncharacterized open reading frames (Figure 1a). The corresponding products show the typical architecture of bactofilins, comprising a central bactofilin (DUF583) domain that is flanked by short, unstructured N- and C-terminal regions (Figure 1b). Notably, BacP has a longer C-terminal region than its paralogs, suggesting a distinct functional role for this protein.

Previous studies have shown that BacM has a variable localization pattern, forming either helical cables that extend throughout the cell or rod-like filaments originating at its poles (Koch *et al.*, 2011, Kühn *et al.*, 2010). By contrast, BacP consistently assembles into extended subpolar patches at one or both ends of the cell (Bulyha *et al.*, 2013). The clustering of *bacNOP* suggested a functional relationship between the three gene products. To test whether BacNOP co-assembled into a single polymeric structure *in vivo*, we first reanalyzed the localization pattern of BacP using immunofluorescence microscopy (Figure 1c, upper panels). We observed that the shortest cells only contained a single full-sized subpolar patch of 1-2 µm length, whereas no or only faint fluorescence was observed on the opposite side of the cell. Longer cells displayed signals in both subpolar regions, which tended to differ slightly in dimension and intensity. Moreover, they frequently displayed an additional BacP patch at their center, the size of which increased with increasing cell length. Because the length of cells closely correlates with their cell cycle stage (Harms *et al.*, 2013), these results indicate that cells are born with one mature and one nascent BacP patch, the latter of which gradually grows to full size as the cells elongate. In parallel, a new patch starts to assemble at midcell, which is then split during cytokinesis, explaining the asymmetric distribution of BacP immediately after fission. Analyzing the localization patterns of BacO and a BacN derivative tagged with a hemagglutinin epitope (BacN-HA), we observed very similar localization patterns (Figure 1c, middle and lower panels). The three proteins thus appear to occupy the same subcellular sites, suggesting that they could indeed co-assemble into a joint structure.

To determine whether BacP, BacO, and BacN in fact bind to each other, we performed co-localization analyses in the heterologous host *Escherichia coli*, a species lacking endogenous bactofilin homologs. When produced together, mCherry-BacP, CFP-BacO, and YFP-BacN formed extended subpolar or midcell patches whose signals were perfectly superimposable (Figure 1d). These assemblies did not colocalize with the inclusion body-associated chaperone IbpA (Supplementary Figure 1a) and were permeable to freely diffusible YFP (compare Supplementary Figure 5a). In addition, they were able to

specifically recruit interacting proteins (see below), suggesting that they represent loose networks of BacNOP polymers rather than compact aggregates of misfolded protein. Additional support for a close association between the three bactofilins came from the observation that it was possible to co-purify BacP and BacO with BacN-HA from *M. xanthus* cell lysates using anti-HA affinity beads (Figure 1e). Moreover, localization studies showed that in *M. xanthus* BacP patches were fragmented and less organized in the absence of BacO. Conversely, BacO localization was severely impaired in a *bacP* mutant, with filaments of varying length projecting from one of the cell poles (Supplementary Figure 1b). Loss of BacN or BacM, by contrast, had no effect on the positioning of the remaining bactofilin homologs (Supplementary Figure 1c). Immunoblot analysis confirmed that BacNOP accumulated independently of each other (Supplementary Figure 1d). Together, these findings strongly suggest that the three bactofilins interact directly to form a single heteropolymeric scaffold, with BacP constituting its core and BacO contributing to its positioning and integrity. BacN, by contrast, does not seem to have a significant role in the assembly process.

In an attempt to study BacNOP dynamics in live cells, we replaced individual bactofilin genes in *M. xanthus* with hybrids encoding N- or C-terminal fluorescent protein fusions. However, in all cases, the products formed only a single filament per cell that was detached from the cell poles, suggesting that modification of the termini interfered with the proper localization of BacNOP(Kühn *et al.*, 2010). Notably, however, fusion of BacN to the small HA affinity epitope had no effect on the positioning or biological activity of the structures (as shown below).

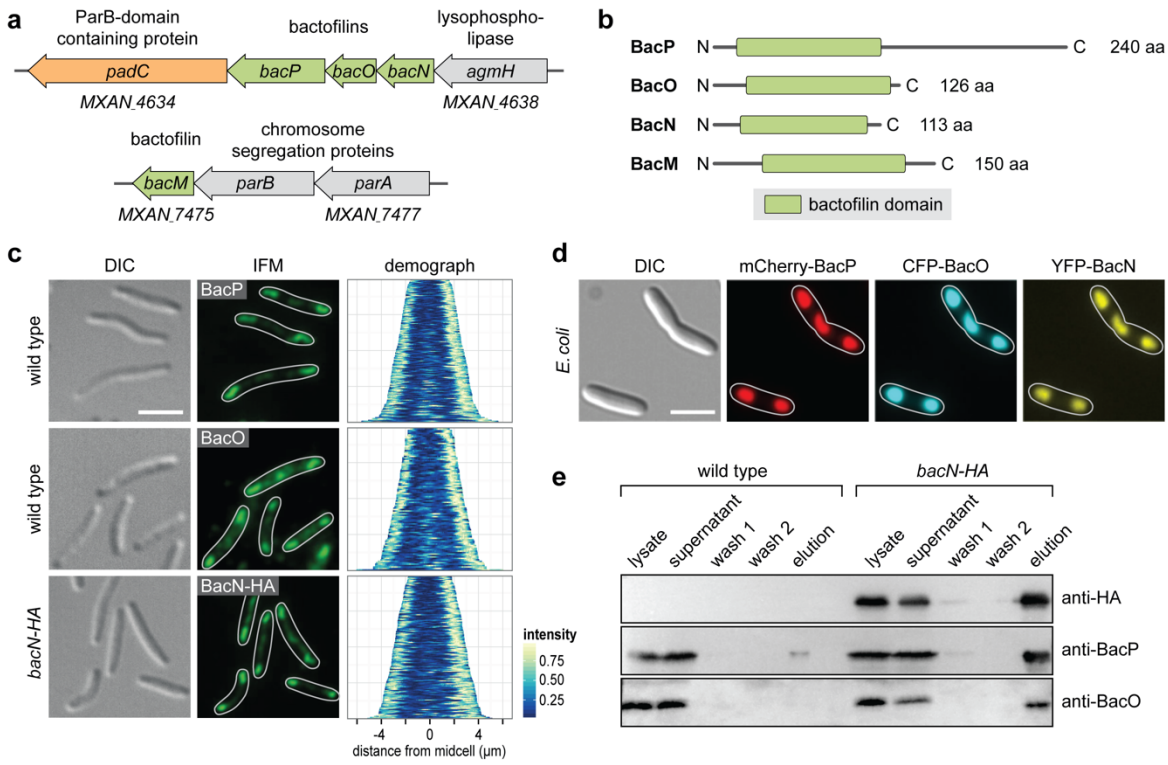

Figure 1. BacNOP co-assemble into extended bipolar structures. **(a)** Chromosomal context of the four bactofilin genes (*bacM*, *bacN*, *bacO*, and *bacP*) present in the *M. xanthus* DK1622 genome. Arrows indicate the direction of transcription. **(b)** Domain organization of the *M. xanthus* bactofilin homologs. The bactofilin (DUF583) domain is shown as a green box. Disordered regions are represented by black lines. **(c)** Subcellular localization of BacP, BacO, and BacN-HA. Cells of strains DK1622 (WT) or LL033 (*bacN::bacN-HA*) were analyzed by immunofluorescence microscopy (IFM), using anti-BacP, anti-BacO (DK1622), or anti-HA (LL033) primary antibodies and an Alexa-Fluor 488-conjugated secondary antibody (bar: 3 µm). In the demographs on the right, the fluorescence profiles of individual cells were sorted according to cell length and stacked on each other, with the shortest cell shown at the top and the longest cell shown at the bottom (n = 165 cells for BacP, 100 cells for BacO, and 150 cells for BacN-HA). **(d)** Heterologous reconstitution of the BacNOP complex in *E. coli*. *E. coli* strain Rosetta(DE3)pLysS bearing plasmids pLL54 (P_{T7}-*mCherry-bacP* e*cfp-bacO*) and pPS20 (P_{tet}-e*yfp-bacN*) was induced with 0.5 mM IPTG (for 3.5 h) and 0.2 µg/ml aTet (for 2 h) to stimulate the synthesis of fluorescently tagged bactofilin variants. Cells were analyzed by differential interference contrast (DIC) and fluorescence microscopy (bar: 3 µm). The Pearson's correlation coefficients (PCCs) for the patterns observed are 0.95 ± 0.04 (mCherry-BacP/CFP-BacO, n = 119 cells) and 0.94 ± 0.06 (mCherry-BacP/YFP-BacN, n = 119 cells). Note that despite the use of the strong T7 and *tet* promoters, the bactofilin fusions are only produced at moderate levels (Supplementary Figure 9). **(e)** Co-purification of BacN-HA, BacO, and BacP. Cell lysates of strains DK1622 (wild type) and LL033 (BacN-HA) were incubated with anti-HA affinity beads. After isolation of the beads and two washes, interacting proteins were eluted and detected by immunoblot analysis with anti-HA, anti-BacP, and anti-BacO antibodies. Samples of the cell lysates and the supernatants obtained during the isolation and washing steps were analyzed as controls. Full scans of the Western blots are shown in Supplementary Figure 10.

BacNOP mediate the subpolar localization of ParAB*S* in *M. xanthus*

In *M. xanthus*, ParA and ParB display unique localization patterns, with ParA forming elongated subpolar patches whose distal ends are associated with the origin-bound ParB·*parS* complex (as

verified in Figure 2a). Moreover, additional ParA patches are observed at the cell center during later stages of the cell cycle (Harms *et al.*, 2013, Iniesta, 2014). The striking similarity between the subcellular distributions of ParA and BacNOP, together with the proximity of the *bacM* and *parAB* genes (Figure 1a), raised the possibility that bactofilins were functionally associated with the ParAB*S* system. Consistent with this idea, we observed that a ParA-mCherry fusion (Harms *et al.*, 2013) failed to form subpolar patches in cells lacking the whole *bacNOP* cluster or only the *bacP* gene (Figure 2b). In the *bacP* mutant, the typical bipolar pattern of ParA was restored by ectopic expression of a complementing *bacP* copy (Supplementary Figure 2a), excluding polar effects of the mutation. Deletion of *bacO*, on the other hand, still allowed for the formation of subpolar ParA-mCherry patches (Supplementary Figure 2b), which however were highly irregular and reminiscent of the BacP structures observed in the Δ*bacO* background (compare Supplementary Figure 1b). In the absence of BacN, ParA localization was only slightly altered, whereas deletion of *bacM* had no significant effect (Supplementary Figure 2b). Based on these results, we conclude that bactofilins are necessary for maintaining the proper subcellular arrangement of ParA, with BacP playing a central role in this process.

Next, we analyzed the positioning of ParB in different bactofilin mutants. As previously reported(Harms *et al.*, 2013, Iniesta, 2014), wild-type cells generally showed one or two ParB-YFP foci that were placed at a distance of about 15-25% of the cell length from the nearest cell pole (Figure 2c). In cases with two foci, the signals were typically arranged symmetrically within the cell, indicating that origin replication and segregation had finished successfully (Figures 2c-f). However, in the Δ*bacMNOP* mutant, this highly regular pattern was severely disturbed, as indicated by a significantly lower segregation symmetry coefficient and a considerable increase in the distance (D_{min}) of foci from the nearest cell pole. Similar defects were observed when only *bacP* or *bacO* was deleted. Other bactofilin single-mutants, by contrast, showed only minor (Δ*bacN*) or no (Δ*bacM*) changes in ParB-YFP localization (Figures 2d-f). Thus, formation of subpolar BacNOP assemblies is critical for proper positioning of the ParB·*parS* complexes.

The involvement of BacNOP in ParAB positioning pointed to an interaction between these proteins. Co-localization analysis revealed that ParB-YFP was indeed consistently detected at the pole-distal ends of the BacNOP structures (Supplementary Figures 2c and 2d). Moreover, when cells were treated with the division inhibitor cephalexin, they formed extensive non-polar BacNOP assemblies with ParB-YFP foci positioned at both of their ends (Supplementary Figure 2e). These findings suggested that ParB specifically associates with the terminal regions of the bactofilin structures. To further test this possibility, we performed pull-down experiments on crude cell extracts of *M. xanthus* wild-type cells using purified StrepII-ParB as a bait. We found that BacP was retained on affinity beads loaded with

ParB but not on control beads lacking immobilized protein (Supplementary Figure 2f), supporting a role of BacP in ParB recruitment. However, subsequent *in vitro* analyses did not provide any evidence for a direct association between the two proteins (Supplementary Figure 2g). Similarly, bactofilin polymers did not appear to bind directly to ParA (see below). These results implied the existence of an additional, as-yet unknown factor that mediates the recruitment of ParAB to BacNOP patches.

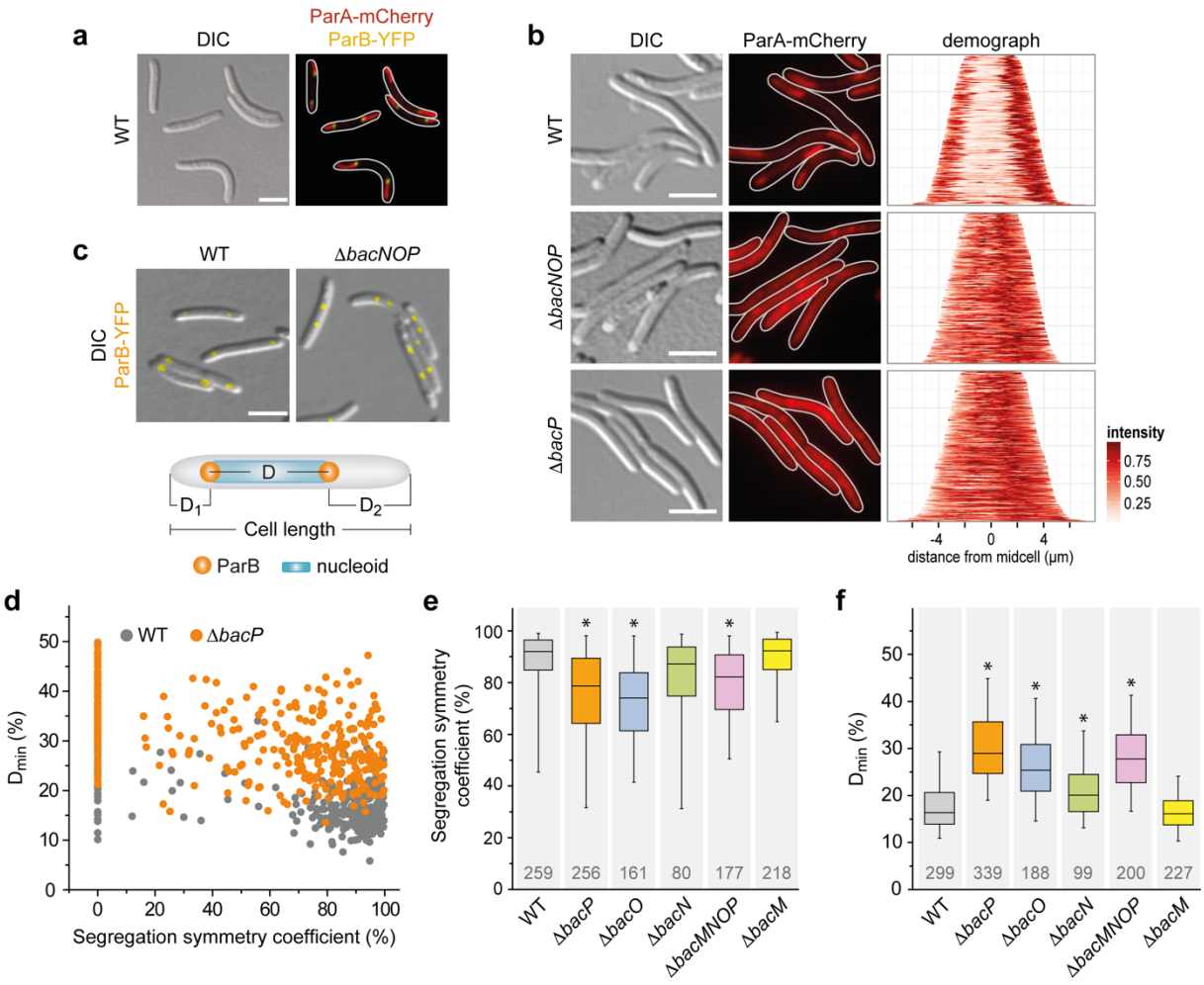

Figure 2. BacNOP are critical for proper localization of the ParAB chromosome segregation proteins. (a) Colocalization of ParA and ParB in *M. xanthus*. Strain LL162 (P_{parA}-*parA-mCherry* P_{cuoA}-*parB-eyfp*) was induced for 20 h with 100 µM $CuSO_4$ before imaging. Shown are a DIC micrograph and an overlay of the corresponding mCherry and YFP fluorescence images (bar: 3 µm). **(b)** Mislocalization of ParA in the absence of BacP. Cells of strains LL145 (P_{parA}-*parA-mCherry*), LL147 (Δ*bacNOP* P_{parA}-*parA-mCherry*) and LL152 (Δ*bacP* P_{parA}-*parA-mCherry*) were analyzed by DIC and fluorescence microscopy (bar: 3 µm). Demographs summarizing the single-cell fluorescence profiles observed for the three strains are given on the right (n = 166 cells for WT, 187 cells for Δ*bacNOP*, and 225 cells for Δ*bacP*). **(c)** Mislocalization of ParB in the absence of BacNOP. Shown are overlays of DIC and fluorescence micrographs of strains LL012 (P_{parB}-*parB-eyfp*) and LL019 (Δ*bacNOP* P_{parB}-*parB-eyfp*) (bar: 3 µm). The schematic explains the parameters used for the analysis in panels d-f. **(d)** Quantitative analysis of ParB localization in wild-type and Δ*bacP* populations. Cells of strain LL012 (P_{parB}-*parB-eyfp*) and LL015 (Δ*bacP* P_{parB}-*parB-eyfp*) were analyzed by DIC and fluorescence microscopy (n = 299 cells and 339 cells, respectively). Overlays of the images were used to determine the cell lengths and the distances of the ParB-YFP foci from the cell poles (D_1 and D_2; see panel c). The segregation symmetry coefficient *S* indicates how symmetrically ParB-YFP foci are arranged within the cell, with *S* = D/(D+D2-D1)x100% and D = cell

length-D1-D2. D_{min} gives the smallest distance between a ParB-YFP focus and a cell pole normalized to cell length, with $D_{min} = D_1$/cell lengthx100%. Note that, by definition, *S* = 0 % for cells containing only a single ParB-YFP focus. **(e and f)** Aberrant segregation and positioning of the ParB·origin complexes in the absence of bactofilins. The segregation symmetry coefficient (E) and D_{min} (F) were determined for strain LL012 (P_{parB}-*parB-eyfp*) (WT) and its derivatives LL015 (Δ*bacP*), LL018 (Δ*bacO*), LL014 (Δ*bacN*), LL016 (Δ*bacM* Δ*bacNOP*), and LL013 (Δ*bacM*). The data are represented by box plots. The center line shows the median, the box limits indicate the 25th and 75th percentile, and whiskers extend to the 5th and 95th percentile. Only cells containing two ParB-YFP foci were considered in panel e. The number of cells analyzed for each strain is given underneath the plots. Significant differences between the wild-type and mutant strains are indicated by asterisks ($p < 0.0001$; Mann-Whitney test).

BacNOP structures interact with the novel ParB-like protein PadC

In search of a potential adapter protein, we turned our attention to MXAN_4634, an uncharacterized open reading frame located immediately downstream of *bacNOP* (Figure 1a). Its predicted gene product features a long disordered N-terminal region and C-terminal segment that includes a ParB-like nuclease ($ParB_C$) domain (Figure 3a). $ParB_C$ domains are typically found in chromosome partitioning proteins of the ParB family, where they mediate the interaction with the centromeric *parS* sites, lacking nuclease activity[33]. The clustering of *bacNOP* and MXAN_4634, hereafter referred to as *padC* (*Par*B_C *d*omain-*c*ontaining protein), is conserved among various members of the *Myxococcales*, suggesting a functional connection between these genes (Supplementary Figure 3). To test for a role of PadC in bactofilin function, we first determined the subcellular localization of the protein. Intriguingly, in a merodiploid strain, PadC-mCherry showed the same bipolar distribution as BacNOP and ParA (Figures 3b and 3c). Colocalization studies verified that the signals produced by PadC-YFP and ParA-mCherry are indeed perfectly superimposable, suggesting that PadC could be part of the bactofilin·ParA complex (Figure 3d). To test this possibility, we determined the subcellular distribution of PadC in different bactofilin mutant backgrounds, using strains that carried a *padC-mCherry* fusion in place of the wild-type *padC* gene (Figure 3e and Supplementary Figures 4a and 4b). Of note, in the absence of the wild-type protein, the fusion often formed polar or sub-polar foci instead of coherent patches that were localized to the ends of the bactofilin structures, in line with the finding that the tagged protein is only partially functional (see Figures 4c-e and below). Importantly, however, upon deletion of the whole *bacNOP* cluster (Supplementary Figure 4a) or only the *bacP* gene (Figure 3e), PadC-mCherry lost this localization pattern and became evenly distributed within the cell. This effect was fully reversed by expression of a complementing copy of *bacP* in the Δ*bacP* mutant, excluding any polar effects of the mutation. In the absence of *bacO*, PadC-mCherry still formed foci, which were however mis-localized, whereas no major changes were observed in Δ*bacN* cells (Supplementary Figure 4b). Western blot analysis showed that mutations in the *bacNOP* genes did not affect the level of PadC (Supplementary Figure 4c). These results suggest that PadC is recruited to the bactofilin patches through interaction with BacP.

To determine whether PadC can directly associate with bactofilin complexes, we analyzed the ability of PadC-YFP to associate with a complex of mCherry-BacP and CFP-BacO in *E. coli*. A PadC-YFP fusion indeed perfectly colocalized with the bactofilin structures (Figure 3f), whereas YFP alone did not show any apparent affinity for them (Supplementary Figure 5a). A similar result was obtained for a truncated variant of PadC lacking the disordered N-terminal region (Venus-PadC$_{\Delta 1\text{-}239}$), suggesting that PadC may be recruited to the bactofilin patches through its C-terminal ParB$_C$ domain (Supplementary Figure 5b). This notion is supported by the finding that BacO and BacP can be pulled down from whole-cell extracts of *M. xanthus* wild-type cells using affinity beads loaded with hexahistidine-tagged PadC$_{\Delta 1\text{-}239}$ (Figure 3g).

To verify the interaction between bactofilins and PadC, we aimed to perform *in vitro* binding studies with purified components. The above results indicated that BacP was necessary and sufficient to recruit PadC. However, due to its tendency to form large polymeric assemblies, the full-length protein was not amenable to quantitative biochemical analyses. A distinctive feature of BacP is its unusually long C-terminal extension (Figure 1b). As the bactofilin domains of BacNOP are highly similar, we hypothesized that the determinants specifically recognized by PadC may be located in this unique, disordered region. To test this idea, we purified a C-terminal fragment of BacP (BacP$_C$) and analyzed it for its binding to an N-terminally truncated variant of PadC (PadC$_{\Delta N}$) using bio-layer interferometry (Figure 3h and Supplementary Figures 5c and 5d). Titration experiments revealed that the two fragments indeed interacted with high affinity (K_D = 340 nM). Collectively, these results demonstrate that PadC associates with bactofilin complexes both *in vivo* and *in vitro*.

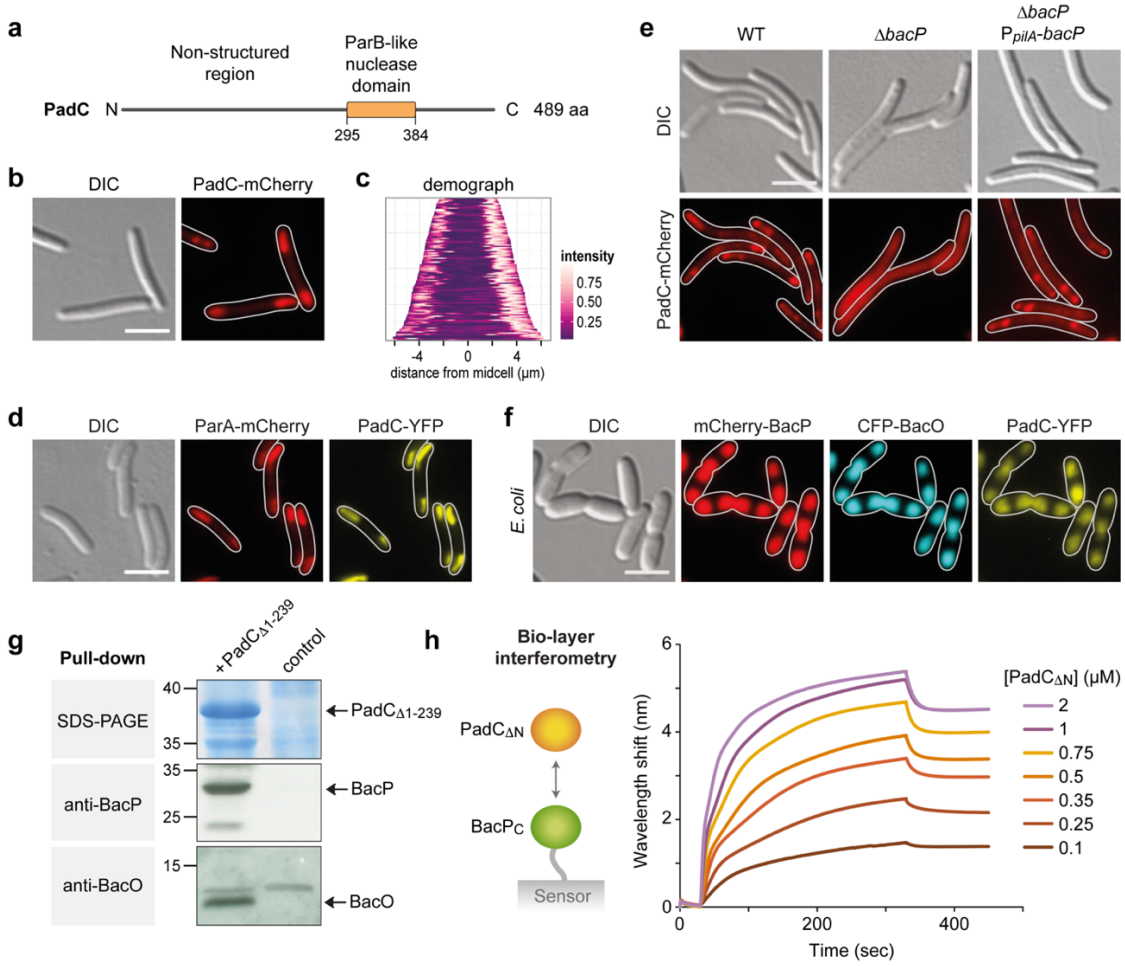

Figure 3. BacP interacts with the ParB-like nuclease domain-containing protein PadC. **(a)** Domain organization of PadC. The ParB-like nuclease ($ParB_C$) domain is indicated in orange. Numbers indicate its position within the polypeptide chain. **(b)** Subcellular localization of PadC in *M. xanthus*. Cells of strain LL134 (P_{cuoA}-*padC-mCherry*) were induced overnight with 200 µM $CuSO_4$ and analyzed by DIC and fluorescence microscopy (bar: 3 µm). **(c)** Demograph showing the subcellular distribution of PadC-mCherry in strain LL134 (see panel b; n = 109 cells). **(d)** Co-localization of PadC with ParA in *M. xanthus*. Strain LL201 (P_{parA}-*parA-mCherry* P_{van}-*padC-eyfp*) was induced for 2 h with 5 µM vanillate before imaging (bar: 3 µm). **(e)** Dependence of PadC localization on the presence of BacP. Cells of strains LL116 (*padC-mCherry*), LL130 (Δ*bacP padC-mCherry*), and LL135 (Δ*bacP* P_{pilA}-*bacP padC-mCherry*) were analyzed by DIC and fluorescence microscopy (bar: 3 µm). **(f)** Heterologous reconstitution of the BacP·BacO·PadC complex in *E. coli*. Cells of *E. coli* BL21(DE3) bearing plasmids pLL54 (P_{T7}-*mCherry-bacP cfp-bacO*) and pLL101 (P_{T7}-*padC-eyfp*) were induced for 1.5 h with 0.5 mM IPTG before imaging. (bar: 3 µm). The PCC for the mCherry-BacP and PadC-YFP signals is 0.92 ± 0.03 (n = 50 cells). **(g)** Co-purification of BacP and BacO with PadC. A whole-cell lysate of wild-type strain DK1622 was incubated with Ni-NTA beads loaded with purified His_6-$PadC_{Δ1-239}$ (+ PadC). After isolation of the beads, bound protein was eluted and subjected to SDS-PAGE and to immunoblot analysis with anti-BacP and anti-BacO antibodies, respectively. A reaction with beads not pre-incubated with purified protein served as a control. A molecular mass standard (in kDa) is given on the left. Arrows indicate the positions of the target proteins. Full scans of the SDS-gel and the Western blots are shown in Supplementary Figure 14. **(h)** Bio-layer interferometric analysis of the interaction between PadC and BacP. Sensors loaded with biotinylated $BacP_{Δ1-115}$ ($BacP_C$) were probed with the indicated concentrations of $PadC_{Δ1-281}$ ($PadC_{ΔN}$). The interaction kinetics were followed by monitoring the wavelength shifts resulting from changes in

the optical thickness of the sensor surface during association or dissociation of the analyte. The extent of non-specific binding of $PadC_{\Delta N}$ to the sensor surface was negligible (Supplementary Figure 5d).

PadC is required for proper ParAB*S* positioning

Having identified PadC as a new interactor of the BacNOP complex, we explored whether this protein could serve as an adapter recruiting ParA to the bactofilin patches. In support of this notion, ParA-mCherry lost its typical bipolar distribution in a Δ*padC* mutant and instead accumulated over the nucleoids, often forming distinct foci that could reflect its interaction with ParB·*parS* complexes (Figure 4a). This phenotype was reversed by expressing a complementing copy of *padC*, excluding any polar effects of the mutation (Figure 4a). Prompted by this finding, we further tested for a role of PadC in ParB localization. Quantitative analysis of the positions of ParB-YFP foci in Δ*padC* cells revealed a severe defect in the positioning of the chromosomal origin region (Figures 4b-e), similar to that observed in the Δ*bacP* background (compare Figures 2e and 2f). Concomitant deletion of *padC* and *bacNOP* did not produce a synthetic phenotype (Figures 4d and 4e). These results indicate that PadC cooperates with bactofilin complexes to properly localize the ParAB*S* chromosome partitioning machinery. Notably, we observed that deletion of *padC* appeared to affect the integrity of the bactofilin patches (Supplementary Figure 5e). PadC may thus mediate the positioning of ParB both by controlling the subcellular arrangement of ParA and by ensuring the correct assembly of bactofilin patches at the two cell poles.

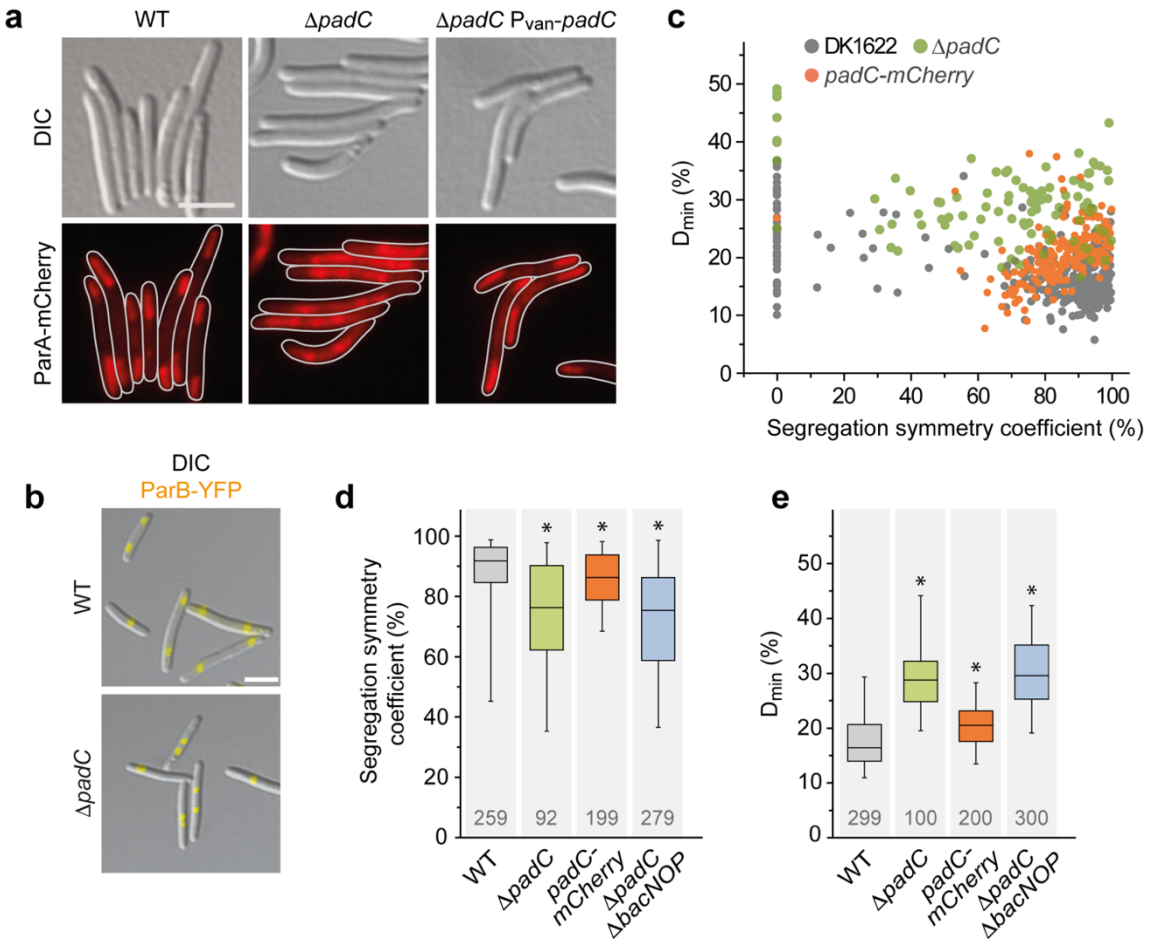

Figure 4. PadC is required for the subpolar localization of ParA and ParB. (a) Mislocalization of ParA in the absence of PadC. Cells of strains of LL145 (P_{parA}-*parA-mCherry*), LL154 (Δ*padC* P_{parA}-*parA-mCherry*) and LL192 (Δ*padC* P_{parA}-*parA-mCherry* P_{van}-*padC*) were analyzed by DIC and fluorescence microscopy. LL192 was induced for 2 h with 5 µM vanillate before imaging (bar: 3 µm). **(b)** Mislocalization of ParB in the absence of PadC. Cells of strains LL012 (P_{parB}-*parB-eyfp*) and LL102 (Δ*padC* P_{parB}-*parB-eyfp*) were visualized by DIC and fluorescence microscopy. Shown is an overlay of the two images (bar: 3 µm). **(c)** Quantitative analysis of ParB localization in strains expressing wild-type or mutant *padC* alleles. Cells of strains LL012 (P_{parB}-*parB-eyfp*), LL102 (*ΔpadC* P_{parB}-*parB-eyfp*) and LL118 (*padC-mCherry* P_{parB}-*parB-eyfp*) were analyzed by DIC and fluorescence microscopy (n = 299 cells for LL012, 100 cells for LL102, and 200 cells for LL118). Overlays of the images were used to determine D_{min} and the segregation symmetry of ParB-YFP foci (as described for Figure 2d). **(d and e)** Aberrant segregation and positioning of the ParB·origin complexes in *padC* and bactofilin mutants. The segregation symmetry (K) and D_{min} (L) were determined for strain LL012 (P_{parB}-*parB-eyfp*) (WT) and its derivatives LL102 (Δ*padC* P_{parB}-*parB-eyfp*), LL118 (*padC-mCherry* P_{parB}-*parB-eyfp*), and LL176 (Δ*padC* Δ*bacNOP* P_{parB}-*parB-eyfp*). Values are represented by box plots (defined in the legend to Figures 2e and 2f). Only cells containing two ParB-YFP foci were considered in panel d. The number of cells analyzed for each strain is given. Significant differences between the wild-type and mutant strains are indicated by asterisks ($p < 0.0001$; Mann-Whitney test).

PadC interacts with ParA

Because PadC was colocalized with ParA and required for the recruitment of ParA to the BacNOP complexes, we aimed to test for a direct interaction between the two proteins *in vitro* (Figure 5a). As observed for other ParA orthologs(Lim *et al.*, 2014), ParA from *M. xanthus* was only soluble in the

presence of ATP, which restricted biochemical analyses to the dimeric form of the protein (see also Figure 5b). Bio-layer interferometric analysis showed that $PadC_{\Delta N}$ and purified ParA·ATP indeed tightly bind to each other (K_D = 0.9 µM), supporting a direct role of PadC in regulation of ParA localization. To further investigate the interplay between these two proteins, we turned to *in vivo* interaction studies. Interestingly, when produced heterologously in *E. coli*, PadC-YFP associated with the chromosomal DNA, leading to strong nucleoid condensation, whereas no such effect was observed upon synthesis of YFP alone (Figure 5c). This observation is consistent with the presence of a potential, although low-scoring, helix-turn-helix motif in the conserved $ParB_C$ domain of PadC (amino acids 346-367). Upon co-production of PadC-YFP and ParA-mCherry, the two fusions colocalized on the condensed nucleoids (Figure 5d). However, due to the non-specific DNA-binding activity of ParA (Supplementary Figure 6a; wild type), it was difficult to draw conclusions on the ability of the proteins to interact with each other. To solve this issue, we generated ParA-mCherry variants with substitutions (R209A and R238E) in conserved residues shown to be involved in DNA binding (Hester & Lutkenhaus, 2007) (Figure 5b). These variants no longer associated with the chromosome in *E. coli* (Supplementary Figure 6a). However, upon co-expression with PadC-YFP, they again localized to the condensed nucleoids (Figure 5d and Supplementary Figure 6b), demonstrating a direct interaction between ParA-mCherry and the DNA-bound PadC-YFP fusion.

ParA cycles between a monomeric and dimeric state, dependent on nucleotide binding and hydrolysis (Figure 5b). To clarify how the interaction pattern of ParA correlates with its oligomerization state, we made substitutions in the protein that were predicted to block its ATPase cycle at the steps of dimerization (K31A and G32V) or nucleotide hydrolysis (K36R and D60A), based on previous studies of other ParA homologs(Toro *et al.*, 2008, Leonard *et al.*, 2005, Kiekebusch & Thanbichler, 2014, Vecchiarelli *et al.*, 2013a). As expected, the K31A and G32V variants lacked non-specific DNA-binding activity when synthesized in *E. coli* (Supplementary Figure 6a). Nevertheless, they localized to the condensed nucleoids upon co-expression with PadC-YFP, demonstrating that PadC is able to interact with ParA monomers (Figure 5d and Supplementary Figure 6b). This result was corroborated by ectopic expression of alleles encoding mutant ParA-YFP fusions in *M. xanthus* cells, which showed that both monomeric variants adopted the typical bipolar pattern observed for PadC (Figure 5e and Supplementary Figure 6c; compare Figure 3d). The ATP-locked, dimeric K36R and D60A variants, by contrast, still exhibited DNA-binding activity in *E. coli* (Supplementary Figure 6a). When expressed in *M. xanthus*, they lacked the typical bipolar distribution and instead formed a variable number of distinct foci (Figure 5e and Supplementary Figure 6c), likely positioned over the nucleoid. These results indicate that the bactofilin·PadC complex mostly associates with the monomeric form of ParA *in vivo*. However, DNA binding-defective variants of ParA (R209A and R238E) also colocalized with PadC

(Figures 5d and 5e and Supplementary Figure 6b), even though a sizable fraction of these proteins may be in the dimeric state (compare Figure 5b). Similarly, a constitutively dimeric ParA-mCherry variant defective in DNA binding (D60A R238E) (Supplementary Figure 6a) still colocalized with PadC-YFP in *E. coli* (Supplementary Figure 6b). Consistent with the *in vitro* data (see Figure 5a), PadC is thus also capable of interacting with ParA dimers, although this ParA species may be largely sequestered to the nucleoid and/or the origin-bound ParB complexes under normal conditions.

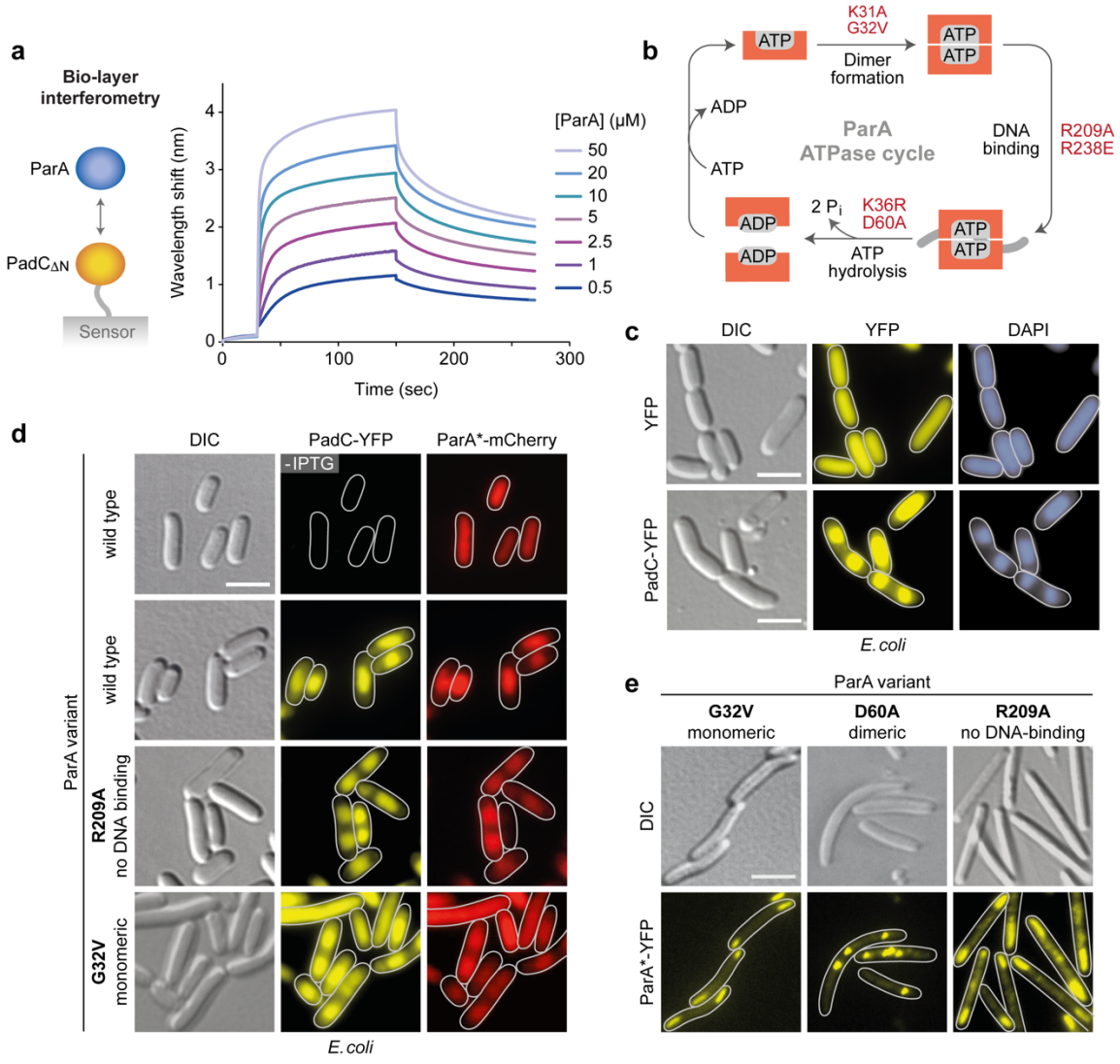

Figure 5. PadC interacts with ParA. **(a)** Bio-layer interferometric analysis of the interaction between PadC and ParA. Sensors loaded with biotinylated PadC$_{\Delta 1\text{-}281}$ (PadC$_{\Delta N}$) were probed with the indicated concentrations of ParA. The extent of non-specific binding of ParA to the sensor surface was negligible (Supplementary Figure 5d). **(b)** Putative ATPase cycle of ParA. Monomeric ParA binds ATP and dimerizes. The dimeric complex is able to interact non-specifically with chromosomal DNA. Spontaneous or ParB-stimulated ATP hydrolysis leads to dissociation of the ParA dimer and nucleotide exchange, thereby restarting the cycle. Mutations affecting specific steps of the ParA ATPase cycle are indicated in red. **(c)** DNA-binding activity of PadC. Cells of *E. coli* BL21(DE3) were transformed with plasmids pLL137(P$_{T7}$-*eyfp*) or pLL101 (P$_{T7}$-*padC-eyfp*) and induced for 4 h with 0.5 mM IPTG before imaging. DNA was stained with DAPI (bar: 3 µm). The PCC for the DAPI and PadC-YFP signals

is 0.94 ± 0.04 (n = 47 cells).**(d)** Co-localization of PadC with different ParA variants in *E. coli*. Cells of *E. coli* BL21(DE3) bearing pLL101 (P_{T7}-*padC-eyfp*) were transformed with pLL100 (P_{tet}-*parA-mCherry*), pLL124 (P_{tet}-$parA_{R209A}$-*mCherry*), or pLL172 (P_{tet}-$parA_{G32V}$-*mCherry*) and induced with 0.5 mM IPTG (for 2 h) and/or 0.2 µg/ml aTet (for 1 h) before imaging (bar: 3 µm). The PCCs for the PadC-YFP and ParA*-mCherry signals are 0.93 ± 0.05 (WT, n = 52 cells), 0.92 ± 0.11 (R209A, n = 52 cells), 0.90 ± 0.10 (G32V, n = 51 cells). **(e)** Subcellular localization of mutant ParA variants in *M. xanthus*. Cells of strain LL211 (P_{van}-$parA_{G32V}$-*eyfp*), LL218 (P_{van}-$parA_{D60A}$-*eyfp*), or LL193 (P_{van}-$parA_{R209A}$-*eyfp*) were induced for 5.5 h with 3 µM vanillate before imaging (bar: 3 µm).

PadC recruits ParA to bactofilin structures

The above results show that ParA binds to the $ParB_C$ domain of PadC. To further clarify the role of this interaction, we explored whether PadC was sufficient to mediate the recruitment of ParA to bactofilin structures. As a first approach, we set out to reconstitute a ternary BacP·PadC·ParA complex *in vitro*. To this end, a fragment comprising the C-terminal extension of BacP ($BacP_C$) was immobilized on a bio-layer interferometry sensor and incubated with $PadC_{\Delta N}$. Subsequent titration of the sensors with purified ParA led to the concentration-dependent formation of a stable ternary complex (Figure 6a). By contrast, no interaction was observed in control reactions lacking $PadC_{\Delta N}$ (Supplementary Figure 7a), supporting the idea that PadC functions as an adapter mediating the bactofilin-ParA interaction. To validate this hypothesis, we tested for the ability of PadC to recruit ParA-YFP to a complex of mCherry-BacP and CFP-BacO after heterologous expression in *E. coli* (Figure 6b). Consistent with the above results (Supplementary Figure 6a), wild-type ParA-YFP was quantitatively associated with the nucleoids in cells lacking PadC (Figure 6b; top row). By contrast, the fusion became partly associated with the bactofilin structures upon co-expression of *padC* (Figure 6b, middle row). When the same analysis was repeated with a monomeric, DNA binding-deficient variant (G32V) of ParA-YFP, the protein completely colocalized with the bactofilin structures (Figure 6b, bottom row), whereas a control strain producing YFP instead of the fusion protein displayed even fluorescence throughout the cell (Supplementary Figure 7b). In the absence of PadC, the monomeric variant was largely dispersed within the cell, although a minor fraction appeared associated with the bactofilin complexes (Supplementary Figure 7c). Together, these results strongly support the notion that PadC is necessary and sufficient to recruit ParA, and in particular its monomeric form, to the BacNOP complexes.

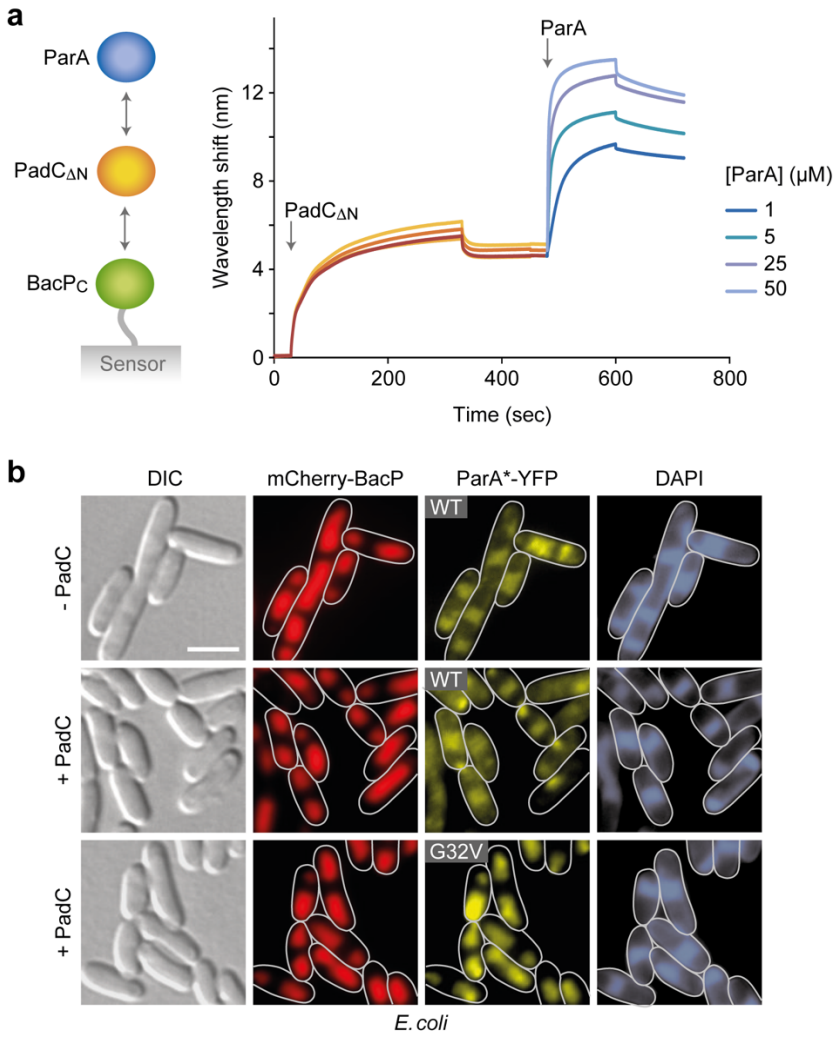

Figure 6. PadC recruits ParA to bactofilin polymers. **(a)** *In vitro* reconstitution of the ternary BacP·PadC·ParA complex. Biolayer interferometry sensors loaded with biotinylated $BacP_{\Delta 1\text{-}115}$ ($BacP_C$) were first incubated with 5 µM $PadC_{\Delta 1\text{-}281}$ ($PadC_{\Delta N}$). After the dissociation of loosely bound protein, the sensors were transferred into solutions containing the indicated concentrations of ParA (arrow) to monitor the interaction of ParA with the $BacP_C$·$PadC_{\Delta N}$ complex. The extent of non-specific binding of ParA to $BacP_C$-loaded sensors was negligible (Supplementary Figure 7a). **(b)** PadC-mediated recruitment of ParA to bactofilin complexes in the heterologous host *E. coli*. Cells of *E. coli* BL21(DE3) bearing plasmid pLL54 (P_{T7}-*mCherry-bacP cfp-bacO*) were transformed with plasmid pLL86 (P_{tet}-*parA-eyfp*) (WT) or pLL215 (P_{tet}-$parA_{G32V}$-*eyfp*) (G32V) and, when indicated (+ PadC), with plasmid pLL205 (P_{T7}-*padC*). Transformants were induced with 0.5 mM IPTG (for 3.5 h) and 0.2 µg/ml aTet (for 2.5 h) before imaging (bars: 3 µm). The PCCs for the mCherry-BacP and ParA*-YFP signals are 0.1 ± 0.27 (WT without PadC, n = 115 cells), 0.51 ± 0.23 (WT with PadC, n = 114 cells), and 0.93 ± 0.06 (G32V with PadC, n = 97 cells).

Defects in BacNOP or PadC affect chromosome structure and segregation

The lack of BacNOP or PadC strongly affects the subcellular arrangement of the ParAB*S* chromosome partitioning machinery. To clarify the physiological consequences, we first determined the dimensions of the nucleoids in various mutant backgrounds. Although bactofilin-deficient strains did not show any appreciable changes in cell length and growth rate (Supplementary Figures 8a and 8b), the nucleoids of bactofilin and *padC* mutants were significantly more compact, with their longitudinal sizes

decreasing from 51% of the cell length in the wild type to only 37% in the Δ*bacNOP* Δ*padC* strain (Figure 7a). Apart from this change in nucleoid size, bactofilin mutants often displayed an abnormal chromosome arrangement, with their origin regions displaced from the pole-proximal edges to more central regions of the nucleoids (Figure 7b). Notably, using ParB-YFP as a label for the chromosomal origin regions, we identified a moderate increase in origin copy numbers in the Δ*bacP* background (Supplementary Figure 8d). In line with this observation, populations of Δ*bacNOP* cells exhibited a noticeable fraction of cells with abnormally high DNA content (Figure 7c), suggesting that the proper positioning of ParAB*S* helps to make chromosome segregation more robust.

We fortuitously observed that fusion of BacP with the HA affinity tag created a variant that formed extended unipolar, instead of bipolar, patches (Figure 7d), providing a means to test the role of bactofilins on ParAB localization in a non-native context. Interestingly, *bacP-HA* cells showed impaired growth (Supplementary Figure 8c) and a severe chromosome segregation defects, with many of them containing either more than two (17 %) or no (8 %) ParB-YFP complexes (Supplementary Figure 8d). Consistently, a large fraction of the population contained an abnormal number of chromosome equivalents (Figure 7c), resulting in part from divisions over the nucleoid (Figure 7e). Moreover, even in cells containing two chromosomes, the origin regions were severely mislocalized and, in most cases, located in close proximity rather than at opposite edges of the nucleoid (Figure 7e). Importantly, in the mutant cells, ParA-mCherry had lost its typical bipolar localization pattern and displayed the same unipolar distribution as BacP-HA (Figure 7f). The asymmetric positioning of ParA and the concomitant sequestration of multiple chromosomal origin regions to a single bactofilin patch (see also Supplementary Figure 8e) thus appears to severely impede chromosome segregation. Collectively, these findings strongly support a model in which BacNOP form cytoskeletal structures that control the positioning of the ParAB*S* chromosome segregation machinery within the cell.

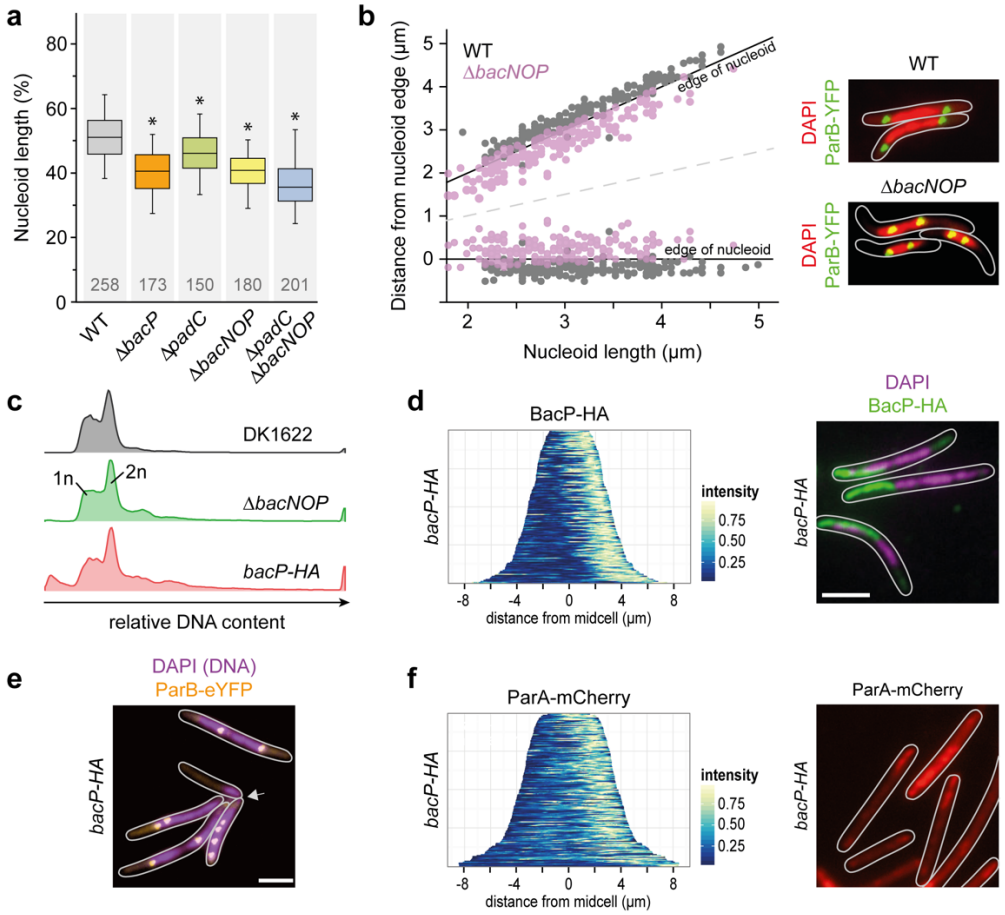

Figure 7. The BacNOP·PadC complex functions in nucleoid organization and DNA segregation. (a) Shortening of the nucleoids in the absence of bactofilins or PadC. Strains DK1622 (WT), LL001 (Δ*bacP*), LL101 (Δ*padC*), MT295 (Δ*bacNOP*), and LL174 (Δ*bacNOP* Δ*padC*) were stained with DAPI and analyzed by DIC and fluorescence microscopy. Shown is the length of the nucleoid along the longitudinal axis of the cell normalized to cell length. Values are represented as box plots (defined in the legend to Figures 2e and 2f). The number of cells analyzed for each strain is given. Significant differences between the wild-type and mutant strains are indicated by asterisks ($p < 0.001$; *t*-test). **(b)** Aberrant positioning of the chromosomal origin regions in the absence of BacNOP. Cells of strains LL012 (P_{parB}-*parB-eyfp*) and LL019 (Δ*bacNOP* P_{parB}-*parB-eyfp*) were analyzed by fluorescence microscopy to determine the positions of ParB-YFP foci relative to the edges of the nucleoid, as visualized by DAPI staining (n = 179 cells for LL012 and 181 cells for LL019). Images of exemplary cells are given on the right. **(c)** Changes in DNA content upon mutation of bactofilin genes. Cells of strains DK1622 (WT), MT295 (Δ*bacNOP*), and LL032 (*bacP-HA*) were incubated with a fluorescent DNA stain and subjected to flow cytometric analysis. Shown are histograms giving the distribution of fluorescence intensities in the different cell populations (n = 30,000 cells per strain). **(d)** Asymmetric subcellular distribution of BacP-HA. Cells of strain LL046 (*bacP-HA* P_{parB}-*parB-eyfp*) were subjected to immunofluorescence microscopy with anti-HA antibodies and treated with DAPI to visualize the nucleoids. The population-wide distribution of the immunofluorescence signals was visualized by demographic analysis (on the left; n = 150 cells). An exemplary overlay of the immunofluorescence and DAPI signals is shown on the right (bar: 3 µm). **(e)** Unequal distribution of chromosomal DNA and ParB·origin complexes in the presence of BacP-HA. Cells of strain LL046 were treated with DAPI and analyzed by fluorescence microscopy (bar: 3 µm). **(f)** Asymmetric subcellular distribution of ParA-mCherry in the presence of BacP-HA. Cells of strain LL150 (*bacP-HA* P_{parA}-*parA-mCherry*) were imaged by fluorescence microscopy. The population-wide distribution of the fluorescence signals was visualized by demographic analysis (on the left; n = 116 cells). An exemplary fluorescence image is given on the right (bar: 3 µm).

DISCUSSION

Apart from the universally conserved homologs of actin and tubulin, there are several groups of cytoskeletal proteins that are exclusively found in bacteria. Among them are the bactofilins, a widespread and highly conserved group of proteins whose biology is still largely unexplored (Lin & Thanbichler, 2013). In this work, we demonstrate that three bactofilin homologs in *M. xanthus* co-assemble into extended subpolar scaffolds which, together with the newly discovered protein PadC, control the positioning of the chromosomal origin segregation machinery. Unlike other bacterial landmark proteins, these structures do not recruit their interaction partners to the very tips of the cells but to well-defined positions within the cytoplasmic space, located at a considerable distance from the cell poles. The establishment of this additional, subpolar domain expands the range of potential protein localization sites, providing a new mechanism for cellular organization that may facilitate the assembly of multiple large macromolecular complexes within the polar or subpolar regions of the cell.

This study shows that BacN, BacO, and BacP consistently colocalize in the cell, indicating that they assemble into a joint polymeric structure. However, each of the three proteins can form filaments on its own *in vitro* (Kühn *et al.*, 2010). Therefore, it remains to be clarified whether the three paralogs polymerize into homopolymeric structures that subsequently assemble into heteromeric complexes or whether they associate randomly into mixed polymers. Notably, the functional contributions of the different paralogs vary significantly. Whereas BacN is largely redundant for the processes analyzed in this study, BacO is important for proper assembly of the bactofilin patches. The most pronounced phenotypes, however, are observed upon inactivation of BacP, which not only plays a central role in the formation of bactofilin patches but also mediates the recruitment of PadC and, thus, ParA to these structures. Apart from the architecture of the BacNOP complex, the precise subcellular location of the polymers formed is still unknown. BacNOP could potentially assemble into cytoplasmic filament bundles. On the other hand, recent work has demonstrated that bactofilins not only form filaments but also extensive two-dimensional arrays *in vitro*, depending on the experimental conditions (Vasa *et al.*, 2015). Consistently, live-cell imaging and electron cryo-tomographic studies suggest that the *C. crescentus* homologs assemble into sheet-like structures lining the inner face of the cytoplasmic membrane *in vivo* (Kühn *et al.*, 2010). It is, therefore, conceivable that *M. xanthus* BacNOP may form similar membrane-associated assemblies, but clarification of this issue will require the development of fully functional fluorescent protein fusions.

Despite the lack of nucleotide cofactors, the BacNOP structures assemble in a tightly controlled and cell cycle-dependent manner. New-born cells often display two differently sized complexes, a longer one at the old pole and a shorter one at the new pole, whose lengths gradually equalize as the cells grow. Before cell division, an additional patch is formed at midcell. Its dissection during cytokinesis

then re-establishes a nascent bactofilin complex at the new pole of the daughter cells (Figure 8a). Notably, cell cycle-regulated localization dynamics have also been observed for the bactofilin clusters of *C. crescentus* (Kühn *et al.*, 2010). The mechanisms controlling BacNOP assembly and localization still remain to be determined. However, given that bactofilins polymerize independently of nucleotide cofactors (Kühn *et al.*, 2010, Zuckerman *et al.*, 2015), their assembly may be regulated through protein-protein interactions. Of notice, inactivation of PadC led to a change in the localization pattern of BacNOP (Supplementary Figure 5e). Apart from recruiting ParA, this protein could therefore also be involved in coordinating bactofilin patch formation with cell cycle events such as chromosome replication or segregation.

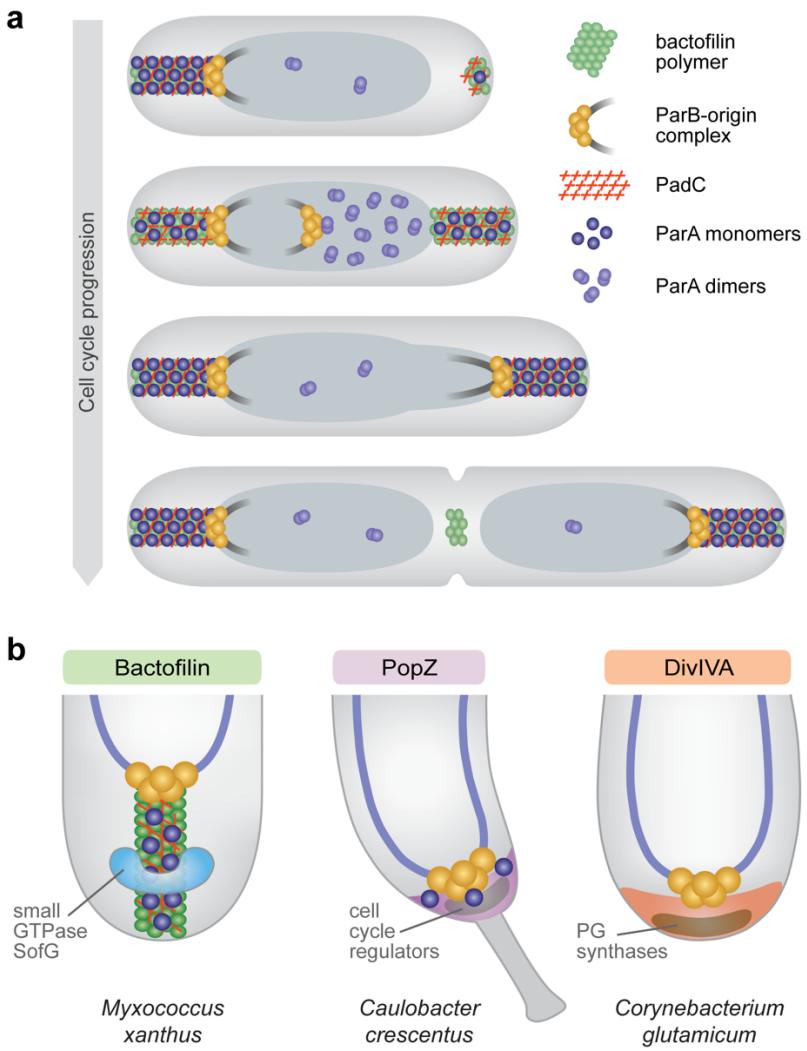

Figure 8. Model for the function of bactofilins in *M. xanthus*. (a) Organization of the *M. xanthus* chromosome segregation machinery by bipolar BacNOP·PadC complexes. Bactofilin structures assemble in a cell cycle-dependent manner. They interact with the adapter protein PadC, which in turn captures ParA monomers and thus mediates their retention in the subpolar regions of the cell. The tips of the bactofilin structures bind to the chromosomal ParB·*parS* complexes, thereby ensuring the proper arrangement of the two sister chromosomes after their segregation by nucleoid-associated ParA dimers. **(b)** Comparison of the polar scaffolding proteins BacNOP from *M. xanthus*, PopZ from *C. crescentus*, and DivIVA from the

actinomycete *C. glutamicum*. Despite their distinct evolutionary origins, all of these proteins function in the organization of the ParAB*S* chromosome segregation machinery. Moreover, they all interact with additional pole-associated factors, serving as multi-purpose hubs that help to spatially organize distinct cellular pathways.

We show that BacNOP serve to position the ParAB*S* chromosome segregation machinery within the cell. Interestingly, despite being encoded immediately downstream of the *parAB* genes, their paralog BacM appears not to be involved in this process but to function exclusively in cell shape maintenance (Koch *et al.*, 2011). Consistent with this notion, it lacks the typical bipolar localization pattern of BacNOP (Kühn *et al.*, 2010, Koch *et al.*, 2011), supporting the idea that paralogous bactofilins can act independently in distinct cellular pathways. Despite their functional diversity, bactofilins from different species may share a common role as localization factors for other proteins (Lin & Thanbichler, 2013). However, the determinants responsible for the recruitment of interacting factors have remained unknown. Our results now identify the long C-terminal extension of BacP as a central mediator of bactofilin function in *M. xanthus*, serving as a hub for the assembly of the PadC·ParA complex. Intriguingly, the ParA-binding ($ParB_C$) domain of PadC bears resemblance to the centromer-binding protein ParB, suggesting that the two proteins may use a similar mode of interaction with their common target ParA. However, structural analyses of the respective complexes are necessary to further investigate this possibility. Whereas our results clarify the pathway of ParA recruitment, the mechanisms underlying the immobilization of ParB at the ends of the BacNOP·PadC assemblies is still unclear. We did not observe any binding of purified ParB to the C-terminal extension of BacP, the $ParB_C$ domain of PadC *in vitro* (Supplementary Figure 2g). The protein may thus interact with the bactofilin core domain or other regions of BacP, BacO, and/or PadC, which are however not amenable to biochemical analysis at this point.

Interestingly, there are striking parallels in the (sub)polar targeting of ParA in *M. xanthus* and *C. crescentus*. Only the monomeric forms of *M. xanthus* ParA are efficiently recruited to the bactofilin·PadC complex *in vivo*. Dimeric variants, by contrast, localize to the nucleoid or ParB, but they are redirected to the subpolar regions when impaired in DNA binding. Exactly the same pattern was observed for the interaction of ParA with the polar scaffolding protein PopZ in *C. crescentus* (Schofield *et al.*, 2010, Ptacin *et al.*, 2010). In this species, the accumulation of ParA monomers within the PopZ matrix was suggested to confine ParA dimerization to the polar regions of the cell, thereby creating a gradient of DNA-bound dimers that dictates the directionality of the segregation process (Ptacin *et al.*, 2014). It is likely that the sequestration of ParA by the bactofilin·PadC complex serves a similar function during chromosome segregation in *M. xanthus*, but the precise mechanistic implications of this phenomenon still remain to be investigated. Interestingly, although ParA and ParB are essential in *M. xanthus*[50,51], inactivation of BacNOP or PadC has only a moderate effect on the overall efficiency of chromosome segregation, at least during vegetative growth. The BacNOP-PadC system may thus have

an auxiliary function that optimizes cellular fitness by enhancing the robustness of the segregation process. However, it remains to be clarified whether it may play a more critical role during the formation or outgrowth of myxospores, a feature typical of many species that possess the BacNOP and PadC proteins.

Apart from its role in chromosome organization, BacP has also been implicated in the positioning of a small GTPase, SofG, involved in the regulation of *M. xanthus* motility (Bulyha *et al.*, 2013). BacNOP structures thus serve as multi-purpose scaffolds that interact with factors involved in seemingly unrelated cellular pathways. A similar functional versatility is observed when comparing bactofilin homologs from different bacterial species (Lin & Thanbichler, 2013). It is likely that all bactofilins share the ability to form polymeric structures, based on their conserved DUF583 domain (Vasa *et al.*, 2015), serving as scaffolds for the assembly and localization of protein complexes. However, the nature of the proteins they recruit appears to vary between systems, resulting in the observed functional diversification.

Intriguingly, there are striking functional analogies between BacNOP and other polar scaffolding proteins such as PopZ and DivIVA, although there is no evolutionary or structural relationship between these factors (Figure 8b). Similar to BacNOP patches, *C. crescentus* PopZ (Bowman *et al.*, 2008, Ebersbach *et al.*, 2008) and DivIVA homologs from actinomycetes (Donovan *et al.*, 2012) interact with the centromere-binding protein ParB to control the positioning of the chromosomal origin regions. Moreover, both proteins interact with the chromosome partitioning ATPase ParA. This association can be either direct, as reported for PopZ and DivIVA from *M. smegmatis* (Ptacin *et al.*, 2014, Ginda *et al.*, 2013), or mediated through an adapter protein such as the coiled-coil-rich protein Scy in *S. coelicolor* (Ditkowski *et al.*, 2013). Moreover, each of these proteins interacts with additional factors not involved in chromosome segregation. PopZ, for instance, also mediates the polar localization of various proteins involved in *C. crescentus* cell cycle regulation (Ebersbach *et al.*, 2008, Bowman *et al.*, 2010), whereas DivIVA additionally organizes the polar peptidoglycan biosynthetic machinery of actinomycete species (Meniche *et al.*, 2014, Sieger *et al.*, 2013, Flardh, 2003). Moreover, DivIVA was shown to recruit another cytoskeletal structure, formed by the intermediate-filament-like protein FilP, to the growing cell poles of *S. coelicolor* hyphae (Fuchino *et al.*, 2013, Holmes *et al.*, 2013). Notably, there are also non-polymerizing proteins that act as multi-functional polar localization factors, including HubP, which mediates the polar recruitment of ParA, the flagellar apparatus, and chemotaxis arrays in *Vibrio cholerae* (Yamaichi *et al.*, 2012). Thus, many bacteria have a common need for pole-organizing factors that help arrange the chromosome segregation machinery and diverse macromolecular complexes within the cell. However, different evolutionary lineages have obviously found very different solutions to cope with this problem.

The reason why *M. xanthus* has evolved a mechanism to position proteins in the subpolar regions and not, as observed for other species, at the very poles of the cell is still unclear. However, a prominent feature of *M. xanthus* is its intricate motility machinery, whose coordination and activity involves an array of pole-associated structural and regulatory proteins (Zhang *et al.*, 2012). These factors may occupy a large part of the polar cell envelope and thus not leave sufficient space for other large macromolecular structures to assemble at the same site without causing steric or regulatory interference. It will be interesting to see whether other bacterial groups also use bactofilins to establish comparable subpolar domains and, thereby, expand their repertoire of potential protein localization sites.

METHODS

Media and growth conditions

M. xanthus DK1622 and its derivatives were grown at 32 °C in CTT medium(Hodgkin & Kaiser, 1977), supplemented with kanamycin (50 µg/ml) or oxytetracycline (10 µg/ml) when appropriate. *E. coli* strains were cultivated at 37 °C in LB medium containing antibiotics at the following concentrations (µg/ml in liquid/solid medium): ampicillin (100/200), chloramphenicol (20/30), kanamycin (30/50), tetracycline (15/15), gentamycin (15/20), spectinomycin (50/100). To induce the expression of genes from the P*van*, P*cop*, P*tet* or P*lac* promoters, media were supplemented with sodium vanillate, copper sulfate, anhydrotetracycline (aTet) or isopropyl-β-D-thiogalactopyranoside (IPTG), respectively, as indicated in the text.

Construction of plasmids and strains

The bacterial strains and plasmids used in this work are described in Supplementary Tables 1-4. The oligonucleotides used for their construction are listed in Supplementary Table 5. All plasmids were verified by DNA sequencing. *M. xanthus* was transformed by electroporation (Kashefi & Hartzell, 1995). Non-replicating plasmids were integrated into the *M. xanthus* chromosome by site-specific recombination at the phage Mx8 *attB* site (Magrini *et al.*, 1999) or by single-homologous recombination at the *cuoA* (Gomez-Santos *et al.*, 2012) or MXAN_18/19 (Iniesta *et al.*, 2012) locus. Gene replacement was achieved by double-homologous recombination using the counter-selectable *galK* marker (Ueki *et al.*, 1996). Proper chromosomal integration or gene replacement was verified by colony PCR.

Live-cell imaging

Exponentially growing cells were spotted on pads made of 1.5 % agarose in H_2O (*E. coli*) or 1.5 % agarose in TPM buffer (10 mM Tris/HCl, 1 mM potassium phosphate, 8 mM $MgSO_4$, pH 7.6) (*M. xanthus*). Images were taken with a Zeiss Axio Imager.M1 microscope equipped with a Zeiss Plan Apochromat 100x/1.40 Oil DIC objective and a Cascade:1K CCD camera (Photometrics) or with a Zeiss Axio Imager.Z1 microscope equipped with a 100x/1.46 Oil DIC objective and a pco.edge sCMOS camera (PCO). An X-Cite 120PC metal halide light source (EXFO, Canada) and ET-DAPI, ET-CFP, ET-YFP or ET-TexasRed filter cubes (Chroma, USA) were used for fluorescence detection. Nucleoids were visualized by incubating cells with 0.5 µg/ml 4',6-diamidino-2-phenylindole (DAPI) for 15-20 min prior to analysis. Images were recorded and processed with Metamorph 7.7 (Molecular Devices).

Immunofluorescence microscopy

Immunofluorescence microscopy was performed essentially as described (Bulyha *et al.*, 2009). Cells were grown to exponential phase and fixed with 1.6-2.6 % (w/v) paraformaldehyde and 0.008 % (w/v)

glutaraldehyde. After permeabilization in GTE buffer (20 mM Tris/HCl, pH 7.6, 50 mM glucose, 10 mM EDTA), the fixed cells were incubated with suitable antibodies in PBS buffer (137 mM NaCl, 2.7 mM KCl, 10 mM Na_2HPO_4, 2 mM KH_2PO_4) containing 2 % (w/v) bovine serum albumin (BSA; Carl-Roth, Germany). First, target proteins were labeled with a polyclonal anti-BacO or anti-BacP (Bulyha *et al.*, 2013) antibody or a monoclonal anti-HA antibody (Millipore) at dilutions of 1:500, 1:400, and 1:200, respectively. Immunocomplexes were then visualized with Alexa-Fluor 594 Goat Anti-Rabbit or Alexa-Fluor 488 Goat Anti-Rabbit secondary antibodies (Molecular Probes) at a dilution of 1:200. Before imaging, SlowFade® Antifade (Invitrogen) was applied to each sample.

Flow cytometry

Cultures were grown to exponential phase, diluted to an OD_{550} of 0.1, and treated for 40 min with the DNA-specific fluorescent dye Vybrant DyeCycle Orange (Invitrogen) at a final concentration of 10 µM. Subsequently, cells were analyzed by flow cytometry in a customized Fortessa Flow Cytometer (BD Biosciences), using an excitation wavelength of 488 nm and a Blue Green 542/27 band-pass emission filter. Data were acquired using FACSdiva 8.0 (BD Biosciences) and processed in FlowJo v10 (FlowJo LLC).

Growth curves

M. xanthus cells were grown to exponential phase, diluted with fresh medium to an OD_{550} of 0.025, and transferred in 24-well polystyrene microtiter plates. Growth was then monitored in an Infinite® M1000 PRO scanner (Tecan) by measuring the optical density at 550 nm (OD_{550}) at 15 min intervals, with three replicates per strain. Alternatively, cells were grown in Erlenmeyer flasks, sampled manually at defined intervals, and analyzed in an Ultrospec 2100 pro spectrophotometer (GE Healthcare).

Protein purification

To purify His_6-$BacP_{\Delta 1\text{-}115}$ ($BacP_C$), *E. coli* Rosetta(DE3)pLysS was transformed with plasmid pIB154 (Bulyha *et al.*, 2013) and grown at 37°C in LB medium. At an OD_{600} of 0.6, the cells were induced with 1 mM IPTG and cultivated for another 12 h at 18°C. They were then harvested by centrifugation, washed twice with buffer B1 (50 mM NaH_2PO_4, 300 mM NaCl, 10 mM imidazole, adjusted to pH 8.0 with NaOH), and stored at -80 °C. Thawed cells were resuspended in buffer B2 (50 mM NaH_2PO_4, 300 mM NaCl, 10 mM imidazole, 1 mM ß-mercaptoethanol, pH 8.0) containing 10 µg/ml DNase I and 100 µg/ml PMSF and disrupted by three passages through a French press (16,000 psi). After the removal of cell debris by centrifugation for 30 min at 30,000 xg, the cleared lysate was applied to a 5 ml HisTrap HP column (GE Healthcare) equilibrated with buffer B3 (50 mM NaH_2PO_4, 300 mM NaCl, 1 mM β-mercaptoethanol, pH 8.0) containing 20 mM imidazole. The column was washed with 5 column volumes (CV) of the same buffer, and protein was eluted with a linear imidazole gradient (20-250 mM in buffer B3) at a flow rate of 2 ml/min. Fractions containing high concentrations of protein were

pooled and dialyzed against 3 l of buffer P (25 mM HEPES/KOH, pH 7.6, 100 mM KCl, 10% (v/v) glycerol), The solution was then aliquoted, snap-frozen in liquid N_2, and stored at -80°C until further use.

To purify His_6-$PadC_{\Delta 1\text{-}281}$ ($PadC_{\Delta N}$), *E. coli* Rosetta(DE3)pLysS was transformed with plasmid pMO002 and grown at 37 ˚C in LB medium (3 l). At an OD_{600} of 0.8, protein overproduction was induced with 0.5 mM IPTG for 4 h. Cells were harvested, washed with buffer, and resuspended in buffer B2 containing 10 µg/ml DNase I and 100 µg/ml PMSF. After three passages through a French press (16,000 psi), the cell lysate was clarified by centrifugation at 30,000 g for 30 min, and the supernatant was applied onto a 5 ml HisTrap HP column (GE Healthcare) previously equilibrated with buffer B3 containing 20 mM imidazole. The column was washed with 5 CV of the same buffer, and protein was eluted with a linear imidazole gradient (20-250 mM in buffer B3) at a flow rate of 2 ml/min. Fractions containing high concentrations of protein were pooled and dialyzed against 3 l of buffer B5 (20 mM Tris/HCl, pH 8.0, 10 mM NaCl, 1 mM β-mercaptoethanol) at 4°C. After the removal of precipitates by centrifugation at 30,000 xg for 30 min, the solution was loaded onto a MonoQ 5/50 column (GE Healthcare) equilibrated with buffer B5. The column was washed with 20 CV of buffer B5 prior the application of a linear NaCl gradient (0.01-1 M NaCl in buffer B5) at a flow rate of 1 ml/min. Fractions containing the purified protein were pooled and dialyzed against 2 l of buffer C7 (25 mM HEPES/KOH, pH 8.0, 20 mM NaCl, 0.1 mM EDTA, 5 mM $MgCl_2$, 1 mM β-mercaptoethanol, 10 % (v/v) glycerol), snap-frozen, and stored at -80 ˚C until further use.

His_6-ParA was purified essentially as described previously (Lim *et al.*, 2014). *E. coli* Rosetta(DE3)pLysS cells carrying plasmid pAH17 (Harms *et al.*, 2013) were grown to an OD_{600} of 0.6 at 37 °C in LB medium (3 l). The cultures were chilled to 18°C, and 1 mM IPTG was added to induce His_6-ParA synthesis overnight at 18 °C. Cells were harvested by centrifugation, washed twice with buffer A1 (100 mM HEPES/KOH, pH 7.4, 100 mM KCl, 100 mM EDTA, 10% (v/v) glycerol), and resuspended in 25 ml of buffer A1 containing 10 µg/mL DNase I, 100 µg/mL PMSF, 0.5 mM MgATP, and 1 mM DTT. The cell suspension was incubated on ice for 20 min prior to addition of 4 M KCl to a final concentration of 1 M. Cells were disrupted by three passages through a French press (16,000 psi), and cell debris was removed by centrifugation at 30,000 xg and 4 °C for 30 min at. The clarified lysate was applied onto a 5 ml HisTrap HP column (GE Healthcare) equilibrated with buffer A2 (25 mM HEPES/KOH, pH 7.4, 450 mM KCl, 50 mM potassium glutamate, 1 mM $MgSO_4$, 1 mM DTT, 100 µM magnesium-ATP) containing 40 mM imidazole. After a wash with 5 CV of the same buffer, protein was eluted with a linear imidazole gradient (40-300 mM in buffer A2) at a flow rate of 2 ml/min. Fractions containing high concentrations of His_6-ParA were pooled, dialyzed against 2 l of buffer A4 (25 mM HEPES/KOH, pH 7.4, 100 mM KCl, 200 mM potassium glutamate, 1 mM $MgSO_4$, 1 mM DTT, 100 µM magnesium-ATP, 20% (v/v) glycerol),

snap-frozen, and stored at -80 ˚C until further use. BacO-His_6 was produced and purified as described previously[41].

To purify StrepII-ParB, *E. coli* Rosetta(DE3)pLysS was transformed with pLL80 and grown at 37 ˚C in 500 ml of LB medium. At an OD_{600} of 1, expression was induced with 0.5 mM IPTG for 3 h. Cells were harvested, washed twice with buffer B1, and resuspended in buffer NP (50 mM NaH_2PO_4, 300 mM NaCl, adjusted to pH 8.0 with NaOH) containing 10 µg/ml DNase I and 100 µg/ml PMSF. After three passages of the cells through a French press (16,000 psi), the lysates were cleared by centrifugation at 30,000 g for 30 min, mixed with Strep-Tactin® Superflow Plus (Qiagen) resin, and incubated with gentle agitation for 2 h at 4 ˚C. The resin was washed three times with buffer NP, and proteins were eluted with buffer NPD (50 mM NaH_2PO_4, 300 mM NaCl, 2.5 mM dethiobiotin, adjusted to pH 8.0 with NaOH). The eluate was dialyzed against 2.5 l dialysis buffer (50 mM NaH_2PO_4, 150 mM NaCl, 1 mM EDTA, adjusted to pH 8.0 with NaOH), snap-frozen, and stored at -80 ˚C until further use.

To purify His_6-$PadC_{\Delta 1\text{-}239}$, *E. coli* Rosetta(DE3)pLysS was transformed with pLL105 and grown at 37 ˚C in 750 ml of LB medium. At an OD_{600} of 0.8, expression was induced with 0.5 mM IPTG for 4 h. Cells were harvested, washed with buffer B1, and resuspended in buffer B2 containing 10 µg/ml Dnase I and 100 µg/ml PMSF. After three passages through a French press (16,000 psi), cell debris was removed by centrifugation at 30,000 g for 30 min. The cleared lysates were then mixed with Ni-NTA agarose beads (Qiagen) that had been equilibrated with buffer B2 for 2 h at 4 ˚C. The beads were washed with buffer B3 containing 20 mM imidazole, and protein was eluted with buffer B3 containing 250 mM imidazole. The eluate was dialyzed against 3 l of buffer B6 (50 mM HEPES, pH 7.2, 50 mM NaCl, 5 mM $MgCl_2$, 0.1 mM EDTA, 10% (v/v) glycerol, 1 mM ß-mercaptoethanol), snap-frozen, and stored at -80 ˚C until further use.

Antibodies and immunoblot analysis

Polyclonal anti-BacO and anti-PadC antibodies were raised by immunization of rabbits with purified BacO-His_6 or His_6-$PadC_{\Delta 1\text{-}239}$ (Eurogentec). Immunoblot analysis was performed as described previously (Thanbichler & Shapiro, 2006), using a polyclonal anti-BacO, anti-BacP (Bulyha *et al.*, 2013), anti-PadC, or anti-ParB(Harms *et al.*, 2013) antibody or a monoclonal anti-HA antibody (Millipore) at dilutions of 1:7500 (anti-BacO), 1:1000 (anti-BacP), 1:2500 (anti-PadC), 1:5000 (anti-ParB), or 1:8000 (anti-HA).

Bio-layer interferometry

Bio-layer interferometry experiments were conducted using a BLItz system equipped with High Precision Streptavidin (SAX) Biosensors (ForteBio). $BacP_C$ and $PadC_{\Delta N}$ were biotinylated with EZ-Link NHS-PEG4-Biotin (Thermo Scientific) as recommended by the manufacturer. After immobilization of the biotinylated proteins on the sensors and establishment of a stable baseline, association reactions were monitored at various analyte concentrations. At the end of each binding step, the sensor was

transferred into analyte-free buffer to follow the dissociation kinetics. The extent of non-specific binding was assessed by monitoring the interaction of analyte with unmodified sensors. All analyses were performed in BLItz binding buffer (25 mM HEPES/KOH, pH 7.6, 100 mM KCl, 10 mM $MgSO_4$, 1 mM DTT, 10 µM BSA, 0.01 % Tween). Reactions involving ParA were additionally supplemented with 150 mM potassium glutamate, 5 % glycerol, and 10 mM ATP.

Co-purification analysis

To identify interaction partners of BacN-HA, exponentially growing cultures (500 ml) of strains DK1622 and LL033 were treated for 20 min at 37°C with 0.6 % paraformaldehyde in PBS (pH 8.0). The cross-linking reaction was stopped by addition of 125 mM glycine in PBS (pH 8.0), and the culture was harvested by centrifugation at 12,000 g for 20 min at 4°C. After three washes with 200 ml PBS (pH 8.0), the cells were resuspended in 6 mL of Co-IP buffer (50 mM Tris/HCl, pH 7.6, 150 mM NaCl, 0.1% Triton X-100) supplemented with Complete Mini EDTA-free protease inhibitor (Roche) and disrupted by three passages through a French press (16,000 psi). The suspension was clarified by centrifugation at 12,000 g for 10 min at 4°C, and the supernatant was incubated with anti-HA-tag mAb Magnetic Beads (MBL Life science) for 12 h at 4°C. The beads were then washed three times with 1.5 ml of Co-IP buffer, resuspended in SDS sample buffer, and incubated for 20 min at 99 °C to elute bound protein. Samples were taken at different steps of the procedure and subjected to immunoblot analysis using anti-HA, anti-BacP and anti-BacO antibodies.

To identify interaction partners of StrepII-ParB, an exponentially growing culture (1 l) of wild-type strain DK1622 was treated with 0.6 % paraformaldehyde in PBS. The cross-linking reaction was stopped by addition of 125 mM glycine in PBS. Cells were harvested, resuspended in 15 ml buffer S (20 mM Tris-HCl, pH 7.6, 200 mM NaCl) supplemented with Complete Mini with EDTA protease inhibitor (Roche), and lysed by three passages through a French press (16,000 psi). After the removal of cell debris, the cleared lysate was mixed with Strep-Tactin® Superflow Plus resin that had been pre-incubated with 1 mg purified StrepII-ParB in buffer S. A similar mixture with beads not coupled to purified protein served as a negative control. After incubation overnight at 4 ˚C, the beads were washed with buffer S, and protein was eluted with NPD buffer (50 mM NaH_2PO_4, 300 mM NaCl, 2.5 mM dethiobiotin, adjusted to pH 8.0 with NaOH). The eluates were then concentrated with trichloroacetic acid and probed with anti-BacP antibodies.

To identify interaction partners of His_6-$PadC_{\Delta 1\text{-}239}$, cells of wild-type strain DK1622 (2 l) were treated with paraformaldehyde, harvested, and washed as described for StrepII-ParB. The cells were resuspended in 20 ml buffer S supplemented with Complete Mini without EDTA protease inhibitor (Roche) and lysed by three passages through a French press (16,000 psi). After the removal of cell debris, the cleared lysate was mixed with Ni-NTA agarose (Qiagen) beads that had been pre-incubated

for 1.5 h in buffer S with 1.5 mg purified His_6-$PadC_{\Delta 1-239}$. A similar mixture containing beads not coupled to purified protein served as negative control. After incubation overnight at 4 ˚C, the beads were washed with buffer S, and protein was eluted with buffer B3 (50 mM NaH_2PO_4, 300 mM NaCl, 1 mM ß-mercaptoethanol, adjusted to pH 8.0 with NaOH) containing 250 mM imidazole. The eluate was then subjected to immunoblot analysis with anti-BacP or anti-BacO antibodies.

Statistical and bioinformatic analysis

Data were plotted using Origin 6.1 (OriginLab) and QtiPlot 0.9.8.7 (http://www.qtiplot.com/). *t*-tests and Mann-Whitney rank sum tests were performed in SigmaPlot 13 (Systat Software), assuming two independent populations with a significance level of p=0.001. To generate demographs, fluorescence intensity profiles were measured with ImageJ 1.47v (http://imagej.nih.gov/ij). The data were then processed in R version 3.0.2 (The R Foundation for Statistical Computing; http://www.r-project.org) using the Cell Profiles script (http://github.com/ta-cameron/Cell-Profiles) (Cameron *et al.*, 2014). Pearson's correlation coefficients were determined using the Coloc 2 plugin for ImageJ (https://imagej.net/Coloc_2). Nucleotide and amino acid sequences and information on the domain structure of proteins were obtained from the National Center for Biotechnology Information (NCBI) (http://www.ncbi.nlm.nih. gov) (Coordinators, 2016). Protein secondary structures were predicted using the PSIPRED Protein Sequence Analysis Workbench (http://bioinf.cs.ucl.ac.uk/psipred) (Jones, 1999). The prediction of helix-turn-helix motifs was performed at the Pole BioInformatique Lyonnais (https://prabi.ibcp.fr) (Dodd & Egan, 1990). The domain structure of proteins was analyzed using the Pfam server (Finn *et al.*, 2016).

Data availability

The authors declare that all relevant data supporting the conclusions of this study are included in the published article and the accompanying Supplementary Information files. Any additional information is available from the corresponding author upon request.

ACKNOWLEDGEMENTS

We thank Julia Rosum for excellent technical assistance, Todd A. Cameron for help with the generation of demographs, Silvia G. Sierra for assistance with the flow cytometry analysis, and Patrick Schall for the construction of plasmids. This work was supported by funds from the Max Planck Society (to L.S.-A. and M.T.) and a Young Investigator Grant (RGY0076/2013-C104) from the Human Frontier Science Program (to M.T.). M.T. and L.S.-A. acknowledge funding from the German Research Foundation (DFG) through the Collaborative Research Center “Spatiotemporal dynamics of bacterial cells” (TRR 174). L.L. was supported by the DFG-funded Research Training Group “Intra- and Intercellular Transport and Communication” (GRK 1216). M.O.V. is a fellow of the International Max Planck Research School for Environmental, Cellular and Molecular Microbiology (IMPRS-Mic).

AUTHOR CONTRIBUTIONS

L.L. and A.H. performed the *in vivo* experiments. M.O.V. and L.L. performed the biochemical interaction analyses. L.L., M.O.V., M.T., A.H. and L.S.-A. analyzed the data. L.L., M.T. and M.O.V. conceived the study. L.L. and M.T. wrote the manuscript, with input from all other authors.

COMPETING FINANCIAL INTERESTS

The authors declare no competing financial interests.

REFERENCES

Rudner, D. Z. & Losick, R. Protein subcellular localization in bacteria. *Cold Spring Harbor Perspect. Biol.* **2**, a000307 (2010).

Shapiro, L., McAdams, H. H. & Losick, R. Why and how bacteria localize proteins. *Science* **326**, 1225-1228 (2009).

Schlimpert, S. *et al.* General protein diffusion barriers create compartments within bacterial cells. *Cell* **151**, 1270-1282 (2012).

Lin, L. & Thanbichler, M. Nucleotide-independent cytoskeletal scaffolds in bacteria. *Cytoskeleton* **70**, 409-423 (2013).

Treuner-Lange, A. & Søgaard-Andersen, L. Regulation of cell polarity in bacteria. *J. Cell Biol.* **206**, 7-17 (2014).

Laloux, G. & Jacobs-Wagner, C. How do bacteria localize proteins to the cell pole? *J. Cell Sci.* **127**, 11-19 (2014).

Stahlberg, H. *et al.* Oligomeric structure of the *Bacillus subtilis* cell division protein DivIVA determined by transmission electron microscopy. *Mol. Microbiol.* **52**, 1281-1290 (2004).

Oliva, M. A. *et al.* Features critical for membrane binding revealed by DivIVA crystal structure. *EMBO J.* **29**, 1988-2001 (2010).

Ramamurthi, K. S. & Losick, R. Negative membrane curvature as a cue for subcellular localization of a bacterial protein. *Proc. Natl. Acad. Sci. USA* **106**, 13541-13545 (2009).

Eswaramoorthy, P. *et al.* Cellular architecture mediates DivIVA ultrastructure and regulates min activity in *Bacillus subtilis*. *mBio* **2**, e00257-00211 (2011).

Lenarcic, R. *et al.* Localisation of DivIVA by targeting to negatively curved membranes. *EMBO J.* **28**, 2272-2282 (2009).

Bramkamp,, M., Emmins, R., Weston, L., Donovan, C., Daniel, R. A. & Errington J. A novel component of the division-site selection system of *Bacillus subtilis* and a new mode of action for the division inhibitor MinCD. *Mol. Microbiol.* **70**, 1556-1569 (2008).

Patrick, J. E. & Kearns, D. B. MinJ (YvjD) is a topological determinant of cell division in *Bacillus subtilis*. *Mol. Microbiol.* **70**, 1166-1179 (2008).

Ben-Yehuda, S., Rudner, D. Z. & Losick, R. RacA, a bacterial protein that anchors chromosomes to the cell poles. *Science* **299**, 532-536 (2003).

Wu, L. J. & Errington, J. RacA and the Soj-Spo0J system combine to effect polar chromosome segregation in sporulating *Bacillus subtilis*. *Mol. Microbiol.* **49**, 1463-1475 (2003).

Ginda, K., Bezulska, M., Ziolkiewicz, M., Dziadek, J., Zakrzewska-Czerwinska, J. & Jakimowicz, D. ParA of *Mycobacterium smegmatis* co-ordinates chromosome segregation with the cell cycle and interacts with the polar growth determinant DivIVA. *Mol. Microbiol.* **87**, 998-1012 (2013).

Donovan, C., Sieger, B., Kramer, R. & Bramkamp, M. A synthetic *Escherichia coli* system identifies a conserved origin tethering factor in Actinobacteria. *Mol. Microbiol.* **84**, 105-116 (2012).

Ditkowski. B*. et al.* Dynamic interplay of ParA with the polarity protein, Scy, coordinates the growth with chromosome segregation in *Streptomyces coelicolor*. *Open Biol.* **3**, 130006 (2013).

Hempel, A. M., Wang, S. B., Letek, M., Gil, J. A. & Flärdh, K. Assemblies of DivIVA mark sites for hyphal branching and can establish new zones of cell wall growth in *Streptomyces coelicolor*. *J. Bacteriol.* **190**, 7579-7583 (2008).

Letek, M. *et al.* DivIVA is required for polar growth in the MreB-lacking rod-shaped actinomycete *Corynebacterium glutamicum*. *J. Bacteriol.* **190**, 3283-3292 (2008).

Sieger, B., Schubert, K., Donovan, C. & Bramkamp, M. The lipid II flippase RodA determines morphology and growth in *Corynebacterium glutamicum*. *Mol. Microbiol.* **90**, 966-982 (2013).

Ebersbach, G., Briegel, A., Jensen, G. J. & Jacobs-Wagner, C. A self-associating protein critical for chromosome attachment, division, and polar organization in *Caulobacter*. *Cell* **134**, 956-968 (2008).

Bowman, G. R. *et al.* A polymeric protein anchors the chromosomal origin/ParB complex at a bacterial cell pole. *Cell* **134**, 945-955 (2008).

Bowman, G. R. *et al.* Oligomerization and higher-order assembly contribute to sub-cellular localization of a bacterial scaffold. *Mol. Microbiol.* **90**, 776-795 (2013).

Laloux, G. & Jacobs-Wagner, C. Spatiotemporal control of PopZ localization through cell cycle-coupled multimerization. *J. Cell Biol.* **201**, 827-841 (2013).

Bowman, G. R*. et al. Caulobacter* PopZ forms a polar subdomain dictating sequential changes in pole composition and function. *Mol. Microbiol.* **76**, 173-189 (2010).

Gerdes, K., Howard, M. & Szardenings, F. Pushing and pulling in prokaryotic DNA segregation. *Cell* **141**, 927-942 (2010).

Wang, X., Montero Llopis, P. & Rudner, D. Z. Organization and segregation of bacterial chromosomes. *Nat. Rev. Genet.* **14**, 191-203 (2013).

Mohl, D. A. & Gober, J. W. Cell cycle-dependent polar localization of chromosome partitioning proteins in *Caulobacter crescentus*. *Cell* **88**, 675-684 (1997).

Thanbichler, M. & Shapiro, L. MipZ, a spatial regulator coordinating chromosome segregation with cell division in *Caulobacter*. *Cell* **126**, 147-162 (2006).

Toro, E., Hong, S. H., McAdams, H. H. & Shapiro, L. *Caulobacter* requires a dedicated mechanism to initiate chromosome segregation. *Proc. Natl. Acad. Sci. USA* **105**, 15435-15440 (2008).

Shebelut, C. W., Guberman, J. M., van Teeffelen, S., Yakhnina, A. A. & Gitai, Z. *Caulobacter* chromosome segregation is an ordered multistep process. *Proc. Natl. Acad. Sci. USA* **107**, 14194-14198 (2010).

Leonard, T. A., Butler, P. J. & Löwe, J. Bacterial chromosome segregation: structure and DNA binding of the Soj dimer – a conserved biological switch. *EMBO J.* **24**, 270-282 (2005).

Schofield, W. B., Lim, H. C. & Jacobs-Wagner, C. Cell cycle coordination and regulation of bacterial chromosome segregation dynamics by polarly localized proteins. *EMBO J.* **29**, 3068-3081 (2010).

Ptacin, J. L. *et al.* A spindle-like apparatus guides bacterial chromosome segregation. *Nat. Cell Biol.* **12**, 791-798 (2010).

Vecchiarelli, A. G., Hwang, L. C. & Mizuuchi, K. Cell-free study of F plasmid partition provides evidence for cargo transport by a diffusion-ratchet mechanism. *Proc. Natl. Acad. Sci. USA* **110**, E1390-1397 (2013).

Hwang, L. C. *et al.* ParA-mediated plasmid partition driven by protein pattern self-organization. *EMBO J.* **32**, 1238-1249 (2013).

Lim, H. C., Surovtsev, I. V., Beltran, B. G., Huang, F., Bewersdorf, J. & Jacobs-Wagner, C. Evidence for a DNA-relay mechanism in ParABS-mediated chromosome segregation. *eLife* **3**, e02758 (2014).

Fogel, M. A. & Waldor, M. K. A dynamic, mitotic-like mechanism for bacterial chromosome segregation. *Genes Dev.* **20**, 3269-3282 (2006).

Ptacin, J. L. *et al.* Bacterial scaffold directs pole-specific centromere segregation. *Proc. Natl. Acad. Sci. USA* **111**, E2046-2055 (2014).

Kühn, J. *et al.* Bactofilins, a ubiquitous class of cytoskeletal proteins mediating polar localization of a cell wall synthase in *Caulobacter crescentus*. *EMBO J.* **29**, 327-339 (2010).

Koch, M. K., McHugh, C. A. & Hoiczyk, E. BacM, an N-terminally processed bactofilin of *Myxococcus xanthus*, is crucial for proper cell shape. *Mol. Microbiol.* **80**, 1031-1051 (2011).

Shi. C. *et al.* Atomic-resolution structure of cytoskeletal bactofilin by solid-state NMR. *Sci Adv* **1**, e1501087 (2015).

Vasa, S. *et al.* beta-Helical architecture of cytoskeletal bactofilin filaments revealed by solid-state NMR. *Proc. Natl. Acad. Sci. USA* **112**, E127-136 (2015).

Zuckerman, D. M., Boucher, L. E., Xie, K., Engelhardt, H., Bosch, J. & Hoiczyk, E. The bactofilin cytoskeleton protein BacM of *Myxococcus xanthus* Forms an extended β-sheet structure likely mediated by hydrophobic interactions. *PloS One* **10**, e0121074 (2015).

Kassem, M. M., Wang, Y., Boomsma, W. & Lindorff-Larsen, K. Structure of the bacterial cytoskeleton protein bactofilin by NMR chemical shifts and sequence variation. *Biophys. J.* **110**, 2342-2348 (2016).

Sycuro, L. K. *et al.* Peptidoglycan crosslinking relaxation promotes *Helicobacter pylori*'s helical shape and stomach colonization. *Cell* **141**, 822-833 (2010).

El Andari, J., Altegoer, F., Bange, G. & Graumann, P. L. *Bacillus subtilis* bactofilins are essential for flagellar hook- and filament assembly and dynamically localize into structures of less than 100 nm diameter underneath the cell membrane. *PloS One* **10**, e0141546 (2015).

Bulyha, I. *et al.* Two small GTPases act in concert with the bactofilin cytoskeleton to regulate dynamic bacterial cell polarity. *Dev. Cell* **25**, 119-131 (2013).

Harms, A., Treuner-Lange, A., Schumacher, D. & Søgaard-Andersen, L. Tracking of chromosome and replisome dynamics in *Myxococcus xanthus* reveals a novel chromosome arrangement. *PLoS Genet.* **9**, e1003802 (2013).

Iniesta, A. A. ParABS system in chromosome partitioning in the bacterium *Myxococcus xanthus*. *PloS One* **9**, e86897 (2014).

Hester, C. M. & Lutkenhaus, J. Soj (ParA) DNA binding is mediated by conserved arginines and is essential for plasmid segregation. *Proc. Natl. Acad. Sci. USA* **104**, 20326-20331 (2007).

Kiekebusch, D. & Thanbichler, M. Spatiotemporal organization of microbial cells by protein concentration gradients. *Trends Microbiol.* **22**, 65-73 (2014).

Vecchiarelli, A. G., Havey, J. C., Ing, L. L., Wong, E. O., Waples, W. G. & Funnell, B. E. Dissection of the ATPase active site of P1 ParA reveals multiple active forms essential for plasmid partition. *J. Biol.Chem.* **288**, 17823-17831 (2013).

Meniche, X. *et al.* Subpolar addition of new cell wall is directed by DivIVA in mycobacteria. *Proc. Natl. Acad. Sci. USA* **111**, E3243-3251 (2014).

Flärdh, K. Essential role of DivIVA in polar growth and morphogenesis in *Streptomyces coelicolor* A3(2). *Mol. Microbiol.* **49**, 1523-1536 (2003).

Fuchino, K*. et al.* Dynamic gradients of an intermediate filament-like cytoskeleton are recruited by a polarity landmark during apical growth. *Proc. Natl. Acad. Sci. USA* **110**, E1889-1897 (2013).

Holmes, N. A. *et al.* Coiled-coil protein Scy is a key component of a multiprotein assembly controlling polarized growth in *Streptomyces*. *Proc. Natl. Acad. Sci. USA* **110**, E397-406 (2013).

Yamaichi, Y. *et al.* A multidomain hub anchors the chromosome segregation and chemotactic machinery to the bacterial pole. *Genes Dev.* **26**, 2348-2360 (2012).

Zhang, Y., Ducret, A., Shaevitz, J. & Mignot, T. From individual cell motility to collective behaviors: insights from a prokaryote, *Myxococcus xanthus*. *FEMS Microbiol. Rev.* **36**, 149-164 (2012).

Hodgkin, J. & Kaiser, D. Cell-to-cell stimulation of movement in nonmotile mutants of *Myxococcus*. *Proc. Natl. Acad. Sci. USA* **74**, 2938-2942 (1977).

Kashefi, K. & Hartzell, P. L. Genetic suppression and phenotypic masking of a *Myxococcus xanthus frzF*$^-$ defect. *Mol. Microbiol.* **15**, 483-494 (1995).

Magrini, V., Creighton, C. & Youderian, P. Site-specific recombination of temperate *Myxococcus xanthus* phage Mx8: genetic elements required for integration. *J. Bacteriol.* **181**, 4050-4061 (1999).

Gomez-Santos, N. *et al.* Comprehensive set of integrative plasmid vectors for copper-inducible gene expression in *Myxococcus xanthus*. *Appl. Environ. Microbiol.* **78**, 2515-2521 (2012).

Iniesta, A. A., Garcia-Heras, F., Abellon-Ruiz, J., Gallego-Garcia, A. & Elias-Arnanz M. Two systems for conditional gene expression in *Myxococcus xanthus* inducible by isopropyl-beta-D-thiogalactopyranoside or vanillate. *J. Bacteriol.* **194**, 5875-5885 (2012).

Ueki, T., Inouye, S. & Inouye, M. Positive-negative KG cassettes for construction of multi-gene deletions using a single drug marker. *Gene* **183**, 153-157 (1996).

Bulyha, I. *et al.* Regulation of the type IV pili molecular machine by dynamic localization of two motor proteins. *Mol. Microbiol.* **74**, 691-706 (2009).

Cameron, T. A., Anderson-Furgeson, J., Zupan, J. R., Zik, J. J. & Zambryski, P. C. Peptidoglycan synthesis machinery in *Agrobacterium tumefaciens* during unipolar growth and cell division. *mBio* **5**, e01219-01214 (2014).

NCBI Resource Coordinators. Database resources of the National Center for Biotechnology Information. *Nucleic Acids Res.* **44**, D7-19 (2016).

Jones, D. T. Protein secondary structure prediction based on position-specific scoring matrices. *J. Mol. Biol.* **292**, 195-202 (1999).

Dodd, I. B. & Egan, J. B. Improved detection of helix-turn-helix DNA-binding motifs in protein sequences. *Nucleic Acids Res.* **18**, 5019-5026 (1990).

Finn, R. D. *et al.* The Pfam protein families database: towards a more sustainable future. *Nucleic Acids Res.* **44**, D279-285 (2016).

SUPPLEMENTARY FIGURES

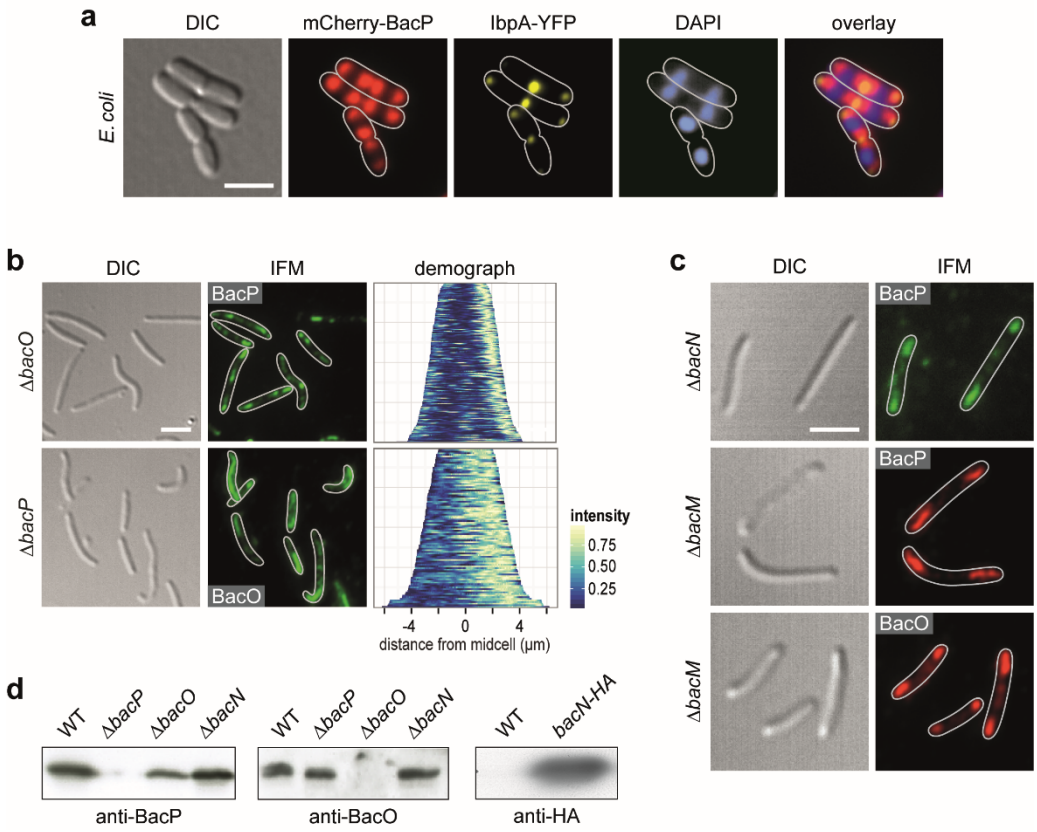

Supplementary Figure 1. Localization and stability of BacP, BacO, and BacN. (a) Differential localization of the bactofilin complexes and inclusion bodies in *E. coli*. Strain BL21(DE3) bearing plasmids pLL54 (P_{T7}-*mCherry-bacP* e*cfp-bacO*) and pLL235 (P_{T7}-*ibpA-eyfp*) was induced with 0.5 mM IPTG (for 1 h) and treated with 30 µg/ml chloramphenicol (for 30 min). After the staining of DNA with DAPI, cells were analyzed by differential interference contrast (DIC) and fluorescence microscopy (bar: 3 µm). Note that the chaperone IbpA is specifically associated with protein aggregates and thus serves as a marker for the subcellular position of inclusion bodies in *E. coli*[1]. **(b)** Interdependence of BacP and BacO localization. Cells of strains LL002 (Δ*bacO*) and LL001 (Δ*bacP*) were analyzed by immunofluorescence microscopy using anti-BacP or anti-BacO antibodies, respectively. An Alexa-Fluor 488-conjugated secondary antibody was used to detect the immunocomplexes (bar: 3 µm). The panels on the right show demographs visualizing the subcellular distributions of BacP and BacO as a function of cell length (n = 172 cells for LL002 and 99 cells for LL001). **(c)** Localization of BacP and BacO in the absence of other bactofilin homologs. Strains LL003 (Δ*bacN*) and MT300 (Δ*bacM*) were analyzed by immunofluorescence microscopy using anti-BacP and/or anti-BacO antibodies, respectively (bar: 3 µm). **(d)** Immunoblot analysis of BacP, BacO, and BacN-HA accumulation in different genetic backgrounds. Strains DK1622 (WT), LL001 (Δ*bacP*), LL002 (Δ*bacO*), LL003 (Δ*bacN*), and LL033 (*bacN-HA*) were subjected to immunoblot analysis with anti-BacP, anti-BacO, or anti-HA antibodies, respectively. Full blots are shown in Supplementary Figure 11.

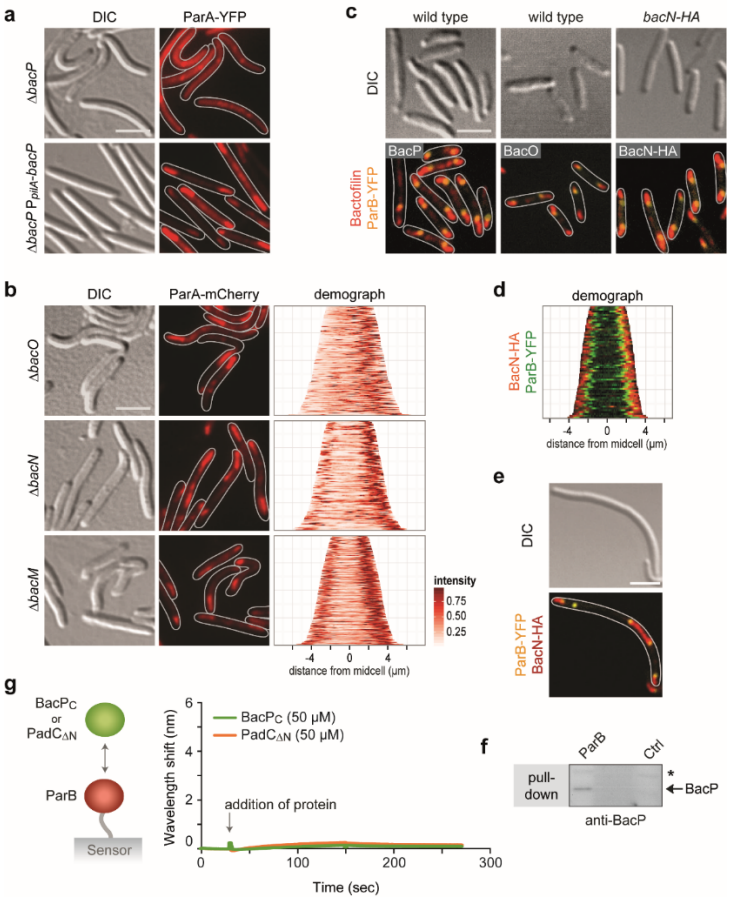

Supplementary Figure 2. BacNOP are important for the subpolar localization of ParA and ParB in *M. xanthus*. (a) Restoration of proper ParA localization by complementation of the *bacP* mutation. Cells of strains LL186 (Δ*bacP* P_{van}-*parA-eyfp*) and LL188 (Δ*bacP* P_{van}-*parA-eyfp* P_{pilA}-*bacP*) were grown in CTT medium, diluted with CTT supplemented with 5 µM vanillate to an OD_{550} of 0.1, and then further incubated for 2 h before imaging (bar: 3 µm). For visualization, the fluorescence signal was false-colored in red. **(b)** Localization of ParA in the absence of BacO, BacN, or BacM. Cells of strains LL148 (Δ*bacO* P_{parA}-*parA-mCherry*), and LL149 (Δ*bacN* P_{parA}-*parA-mCherry*), and LL151 (Δ*bacM* P_{parA}-*parA-mCherry*) were analyzed by DIC and fluorescence microscopy. Demographs summarizing the single-cell fluorescence profiles observed for the three strains are given on the right (n = 162 cells for LL148, 112 cells for LL149, and 234 cells for LL151). **(c)** Colocalization of ParB with polar bactofilin patches. Cells of strains LL012 (P_{parB}-*parB-eyfp*) and LL040 (*bacN-HA* P_{parB}-*parB-eyfp*) were analyzed by immuno-fluorescence microscopy, using anti-BacP, anti-BacO (LL012), or anti-HA (LL040) antibodies. The resulting images were overlaid with the ParB-YFP fluorescence signals (bar: 3 µm). **(d)** Localization of ParB to the ends of bactofilin patches. Cells of strain LL040 (*bacN-HA* P_{parB}-*parB-eyfp*) were analyzed as described for panel C. Fluorescence profiles showing the subcellular distribution of BacN-HA and ParB-YFP were then arranged according to cell length in a demograph (n = 63 cells). **(e)** Colocalization of ParB with bactofilin structures in filamentous cells. Strain LL040 (*bacN-HA* P_{parB}-*parB-eyfp*) was treated for 8 h with 100 µM cephalexin to block cell division and then subjected to immunofluorescence microscopy with an anti-HA primary antibody and an Alexa-Fluor 594-conjugated secondary antibody. Shown are a DIC image and an overlay of the Alexa Fluor 594 and ParB-YFP signals (bar: 3 µm). **(f)** Co-purification of BacP with ParB. A whole-cell lysate of wild-type strain DK1622 was incubated with beads coupled to purified StrepII-ParB. After isolation of the beads, bound protein was eluted, concentrated with trichloroacetic acid, and subjected to immunoblot analysis with anti-BacP antibodies. A reaction performed with beads not pre-incubated with StrepII-ParB served as a control. The full blot is shown in Supplementary Figure

12. **(g)** Bio-layer interferometric analysis showing the absence of a direct interaction between ParB and BacP or PadC *in vitro*. Sensors carrying purified ParB (an amount equivalent to a 3 nm wavelength shift) were probed with 50 µM $BacP_C$ or $PadC_{\Delta N}$.

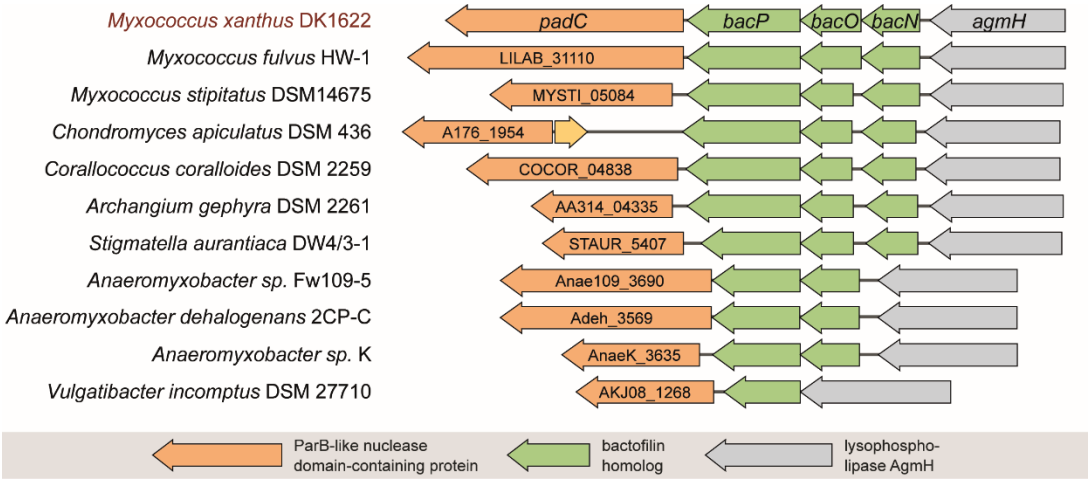

Supplementary Figure 3. Conservation of the *bacP* gene neighborhood in the delta-proteobacterial suborder *Cystobacterineae*. Shown is a comparison of the organization of the bactofilin gene cluster and its neighborhood in representative species of the *Cystobacterineae*. The data were obtained from the SyntTax server[2], using the sequence of *bacP* from *M. xanthus* DK1622 as a query.

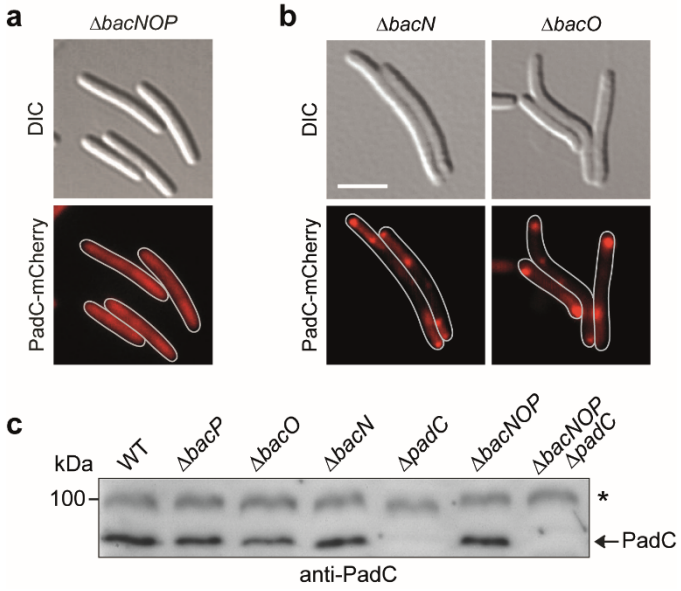

Supplementary Figure 4. PadC is required for the bactofilin-mediated positioning of ParA and ParB. (a) Critical role of bactofilins in PadC localization. Cells of strain LL117 (Δ*bacNOP padC-mCherry*) were visualized by DIC and fluorescence microscopy (bar: 3 µm). **(b)** Localization of PadC in the absence of BacN or BacO. Strains LL142 (Δ*bacN padC-mCherry*) and LL141 (Δ*bacO padC-mCherry*) were analyzed by DIC and fluorescence microscopy (bar: 3 µm). **(c)** Levels of PadC in different mutant backgrounds. Cells of strains DK1622 (WT), LL001 *(*Δ*bacP*), LL002 *(*Δ*bacO*), LL003 *(*Δ*bacN*), LL101 *(*Δ*padC*), MT295

(ΔbacNOP), and LL174 *(ΔbacNOP ΔpadC)* were subjected immunoblot analysis with anti-PadC antibodies. A non-specific cross-reaction with a protein of ~100 kDa (*) serves as a loading control. The full blot is shown in Supplementary Figure 13.

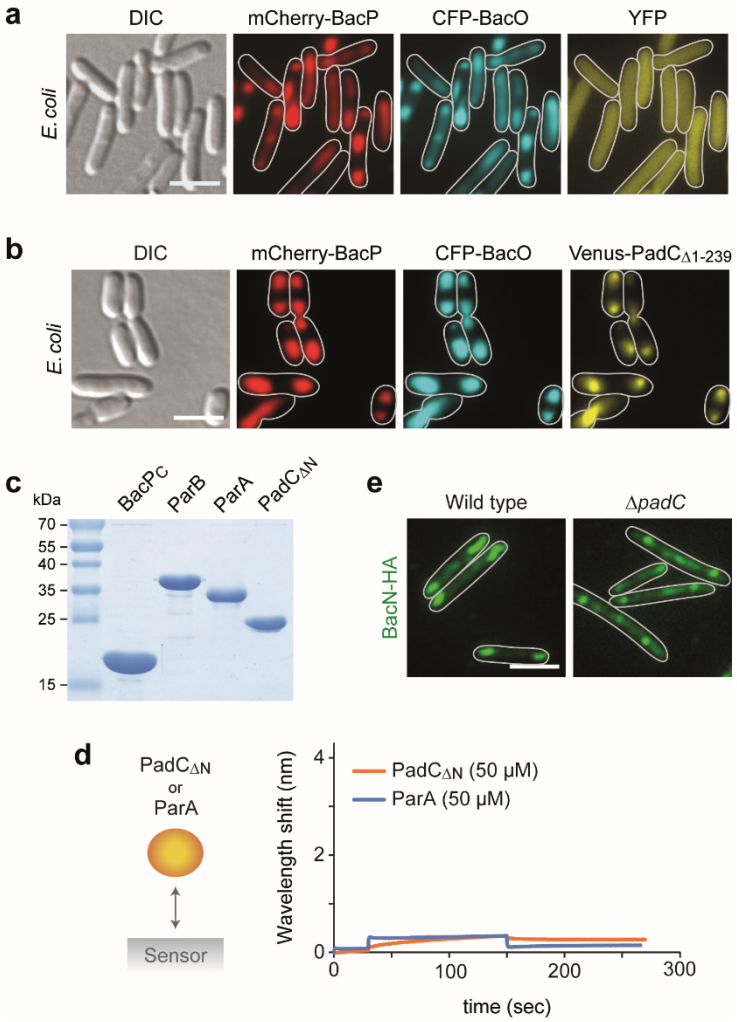

Supplementary Figure 5. PadC is required for the bactofilin-mediated positioning of ParA and ParB. (a) Diffuse localization of YFP in *E. coli* cells accumulating bactofilin polymers. Cells of *E. coli* Rosetta(DE3)pLysS bearing plasmids pLL54 (P_{T7}-*mCherry-bacP cfp-bacO*) and pLL61 (P_{tet}-*eyfp*) were induced with 0.5 mM IPTG (for 3.5 h) and 0.2 µg/ml aTet (for 2.5 h) before imaging (bar: 3 µm). The PCC for the mCherry-BacP and YFP signals is 0.45 ± 0.18 (n = 166). **(b)** Co-localization of a PadC derivative lacking the non-structured N-terminal region ($PadC_{Δ1-239}$) with bactofilin polymers in *E. coli*. Cells of *E. coli* BL21(DE3) bearing plasmids pLL54 (P_{T7}-*mCherry-bacP cfp-bacO*) and pLL120 (P_{T7}-*venus-padC*$_{Δ1-239}$) were induced for 3 h with 0.5 mM IPTG before imaging (bar: 3 µm). The PCC for the mCherry-BacP and Venus-$PadC_{Δ1-239}$ signals is 0.89 ± 0.05, n = 61). **(c)** Purity of the proteins used for the bio-layer interferometric analyses. The indicated proteins (10 µg per lane) were separated by SDS gel electrophoresis and stained with Coomassie brilliant blue. A mixture of standard proteins was applied in the rightmost lane. The corresponding molecular weights are indicated next to the gel. **(d)** Lack of interaction between ParA or PadC with unmodified bio-layer interferometry sensors. Sensors lacking any immobilized protein were probed with 50 µM $PadC_{Δ1-281}$ or ParA, respectively. **(e)** Aberrant organization of bactofilin structures in the absence of PadC. Cells of strain LL110 (*ΔpadC bacN-HA*) were analyzed by immunofluorescence microscopy using an anti-HA primary antibody and an Alexa-Fluor 488-conjugated

secondary antibody. The fluorescence signals obtained are overlaid with the outlines of the cells generated on the basis of DIC images.

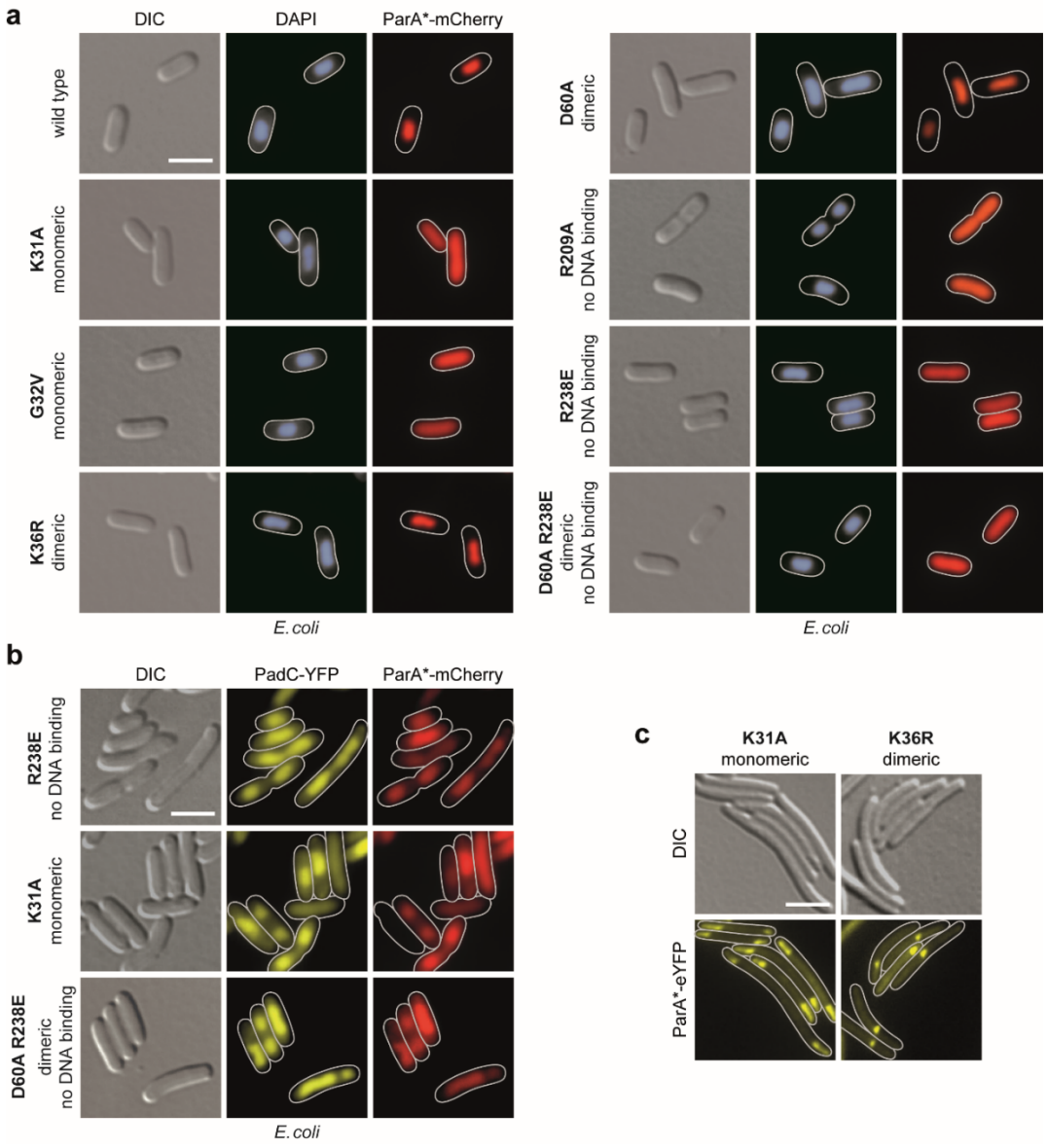

Supplementary Figure 6. PadC interacts with ParA. (a) DNA-binding activity of wild-type and mutant ParA variants upon heterologous expression in *E. coli*. Cells of *E. coli* BL21(DE3) bearing plasmid pLL100 (P_{tet}-*parA-mCherry*) or derivatives thereof encoding the indicated mutant ParA variants (pLL122, pLL124, pLL171, pLL172, pLL173, pLL178, or pLL202) were treated with 0.2 µg/ml aTet (for 1 h) to induce the synthesis of the ParA fusion proteins. Subsequently, 30 µg/ml chloramphenicol was added to induce nucleoid condensation. After 30 min of incubation, DNA was stained with DAPI and cells were analyzed by DIC and fluorescence microscopy (bar: 3 µm). The PCCs determined for the DAPI and ParA*-mCherry signals are 0.91 ± 0.18 (WT, n = 55 cells), 0.72 ± 0.17 (K31A, n = 32 cells), 0.72 ± 0.12 (G32V, n = 37 cells), 0.95 ± 0.03 (K36R, n = 51 cells), 0.97 ± 0.02 (D60A, n = 50 cells), 0.71 ± 0.09 (R209A, n = 51 cells), 0.79 ± 0.08 (R238E, n = 54 cells), and 0.67 ± 0.17 (D60A R238E, n = 42 cells). **(b)** Colocalization of different ParA variants with PadC in *E. coli*. Cells of *E. coli* BL21(DE3) bearing plasmid pLL101 (P_{T7}-*padC-eyfp*) were co-transformed with pLL122 (P_{tet}-$parA_{R238E}$-*mCherry*), pLL171 (P_{tet}-$parA_{K31A}$-*mCherry*), or pLL202 (P_{tet}-$parA_{D60A\ R238E}$-*mCherry*) and induced with 0.5 mM IPTG and/or 0.2 µg/ml aTet before imaging (bar: 3 µm). The PCCs for the

PadC-YFP and ParA*-mCherry signals are 0.96 ± 0.06 (R238E, n = 51 cells), 0.93 ± 0.07 (K31A, n = 51 cells), and 0.92 ± 0.06 (D60A R238E, n = 49 cells). **(c)** Subcellular localization of mutant ParA variants in *M. xanthus*. Cells of strains LL210 (P_{van}-*parA*$_{K31A}$-*eyfp*) or LL212 (P_{van}-*parA*$_{K36R}$-*eyfp*) were induced for 5.5 h with 3 µM vanillate and analyzed by DIC and fluorescence microscopy (bar: 3 µm).

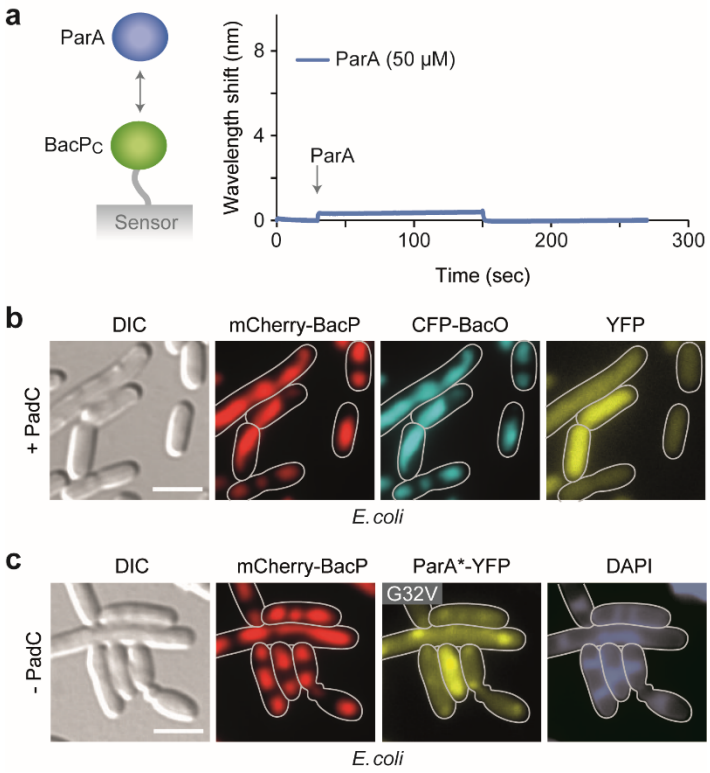

Supplementary Figure 7. PadC is required to recruit ParA to bactofilin complexes. **(a)** Lack of interaction between BacP and ParA. Bio-layer interferometry sensors loaded with BacP$_{\Delta 1\text{-}115}$ were probed with 50 µM ParA. **(b)** Localization of eYFP in the presence of the BacP·BacO·PadC complex in *E. coli*. Cells of *E. coli* BL21(DE3) were transformed with pLL54 (P_{T7}-*mCherry-bacP cfp-bacO*), pLL205 (P_{T7}-*padC*), and pLL61 (P_{tet}-*eyfp*) and induced with 0.5 mM IPTG (for 3.5 h) and 0.2 µg/ml aTet (for 2.5 h) before imaging (bar: 3 µm). The PCC for the mCherry-BacP and YFP signals is 0.57 ± 0.28 (n = 60 cells). **(c)** Interaction of monomeric ParA$_{G32V}$ with a BacP·BacO complex in the absence of PadC. *E. coli* BL21(DE3) was transformed with pLL54 (P_{T7}-*mCherry-bacP cfp-bacO*) and pLL215 (P_{tet}-*parA*$_{G32V}$-*eyfp*). Cells were grown in LB medium and induced with 0.5 mM IPTG (for 3.5 h) and 0.2 µg/ml aTet (for 2.5 h) before imaging. The PCC for the mCherry-BacP and ParA$_{G32V}$-YFP signals is 0.75 ± 0.09 (n = 114 cells).

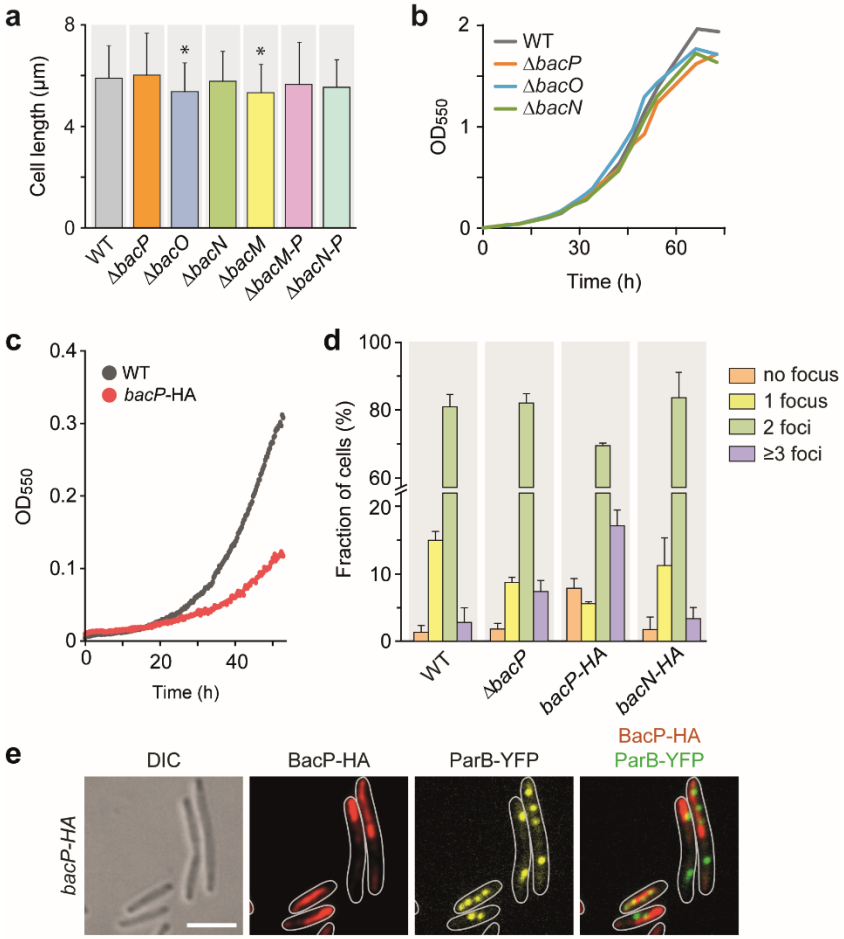

Supplementary Figure 8. A dominant variant of BacP severely affects origin segregation and cell growth. (a) Cell lengths of bactofilin mutants. Cells of strains DK1622 (WT), LL001 (Δ*bacP*), LL002 (Δ*bacO*), LL003 (Δ*bacN*), MT300 (Δ*bacM*), JK328 (Δ*bacMNOP*), and MT295 (Δ*bacNOP*) were visualized by DIC microscopy and analyzed for their lengths. Shown are the average values (± SD; n > 99 cells per strain). Significant differences between the wild-type and the mutant strains are indicated by asterisks ($p < 0.00001$; *t*-test). **(b)** Growth rates of bactofilin-deficient cells. Exponentially growing cultures of strains DK1622 (WT), LL001 (Δ*bacP*), LL002 (Δ*bacO*), and LL003 (Δ*bacN*) were diluted in fresh medium and analyzed for their optical density (OD_{550}) over a period of 75 h. **(c)** Impaired growth of *M. xanthus* in the presence of BacP-HA. Cells of strains DK1622 (WT) and LL032 (*bacP-HA*) were grown to exponential phase and diluted to an OD_{550} of 0.025. Growth was then monitored by following the OD_{550} at intervals of 15 min. **(d)** Increased number of ParB·origin complexes in bactofilin mutants. Strains LL012 (P_{parB}-*parB-eyfp*), LL015 (Δ*bacP* P_{parB}-*parB-eyfp*), LL046 (*bacP-HA* P_{parB}-*parB-eyfp*), and LL040 (*bacN-HA* P_{parB}-*parB-eyfp*) were analyzed by DIC and fluorescence microscopy. Shown are histograms of the number of ParB-YFP foci per cell (± SD; n > 500 cells per strain). **(e)** Abnormal localization of BacP-HA in *M. xanthus*. Cells of strain LL046 (*bacP-HA* P_{parB}-*parB-eyfp*) were analyzed by immunofluoresence microscopy using an anti-HA primary antibodies and an Alexa-Fluor 594-conjugated secondary antibody. In parallel, ParB-YFP was detected by fluorescence microscopy (bar: 3 µm).

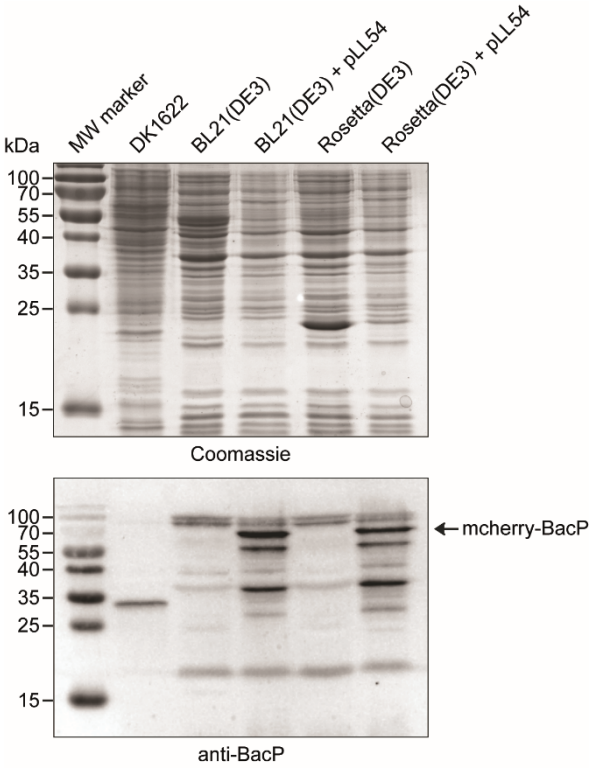

Supplementary Figure 9. Expression levels of fluorescently tagged bactofilin derivatives in *E. coli*. *E. coli* strains BL21(DE3) and Rosetta(DE3)pLysS transformed with plasmid pLL54 (P_{T7}-*mCherry-bacP ecfp-bacO*) were grown to exponential phase and induced for 3.5 h with 0.5 mM IPTG. Lysates of the cells were applied to SDS-polyacrylamide gels and analyzed by Coomassie Blue staining (upper panel) and by immunoblotting with anti-BacP antibodies (lower panel). For comparison, plasmid-free host cells and *M. xanthus* wild-type strain DK1622 were investigated in parallel. Samples were normalized to cell density. A molecular mass standard (in kDa) is shown on the left. The position of the mCherry-BacP fusion is indicated by an arrow.

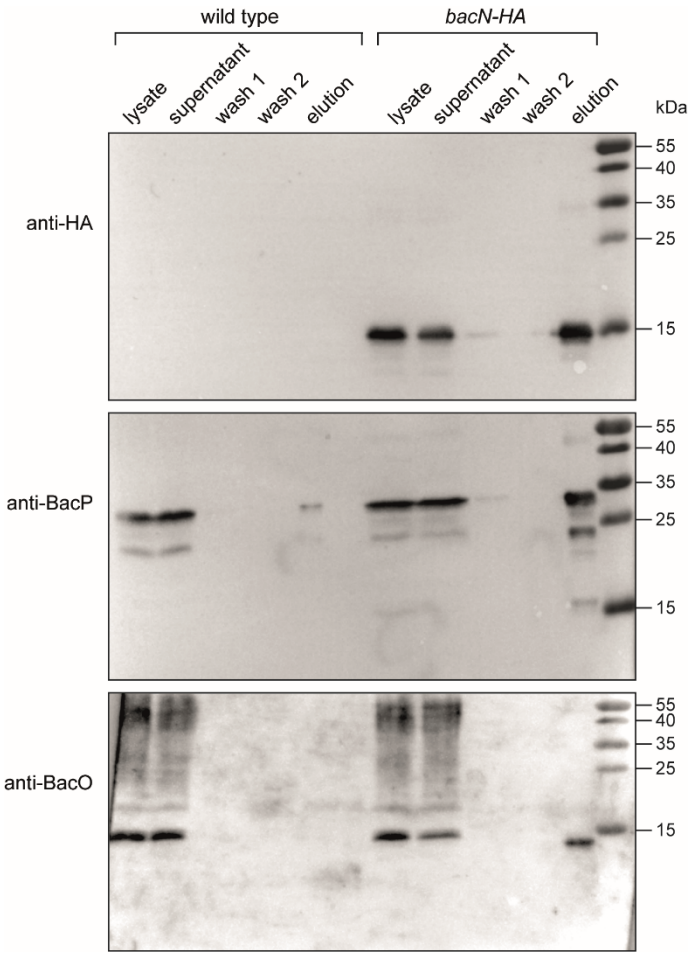

Supplementary Figure 10. Full scans of the Western blots shown in Figure 1e. Cell lysates of strains DK1622 (wild type) and LL033 (BacN-HA) were incubated with anti-HA affinity beads. After isolation of the beads and two washes, interacting proteins were eluted and detected by immunoblot analysis with anti-HA, anti-BacP, and anti-BacO antibodies. Samples of the cell lysates and the supernatants obtained during the isolation and washing steps were analyzed as controls. A molecular mass standard (in kDa) is given on the right.

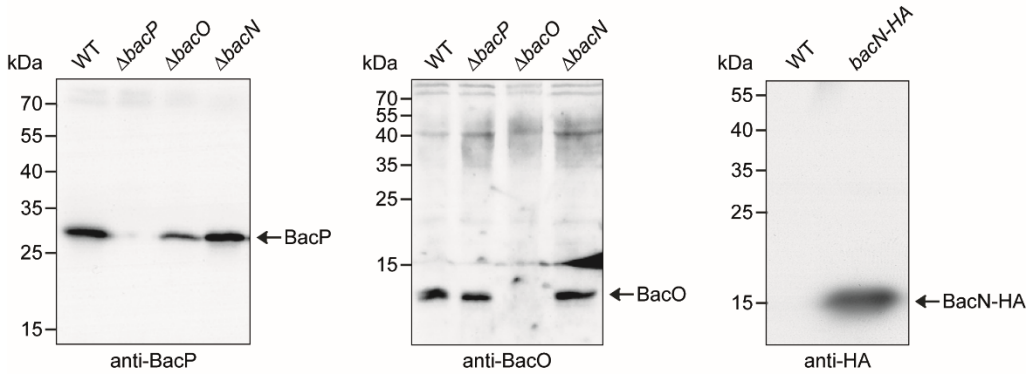

Supplementary Figure 11. Full scans of the Western blots shown in Supplementary Figure 1d. Strains DK1622 (WT), LL001 (Δ*bacP*), LL002 (Δ*bacO*), LL003 (Δ*bacN*), and LL033 (*bacN-HA*) were subjected to immunoblot analysis with anti-BacP, anti-BacO, or anti-HA antibodies. A molecular mass standard (in kDa) is given on the left. The positions of the target proteins are indicated by arrows.

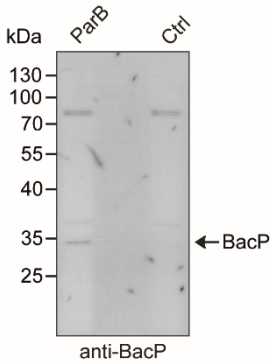

Supplementary Figure 12. Full scan of the Western blot shown in Supplementary Figure 2f. A whole-cell lysate of wild-type strain DK1622 was incubated with beads coupled to purified StrepII-ParB. After isolation of the beads, bound protein was eluted, concentrated with trichloroacetic acid, and subjected to immunoblot analysis with anti-BacP antibodies. A reaction performed with beads not pre-incubated with StrepII-ParB served as a control. A molecular mass standard (in kDa) is given on the left. The position of the BacP signal is indicated by an arrow.

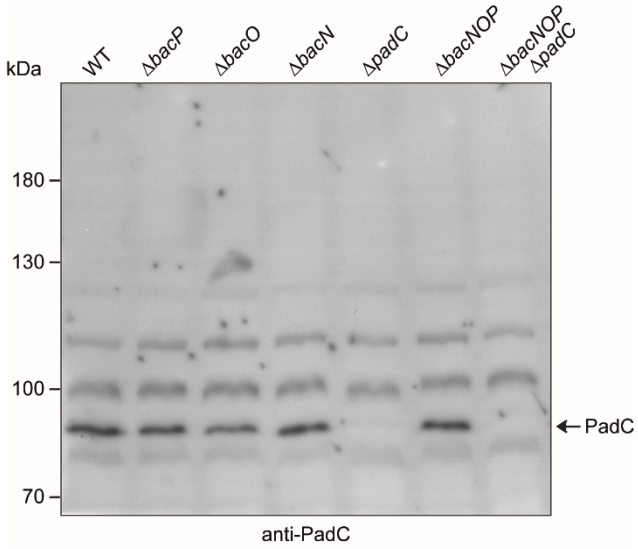

Supplementary Figure 13. Full scan of the Western blot shown in Supplementary Figure 4c. Cells of strains DK1622 (WT), LL001 *(ΔbacP*), LL002 *(ΔbacO*), LL003 *(ΔbacN*), LL101 *(ΔpadC*), MT295 *(ΔbacNOP*), and LL174 *(ΔbacNOP ΔpadC*) were subjected immunoblot analysis with anti-PadC antibodies. A molecular mass standard (in kDa) is given on the left. The position of the PadC signal is indicated by an arrow.

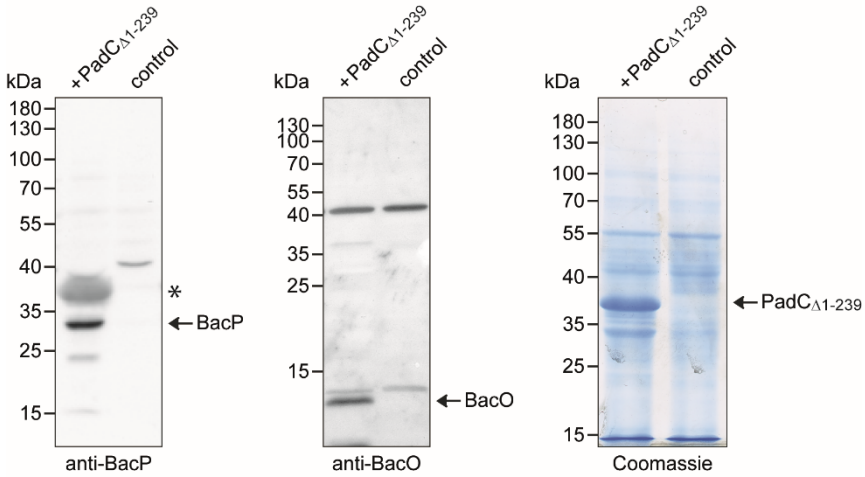

Supplementary Figure 14. Full scans of the Western blots and the Coomassie blue-stained SDS-gel shown in Figure 3g. A whole-cell lysate of wild-type strain DK1622 was incubated with Ni-NTA beads loaded with purified His_6-$PadC_{\Delta 1\text{-}239}$ (+ PadC). After isolation of the beads, bound protein was eluted and subjected to SDS-PAGE and to immunoblot analysis with anti-BacP and anti-BacO antibodies, respectively. A reaction with beads not pre-incubated with purified protein served as a control. A molecular mass standard (in kDa) is given on the left. The positions of the target proteins are indicated by arrows. The asterisk marks a non-specific cross-reaction of the anti-BacP antibody with $PadC_{\Delta 1\text{-}239}$.

SUPPLEMENTARY TABLES

Supplementary Table 1. *M. xanthus* strains used in this study.

Strain	Genotype/description	Construction	Reference
DK1622	*M. xanthus* wild-type strain		Kaiser[3]
MT295	DK1622 *ΔbacNOP*		Kühn *et al.*[4]
MT300	DK1622 *ΔbacM*		Kühn *et al.*[4]
JK328	DK1622 *ΔbacMNOP*		Kühn *et al.*[4]
LL001	DK1622 *ΔbacP*		Bulyha *et al.*[5]
LL002	DK1622 *ΔbacO*		Bulyha *et al.*[5]
LL003	DK1622 *ΔbacN*		Bulyha *et al.*[5]
LL012	DK1622 *attB*::P_{parB}-*parB-eyfp*	Integration of pAH7 in DK1622	This work
LL013	DK1622 *ΔbacM attB*::P_{parB}-*parB-eyfp*	Integration of pAH7 in MT300	This work
LL014	DK1622 *ΔbacN attB*::P_{parB}-*parB-eyfp*	Integration of pAH7 in LL003	This work
LL015	DK1622 *ΔbacP attB*::P_{parB}-*parB-eyfp*	Integration of pAH7 in LL001	This work
LL016	DK1622 *ΔbacMNOP attB*::P_{parB}-*parB-eyfp*	Integration of pAH7 in JK328	This work
LL018	DK1622 *ΔbacO attB*::P_{parB}-*parB-eyfp*	Integration of pAH7 in LL002	This work
LL019	DK1622 *ΔbacNOP attB*::P_{parB}-*parB-eyfp*	Integration of pAH7 in MT295	This work
LL032	DK1622 *bacP-HA*	Gene replacement in DK1622 using pLL9	This work
LL033	DK1622 *bacN-HA*	Gene replacement in DK1622 using pLL11	This work
LL040	DK1622 *bacN-HA attB*::P_{parB}-*parB-eyfp*	Integration of pAH7 in LL033	This work
LL046	DK1622 *bacP-HA attB*::P_{parB}-*parB-eyfp*	Integration of pAH7 in LL032	This work
LL101	DK1622 *ΔpadC*	In-frame deletion of *padC* in DK1622 using pLL38	This work
LL102	DK1622 *ΔpadC attB*::P_{parB}-*parB-eyfp*	Integration of pAH7 in LL101	This work
LL110	DK1622 *ΔpadC bacN-HA*	In-frame deletion of *padC* in LL033 using pLL38	This work
LL116	DK1622 *padC-mCherry*	Gene replacement in DK1622 using pLL72	This work
LL117	DK1622 *ΔbacNOP padC-mCherry*	Gene replacement in MT295 using pLL72	This work
LL118	DK1622 *padC-mCherry attB*::P_{parB}-*parB-eyfp*	Integration of pAH7 in LL116	This work
LL130	DK1622 *ΔbacP padC-mCherry*	Gene replacement in LL001 using pLL72	This work
LL134	DK1622 *attB*::P_{cuoA}-*padC-mCherry*	Integration of pLL74 in DK1622	This work
LL135	DK1622 *ΔbacP padC-mCherry attB*::P_{pilA}-*bacP*	Integration of pLL33 in LL130	This work
LL141	DK1622 *ΔbacO padC-mCherry*	Gene replacement in LL002 using pLL72	This work
LL142	DK1622 *ΔbacN padC-mCherry*	Gene replacement in LL003 using pLL72	This work
LL145	DK1622 *attB*::P_{parA}-*parA-mCherry*	Integration of pAH59 in DK1622	This work
LL147	DK1622 *ΔbacNOP attB*::P_{parA}-*parA-mCherry*	Integration of pAH59 in MT295	This work
LL148	DK1622 *ΔbacO attB*::P_{parA}-*parA-mCherry*	Integration of pAH59 in LL002	This work
LL149	DK1622 *ΔbacN attB*::P_{parA}-*parA-mCherry*	Integration of pAH59 in LL003	This work
LL150	DK1622 *bacP-HA attB*::P_{parA}-*parA-mCherry*	Integration of pAH59 in LL032	This work
LL151	DK1622 *ΔbacM attB*::P_{parA}-*parA-mCherry*	Integration of pAH59 in MT300	This work
LL152	DK1622 *ΔbacP attB*::P_{parA}-*parA-mCherry*	Integration of pAH59 in LL001	This work
LL154	DK1622 *ΔpadC attB*::P_{parA}-*parA-mCherry*	Integration of pAH59 in LL101	This work
LL162	DK1622 *attB*::P_{parA}-*parA-mCherry* P_{cuoA}::P_{cuoA}-*parB-eyfp*	Integration of pAH73 in LL145	This work
LL174	DK1622 *ΔbacNOP ΔpadC*	In-frame deletion of *bacP-padC* in DK1622 using pLL104	This work
LL176	DK1622 *ΔbacNOP ΔpadC attB*::P_{parB}-*parB-eyfp*	Integration of pAH7 in LL174	This work
LL186	DK1622 *ΔbacP MXAN18/19*::P_{van}-*parA-eyfp*	Integration of pLL116 in LL001	This work
LL188	DK1622 *ΔbacP MXAN18/19*::P_{van}-*parA-eyfp attB*::P_{pilA}-*bacP*	Integration of pLL33 in LL186	This work
LL192	DK1622 *ΔpadC attB*::P_{parA}-*parA-mCherry MXAN18/19*::P_{van}-*padC*	Integration of pLL126 in LL154	This work
LL193	DK1622 *MXAN18/19*::P_{van}-$parA_{R209A}$-*eyfp*	Integration of pLL130 in DK1622	This work
LL201	DK1622 *attB*::P_{parA}-*parA-mCherry MXAN18/19*::P_{van}-*padC-eyfp*	Integration of pLL143 in LL145	This work
LL210	DK1622 *MXAN18/19*::P_{van}-$parA_{K31A}$-*eyfp*	Integration of pLL155 in DK1622	This work
LL211	DK1622 *MXAN18/19*::P_{van}-$parA_{G32V}$-*eyfp*	Integration of pLL156 in DK1622	This work
LL212	DK1622 *MXAN18/19*::P_{van}-$parA_{K36R}$-*eyfp*	Integration of pLL165 in DK1622	This work
LL218	DK1622 *MXAN18/19*::P_{van}-$parA_{D60A}$-*eyfp*	Integration of pLL166 in DK1622	This work

Supplementary Table 2. *E. coli* strains used in this study.

Strain	Genotype	Source
TOP10	F⁻ ***mcr***A Δ(***mrr-hsd***RMS-***mcr***BC) Φ80***lac***ZΔM15 Δ***lac***X74 ***rec***A1 ***ara***D139 Δ(***ara leu***) 7697 ***gal***U ***gal***K ***rps***L (Str^R) ***end***A1 ***nup***G	Invitrogen
Rosetta(DE3)pLysS	F⁻ *ompT hsdS*$_B$(r_{B^-} m_{B^-}) *gal dcm* (DE3) pLysSRARE (Cam^R)	Merck Millipore
BL21(DE3)	F⁻ ***omp***T ***hsd***SB(rB^-, mB^-) ***gal dcm*** (DE3)	Novagen

Supplementary Table 3. General plasmids used in this work.

Plasmid	Description	Reference/Source
pAH7	pSWU30 carrying P_{parB}-*parB-eyfp*	Treuner-Lange *et al.*[6]
pAH17	pET45b(+) carrying *parA*	Harms *et al.*[7]
pAH59	pSWU30 carrying P_{parA}-*parA-mCherry*	Harms *et al.*[7]
pAH73	pMAT15 carrying *parB-eyfp*	Harms *et al.*[7]
pBJ114	*galK*-containing suicide vector for double homologous recombination in *M. xanthus*, Kan^R	Julien *et al.*[8]
pET28a(+)	Vector for overexpression of N-terminally His_6-tagged proteins, Kan^R	Novagen
pET51b(+)	Vector for overexpression of N-terminally StrepII-tagged proteins, Amp^R	Novagen
pETDuet-1	Vector for coexpression of two target genes, Amp^R	Novagen
pIB145	pET45b(+) carrying $bacP_{\Delta aa1\text{-}115}$	Bulyha *et al.*[5]
pMAT4	Vector for genes ligated to *cuoA* promoter integrating at *M. xanthus* chromosomal Mx8 *attB* site, Kan^R	Gomez-Santos *et al.*[9]
pMAT15	Vector for genes ligated to *cuoA* promoter integrating at *M. xanthus PcuoA* site, Kan^R	Harms *et al.*[7]
pMCS-2	Cloning vector	Thanbichler *et al.*[10]
pMR3690	Vector for the expression of a gene under the control of the *vanA* promoter, integrating at the *M. xanthus* Mxan18_19 chromosomal locus, Kan^R	Iniesta *et al.*[11]
pMR3691	Vector for the expression of a gene under the control of the *vanA* promoter, integrating at the *M. xanthus* Mxan18_19 chromosomal locus, tet^R	Iniesta *et al.*[11]
pMT325	pASK-IBA3plus derivative with pBBR1MCS-5 backbone, Amp^R, Gm^R	Thanbichler & Shapiro[12]
pRSFDuet-1	Vector for co-expression of two target genes under the control of P_{T7}, Kan^R	Novagen
pSW17	pET21a(+) carrying *bacO*	Kühn *et al.*[4]
pSW105	Vector for genes ligated to *pilA* promoter integrating at *M. xanthus* chromosomal Mx8 *attB* site, Kan^R	Jakovljevic *et al.*[13]
pSWU30	Vector for integrating at *M. xanthus* chromosomal Mx8 *attB* site, Tet^R	Wu *et al.*[14]
pVCFPN-4	Integration plasmid to fuse 5' end us of a target gene to *cfp* under the control of P_{van}, Gent^R	Thanbichler *et al.*[10]
pXCHYC-1	Integration plasmid to fuse 3' end us of a target gene to *mCherry* under the control of P_{xyl}, Strep/Spec^R	Thanbichler *et al.*[10]
pXCHYN-2	Integration plasmid to fuse 5' end of a target gene to *mCherry* under the control of P_{xyl}, Kan^R	Thanbichler *et al.*[10]
pXVENN-2	Integration plasmid to fuse 5' end us of a target gene to *venus* under the control of P_{xyl}, Kan^R	Thanbichler *et al.*[10]
pXYFPC-2	Integration plasmid to fuse 3' end us of a target gene to *eyfp* under the control of P_{xyl}, Kan^R	Thanbichler *et al.*[10]
pXYFPN-1	Integration plasmid to fuse 5' end us of a target gene to *eyfp* under the control of P_{xyl}, Strep/Spec^R	Thanbichler *et al.*[10]

Supplementary Table 4. Plasmids generated in this work.

Plasmid	Description	Construction
pLL9	pBJ114 derivative for replacing native *bacP* with *bacP-HA*	a) PCR amplification of *bacP-HA* with primers MXAN4635-HA-1 and MXAN4635-HA-2 b) digestion of the product with HindIII and BamHI c) PCR amplification of the *bacP* downstream region with primers MXAN4635HA-down-for and MXAN4635HA-down-rev d) digestion of the product with with BamHI and EcoRI e) ligation of the fragments into pBJ114 cut with HindIII and EcoRI
pLL11	pBJ114 derivative for replacing native *bacN* with *bacN-HA*	a) PCR amplification of a fragment including 275 bp of the *bacN* upstream region and *bacN-HA* with primers MXAN4637-HA-1 and MXAN4637-HA-2, b) digestion of the product with HindIII and BamHI c) PCR amplification of the *bacN* downstream region with primers MXAN4637HA-down-for and MXAN4637HA-down-rev d) digestion of the product with BamHI and EcoRI e) ligation of the two fragments into pBJ114 cut with HindIII and EcoRI
pLL17	pXCHYN-2 bearing *bacP*	a) PCR amplification of *bacP* with primers MXAN4635-For and MXAN4635-Rev b) digestion of the product with BglII and NheI c) ligation of the fragment into pXCHYN-2 cut with BglII and NheI
pLL33	pSW105 bearing *bacP*	a) PCR amplification of *bacP* with primers Comp MXAN4635-for and Comp MXAN4635-rev b) digestion of the product with XbaI and HindIII c) ligation of the fragment into pSW105 cut with XbaI and HindIII
pLL38	pBJ114 derivative for generating an in-frame deletion of *padC*	a) PCR amplification of the *padC* downstream region and the last 36 bp of *padC* with primers MXAN4634-down-for and MXAN4634-down-rev b) digestion of the product with BamHI and EcoRI c) PCR amplification of the *padC* upstream region and the first 36 bp of *padC* with primers MXAN4634-up-for and MXAN4634-up-rev d) digestion of the product with BamHI and HindIII e) ligation of the two fragments into pBJ114 cut with HindIII and EcoRI
pLL47	pVCFPN-4 bearing *bacO*	a) PCR amplification of *bacO* with primers MXAN4636-For and MXAN4636-Rev b) digestion of the product with BglII and NheI c) ligation of the fragment into pVCFPN-4 cut with BglII and NheI
pLL48	pETDuet-1 bearing *mCherry-bacP*	a) PCR amplification of *mCherry-bacP* from pLL17 with primers mCherry-For-NdeI and mCherry-MXAN4635-Rev-XhoI b) restriction of the product with NdeI and XhoI c) ligation of the fragment into equally treated pETDuet-1.
pLL51	pETDuet-1 bearing *cfp-bacO*	a) PCR amplification of *cfp-bacO* from pLL47 using primers NcoI-CFP-For and CFP-MXAN4636-Rev-EcoRI b) digestion of the product with NcoI and EcoRI c) ligation of the fragment into pETDuet-1 cut with NcoI and EcoRI
pLL54	pETDuet-1 bearing *mCherry-bacP cfp-bacO*	a) PCR amplification of *mCherry-bacP* from pLL17 using primers mCherry-For-NdeI and mCherry-MXAN4635-Rev-MfeI b) digestion of the product with NdeI and MfeI c) ligation of the fragment into pLL51 cut with NdeI and MfeI
pLL61	pMT325 bearing *eyfp*	a) PCR amplification of *eyfp* from pAH7 with primers XbaI-RBS-eYFP-for and parB-yfp-Rev-XmaI b) digestion of the product with XbaI and XmaI c) ligation of the fragment into pMT325 cut with XbaI and XmaI
pLL64	pXCHYC-1 bearing *padC*	a) amplification of *padC* with primers MXAN4634-new-For-NdeI and MXAN4634-new-Rev-EcoRI b) digestion of the product with NdeI and EcoRI c) ligation of the fragment into pXCHYC-1 cut with NdeI and EcoRI
pLL66	pLL64 carrying the *padC* downstream region	a) amplification of the *padC* downstream region with primers MXAN4634down-for-2 and MXAN4634-down-rev b) digestion of the product with NheI and EcoRI c) ligation of the fragment into pLL64 cut with NheI and EcoRI
pLL72	pBJ114 derivative for replacing native *padC* with *padC-mCherry*	a) PCR amplification of a fragment containing *padC-mCherry* and the *padC* downstream region from pLL66 using primers MXAN4634-For-XbaI and MXAN4634down-Rev-NheI b) digestion of the product with XbaI and NheI, followed by blunting of the fragment with T4 DNA polymerase c) ligation of the product into pBJ114 cut with XbaI and blunted with T4 DNA polymerase
pLL74	pMAT4 bearing *padC-mCherry*	a) PCR amplification of the *padC-mCherry* fragment from pLL72 using primers MXAN4634-For-XbaI and mCherry-Rev-NheI b) digestion of the product with NheI, treatment with T4 DNA polymerase, and subsequent digestion with XbaI c) ligation of the fragment into pMAT4 that had been cut with HindIII, treatment with T4 DNA polymerase, and subsequently digestion with XbaI

Supplementary Table 4. Plasmids generated in this work (continued).

Plasmid	Description	Construction
pLL80	pET51b(+) bearing *parB*	a) PCR amplification of *parB* using primers ParB-for-BamHI strep and ParB-rev-NotI strep b) digestion of the product with BamHI and NotI c) ligation of the fragment into pET51b(+) cut with BamHI and NotI
pLL85	pXYFPC-2 bearing *parA*	a) PCR amplification of *parA* with primers ParA-for-NdeI and ParA-rev-EcoRI b) digestion of the product with NdeI and EcoRI c) ligation of the fragment into pXYFPC-2 cut with NdeI and EcoRI
pLL86	pMT325 bearing *parA-eyfp*	a) PCR amplification of *parA-eyfp* from pLL85 using primers ParA-eyfp-for-XbaI and ParA-eyfp-rev-XmaI b) digestion of the product with XbaI and XmaI c) ligation of the fragment into pMT325 cut with XbaI and XmaI
pLL87	pXYFPC-2 bearing *padC*	a) PCR amplification of *padC* with primers MXAN4634-For-new-NdeI and MXAN4634-Rev-new-EcoRI b) digestion of the product with NdeI and EcoRI c) ligation of the fragment into pXYFPC-2 cut with NdeI and EcoRI
pLL89	pSWU30 bearing P_{parA}-*parA-eyfp*	a) amplification of *eyfp* from pXYFPC-2 using primers eYFP-for-BamHI and eYFP-rev-HindIII b) digestion of the product with BamHI and HindIII c) ligation of the fragment into pAH59 cut with BamHI and HindIII
pLL100	pMT325 bearing *parA-mCherry*	a) PCR amplification of *parA-mCherry* from pAH59 using primers ParA-eyfp-for-XbaI and mCherry-rev-HindIII b) digestion of the product with XbaI and HindIII c) ligation of the fragment into pMT325 cut with XbaI and HindIII
pLL101	pRSFDuet-1 bearing *padC-eyfp*	a) PCR amplification of *padC-eyfp* from pLL87 using primers MXAN4634-For-new-NdeI and eYFP-rev-NheI b) digestion of the product with NheI and treatment with T4 DNA polymerase c) digestion of pRSFDuet-1 with KpnI, followed by the treatment with T4 DNA polymerase d) digestion of both the *padC-eyfp* fragment and linearized pRSFDuet-1 with NdeI e) ligation of the two restriction products
pLL104	pBJ114 derivative for generating an in-frame deletion of MXAN4634-7	a) PCR amplification of a fragment containing 700 bp of the *padC* downstream region and the last 36 bp of *padC* with primers MXAN4634down-1-HindIII and MXAN4634down-2-BamHI b) digestion of the product with HindIII and BamHI c) PCR amplification of a fragment containing 736 bp of the *bacN* upstream region and the first 36 bp of *bacN* with primers BacN-up-1-BamHI and BacN-up-2-EcoRI d) digestion of the product with BamHI and EcoRI e) ligation of the two fragments into HindIII/EcoRI-treated pBJ114
pLL105	pET28a(+) bearing $padC_{\Delta AA1-239}$	a) PCR amplification of $padC_{\Delta AA1-239}$ with primers mxan4634c-for and mxan4634c-rev b) digestion of the product with NdeI and EcoRI c) ligation of the fragment into NdeI/EcoRI-treated pET28a(+)
pLL116	pMR3691 bearing *parA-eyfp*	a) PCR amplification of *parA-eyfp* from pLL85 with primers ParA-for-NdeI and eYFP-rev-NheI b) digestion of the product with NdeI and NheI c) ligation of the fragment into NdeI/NheI-treated pMR3691
pLL118	pXVENN-2 bearing $padC_{\Delta AA1-239}$	a) PCR amplification of $padC_{\Delta AA1-239}$ with primers MXAN4634c-for-BglII and mxan4634c-rev b) digestion of the product with BglII and EcoRI c) ligation of the fragment into pXVENN-2 cut with BglII and EcoRI
pLL119	pXYFPC-2 bearing $parA_{R209A}$	site-directed mutagenesis of pLL85 with primers parA(R209A)-for and parA(R209A)-rev
pLL120	pRSFDuet-1 bearing *venus-*$padC_{\Delta AA1-239}$	a) PCR amplification of *venus-*$padC_{\Delta AA1-239}$ from pLL118 using primers NcoI-CFP-For and mxan4634c-rev b) restriction of the product with NcoI and EcoRI c) ligation of the fragment into pRSFDuet-1 cut with NcoI and EcoRI
pLL121	pXCHYC-1 bearing $parA_{R238E}$	a) site-directed mutagenesis of pLL85 with primers parA(R238E)-for and parA(R238E)-rev b) release of the $parA_{R238E}$ gene by digestion with NdeI and EcoRI c) ligation of $parA_{R238E}$ into NdeI/EcoRI-treated pXCHYC-1
pLL122	pMT325 bearing $parA_{R238E}$-*mCherry*	a) PCR amplification of $parA_{R238E}$-*mCherry* from pLL121 using primers ParA-eyfp-for-XbaI and mCherry-rev-HindIII b) digestion of the product with XbaI and HindIII c) ligation of the fragment into XbaI/HindIII-treated pMT325
pLL123	pXCHYC-1 bearing $parA_{R209A}$	a) PCR amplification of $parA_{R209A}$ from pLL119A with primers ParA-for-NdeI and ParA-rev-EcoRI b) ligation of $parA_{R209A}$ into NdeI/EcoRI-treated pXCHYC-1
pLL124	pMT325 bearing $parA_{R209A}$-*mCherry*	a) PCR amplification of $parA_{R209A}$-mCherry from pLL123 using primers ParA-eyfp-for-XbaI and mCherry-rev-HindIII b) digestion of the product with XbaI and HindIII c) ligation of the fragment into pMT325 cut with XbaI and HindIII

Supplementary Table 4. Plasmids generated in this work (continued).

Plasmid	Description	Construction
pLL126	pMR3690 bearing *padC*	a) PCR amplification of *padC* with primers MXAN4634-For-new-NdeI and mxan4634c-rev b) digestion of the product with NdeI and EcoRI c) ligation of the fragment into pMR3690 cut with NdeI and EcoRI
pLL130	pMR3691 bearing *parA*$_{R209A}$-*eyfp*	a) PCR amplification of *parA*$_{R209A}$-*eyfp* from pLL119 with primers ParA-for-NdeI and eYFP-rev-NheI b) digestion of the product with NdeI and NheI c) ligation of the fragment into NdeI/NheI-treated pMR3691
pLL137	pRSFDuet-1 bearing *eyfp*	a) PCR amplification of *eyfp* from pLL116 with primers NcoI-CFP-For and eYFP-rev-HindIII, b) digestion of the product with NcoI and HindIII c) ligation of the fragment into pRSFDuet-1 cut with NcoI and HindIII
pLL143	pMR3690 bearing *padC-eyfp*	a) release of *padC-eyfp* from pLL87 by digestion with NdeI and NheI b) ligation of the product into NdeI/NheI-treated pMR3690
pLL147	pXYFPC-2 bearing *parA*$_{K31A}$	site-directed mutagenesis of pLL85 with primers parA(K31A)-for and parA(K31A)-rev
pLL148	pXYFPC-2 bearing *parA*$_{G32V}$	site-directed mutagenesis of pLL85 with primers parA(G32V)-for and parA(G32V)-rev
pLL150	pXYFPC-2 bearing *parA*$_{K36R}$	site-directed mutagenesis of pLL85 with primers parA(K36R)-for and parA(K36R)-rev
pLL151	pXYFPC-2 bearing *parA*$_{D60A}$	site-directed mutagenesis of pLL85 with primers parA(D60A)-for and parA(D60A)-rev
pLL155	pMR3691 bearing *parA*$_{K31A}$-*eyfp*	a) PCR amplification of parAK31A-eyfp from pLL147 with primers ParA-for-NdeI and eYFP-rev-NheI b) digestion of the product with NdeI and NheI c) ligation of the fragment into pMR3691 cut with NdeI and NheI
pLL156	pMR3691 bearing *parA*$_{G32V}$-*eyfp*	a) PCR amplification of *parA*$_{G32V}$-*eyfp* from pLL148 with primers ParA-for-NdeI and eYFP-rev-NheI b) digestion of the product with NdeI and NheI c) ligation of the fragment into pMR3691 cut with NdeI and NheI
pLL157	pXCHYC-1 bearing *parA*$_{K31A}$	a) PCR amplification of *parA*$_{K31A}$ from pLL147 with primers ParA-for-NdeI and ParA-rev-EcoRI b) digestion of the product with NdeI and EcoRI c) ligation of the fragment into pXCHYC-1 cut with NdeI and EcoRI
pLL158	pXCHYC-1 bearing *parA*$_{G32V}$	a) PCR amplification of *parA*$_{G32V}$ from pLL148 with primers ParA-for-NdeI and ParA-rev-EcoRI b) digestion of the product with with NdeI and EcoRI c) ligation of the fragment into pXCHYC-1 cut with NdeI and EcoRI
pLL159	pXCHYC-1 bearing *parA*$_{K36R}$	a) PCR amplification of *parA*$_{K36R}$ from pLL150 with primers ParA-for-NdeI and ParA-rev-EcoRI b) digestion of the product with NdeI and EcoRI c) ligation of the fragment into pXCHYC-1 cut with NdeI and EcoRI
pLL163	pXCHYC-1 bearing *parA*$_{D60A}$	a) PCR amplification of *parA*$_{D60A}$ from pLL151 with primers ParA-for-NdeI and ParA-rev-EcoRI b) digestion of the product with NdeI and EcoRI c) ligation of the fragment into pXCHYC-1 cut with NdeI and EcoRI
pLL165	pMR3691 bearing *parA*$_{K36R}$-*eyfp*	a) PCR amplification of *parA*$_{K36R}$-*eyfp* from pLL150 with primers ParA-for-NdeI and eYFP-rev-NheI b) digestion of the product with NdeI and NheI c) ligation of the fragment into pMR3691 cut with NdeI and NheI
pLL166	pMR3691 bearing *parA*$_{D60A}$-*eyfp*	a) PCR amplification of *parA*$_{D60A}$-*eyfp* from pLL151 with primers ParA-for-NdeI and eYFP-rev-NheI b) digestion of the product with NdeI and NheI c) ligation of the fragment into pMR3691 cut with NdeI and NheI
pLL171	pMT325 bearing *parA*$_{K31A}$-*mCherry*	a) PCR amplification of *parA*$_{K31A}$-*mCherry* from pLL157 using primers ParA-eyfp-for-XbaI and mCherry-rev-HindIII b) digestion of the product with XbaI and HindIII c) ligation of the fragment into pMT325 cut with XbaI and HindIII
pLL172	pMT325 bearing *parA*$_{G32V}$-*mCherry*	a) PCR amplification of *parA*$_{G32V}$-*mCherry* from pLL158 using primers ParA-eyfp-for-XbaI and mCherry-rev-HindIII b) digestion of the product with XbaI and HindIII c) ligation of the fragment into pMT325 cut with XbaI and HindIII
pLL173	pMT325 bearing *parA*$_{K36R}$-*mCherry*	a) PCR amplification of *parA*$_{K36R}$-*mCherry* from pLL159 using primers ParA-eyfp-for-XbaI and mCherry-rev-HindIII b) digestion of the product with XbaI and HindIII c) ligation of the fragment into pMT325 cut with XbaI and HindIII
pLL178	pMT325 bearing *parA*$_{D60A}$-*mCherry*	a) PCR amplification of *parA*$_{D60A}$-*mCherry* from pLL163 using primers ParA-eyfp-for-XbaI and mCherry-rev-HindIII b) digestion of the product with XbaI and HindIII c) ligation of the fragment into pMT325 cut with XbaI and HindIII
pLL200	pXCHYC-1 bearing *parA*$_{D60AR238E}$	site-directed mutagenesis of pLL163 with primers parA(R238E)-for and parA(R238E)-rev

pLL202	pMT325 bearing $parA_{D60AR238E}$-*mCherry*	a) PCR amplification of $parA_{D60AR238E}$-*mCherry* from pLL200 using primers ParA-eyfp-for-XbaI and mCherry-rev-HindIII b) digestion of the product with XbaI and HindIII c) ligation of the fragment into pMT325 cut with XbaI and HindIII

Supplementary Table 4. Plasmids generated in this work (continued).

Plasmid	Description	Construction
pLL204	pXYFPC-2 bearing *parA*$_{D60AR238E}$	a) PCR amplification of *parA*$_{D60AR238E}$ from pLL200 with primers ParA-for-NdeI and ParA-rev-EcoRI b) digestion of the product with NdeI and EcoRI c) ligation of the fragment into pXYFPC-2 cut with NdeI and EcoRI
pLL205	pRSFDuet-1 bearing *padC*	a) PCR amplification of *padC* using primers MXAN4634-For-new-NdeI and mxan4634c-rev b) digestion of the product with EcoRI and treatment with T4 DNA polymerase c) digestion of pRSFDuet-1 with KpnI and treatment with T4 DNA polymerase d) digestion of both the *padC* fragment and linearized pRSFDuet-1 with NdeI e) ligation of the two restriction products
pLL215	pMT325 bearing *parA*$_{G32V}$-*eyfp*	a) PCR amplification of *parA*$_{G32V}$-*eyfp* from pLL148 using primers ParA-eyfp-for-XbaI and ParA-eyfp-rev-XmaI b) digestion of the product with XbaI and XmaI c) ligation of the fragment into pMT325 cut with XbaI and XmaI
pLL235	pRSFDuet-1 bearing *ibpA-yfp*	a) PCR amplification of *ibpA* from *E. coli* TOP10 with primers IbpA-1 and IbpA-2 b) Fusion of the PCR product with NdeI/EcoRI-treated pXYFPC-2 by Gibson assembly c) PCR amplification of *ibpA-eyfp* from the resulting plasmid using primers IbpA-yfp-g-5 and IbpA-yfp-g-6 d) Fusion of the PCR product with NdeI/KpnI-treated pRSFDuet-1 by Gibson assembly
pMO002	pET28a(+) bearing *padC*$_{\Delta AA1-281}$	a) PCR amplification of *padC*$_{\Delta AA1-281}$ with primers MXAN4634c3-for and MXAN4634c-rev b) digestion of the product with NdeI and EcoRI c) ligation of the fragment into NdeI/EcoRI-treated pET28a(+)
pPS17	pXYFPN-2 bearing *bacN*	a) PCR amplification of *bacN* using primers MXAN4637-for-2 and MXAN4637-rev-2 b) digestion of the product with EcoRI and BamHI c) ligation of the fragment into pXYFPN-2 cut with EcoRI and BamHI
pPS20	pMT325 bearing *eyfp-bacN*	a) PCR amplification of *eyfp-bacN* from pPS17 using primers YFP-MXAN4637-For and YFP-MXAN4637-Rev b) digestion of the product with BamHI and XmaI c) ligation of the fragment into pMT325 cut with BamHI and XmaI

Supplementary Table 5. Oligonucleotides in this work.

Oligonucleotide	Sequence
BacN-up-1-BamHI	AATTGGATCCGCCCTTGCCGATGATGC
BacN-up-2-EcoRI	AATTGAATTCGGCCACGGTAAGGCCGA
CFP-MXAN4636-Rev-EcoRI	AGCTGAATTCTCAGCGCTCCTTCATGTCCATGTC
Comp MXAN4635-for	TTATCTAGAATGGCCACCGCGAAGGAGCTCTCA
Comp MXAN4635-Rev	TTAAAGCTTCTAGCGGGTCTTCTTCTTCACCAC
eYFP-for-BamHI	AATTGGATCCATGGTGAGCAAGGGCGA
eYFP-rev-HindIII	GGCCAAGCTTTTACTTGTACAGCTCGTC
eyfp-rev-NheI	AGCTGCTAGCTTACTTGTACAGCTCGTC
IbpA-1	TTGGGGAGACGACCATATGATGCGTAACTTTGATTTATCCCCGC
IbpA-2	GACGCGTAACGTTCGAATTCGCGTTGATTTCGATACGGCG
IbpA-yfp-g-5	AGAAGGAGATATACATATGCGTAACTTTGATTTATCCCCGCTTTACC
IbpA-yfp-g-6	CAGACTCGAGGGTACCTTACTTGTACAGCTCGTCCATGCC
mCherry-4635-Rev-XhoI	AATTCTCGAGCTAGCGGGTCTTCTTCTTCACCA
mCherry-For-NdeI	AGCTCATATGATGGTGAGCAAGGGCGAGGAG
mCherry-MXAN4635N-rev	AATTCAATTGCTACAGACGTCCCGGCTCCACGTC
mCherry-MXAN4635rev-MfeI	AATTCAATTGCTAGCGGGTCTTCTTCTTCACCA
mCherry-rev-HindIII	ATAAGCTTTTACTTGTACAGCTCGTCCATGCCGCCG
mCherry-Rev-NheI	TATAGCTAGCTTACTTGTACAGCTCGTCCATGCCGCCG
mxan4634c-for	AATTCATATGCCCTCCGACGGCGAGGCCCG
MXAN4634c-for-BglII	AATTAGATCTCCCTCCGACGGCGAGGCC
mxan4634c-rev	AGTCGAATTCTTACAGCCCCTCCAGATAGG
MXAN4634down-1-HindIII	GAGCAAGCTTAGAATCTTCCGGTAGGA
MXAN4634down-2-BamHI	AATTGGATCCTCGTCCGAGCTGGTCAC
MXAN4634-down-for	TAGGATCCTCGTCCGAGCTGGTCACCTATCTGG
MXAN4634down-For-2	TATAGCTAGCGCCATGGCGGAACCTCTCGTGCG
MXAN4634-down-rev	TTAAGAATTCCTCGCGGAAGGACAGCGTCTGCAGCGTC
MXAN4634down-Rev-NheI	TTAAGCTAGCCTCGCGGAAGGACAGCGTCTG
MXAN4634-For-new-NdeI	TATACATATGCGGGCGCGTGGGCTTTTCAGGG
MXAN4634-For-XbaI	TTAATCTAGAATGCGGGCGCGTGGGCTTTTC
MXAN4634-Rev-new-EcoRI	TAGAATTCGACAGCCCCTCCAGATAGGTGACCAG
MXAN4634-up-For	TATAAAGCTTCCTCCTTCAAGGGCAACGTCGAC
MXAN4634-up-Rev	TAGGATCCCATGGTGGCACCCCTGAAAAGCCCA
MXAN4634c3-for	AATTCATATGCCCGAACCCGAGCAGCGCG
MXAN4635-For	TATAGATCTATGGCCACCGCGAAGGAGCTCTCAG
MXAN4635-HA-1	TATAAAGCTTGTGGCCACCGCGAAGGAGCTCTCAG
MXAN4635-HA-2	TAGGATCCCTAAGCGTAGTCTGGGACGTCGTATGGGTAGCGGGTCTTCTTCTTCACCA
MXAN4635HA-down-for	TAGGATCCCGCGCACCGCCCGCGCCGCCAGTCG
MXAN4635HA-down-rev	TTAAGAATTCACTGCTCGGCGCGCCTCCTCGTT
MXAN4635-Rev	TTTTGCTAGCCTAGCGGGTCTTCTTCTTCACCACG
MXAN4636-For	TATAGATCTATGAGCTTCACGCCGCGCACGGCACG
MXAN4636-Rev	TTTTGCTAGCTCAGCGCTCCTTCATGTCCATGTC
MXAN4637-for-2	GCGCGAATTCGGCAACGGGTGAAACGGGCA
MXAN4637-HA-1	TATAAAGCTTCGTGCTGCTGGCGCCGAAGATTCAA
MXAN4637-HA-2	TAGGATCCCTAAGCGTAGTCTGGGACGTCGTATGGGTAAATGTCGTCAGGAAGCCGTAC
MXAN4637HA-down-for	TAGGATCCCGGCTTCCTGACGACATTTGAGCTTCAC
MXAN4637HA-down-rev	TTAAGAATTCGGCAGCGGCTTGCTTCCCAGGCCAC
MXAN4637-rev-2	GCGCGGATCCTCAAATGTCGTCAGGAAGCC
NcoI-CFP-For	AATTCCATGGTGAGCAAGGGCGAGGAGCTGTTCA
parA(D60A)-for	CTGGTGGACATGGCCCCGCAGGGCAAC
parA(D60A)-rev	GTTGCCCTGCGGGGCCATGTCCACCAG
parA(G32V)-for	CTTCCCGACGCCGACCTTCTGGTTGGA
parA(G32V)-rev	TCCAACCAGAAGGTCGGCGTCGGGAAG
parA(K31A)-for	CATCTCCAACCAGGCGGGCGGCGTCGGG
parA(K31A)-REV	CCCGACGCCGCCCGCCTGGTTGGAGATG
parA(K36R)-for	CGGTGGTGGTCCTCCCGACGCCG
parA(K36R)-rev	CGGCGTCGGGAGGACCACCACCG
parA(R209A)-for	ACCATGTTCGACTCGGCGGCGAACATTGCCCA
parA(R209A)-rev	TGGGCAATGTTCGCCGCCGAGTCGAACATGGT
parA(R238E)-for	GTGCCGCGCAACGTGGAGCTGTCCGAGTGCCCC
parA(R238E)-rev	GGGGCACTCGGACAGCTCCACGTTGCGCGGCAC
ParA-eyfp-for-XbaI	AATTCTAGAAGGAGGAATTCACCATGCACTGCATCACGCGCGGGGCC
ParA-eyfp-rev-XmaI	AATTCCCGGGTTACTTGTACAGCTCGTCCAT

Supplementary Table 5. Oligonucleotides in this work (continued).

Oligonucleotide	Sequence
ParA-for-NdeI	AATTCATATGCACTGCATCACGCGCGGG
ParA-rev-EcoRI	AATTGAATTCCCAGCCACGCGCCTGCGA
ParB-for-BamHI strep	TGTAGGATCCGATGGTGAAAGCAGACATG
ParB-rev-NotI strep	AATTGCGGCCGCCTACTCCTTCCTGAGAAGC
parB-yfp-rev-XmaI	GCGCCCCGGGTTACTTGTACAGCTCGTCCATGCCG
XbaI-RBS-eYFP-for	TCTAGAAGGAGGAATTCACCATGGTGAGCAAGGGCGAGGAGC
YFP-MXAN4637-For	GCGCCCCGGGAGGAGGAATTCACCATGGTGAGCAAGGGCGAGGAGCTGT
YFP-MXAN4637-Rev	GCGCGGATCCTCAAATGTCGTCAGGAAGCCG

SUPPLEMENTARY REFERENCES

Lindner, A. B., Madden, R. Demarez, A., Stewart, E. J. & Taddei, F. Asymmetric segregation of protein aggregates is associated with cellular aging and rejuvenation. *Proc. Natl. Acad. Sci. U S A* **105**, 3076-3081 (2008).

Oberto, J. SyntTax: a web server linking synteny to prokaryotic taxonomy. *BMC Bioinformatics* **16**, 4 (2013).

Kaiser, D. Social gliding is correlated with the presence of pili in *Myxococcus xanthus*. *Proc. Natl. Acad. Sci. USA* **76**, 5952-5956 (1979).

Kühn, J., Briegel, A., Mörschel, E., Kahnt, J., Leser, K., Wick, S., Jensen, G. J., and Thanbichler, M. Bactofilins, a ubiquitous class of cytoskeletal proteins mediating polar localization of a cell wall synthase in *Caulobacter crescentus*. *EMBO J.* **29**, 327-339 (2010).

Ben-Yehuda, S., Rudner, D.Z., and Losick, R. (2003) RacA, a bacterial protein that anchors chromosomes to the cell poles. *Science* **299**: 532-536.

Bowman, G.R., Comolli, L.R., Gaietta, G.M., Fero, M., Hong, S.H., Jones, Y., Lee, J.H., Downing, K.H., Ellisman, M.H., McAdams, H.H., and Shapiro, L. (2010) *Caulobacter* PopZ forms a polar subdomain dictating sequential changes in pole composition and function. *Mol Microbiol* **76**: 173-189.

Bowman, G.R., Comolli, L.R., Zhu, J., Eckart, M., Koenig, M., Downing, K.H., Moerner, W.E., Earnest, T., and Shapiro, L. (2008) A polymeric protein anchors the chromosomal origin/ParB complex at a bacterial cell pole. *Cell* **134**: 945-955.

Bowman, G.R., Perez, A.M., Ptacin, J.L., Ighodaro, E., Folta-Stogniew, E., Comolli, L.R., and Shapiro, L. (2013) Oligomerization and higher-order assembly contribute to sub-cellular localization of a bacterial scaffold. *Mol Microbiol* **90**: 776-795.

Bramkamp, M., Emmins, R., Weston, L., Donovan, C., Daniel, R.A., and Errington, J. (2008) A novel component of the division-site selection system of *Bacillus subtilis* and a new mode of action for the division inhibitor MinCD. *Mol Microbiol* **70**: 1556-1569.

Bulyha, I., Lindow, S., Lin, L., Bolte, K., Wuichet, K., Kahnt, J., van der Does, C., Thanbichler, M., and Søgaard-Andersen, L. (2013) Two small GTPases act in concert with the bactofilin cytoskeleton to regulate dynamic bacterial cell polarity. *Developmental cell* **25**: 119-131.

Bulyha, I., Schmidt, C., Lenz, P., Jakovljevic, V., Hone, A., Maier, B., Hoppert, M., and Søgaard-Andersen, L. (2009) Regulation of the type IV pili molecular machine by dynamic localization of two motor proteins. *Mol Microbiol* **74**: 691-706.

Cameron, T.A., Anderson-Furgeson, J., Zupan, J.R., Zik, J.J., and Zambryski, P.C. (2014) Peptidoglycan synthesis machinery in *Agrobacterium tumefaciens* during unipolar growth and cell division. *mBio* **5**: e01219-01214.

Coordinators, N.R. (2016) Database resources of the National Center for Biotechnology Information. *Nucleic acids research* **44**: D7-19.

Ditkowski, B., Holmes, N., Rydzak, J., Donczew, M., Bezulska, M., Ginda, K., Kedzierski, P., Zakrzewska-Czerwinska, J., Kelemen, G.H., and Jakimowicz, D. (2013) Dynamic interplay of ParA with the polarity protein, Scy, coordinates the growth with chromosome segregation in *Streptomyces coelicolor*. *Open biology* **3**: 130006.

Dodd, I.B., and Egan, J.B. (1990) Improved detection of helix-turn-helix DNA-binding motifs in protein sequences. *Nucleic acids research* **18**: 5019-5026.

Donovan, C., Sieger, B., Kramer, R., and Bramkamp, M. (2012) A synthetic *Escherichia coli* system identifies a conserved origin tethering factor in Actinobacteria. *Mol Microbiol* **84**: 105-116.

Ebersbach, G., Briegel, A., Jensen, G.J., and Jacobs-Wagner, C. (2008) A self-associating protein critical for chromosome attachment, division, and polar organization in *Caulobacter*. *Cell* **134**: 956-968.

El Andari, J., Altegoer, F., Bange, G., and Graumann, P.L. (2015) *Bacillus subtilis* bactofilins are essential for flagellar hook- and filament assembly and dynamically localize into structures of less than 100 nm diameter underneath the cell membrane. *PloS one* **10**: e0141546.

Eswaramoorthy, P., Erb, M.L., Gregory, J.A., Silverman, J., Pogliano, K., Pogliano, J., and Ramamurthi, K.S. (2011) Cellular architecture mediates DivIVA ultrastructure and regulates min activity in *Bacillus subtilis*. *mBio* **2**: e00257-00211.

Finn, R.D., Coggill, P., Eberhardt, R.Y., Eddy, S.R., Mistry, J., Mitchell, A.L., Potter, S.C., Punta, M., Qureshi, M., Sangrador-Vegas, A., Salazar, G.A., Tate, J., and Bateman, A. (2016) The Pfam protein families database: towards a more sustainable future. *Nucleic acids research* **44**: D279-285.

Flardh, K. (2003) Essential role of DivIVA in polar growth and morphogenesis in *Streptomyces coelicolor* A3(2). *Mol Microbiol* **49**: 1523-1536.

Fogel, M.A., and Waldor, M.K. (2006) A dynamic, mitotic-like mechanism for bacterial chromosome segregation. *Genes & development* **20**: 3269-3282.

Fuchino, K., Bagchi, S., Cantlay, S., Sandblad, L., Wu, D., Bergman, J., Kamali-Moghaddam, M., Flärdh, K., and Ausmees, N. (2013) Dynamic gradients of an intermediate filament-like cytoskeleton are recruited by a polarity landmark during apical growth. *Proc Natl Acad Sci U S A* **110**: E1889-1897.

Gerdes, K., Howard, M., and Szardenings, F. (2010) Pushing and pulling in prokaryotic DNA segregation. *Cell* **141**: 927-942.

Ginda, K., Bezulska, M., Ziolkiewicz, M., Dziadek, J., Zakrzewska-Czerwinska, J., and Jakimowicz, D. (2013) ParA of *Mycobacterium smegmatis* co-ordinates chromosome segregation with the cell cycle and interacts with the polar growth determinant DivIVA. *Mol Microbiol* **87**: 998-1012.

Gomez-Santos, N., Treuner-Lange, A., Moraleda-Munoz, A., Garcia-Bravo, E., Garcia-Hernandez, R., Martinez-Cayuela, M., Perez, J., Søgaard-Andersen, L., and Munoz-Dorado, J. (2012) Comprehensive set of integrative plasmid vectors for copper-inducible gene expression in *Myxococcus xanthus*. *Applied and environmental microbiology* **78**: 2515-2521.

Harms, A., Treuner-Lange, A., Schumacher, D., and Søgaard-Andersen, L. (2013) Tracking of chromosome and replisome dynamics in *Myxococcus xanthus* reveals a novel chromosome arrangement. *PLoS genetics* **9**: e1003802.

Hempel, A.M., Wang, S.B., Letek, M., Gil, J.A., and Flärdh, K. (2008) Assemblies of DivIVA mark sites for hyphal branching and can establish new zones of cell wall growth in *Streptomyces coelicolor*. *J Bacteriol* **190**: 7579-7583.

Hester, C.M., and Lutkenhaus, J. (2007) Soj (ParA) DNA binding is mediated by conserved arginines and is essential for plasmid segregation. *P Natl Acad Sci USA* **104**: 20326-20331.

Hodgkin, J., and Kaiser, D. (1977) Cell-to-cell stimulation of movement in nonmotile mutants of *Myxococcus*. *Proc Natl Acad Sci USA* **74**: 2938-2942.

Holmes, N.A., Walshaw, J., Leggett, R.M., Thibessard, A., Dalton, K.A., Gillespie, M.D., Hemmings, A.M., Gust, B., and Kelemen, G.H. (2013) Coiled-coil protein Scy is a key component of a multiprotein assembly controlling polarized growth in *Streptomyces*. *Proc Natl Acad Sci U S A* **110**: E397-406.

Hwang, L.C., Vecchiarelli, A.G., Han, Y.W., Mizuuchi, M., Harada, Y., Funnell, B.E., and Mizuuchi, K. (2013) ParA-mediated plasmid partition driven by protein pattern self-organization. *The EMBO journal* **32**: 1238-1249.

Iniesta, A.A. (2014) ParABS system in chromosome partitioning in the bacterium *Myxococcus xanthus*. *PloS one* **9**: e86897.

Iniesta, A.A., Garcia-Heras, F., Abellon-Ruiz, J., Gallego-Garcia, A., and Elias-Arnanz, M. (2012) Two systems for conditional gene expression in *Myxococcus xanthus* inducible by isopropyl-beta-D-thiogalactopyranoside or vanillate. *J Bacteriol* **194**: 5875-5885.

Jones, D.T. (1999) Protein secondary structure prediction based on position-specific scoring matrices. *Journal of molecular biology* **292**: 195-202.

Kashefi, K., and Hartzell, P.L. (1995) Genetic suppression and phenotypic masking of a *Myxococcus xanthus frzF*$^-$ defect. *Mol Microbiol* **15**: 483-494.

Kassem, M.M., Wang, Y., Boomsma, W., and Lindorff-Larsen, K. (2016) Structure of the bacterial cytoskeleton protein bactofilin by NMR chemical shifts and sequence variation. *Biophys J* **110**: 2342-2348.

Kiekebusch, D., and Thanbichler, M. (2014) Spatiotemporal organization of microbial cells by protein concentration gradients. *Trends in microbiology* **22**: 65-73.

Koch, M.K., McHugh, C.A., and Hoiczyk, E. (2011) BacM, an N-terminally processed bactofilin of *Myxococcus xanthus*, is crucial for proper cell shape. *Mol Microbiol* **80**: 1031-1051.

Kühn, J., Briegel, A., Mörschel, E., Kahnt, J., Leser, K., Wick, S., Jensen, G.J., and Thanbichler, M. (2010) Bactofilins, a ubiquitous class of cytoskeletal proteins mediating polar localization of a cell wall synthase in *Caulobacter crescentus*. *EMBO Journal* **29**: 327-339.

Laloux, G., and Jacobs-Wagner, C. (2013) Spatiotemporal control of PopZ localization through cell cycle-coupled multimerization. *J Cell Biol* **201**: 827-841.

Laloux, G., and Jacobs-Wagner, C. (2014) How do bacteria localize proteins to the cell pole? *Journal of cell science* **127**: 11-19.

Lenarcic, R., Halbedel, S., Visser, L., Shaw, M., Wu, L.J., Errington, J., Marenduzzo, D., and Hamoen, L.W. (2009) Localisation of DivIVA by targeting to negatively curved membranes. *The EMBO journal* **28**: 2272-2282.

Leonard, T.A., Butler, P.J., and Löwe, J. (2005) Bacterial chromosome segregation: structure and DNA binding of the Soj dimer – a conserved biological switch. *The EMBO journal* **24**: 270-282.

Letek, M., Ordonez, E., Vaquera, J., Margolin, W., Flärdh, K., Mateos, L.M., and Gil, J.A. (2008) DivIVA is required for polar growth in the MreB-lacking rod-shaped actinomycete *Corynebacterium glutamicum*. *J Bacteriol* **190**: 3283-3292.

Lim, H.C., Surovtsev, I.V., Beltran, B.G., Huang, F., Bewersdorf, J., and Jacobs-Wagner, C. (2014) Evidence for a DNA-relay mechanism in ParABS-mediated chromosome segregation. *eLife* **3**: e02758.

Lin, L., and Thanbichler, M. (2013) Nucleotide-independent cytoskeletal scaffolds in bacteria. *Cytoskeleton* **70**: 409-423.

Magrini, V., Creighton, C., and Youderian, P. (1999) Site-specific recombination of temperate *Myxococcus xanthus* phage Mx8: genetic elements required for integration. *J Bacteriol* **181**: 4050-4061.

Meniche, X., Otten, R., Siegrist, M.S., Baer, C.E., Murphy, K.C., Bertozzi, C.R., and Sassetti, C.M. (2014) Subpolar addition of new cell wall is directed by DivIVA in mycobacteria. *Proc Natl Acad Sci U S A* **111**: E3243-3251.

Mohl, D.A., and Gober, J.W. (1997) Cell cycle-dependent polar localization of chromosome partitioning proteins in *Caulobacter crescentus*. *Cell* **88**: 675-684.

Oliva, M.A., Halbedel, S., Freund, S.M., Dutow, P., Leonard, T.A., Veprintsev, D.B., Hamoen, L.W., and Löwe, J. (2010) Features critical for membrane binding revealed by DivIVA crystal structure. *The EMBO journal* **29**: 1988-2001.

Patrick, J.E., and Kearns, D.B. (2008) MinJ (YvjD) is a topological determinant of cell division in *Bacillus subtilis*. *Mol Microbiol* **70**: 1166-1179.

Ptacin, J.L., Gahlmann, A., Bowman, G.R., Perez, A.M., von Diezmann, A.R., Eckart, M.R., Moerner, W.E., and Shapiro, L. (2014) Bacterial scaffold directs pole-specific centromere segregation. *Proc Natl Acad Sci U S A* **111**: E2046-2055.

Ptacin, J.L., Lee, S.F., Garner, E.C., Toro, E., Eckart, M., Comolli, L.R., Moerner, W.E., and Shapiro, L. (2010) A spindle-like apparatus guides bacterial chromosome segregation. *Nature cell biology* **12**: 791-798.

Ramamurthi, K.S., and Losick, R. (2009) Negative membrane curvature as a cue for subcellular localization of a bacterial protein. *Proc Natl Acad Sci U S A* **106**: 13541-13545.

Rudner, D.Z., and Losick, R. (2010) Protein subcellular localization in bacteria. *Cold Spring Harbor perspectives in biology* **2**: a000307.

Schlimpert, S., Klein, E.A., Briegel, A., Hughes, V., Kahnt, J., Bolte, K., Maier, U.G., Brun, Y.V., Jensen, G.J., Gitai, Z., and Thanbichler, M. (2012) General protein diffusion barriers create compartments within bacterial cells. *Cell* **151**: 1270-1282.

Schofield, W.B., Lim, H.C., and Jacobs-Wagner, C. (2010) Cell cycle coordination and regulation of bacterial chromosome segregation dynamics by polarly localized proteins. *The EMBO journal* **29**: 3068-3081.

Shapiro, L., McAdams, H.H., and Losick, R. (2009) Why and how bacteria localize proteins. *Science* **326**: 1225-1228.

Shebelut, C.W., Guberman, J.M., van Teeffelen, S., Yakhnina, A.A., and Gitai, Z. (2010) Caulobacter chromosome segregation is an ordered multistep process. *Proc Natl Acad Sci U S A* **107**: 14194-14198.

Shi, C., Fricke, P., Lin, L., Chevelkov, V., Wegstroth, M., Giller, K., Becker, S., Thanbichler, M., and Lange, A. (2015) Atomic-resolution structure of cytoskeletal bactofilin by solid-state NMR. *Sci Adv* **1**: e1501087.

Sieger, B., Schubert, K., Donovan, C., and Bramkamp, M. (2013) The lipid II flippase RodA determines morphology and growth in *Corynebacterium glutamicum*. *Mol Microbiol* **90**: 966-982.

Stahlberg, H., Kutejova, E., Muchova, K., Gregorini, M., Lustig, A., Muller, S.A., Olivieri, V., Engel, A., Wilkinson, A.J., and Barak, I. (2004) Oligomeric structure of the *Bacillus subtilis* cell division protein DivIVA determined by transmission electron microscopy. *Mol Microbiol* **52**: 1281-1290.

Sycuro, L.K., Pincus, Z., Gutierrez, K.D., Biboy, J., Stern, C.A., Vollmer, W., and Salama, N.R. (2010) Peptidoglycan crosslinking relaxation promotes *Helicobacter pylori*'s helical shape and stomach colonization. *Cell* **141**: 822-833.

Thanbichler, M., and Shapiro, L. (2006) MipZ, a spatial regulator coordinating chromosome segregation with cell division in *Caulobacter*. *Cell* **126**: 147-162.

Toro, E., Hong, S.H., McAdams, H.H., and Shapiro, L. (2008) *Caulobacter* requires a dedicated mechanism to initiate chromosome segregation. *Proc Natl Acad Sci USA* **105**: 15435-15440.

Treuner-Lange, A., and Søgaard-Andersen, L. (2014) Regulation of cell polarity in bacteria. *J Cell Biol* **206**: 7-17.

Ueki, T., Inouye, S., and Inouye, M. (1996) Positive-negative KG cassettes for construction of multi-gene deletions using a single drug marker. *Gene* **183**: 153-157.

Vasa, S., Lin, L., Shi, C., Habenstein, B., Riedel, D., Kühn, J., Thanbichler, M., and Lange, A. (2015) beta-Helical architecture of cytoskeletal bactofilin filaments revealed by solid-state NMR. *Proc Natl Acad Sci U S A* **112**: E127-136.

Vecchiarelli, A.G., Havey, J.C., Ing, L.L., Wong, E.O., Waples, W.G., and Funnell, B.E. (2013a) Dissection of the ATPase active site of P1 ParA reveals multiple active forms essential for plasmid partition. *The Journal of biological chemistry* **288**: 17823-17831.

Vecchiarelli, A.G., Hwang, L.C., and Mizuuchi, K. (2013b) Cell-free study of F plasmid partition provides evidence for cargo transport by a diffusion-ratchet mechanism. *Proc Natl Acad Sci U S A* **110**: E1390-1397.

Wang, X., Montero Llopis, P., and Rudner, D.Z. (2013) Organization and segregation of bacterial chromosomes. *Nature reviews. Genetics* **14**: 191-203.

Wu, L.J., and Errington, J. (2003) RacA and the Soj-Spo0J system combine to effect polar chromosome segregation in sporulating *Bacillus subtilis*. *Mol Microbiol* **49**: 1463-1475.

Yamaichi, Y., Bruckner, R., Ringgaard, S., Möll, A., Cameron, D.E., Briegel, A., Jensen, G.J., Davis, B.M., and Waldor, M.K. (2012) A multidomain hub anchors the chromosome segregation and chemotactic machinery to the bacterial pole. *Genes & development* **26**: 2348-2360.

Zhang, Y., Ducret, A., Shaevitz, J., and Mignot, T. (2012) From individual cell motility to collective behaviors: insights from a prokaryote, *Myxococcus xanthus*. *FEMS microbiology reviews* **36**: 149-164.

Zuckerman, D.M., Boucher, L.E., Xie, K., Engelhardt, H., Bosch, J., and Hoiczyk, E. (2015) The bactofilin cytoskeleton protein BacM of *Myxococcus xanthus* Forms an extended β-sheet structure likely mediated by hydrophobic interactions. *PloS one* **10**: e0121074.

Chapter III:

ParB-type DNA segregation proteins are CTP-dependent molecular switches

Manuel Osorio-Valeriano[1,2], Florian Altegoer[3,4], Wieland Steinchen[3,4], Svenja Urban[1], Ying Liu[1], Gert Bange[3,4,*], Martin Thanbichler[1,2,3,4,5,*]

This chapter is written in manuscript style and was published in *Cell* in December 2019. My contribution to this work included conceiving the study, designing and performing the biochemical and cell biological experiments, analyzing the data obtained and writing the manuscript together with M.T.

[1] Department of Biology, University of Marburg, 35043 Marburg, Germany
[2] Max Planck Institute for Terrestrial Microbiology, 35043 Marburg, Germany
[3] Department of Chemistry, University of Marburg, 35043 Marburg, Germany
[4] Center for Synthetic Microbiology, 35043 Marburg, Germany
[5] Lead contact
[*] Correspondence: gert.bange@synmikro.uni-marburg.de (G.B.) and thanbichler@uni-marburg.de (M.T.)

SUMMARY

During cell division, newly replicated DNA is actively segregated to the daughter cells. In most bacteria, this process involves the DNA-binding protein ParB, which condenses the centromeric regions of sister DNA molecules into kinetochore-like structures that recruit the DNA partition ATPase ParA and the prokaryotic SMC/condensin complex. Here, we report the crystal structure of a ParB-like protein (PadC) that emerges to tightly bind the ribonucleotide CTP. The CTP-binding pocket of PadC is conserved in ParB and composed of signature motifs known to be essential for ParB function. We found that ParB also interacts with CTP and requires nucleotide binding for DNA condensation *in vivo*. We further show that CTP-binding modulates the affinity of ParB for centromeric *parS* sites, whereas *parS* recognition stimulates its CTPase activity. ParB proteins thus emerge as a new class of CTP-dependent molecular switches that act in concert with ATPases and GTPases to control fundamental cellular functions.

INTRODUCTION

The faithful inheritance of genetic information relies on machinery that actively partitions sister DNA molecules to the offspring during cell division. In most bacteria, chromosomal DNA and low-copy number plasmids are segregated by the ParAB*S* DNA partitioning system (Badrinarayanan et al., 2015). One of its core components is the DNA-binding protein ParB, which recognizes clusters of short palindromic sequences (*parS*) close to the replication origin of target DNA molecules (Lin and Grossman, 1998; Mohl and Gober, 1997). After initial specific interactions with a small number of *parS* sites, ParB condenses the adjacent DNA regions into a large nucleoprotein complex that typically includes 10-20 kb of the origin region (Breier and Grossman, 2007; Lynch and Wang, 1995). This kinetochore-like structure, known as the partition complex, represents a dynamic and poorly organized network of DNA loops that are interconnected by ParB. Its formation is thought to involve the lateral (1D) spreading of ParB into the *parS*-flanking regions (Murray et al., 2006; Rodionov et al., 1999) as well as DNA-bridging (3D) interactions between distally located ParB molecules (Broedersz et al., 2014; Debaugny et al., 2018; Graham et al., 2014; Sanchez et al., 2015; Song et al., 2017; Taylor et al., 2015). However, the precise mechanism controlling the assembly process is still incompletely understood. Once established, partition complexes recruit the P-loop ATPase ParA, which then directs the movement of sister replicons to opposite sides of the cell. This process is driven by a ratchet-like mechanism in which ParB follows a gradient of nucleoid-associated ParA·ATP dimers that is progressively shortened by the ATPase-activating activity of ParB (Fogel and Waldor, 2006; Lim et al., 2014; Vecchiarelli et al., 2014; for a review see Badrinarayanan et al., 2015). In many species, partition complexes additionally serve as a loading platforms for the prokaryotic SMC/condensin complex (Gruber and Errington, 2009; Minnen et al., 2011; Sullivan et al., 2009; Tran et al., 2017), a clamp-like structure that promotes bulk chromosome segregation by actively compacting and aligning the two arms of sister chromatids (Tran et al., 2017; Volkov et al., 2003; Wang et al., 2017).

Although variable in sequence, ParB proteins have a highly conserved general architecture (Funnell, 2016), comprising (i) an N-terminal ParB/Srx domain, (ii) a central DNA-binding domain with a helix-turn-helix (HTH) motif mediating *parS* recognition (Chen et al., 2015 ; Leonard et al., 2004; Schumacher et al., 2010; Surtees and Funnell, 2001) and (iii) a C-terminal dimerization domain with additional non-specific DNA-binding activity (Fisher et al., 2017; Leonard et al., 2004). The ParB/Srx domain is flexible (Hanai et al., 1996; Surtees and Funnell, 1999) and thus difficult to study by X-ray crystallography, with only a few structures available to date (Chen et al., 2015; Leonard et al., 2004; Schumacher et al., 2015). It plays a central role in ParB function and has been implicated in ParA binding (Bouet and Funnell, 1999; Figge et al., 2003; Radnedge et al., 1998; Ringgaard et al., 2009; Surtees and Funnell, 1999) as well as protein oligomerization (Autret et al., 2001; Kusiak et al., 2011; Surtees and Funnell,

1999). In support of its importance, modification of a highly conserved arginine-rich motif in the ParB/Srx domain abolishes partition complex formation and, as a consequence, ParAB*S*-mediated DNA segregation (Autret et al., 2001; Graham et al., 2014; Tran et al., 2018). However, despite almost three decades of intensive research, the molecular mechanism underlying the function of ParB proteins is still incompletely understood.

Interestingly, whereas ParB proteins are thought to have a purely structural role, some of their homologs show catalytic activity. These include the archaeal free serine kinase SerK (Makino et al., 2016; Nagata et al., 2017) as well as the highly conserved eukaryotic protein sulfiredoxin (Srx), which reactivates hyperoxidized cysteine residues in the catalytic center of peroxiredoxins (Chang et al., 2004; Jönsson et al., 2008), thereby facilitating oxidative stress response and H_2O_2-mediated signaling (Rhee et al., 2012). In both cases, the ParB/Srx domain serves as an ATP/ADP-binding module that plays an integral role in the catalytic mechanism (Jönsson et al., 2008; Nagata et al., 2017). Sulfiredoxin was proposed to provide a rare example in which a *bone fide* enzyme has evolved from a non-enzymatic, DNA-binding ancestor (Basu and Koonin, 2005).

Recent work in the social bacterium *Myxococcus xanthus* has identified a new ParB/Srx domain-containing protein, called PadC, that complements the canonical ParAB*S* system of this species (Lin et al., 2017). PadC acts as an adapter protein recruiting inactive ParA molecules to the cell pole-associated bactofilin cytoskeleton, thereby enhancing the robustness of the segregation process. In the present study, we solve the crystal structure of the PadC ParB/Srx domain and show that it contains a tightly bound ligand identified as the ribonucleotide CTP. CTP binding is necessary to stabilize the domain in a conformation that facilitates its interaction with ParA. Importantly, the CTP-binding pocket of PadC is highly conserved in canonical ParB proteins and includes residues known to be critical for partition complex formation. In line with this observation, we demonstrate that ParB from *M. xanthus* binds CTP *in vitro*. Moreover, we reveal a CTP-dependent reciprocal interaction between the ParB/Srx and DNA-binding domains of ParB. Based on this interaction, CTP binding modulates the *parS*-binding affinity of ParB, whereas specific recognition of a *parS* motif stimulates CTP hydrolysis. Finally, we show that CTP binding and hydrolysis are critical for partition complex formation *in vivo*. Collectively, our results identify ParB proteins as a previously unrecognized class of nucleotide-dependent molecular switches that use CTP instead of the purine nucleotide ATP or GTP to control essential biological processes. This finding provides new perspectives in the analysis of prokaryotic chromosome segregation and opens the possibility that CTP-dependent regulation could be a more common theme in biology.

RESULTS

The ParB/Srx domain of PadC is a CTP-binding module

PadC is conserved in various members of the order *Myxococcales*. The *M. xanthus* homolog is composed of a disordered N-terminal region (aa 1-281), which is absent in most other species and dispensable for ParA binding (Lin et al., 2017) (Figure S1), and a conserved C-terminal region containing a predicted ParB/Srx domain. To clarify the function of this protein, we purified a PadC variant lacking the disordered region ($PadC_{\Delta N}$) from an *E. coli* overproduction strain and solved its X-ray crystal structure to 1.7 Å resolution (Table S1). The protein forms a compact dimer made of two interlocking polypeptide chains (Figure 1A and Movie S1). Each subunit contains a globular N-terminal (ParB/Srx) domain composed of a four-stranded β-sheet, with strand S1 connected to S2 by a long loop containing helixes H1/H2 and strands S3 and S4 connected through helix H3 (Figure 1B). This domain is followed by a linker region containing helix H4, which terminates in a small domain made of helices H5 and H6. The two polypeptides cross over in the linker region, so that helices H5 and H6 are juxtaposed to helix H4 of the *trans*-subunit, keeping the dimer in a tightly closed conformation (Movie S2). The C-terminal region (aa 422-489) was not resolved in the crystal structure, suggesting that it is flexible. Intriguingly, we detected additional electron densities in the subunit interface, which were unambiguously identified as two molecules of the ribonucleotide CTP (Figures S2A-F). Nucleotide content analysis showed that $PadC_{\Delta N}$ purified from the native host *M. xanthus* also contained CTP at an ~ 1:1 molar ratio (Figures S2G-I), indicating that the presence of the nucleotide was not an artifact caused by the heterologous production of the crystallized protein. CTP intercalated between helices H2 and H3 of one subunit and helix H4 of the *trans*-subunit (Figures 1B and 1C), forming a dense network of hydrogen bonds with amino acid residues and backbone groups in these regions (Figure 1D). Nucleotide binding thus stabilizes the conformation of the ParB/Srx domain *in cis* and, in addition, mediates an interaction between the two adjacent domains. The nucleobase is located in a pocket that is just large enough to accommodate a pyrimidine ring, thereby excluding the larger purine nucleotides ATP and GTP. Specificity for CTP may be provided by hydrogen-bonding interactions of the amino group at position 4 of the cytosine moiety with the carboxyl group of D322 and the backbone carbonyl of G327 in the *cis*-subunit (Figures 1D and 1G). Notably, the triphosphate moiety of CTP adopts an unusual, highly kinked conformation that was stabilized by interactions of each of the three phosphate groups with a coordinated Mg^{2+} ion (Movie S1). Importantly, the N-terminal region of $PadC_{\Delta N}$ shares high structural similarity with the corresponding region of ParB (Spo0J) from *Thermus thermophilus* (Leonard et al., 2004) and *Saccharolobus solfataricus* (Schumacher et al., 2015), especially in the segments containing the CTP-binding helices H2/H3 and H4 (Figures 1E and S3A). Moreover, sequence comparisons revealed that the amino acids lining the CTP binding pocket of PadC are highly conserved in the ParB protein family (Figures 1F and S3B), with many of the key interacting residues located at

identical positions (Figure 1G). Collectively, these results identify CTP as a novel ligand of the ParB/Srx domain, and they strongly suggest that CTP binding may be a conserved feature of ParB-family proteins.

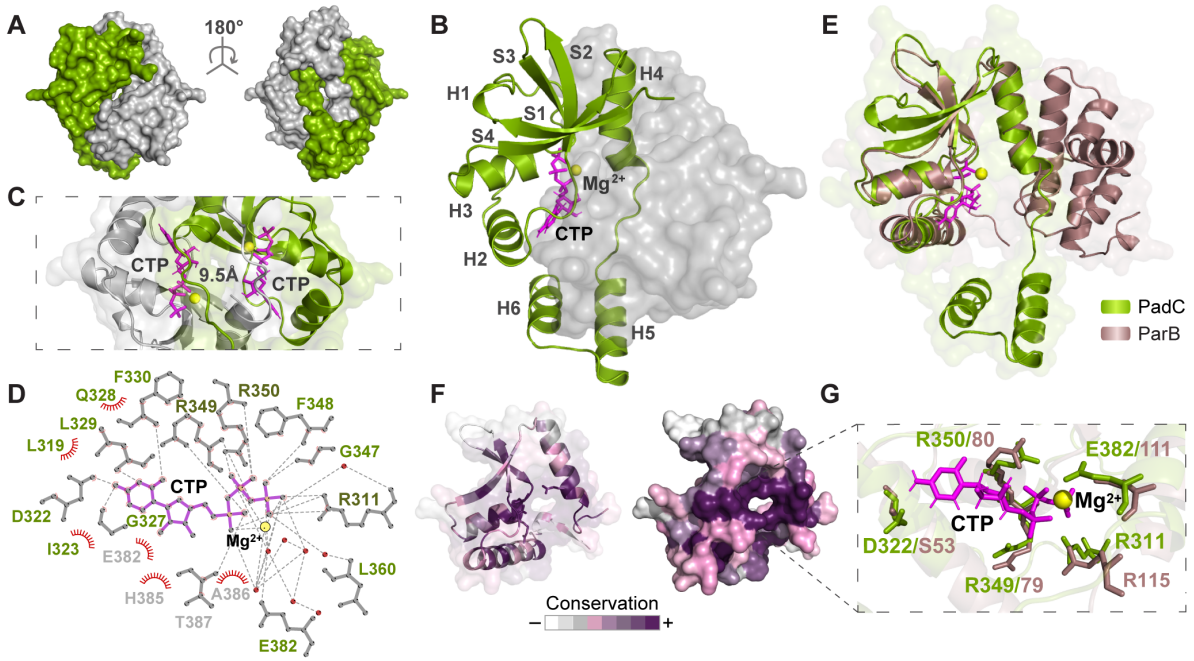

Figure 1. The ParB/Srx domain of PadC is a conserved CTP-binding module. (A) Surface representation of the crystal structure of dimeric $PadC_{\Delta N}$. One monomer is colored in green and the other in light gray. **(B)** Arrangement of secondary structural elements in one monomer of $PadC_{\Delta N}$ in ribbon representation (green). The α-helices are labeled H1 to H6 and the β-strands S1 to S4. The surface of the second monomer is shown in light gray. The CTP molecules and the magnesium ions (Mg^{2+}) are colored in magenta and yellow, respectively. **(C)** PadC dimer interface. The two CTP molecules at the dimer interface keep an average distance of 9.5 Å. **(D)** Protein-ligand interaction 2D map of CTP bound to PadC. Hydrogen bonds (<3.02 Å) are shown as dashed gray lines and hydrophobic interactions as red semicircles. Water molecules are shown as red filled circles. Residues located in the *cis*-subunit are labeled in green, those in the *trans*-subunit in light gray. Residues mutated in this study are highlighted in dark green. **(E)** Structural comparison of the ParB/Srx domains of PadC (in green) and Spo0J (ParB) from *Thermus thermophilus* (PDB 1VZ0) (Leonard et al., 2004) (in dark violet). The two structures show a root mean square deviation (RMSD) of 1.029 Å over 54 paired C_α-atoms. **(F)** Amino acid conservation of the ParB/Srx domain, mapped onto the crystal structure of Spo0J (PDB 1VZ0; residues 23-120) (Leonard et al., 2004). **(G)** Magnification of the CTP-binding pocket of PadC (green), aligned with the corresponding region of Spo0J (dark violet). Residues directly involved in CTP binding are shown in stick representation. See also Figures S1-S3 and Movies S1 and S2.

The ParB/Srx domain of PadC is linked to a C-terminal bactofilin-binding domain

To gain more insight into the domain organization and function of PadC, we studied the determinants mediating its interaction with the bactofilin cytoskeleton. To this end, $PadC_{\Delta N}$ was incubated with a bactofilin fragment ($BacP_C$) that was shown to be necessary and sufficient for PadC binding (Lin et al., 2017). Subsequently, contact sites were mapped by hydrogen-deuterium exchange (HDX) mass spectrometry (Konermann et al., 2011), monitoring local shifts in the accessibility of backbone amide hydrogens caused by the association of $BacP_C$. Notably, the interaction was limited to the flexible C-

terminal region of PadC that was not resolved in the crystal structure (Figure 2A). In support of the HDX data, deletion of this region abolished the interaction of PadC with the polar bactofilin cytoskeleton (but not that with ParA; Figure S1), leading to the dispersal of ParA within the cell (Figure 2B). Moreover, it prevented the interaction of $PadC_{\Delta N}$ with bactofilin *in vitro* (Figure 2C). PadC and ParB thus share a similar overall organization, with a conserved N-terminal ParB/Srx domain fused to a C-terminal target-binding domain that provides specificity for distinct interaction partners.

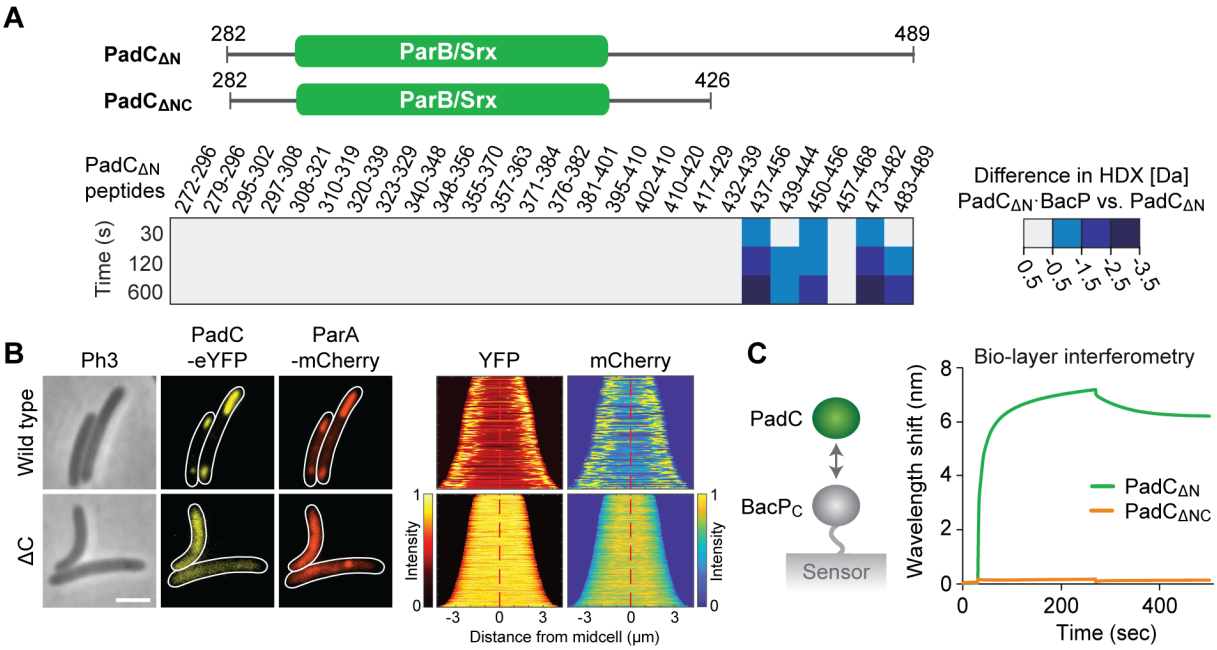

Figure 2. PadC is recruited to the bactofilin cytoskeleton via its C-terminal domain. (A) Hydrogen/deuterium exchange (HDX) analysis of the $BacP_c$·$PadC_{\Delta N}$ complex. The heat plot lists the differences in deuterium uptake between the $PadC_{\Delta N}$·$BacP_c$ complex and $PadC_{\Delta N}$ alone at different incubation times for a series of representative $PadC_{\Delta N}$ peptides (see Data S1 for the full list of peptides). **(B)** Co-localization studies of different PadC-eYFP variants and ParA-mCherry in *M. xanthus*. Cells of *M. xanthus* strains SU1 (Δ*padC* P_{van}-*padC-eyfp* P_{parA}-*parA-mCherry*) (wild type) and MO4 (Δ*padC* P_{van}-$padC_{\Delta C}$-*eyfp* P_{parA}-*parA-mCherry*) (ΔC) were induced for 2 h with 5 µM vanillate before imaging (scale bar: 3 µm). The graphs show the fluorescence profiles of a random subpopulation of cells sorted according to cell length and stacked on top of each other, with the shortest cell on top and the longest cell at the bottom (n=230 cells for SU1 and 480 cells for MO4). **(C)** Biolayer interferometric analysis of the interaction between the C-terminal domain of BacP ($BacP_c$) and the indicated PadC variants. Sensors were loaded with biotinylated $BacP_c$ and probed with saturating concentrations (10 µM) (Lin et al., 2017) of analytes. The kinetics of the interactions were followed by monitoring the wavelength shifts resulting from changes in the optical thickness of the sensor surface during the association and dissociation phases. See also Data S1.

CTP locks the ParB/Srx domain of PadC in a closed conformation

To clarify the role of CTP in PadC function, we generated a $PadC_{\Delta N}$ variant (R350A) lacking a highly conserved arginine residue that contacts the triphosphate moiety of the bound nucleotide (Figures 1D, 1G and S3B). After purification, the mutant protein was nucleotide-free (Figure 3A), indicating that R350 is critical for CTP binding. Gel filtration analysis showed that the R350A variant still formed dimers in solution, likely because of the CTP-independent *inter*-subunit interactions mediated by helices H5

and H6. However, the dimeric complex displayed a slightly larger hydrodynamic radius, suggesting a less compact conformation (Figure S4A). To better understand the effects of CTP binding, we probed the structure of the R350A variant by HDX analysis. We observed significant changes in the N-terminal region of the polypeptide chain, probably resulting from both conformational changes and increased exposure of the dimerization interface. In particular, all elements of the ParB/Srx domain and the adjacent helix H4 were considerably more accessible (Figures 3B and 3C). Importantly, the mutations hardly affected the secondary structure composition of the protein (Figure S4B). The loss of CTP thus causes a rearrangement in the nucleotide-binding region of the PadC dimer, while its overall fold and quarternary structure appears to be maintained. Similar results were obtained for a variant (R311/349/350A) lacking three of the triphosphate-binding arginine residues (Figures S5B-D). Notably, the C-terminal bactofilin-binding domain remained largely unaffected in all cases, indicating that it acts independently of the other parts of the protein (Figures 3B). Consistent with this notion, both mutant variants still showed wild-type affinity for $BacP_C$ in biolayer interferometric analyses (Figure S5A). Thus, CTP binding specifically affects the interaction of the PadC ParB/Srx domain with ParA.

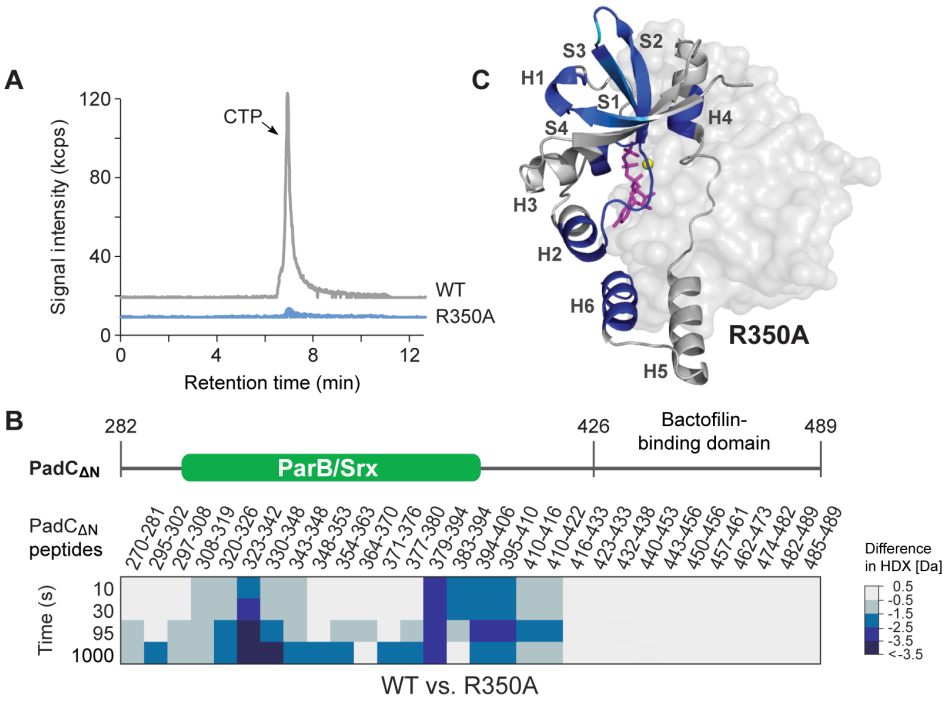

Figure 3. CTP stabilizes the ParB/Srx domain in a closed conformation. **(A)** Loss of CTP from PadC after mutation of the nucleotide-binding pocket. The nucleotide content of wild-type (WT) $PadC_{\Delta N}$ and its R350A variant (80 µM) was analyzed by hydrophilic interaction liquid chromatography. The elution of nucleotides was monitored at a wavelength of 260 nm (kcps, kilocounts per second). **(B)** Hydrogen/deuterium exchange (HDX) analysis of the PadC R350A variant. The heat plots show the differences in deuterium uptake between wild-type (WT) $PadC_{\Delta N}$ and its R350A variant at different incubation times for a series of representative peptides (see Data S1 for the full list of peptides). **(C)** Mapping of the changes in HDX observed for the CTP-free $PadC_{\Delta N}$ R350A variant onto the structure of $PadC_{\Delta N}$ (t=1000 s). The color code is identical to the one used in panel A. Note that the structure does not include the C-terminal bactofilin-binding domain. See also Figures S4 and S5 and Data S1.

CTP-binding to the ParB/Srx domain is required for the interaction of PadC with ParA

Previous work on ParB has mapped the interaction determinants of ParA to the N-terminal ParB/Srx domain (Figge et al., 2003; Surtees and Funnell, 1999; Volante and Alonso, 2015). This finding raised the possibility that PadC could use nucleotide binding to modulate its ParA-binding affinity. We therefore generated a series of PadC-eYFP variants with mutations in the CTP-binding pocket and analyzed their ability to recruit ParA to the polar bactofilin cytoskeleton *in vivo* (Figure 4A). All fusion proteins still localized to the cell poles, verifying the full functionality of the C-terminal bactofilin-binding domain. However, most of them gave rise to aberrant ParA localization patterns (Figures 4A, 4B and S5E). In particular, combinations of mutations in the triphosphate-binding residues R311, R349 and R350 in many cases completely abolished the polar recruitment of ParA. The R350 variant was still partially functional *in vivo*, although it was CTP-free after purification and behaved like the triple arginine mutant *in vitro*. However, considering the multitude of bonds between CTP and PadC (Figure 1D), a single exchange is unlikely to completely abolish nucleotide binding. The mutant protein may therefore still interact with CTP in the cell, but it may have a reduced binding affinity that causes dissociation of the nucleotide during the purification process. In line with this hypothesis, more extensive probing of the CTP-binding pocket showed that the *in vivo* effects became stronger with increasing number of substitutions (Figure S5E), with the R311/349/350 variant lacking any apparent recruitment activity (Figures 4A and 4B). Notably, mutation of a cysteine (C346) located in a similar region as the active-site cysteine of sulfiredoxin (Jönsson et al., 2008) did not affect ParA localization (Figure S5E). To corroborate the imaging data, we further investigated the interaction of ParA with selected PadC variants *in vitro* (Figure 4C). The results showed that the nucleotide-free R350 and R311/349/350A variants indeed had a severe defect in ParA binding. Thus, stabilization of the ParB/Srx domain by CTP may be required to facilitate the interaction between PadC and its target ParA (Figure 4D).

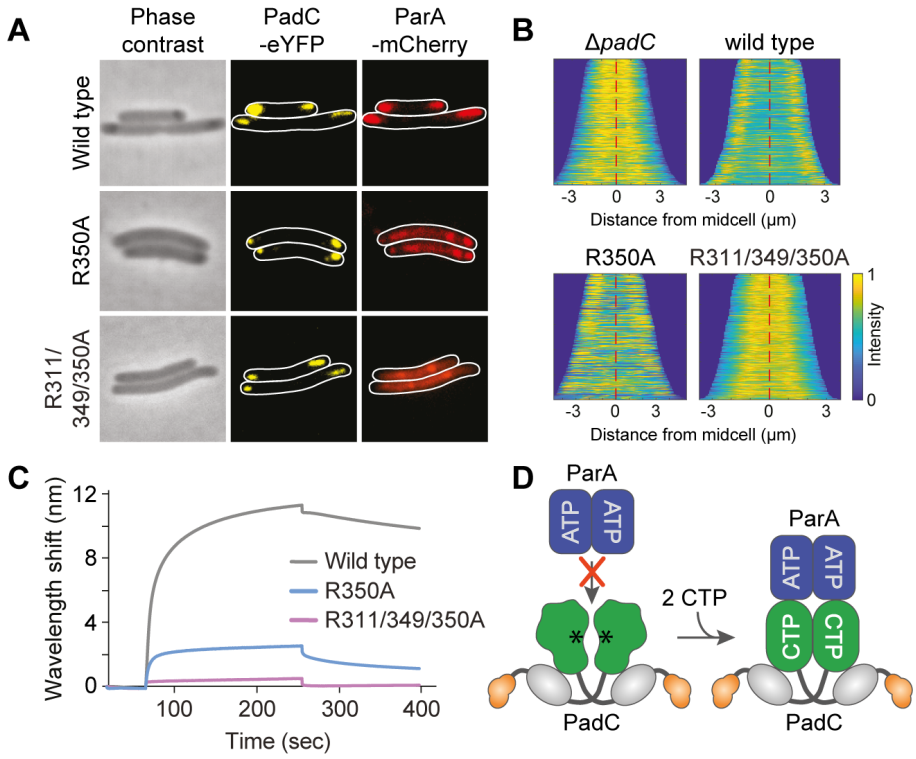

Figure 4. CTP binding is required for the interaction of PadC with ParA. (A) Co-localization studies of different PadC-eYFP variants and ParA-mCherry. *M. xanthus* strains (Δ*padC* P_{parA}-*parA-mCherry*) carrying the indicated *padC-eyfp* alleles under the control of a vanillate-inducible promoter (SU1, SU20, MO33) were cultivated for 2 h with 5 µM vanillate before imaging. Scale bar: 3 µm. **(B)** Demographs showing the localization of ParA-mCherry in the presence of different PadC variants. *M. xanthus* strains (Δ*padC* P_{parA}-*parA-mCherry*) carrying the indicated *padC* alleles under the control of a vanillate-inducible promoter (LL154, LL192, MO64, MO68) were cultivated for 2 h with 5 µM vanillate before imaging. Data were analyzed as described for Figure 2B. n=310 (Δ*padC*), 250 (wild type), 250 (R350A) and 335 (R311/349/350A) cells. **(C)** Biolayer interferometric analysis of the interaction between different PadC variants and ParA. The indicated PadC variants (10 µM) were immobilized on sensors carrying biotinylated $BacP_c$ and probed with ParA (5 µM). **(D)** Model of the regulation of PadC by CTP. The binding of CTP stabilizes the ParB/Srx domain (green) of PadC in a closed conformation, thereby facilitating its interaction with ParA. The dimerization domain (helices H5/H6) is depicted in grey. The C-terminal bactofilin-binding domain, which is not resolved in the crystal structure, is shown in orange. See also Figure S5.

The CTP-binding activity of the ParB/Srx domain is conserved in canonical ParB proteins

Our results show that the structure of the ParB/Srx domain of PadC and, in particular, its CTP-binding pocket are highly conserved among members of the ParB protein family (Figures 1E, 1F and S2), suggesting that canonical ParB homologs may share the ability to interact with CTP. To investigate this possibility, we first studied the effect of CTP on the chromosome partitioning protein ParB from *M. xanthus* (*Mx*ParB) by HDX analysis. In doing so, we employed the non-hydrolyzable CTP analog CTPγS to ensure that only the changes induced by nucleotide binding but not hydrolysis would be monitored during the experiments (Figure S6F). The addition of CTPγS led to the stabilization of the entire ParB/Srx domain, with the strongest changes observed in the regions homologous to those forming the CTP-binding pocket of PadC (Figure 5A). These results clearly demonstrate that *Mx*ParB is

able to interact with CTP. To substantiate this finding, we performed quantitative nucleotide binding assays using isothermal titration calorimetry (ITC). We found that *Mx*ParB binds CTPγS with an appreciable affinity (K_d ~ 60 µM) that ensures its saturation under *in vivo* conditions (Buckstein et al., 2008) (Figure 5B). The relatively high K_d value suggests that, unlike in the case of PadC, the two ParB/Srx domains of a ParB dimer are not stably engaged but in an equilibrium between an open and closed state that permits nucleotide dissociation. We also observed an interaction with CDP, but the binding affinity for this nucleotide was approx. 10-fold lower (K_d ~ 680 µM) (Figure 5C). Collectively, these results show that the ParB/Srx domain of ParB acts as a thus-far unrecognized CTP-binding domain.

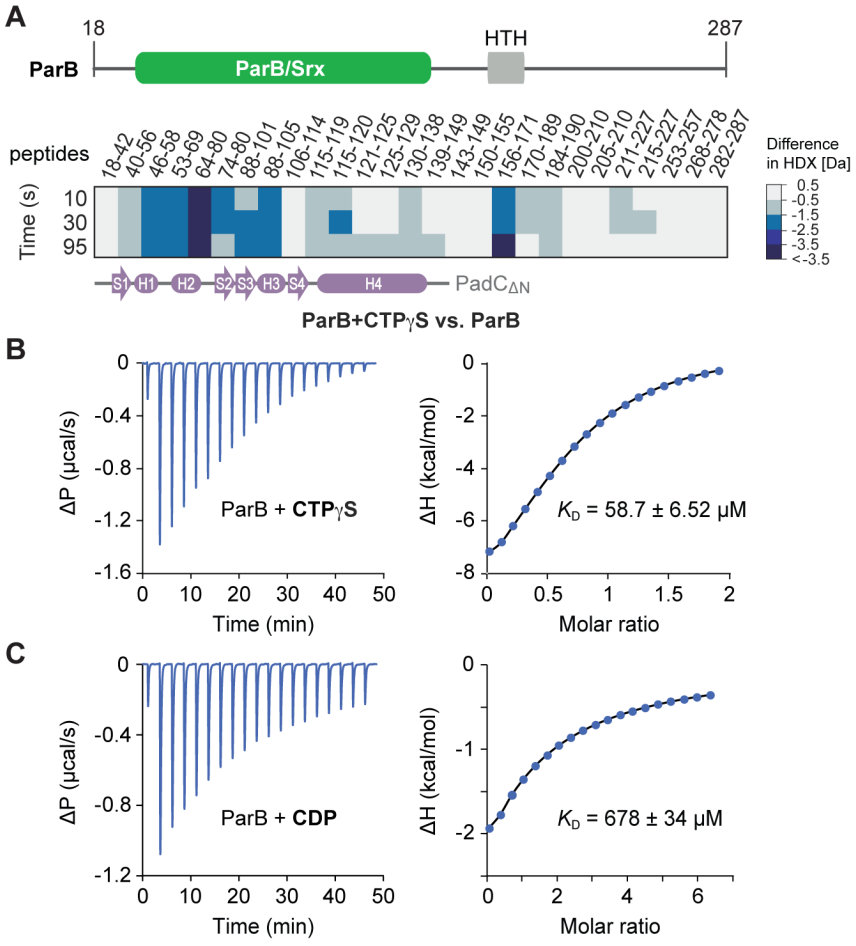

Figure 5. The CTP-binding activity of the ParB/Srx domain is conserved in canonical ParB proteins. (A) HDX analysis of the effect of CTP binding on ParB from *M. xanthus*. The heat plot shows the difference in deuterium uptake between ParB incubated with 4 mM CTPγS and apo-ParB at different incubation times for a series of representative peptides (see **Data S1** for the full list of peptides). The scheme at the bottom shows the secondary structure of the corresponding homologous region of PadC. **(B)** Analysis of the interaction of ParB with CTPγS by isothermal titration calorimetry. A solution of ParB (150 µM) was titrated with 19 consecutive injections (2 µL) of a CTPγS stock solution (1.5 mM). The graph on the left shows the heat changes observed after each injection. The Wiseman plot on the right shows the binding enthalpy obtained for each injection after correction of the data for the heat of dilution. Fitting of the curve to a one-set-of-sites model yield the indicated equilibrium dissociation constant (K_D), with ΔH = -12.5 ± 0.79 (kcal/mol) and ΔG = -5.77 kcal/mol. **(C)** ITC analysis of the interaction of ParB with CDP, performed as described in (A) (using a 5 mM stock solution). The K_D obtained is indicated in the graph, with ΔH = -80 ± 4.24 (kcal/mol) and ΔG = -4.32 kcal/mol. See also Data S1.

ParB shows *parS*-dependent CTPase activity

Intriguingly, our HDX data revealed that CTP not only stabilized the ParB/Srx domain but also the HTH-motif of *Mx*ParB (Figure 5A), which mediates specific recognition of the *parS* motif, suggesting that CTP binding could modulate the DNA-binding properties of ParB. To further test for a potential interplay between the ParB/Srx and DNA-binding domains of ParB, we determined the influence of *parS*-containing DNA on the structure of nucleotide-free *Mx*ParB by HDX analysis (Figure 6A). Consistent with previous structural studies (Chen et al., 2015; Leonard et al., 2004; Schumacher et al., 2010), *parS* binding led to protection of the C-terminal region surrounding the HTH-motif. In addition, it also affected the N-terminal ParB/Srx domain, in particular elements in the predicted domain interface containing the CTP-binding pocket. These results suggest that *parS* binding may promote homodimerization of the two N-terminal domains, and they again point to a direct functional link between the nucleotide- and DNA-binding states of ParB. To further investigate this possibility, we studied the effect of nucleotides on the interaction of *Mx*ParB with a *parS*-containing DNA fragment using biolayer interferometry. In the absence of nucleotide, *Mx*ParB displayed hyperbolic binding curves with an apparent K_d of 0.85 µM (Figures 6B and 6C). Similar results were obtained in reactions containing CDP (Figures S6A and S6B). Upon incubation with CTPγS (Figures 6D and 6E) or CTP (Figures S6C and S6D), however, its affinity for *parS* decreased by approx. 8-fold (K_d ~ 7 µM) and the binding curves adopted a sigmoidal shape, indicative of cooperative behavior. The ParB/Srx domain of ParB thus mediates a CTP-dependent molecular switch that controls the affinity of ParB for its DNA target site. Given that high-affinity interactions with the *parS* motif correlated with the CDP-bound or nucleotide-free states of *Mx*ParB, we wondered whether *parS* binding could trigger CTP hydrolysis. We therefore tested CTP turnover in the absence and presence of *parS*-containing DNA fragments using a coupled-enzyme assay (Figure 6F). While CTP hydrolysis was barely detectable in DNA-free reactions, the hydrolytic activity of *Mx*ParB was significantly (> 10-fold) increased in the presence of *parS*, consistent with observations made for Spo0J from *B. subtilis* (Young-Min Soh and Stephan Gruber, personal communication). No stimulation was observed with a DNA fragment containing a mutated *parS* motif that was no longer recognized by ParB (Figure 6F; see Figure 6B for the $parS_{mut}$ binding data). Importantly, only CTP was turned over efficiently by *Mx*ParB, whereas no activity was observed with other nucleotides (Figure S6E). Collectively, these findings identify ParB as a previously unrecognized regulatory CTPase. Moreover, they demonstrate a close reciprocal link between the CTPase activity of ParB and *parS* recognition (Figure 6G).

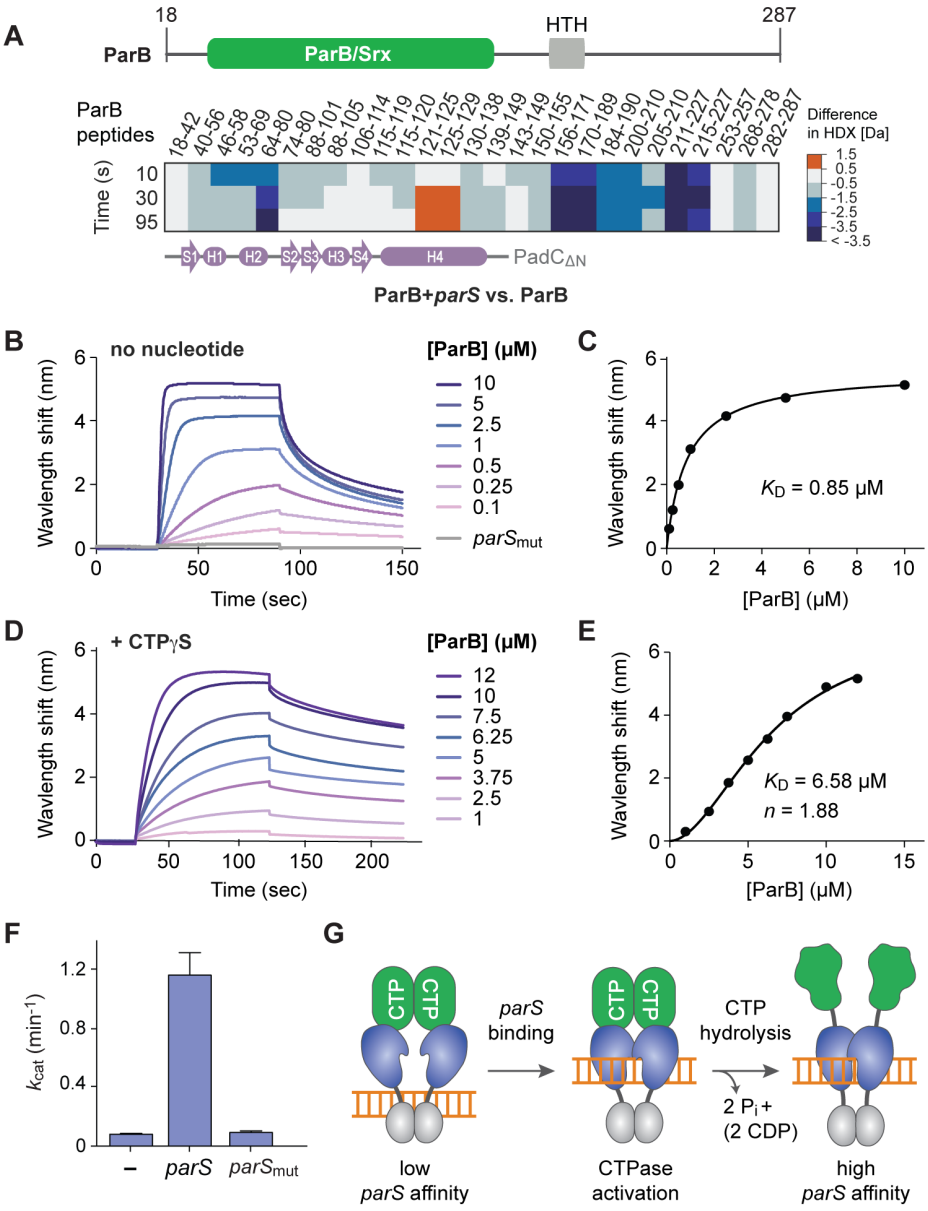

Figure 6. The ParB/Srx domain functionally interacts with the DNA-binding domain of ParB. (A) HDX analysis of the effect of *parS* binding on ParB from *M. xanthus*. The heat plot shows the difference in deuterium uptake between the ParB·*parS* complex and apo-ParB at different incubation times for a series of representative peptides (see Data S1 for the full list of peptides). The scheme at the bottom shows the secondary structure of the corresponding homologous region of PadC. **(B)** Biolayer interferometric analysis of the interaction between ParB and *parS* in the absence of nucleotide. Sensors carrying a double-stranded DNA oligonucleotide with a consensus *parS* motif were incubated with the indicated concentrations of *M. xanthus* ParB. The interaction of ParB with a mutant *parS* motif ($parS_{mut}$) was analyzed as a control. **(C)** Analysis of the binding data shown in panel B. The plot shows the equilibrium levels measured at the different ParB concentrations. The data were fitted to a one-site specific-binding model. The resulting K_D value is given in the graph. **(D)** Biolayer interferometric analysis of the interaction between ParB and *parS* in the presence of 1 mM CTPγS, performed as described in (B). **(E)** Analysis of the binding data shown in panel B. The data were fitted to a cooperative one-site specific-binding model. The resulting K_D value and Hill coefficient (n) are given in the graph. **(F)** Stimulation of the ParB CTPase activity by *parS* binding. ParB (4 μM) was incubated with 1 mM CTP alone (-) or in the presence of a DNA fragment (250 nM) containing a consensus or mutant *parS* motif. The reaction rates were determined with a coupled enzyme assay. Data represent the mean of three experiments

(± SD). **(F)** Model of the functional interdependence of the CTP- and DNA-binding domains of ParB. In the CTP-boud state, the ParB/Srx domain (green) interacts with the DNA-binding domain (blue), thereby reducing its affinity for *parS* sites. The recognition of a *parS* motif triggers a conformational change that stimulates the CTPase activity of ParB. As a consequence, the ParB/Srx domain transitions to an open state that enables ParB oligomerization and partition complex formation. In addition, CTP hydrolysis relieves the inhibition of the DNA-binding domain, leading to enhanced *parS* binding. The C-terminal dimerization domain (grey) of ParB may remain unaffected by the nucleotide state of the ParB/Srx domain and stably connect the two subunits under all conditions. See also Figures S6 and S7 and Data S1.

The CTPase activity of ParB is critical for partition complex formation

To clarify the role of the ParB CTPase activity in partition complex formation, we aimed to study the functionality of variants that were impaired in nucleotide binding or hydrolysis. For this purpose, we mutated conserved residues (R95, E126, N127, R130) in the Box II and Box III (also known as Region II) signature regions of *Mx*ParB for alanine (Figures 7A and S3). R95 and E126 correspond to residues R350 and E382 of PadC, which interact with the triphosphate moiety of CTP (Figures 1D and 3A) or form hydrogen bonds with water molecules in the vicinity of the Mn^{2+} ion and the γ-phospate of CTP (Figure 1D), respectively. N127 and R130, by contrast, are absent in PadC, although they are highly conserved in the ParB protein family and located in a region homologous to helix H4 of PadC, close to the triphosphate moiety. To characterize the mutant proteins, we first tested their ability to interact with CTPγS. ITC analysis showed that exchanges in R95 or R130 completely abolished the nucleotide binding capacity of *Mx*ParB. The E126A and N127A variants, by contrast, still interacted with CTPγS, although the binding affinity of the latter was slightly reduced (Figure 7B). Notably, all four variants lacked CTPase activity, even when assayed in the presence of *parS*-containing DNA (Figure 7C). Taken together, these findings suggest that R95 and R130 are integral parts of the CTP-binding pocket, whereas E126 and N127 may be involved in the catalytic mechanism of nucleotide hydrolysis.

The identification of variants that were locked in the apo- or CTP-bound state provided a means to study the physiological significance of the ParB CTPase cycle *in vivo*. To this end, wild-type *Mx*ParB and its mutant variants were N-terminally tagged with the cyan fluorescent protein sfmTurquoise2^{ox} (Meiresonne et al., 2019) and produced in cells depleted of native ParB (Figure 7D). As expected, wild-type sfmTurquoise2^{ox}-*Mx*ParB condensed into bright subpolar foci, reflecting partition complexes that are attached to the pole-distal ends of the bactofilin cytoskeleton (Lin et al., 2017). The mutant fusion proteins, by contrast, no longer displayed this characteristic localization pattern but were dispersed throughout the cytoplasm, with the E126A variant also forming diffuse speckles and patches (Figure 7E). Concomitantly, the cells showed a high incidence of chromosome segregation defects (Figure 7F), suggesting that the ParAB*S* system was no longer functional. Collectively, these results suggest that ParB requires CTP binding and hydrolysis to drive partition complex formation.

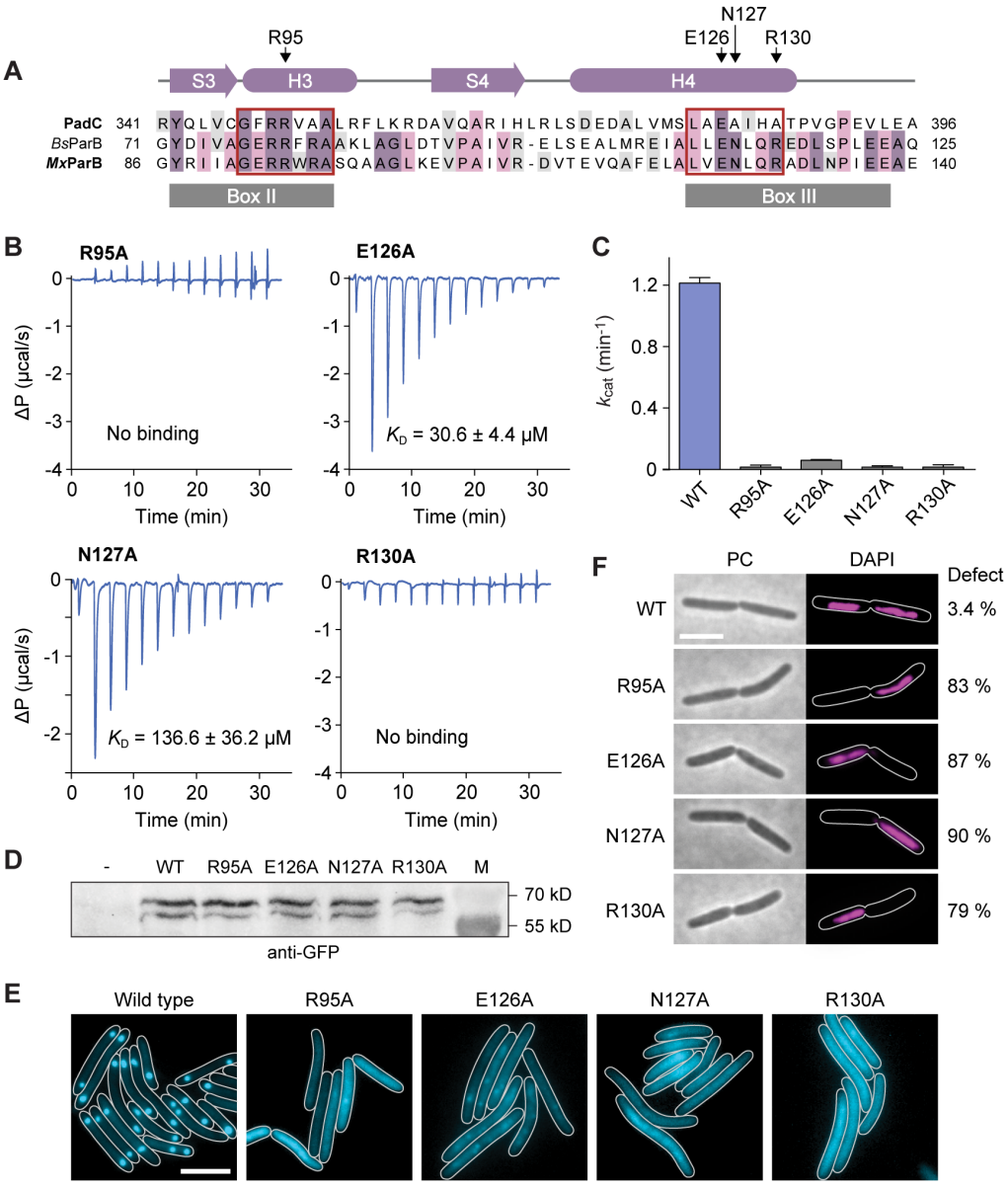

Figure 7. ParB requires CTP binding and hydrolysis for proper partition complex formation. (A) Alignment of the amino acid sequences of PadC, *Bs*ParB and *Mx*ParB (see **Figure S3** for details). Conserved motifs in the signature regions Box II and Box III are highlighted by red frames. The amino acids exchanged in *Mx*ParB are indicated by arrows. The schematic indicates the secondary structure of PadC. **(B)** Analysis of the interaction of mutant ParB variants with CTPγS by isothermal titration calorimetry. A solution of ParB (150 µM) was titrated with 13 consecutive injections of a CTPγS stock solution (1 mM for the 126A variant and 3 mM for the remaining variants). The graphs show the heat changes observed after each injection. The corresponding K_D values (see legend to Figure 5B for details on the analysis) are indicated. **(C)** CTPase activities of mutant ParB variants. The indicated proteins (4 µM) were incubated with 1 mM CTP in the presence of a *parS*-containing DNA fragment (250 nM). The reaction rates were determined with a coupled enzyme assay. Data represent the mean of three experiments (± SD). **(D)** Western blot analysis of strains producing different sfmTurquoise2^{ox}-ParB variants. Strains carrying the endogenous *parB* gene under the control of a Cu^{2+}-inducible promoter and the indicated variants of *sfmTurquoise2^{ox}-parB* under the control of a vanillate-inducible promoter (MO72, MO73, MO75, MO76, MO77) were grown in the presence of 300 µM $CuSO_4$, washed three times and then cultivated for 14 h in medium containing 500 µM vanillate to deplete wild-type ParB and produce the fusion proteins. Samples were subjected to Western blot analysis with anti-GFP antibodies. A

molecular weight marker (M) was applied as a reference. The background strain SA4269 (Δ*parB* P_{cuoA}-*parB*) (-) was analyzed as a negative control. **(E)** Localization patterns of mutant sfmTurquoise2^{ox}-ParB variants. Strains MO72, MO73, MO75, MO76, MO77 were grown as described in (D) and analyzed by fluorescence microscopy (scale bar: 4 µm). **(F)** Chromosome segregation defects of cells producing mutant ParB variants. The strains described in (E) were cultivated for 36 h in medium containing 300 µM vanillate. After staining of the nucleoids with DAPI, cells were imaged by phase contrast (PC) and fluorescence microscopy (scale bar: 4 µm). The numbers on the right give the fractions of dividing cells that show a highly asymmetric nucleoid arrangement. n= 127 cells (WT), 157 cells (R95A), 103 cells (E126A), 95 cells (N127A) and 145 cells (R130A).

DISCUSSION

CTP-dependent function and modularity of ParB and PadC

In this study, we show that the N-terminal ParB/Srx domains of PadC and ParB serve as CTP-binding modules with switch-like properties. The motifs interacting with CTP are highly conserved and located at the interface of two adjacent polypeptide chains, thus likely enabling nucleotide-dependent homo-dimerization of the N-terminal protein regions. CTP binding has profound effects on the interaction properties of PadC and ParB, thereby critically affecting their biological function. Notably, both PadC and ParB possess an additional dimerization domain that stably connects the two subunits and, thus, likely facilitates the association of the N-terminal ParB/Srx domains upon nucleotide binding (Figures 4D and 6G). In the case of PadC, the dimerization domain (helixes H5/H6) is followed by a C-terminal bactofilin-binding domain, which appears to act independently of the remaining parts of the protein. ParB, by contrast, contains a DNA-binding domain that is positioned in the medial regions of the protein and functionally interacts with the ParB/Srx domain. Based on their modular architecture and distinctive domain structure, PadC and ParB thus harnesses the CTP-binding properties of the ParB/Srx domain in different ways to mediate distinct cellular functions.

The fact that ParB proteins can interact with CTP has long remained unrecognized, likely because they bind this ligand with only moderate affinity and, therefore, lose it readily during the purification process. Their identification as nucleotide-dependent regulators in this study was aided by the high CTP-binding affinity of PadC, which enabled us to purify and crystallize its ParB/Srx domain in the nucleotide-bound state. In retrospect, previous studies have already provided circumstantial evidence of the nucleotide-binding ability of ParB homologs. For instance, some of these proteins crystallized with citrate (Schumacher et al., 2015) or phosphate (Maindola et al., 2014; Shaw et al., 2008) ions in regions equivalent to the conserved triphosphate-binding site of PadC (Figure S3A). Moreover, the nucleotide binding sites of PadC and ParB are highly similar to those of the ATP/ADP-dependent enzymes sulfiredoxin (Jönsson et al., 2008) and SerK (Nagata et al., 2017), with the phosphate moieties of all three proteins located in essentially the same position (Figure S3A). The ParB/Srx domain thus appears to be an ancient and widespread nucleotide-binding module with variable base specificity and biological function. It will be interesting to trace back the evolutionary history of this domain and determine its original nucleotide specificity. It will also be interesting to see whether there are other groups of proteins containing a ParB/Srx domain that bind and hydrolyze CTP.

Role of the ParB/Srx domain in PadC function

PadC represents an accessory factor that modulates the activity of the canonical ParAB*S* system by sequestering the pool of monomeric ParA molecules to the subpolar bactofilin cytoskeleton (Lin et al., 2017). Consistent with this functional specialization, it lacks the typical DNA-binding domain of ParB homologs and instead contains a domain that interacts constitutively with the C-terminal region of the *M. xanthus* bactofilin paralog BacP. As observed previously for various members of the ParB family (Bouet and Funnell, 1999; Figge et al., 2003; Radnedge et al., 1998; Ringgaard et al., 2009; Surtees and Funnell, 1999), the determinants mediating the interaction with ParA are located in the ParB/Srx domain of PadC. ParA recruitment to PadC is abolished by mutations that disrupt nucleotide binding, indicating that CTP-induced changes in the conformation of the ParB/Srx domains are required to establish the ParA interaction interface. Considering the high conservation of the CTP-binding pockets, PadC may share the hydrolytic activity of its relative ParB. However, we did not detect any nucleotide hydrolysis under the conditions tested (Figure S7). It is possible that the evolution of PadC into a ParA localization factor went along with the loss of its CTPase activity, as it helps to lock the protein in its active, ParA-binding state. Alternatively, PadC may require to a thus-far unknown stimulus to trigger its hydrolytic activity. The first hypothesis may be supported by the fact that ~100% of the PadC molecules isolated from *M. xanthus* were in the CTP-bound state (Figure S2G-I). Moreover, residue N127 of *Mx*ParB, which critically contributes to CTP hydrolysis, is not conserved in PadC (Figure 7A). However, further studies are required to fully unravel the molecular details underlying the function of this recently identified component of the myxococcal chromosome segregation system.

Role of the ParB/Srx domain in ParB function

Partition complex formation by ParB is a highly controlled and dynamic process, but the underlying regulatory mechanisms have remained unclear. The finding that these proteins act as CTP-dependent molecular switches may now provide the basis for unraveling their precise mode of action. Importantly, the amino acid residues constituting the CTP binding pocket of ParB are part of three signature motifs (Box I, Box II and Box III) that are highly conserved among ParB proteins (Bartosik et al., 2004; Yamaichi and Niki, 2000) (Figure S3B). Box I forms the binding pocket that accommodates the nucleobase and likely confers specificity for CTP, whereas Boxes II and III interact with the triphosphate moiety of CTP (Figures 1D and S3B). Notably, the residues in Box III are located in a region equivalent to helix H4 of PadC that undergoes marked structural changes upon *parS* binding (Figure 6A). Moreover, the mutation of residues in this region abolishes CTP hydrolysis, while still permitting nucleotide binding. We therefore suggest that Box III may play a critical role in the stimulation of the ParB CTPase activity by *parS*. Interestingly, previous work has shown that residues in Boxes I-III are essential for ParB spreading, partition complex formation, proper ParA localization and DNA segregation *in vivo*, and mutation of residues in Box II abolished both the oligomerization and the DNA-

bridging activity of ParB *in vitro* (Autret et al., 2001; Graham et al., 2014; Song et al., 2017). Together, these findings strongly suggest that CTP binding and hydrolysis play a central role in ParB function.

Our biochemical analyses show that ParB has a clear preference for CTP over the hydrolytic product CDP and lacks CTPase activity in the absence of *parS*-containing DNA. It therefore largely exists in the CTP-bound state as long as it is not associated with a chromosomal *parS* site *in vivo*. Upon *parS* recognition, which may potentially occur in a transient high-affinity open state, the DNA-binding domains are placed next to each other on the *parS* motif (Figure 6G). This process may promote the homodimerization of the adjacent ParB/Srx domains, thereby stabilizing the two active sites and stimulating CTP hydrolysis. Due to its weak association with ParB, CDP is likely to dissociate spontaneously from the ParB/Srx domain. Interestingly, a previous structural study of *Helicobacter pylori* ParB in complex with *parS*-containing DNA revealed that the nucleotide-free ParB/Srx domain can open up at a flexible hinge between its N-terminal part and the helix corresponding to H4 of PadC. This conformational change creates a new binding interface that mediates nucleotide-independent head-to-head interactions between ParB/Srx domains from adjacent ParB·*parS* dimers, generating a tetrameric DNA-bridging complex (Chen et al., 2015). Notably, the "arginine patch" in Box II (corresponding to R94 and R95 in *Mx*ParB) plays a central role in the stabilization of this structure (Song et al., 2017), and its mutation abolishes DNA condensation *in vitro* (Graham et al., 2014). The CTP-dependent switch mediated by ParB may therefore serve to occlude this motif until ParB interacts with the centromeric *parS* sites, thereby effectively limiting the nucleation of partition complexes to the replication origin regions. Even in the high-affinity apo state, ParB is not firmly associated with *parS* sites (Figures 6B and 6C). It may therefore eventually release its specific target site and then interact with adjacent DNA region through its non-specific DNA-binding activity (Fisher et al., 2017), making *parS* again available for other ParB molecules. Such a mechanism may explain how a single *parS* site can be sufficient to nucleate a functional partition complex (Wang et al., 2017). Mutant variants impaired in CTP binding may form bridging interactions throughout the nucleoid, thereby failing to condense into a single, functional partition complex. The lack of CTPase activity, by contrast, may impede the self-assembly of ParB after *parS* recognition.

The behavior of ParB is highly reminiscent of the "switch paradigm" established for most GTPases and many ATPases (Bange and Sinning, 2013; Bourne et al., 1990; Gasper et al., 2009), with *parS* serving as a CTPase-activating factor that triggers the transition of ParB between its different functional states. However, additional work is required to verify this model and incorporate the effect of CTP on the interaction of ParB with ParA. Taken together, the identification of ParB as a CTP-binding protein adds an unforeseen layer of complexity to prokaryotic DNA segregation, thereby opening new perspectives in the investigation of the mechanisms that underlie this central process.

Conclusions

Nucleotide-binding proteins have a central role in cell biology. While all previously reported examples depend on ATP or GTP, we now unveil ParB homologs as an emerging new class of regulators that use the pyrimidine nucleotide CTP to control the spatiotemporal dynamics of biological processes. The advantage conferred by their distinct nucleotide specificity remains to be understood. However, it is tempting to speculate that it could provide a regulatory link to CTP-dependent metabolic processes, thereby orchestrating DNA segregation with other cellular processes. Our results open the possibility that CTP-binding and hydrolysis could also control the activity of other protein families and thus be a more general regulatory principle in biology.

ACKNOWLEDGEMENTS

We thank Julia Rosum for excellent technical assistance, Young-Min Soh and Stephan Gruber for sharing unpublished results, Pietro Giammarinaro for assistance with the ITC measurements and Irmgard Sinning for continuous help and support. Moreover, we acknowledge Nicole Paczia at the Core Facility for Metabolomics and Small Molecules MS (MPI for Terrestrial Microbiology, Germany) for performing the nucleotide content analysis and the European Synchrotron Radiation Facility (ESRF, Grenoble, France) for assistance in data collection. This work was funded by the Max Planck Society (Max Planck Fellowship to M.T.), the LOEWE program of the State of Hesse (to G.B.), and the German Research Foundation (DFG) (Project 269423233 - TRR 174 to G.B. and M.T. and Core Facility for Interaction, Dynamics and Macromolecular Assembly Structure to G.B.). M.O.V. was a fellow of the International Max Planck Research School for Environmental, Cellular and Molecular Microbiology (IMPRS-Mic).

AUTHOR CONTRIBUTIONS

M.O.V., S.U. and Y.L. conducted the biochemical and cell biological studies. F.A. performed the crystallization screens and solved the structure of PadC. W.S. performed the HDX analyses. M.O.V., F.A., W.S., G.B. and M.T. analyzed the data. M.O.V. and M.T. conceived the study. G.B. and M.T. secured funding and supervised the study. M.O.V. and M.T. wrote the paper, with input from all other authors.

DECLARATION OF INTERESTS

The authors declare no competing interests.

STAR METHODS

LEAD CONTACT AND MATERIALS AVAILABILITY

Further information and requests for resources and reagents should be directed to and will be fulfilled by the Lead Contact, Martin Thanbichler (thanbichler@uni-marburg.de). All plasmids and strains generated in this study are available from the Lead Contact without restriction.

EXPERIMENTAL MODEL AND SUBJECT DETAILS

Media and growth conditions

M. xanthus DK1622 and derivative strains were grown at 32 °C in CTT medium (Hodgkin and Kaiser, 1977), supplemented with kanamycin (50 µg/mL) or oxytetracycline (10 µg/mL) when appropriate. *E. coli* strains were cultivated at 37 °C in LB medium containing antibiotics at the following concentrations (µg/mL in liquid/solid medium): ampicillin (100/200), chloramphenicol (20/34), kanamycin (30/50). Induction of expression of genes under the control of the P_{van} or P_{lac} promoters (Iniesta et al., 2012) or the P_{cuoA} promoter (Gomez-Santos et al., 2012) was achieved by supplementation of the media with sodium vanillate, isopropyl-β-D-thiogalactopyranoside (IPTG) or $CuSO_4$, respectively, as indicated in the text.

METHOD DETAILS

Plasmid and strain construction

The construction of bacterial strains and plasmids is detailed in Tables S2-S4. *E. coli* TOP10 (Invitrogen) was used as host for cloning purposes. All plasmids were verified by DNA sequencing. *M. xanthus* was transformed by electroporation (Kashefi and Hartzell, 1995). Non-replicating plasmids were integrated into the chromosome by site-specific recombination at the phage Mx8 *attB* site (Magrini et al., 1999) or single-homologous recombination at the MXAN_18/19 locus (Iniesta et al., 2012). Gene replacement was achieved by double-homologous recombination using the counter-selectable *galK* marker (Ueki et al., 1996). Proper chromosomal integration or gene replacement was verified by colony PCR.

Live-cell imaging

Exponentially growing liquid cultures were spotted on 1.5 % agarose pads in TPM buffer (10 mM Tris/HCl, 8 mM $MgSO_4$, 1 mM potassium phosphate, pH 7.6) supplemented with 10% CTT medium (corresponding to a final content of 0.2% casitone) (Schumacher and Søgaard-Andersen, 2018). Images were taken with a Zeiss Axio Imager.M1 microscope equipped with a Zeiss Plan Apochromat ×100/1.40 Oil DIC objective and a pco.edge 3.1 sCMOS camera (PCO) or with a Zeiss Axio Imager.Z1 microscope equipped with a ×100/1.46 Oil DIC objective and a pco.edge 4.2 sCMOS camera (PCO). An X-Cite 120PC metal halide light source (EXFO, Canada) and ET-YFP or ET-TexasRed filter cubes

(Chroma, USA) were used for fluorescence detection. Images were recorded with VisiView 3.3.0.6 (Visitron Systems) and processed with Metamorph 7.7.5 (Molecular Devices) and Adobe Illustrator CS6 (Adobe Systems). The subcellular distribution of fluorescence signals was analyzed with BacStalk (Hartmann et al., 2018).

Protein purification

$PadC_{\Delta N}$ from *E. coli*

The purification of $PadC_{\Delta N}$ (His_6-PadCΔ1-281) was carried out as essentially as described previously (Lin et al., 2017). *E. coli* strain Rosetta (DE3)pLysS transformed with plasmid pMO2 was grown at 37°C in LB medium (3 L) supplemented with kanamycin sulfate (50 µg/mL) and chloramphenicol (34 µg/mL). Protein overproduction was induced at an OD_{600} of 0.8, by the addition of 0.5 mM IPTG for 4 h. Cells were harvested, washed with buffer B1 (50 mM NaH_2PO_4, 300 mM NaCl, 10 mM imidazole, adjusted to pH 8.0 with NaOH), and resuspended in buffer B2 (50 mM NaH_2PO_4, pH 8.0, 300 mM NaCl, 10 mM imidazole, 1 mM ß-mercaptoethanol) supplemented with 10 µg/mL DNase I and 100 µg/mL PMSF. After three passages through a French press (16,000 psi), cell debris were removed by centrifugation at 30,000 ×g for 30 min, and the supernatant was applied onto a 5 mL HisTrap HP column (GE Healthcare) equilibrated with buffer B3 (B2 buffer containing 20 mM imidazole). The column was washed with 10 column volumes (CV) of the same buffer, and protein was eluted with a linear imidazole gradient (20–250 mM in buffer B3) at a flow rate of 1 mL/min. Fractions containing high concentrations of protein were pooled and dialyzed against 3 L of buffer B5 (20 mM Tris/HCl, pH 8.0, 10 mM NaCl, 1 mM β-mercaptoethanol) at 4 °C. After the removal of precipitates by centrifugation at 30,000×g for 30 min, the solution was loaded onto a HiTrap Q HP 5mL column (GE Healthcare) equilibrated with buffer B5. The column was washed with 20 CV of buffer B5 prior the application of a linear NaCl gradient (0.01–1 M NaCl in buffer B5) at a flow rate of 1 mL/min. Fractions containing $PadC_{\Delta N}$ at high purity were pooled and dialyzed against 2 L of buffer B7 (25 mM HEPES/KOH, pH 7.6, 150 mM KCl, 5 mM $MgCl_2$), snap-frozen, and stored at −80 °C until further use.

For the overproduction of mutant PadC variants, cultures were chilled to 18 °C prior to the addition of 0.5 mM IPTG and incubated overnight. Cells were lysed in buffer B2 supplemented with 10% (v/v) glycerol to ensure protein solubility. All subsequent purification steps were performed as described above for the wild type protein.

Selenomethionine-labeled $PadC_{\Delta N}$ (His_6-PadCΔ1-281) was obtained as described previously (Pausch et al., 2015). Briefly, *E. coli* Rosetta(DE3)pLysS transformed with plasmid pMO2 was grown at 37 °C in M9-medium (5 L) supplemented with standard amino acids, L-selenomethionine, kanamycin sulfate (50 µg/mL) and chloramphenicol (34 µg/mL). Protein overproduction was induced at an OD_{600} of 0.6 by

the addition of 0.5 mM IPTG for 20 h. Cells were harvested, resuspended with buffer S1 (20 mM HEPES pH 8.0, 20 mM $MgCl_2$, 20 mM KCl, 250 mM NaCl, 40 mM imidazole) and lysed using a microfluidizer (Microfluidics) at 18.000 psi. Cell debris were removed by centrifugation at 25,000 ×g for 20 min, and the supernatant was applied onto a 5 mL HisTrap HP column (GE Healthcare) equilibrated with buffer A. The column was washed with 10 CV of the same buffer, and protein was eluted with buffer S2 (Buffer S1 with 500 mM imidazole) at a flow rate of 1 mL/min. Fractions containing high concentrations of protein were pooled, concentrated with a spin concentrator (Amicon, MWCO 10.000) and applied onto a size-exclusion column (SEC, HiLoad 16/600 superdex 200 prep grade) equilibrated with a buffer containing 20 mM Tris/HCl (pH 8.0) and 50 mM NaCl. The peak fractions were pooled and concentrated to 170 mg/mL.

PadC$_{\Delta N}$ from *M. xanthus*

For the purification of StrepII-PadC$_{\Delta N}$, *M. xanthus* strain MO11 (DK1622 Δ*padC* P_{pilA}- StrepII-*padC*Δ1-281) was grown at 32 °C in CTT medium (3 L) supplemented with kanamycin sulfate (50 µg/mL) to an OD_{550} of 0.8. Cells were harvested, washed twice with binding buffer (100 mM Tris/HCl pH 8.0, 150 mM NaCl, 1 mM EDTA) and resuspended in 30 mL of the same buffer supplemented with 10 µg/mL DNase I and 100 µg/mL PMSF. After three passages through a French press (16,000 psi), cell debris were removed by centrifugation at 30,000 ×g for 30 min, and the supernatant was applied onto a 1 mL StrepTrap HP column (GE Healthcare) equilibrated with binding buffer. The column was washed with 20 CV of the same buffer, and protein was eluted with elution buffer (100 mM Tris/HCl pH 8.0, NaCl 150 mM, EDTA 1 mM, 2.5 mM desthiobiotin) at a flow rate of 1 mL/min. Fractions containing high concentrations of pure protein were dialyzed against 2 L of buffer B7 (25 mM HEPES/KOH, pH 7.6, 150 mM KCl, 5 mM $MgCl_2$), snap-frozen, and stored at −80 °C until further use.

ParA

His_6-ParA was purified essentially as described previously (Lim et al., 2014). *E. coli* Rosetta(DE3)pLysS cells carrying plasmid pAH17 (Harms et al., 2013) were grown to an OD_{600} of 0.6 at 37 °C in LB medium (3 L) supplemented with ampicillin (200 µg/mL) and chloramphenicol (34 µg/mL). The cultures were chilled to 18 °C, and 1 mM IPTG was added to induce His_6-ParA synthesis overnight at 18 °C. Cells were harvested by centrifugation, washed twice with buffer A1 (100 mM HEPES/KOH pH 7.4, 100 mM KCl, 1 mM EDTA, 10% (v/v) glycerol), and resuspended in 25 mL of buffer A1 containing 10 µg/mL Dnase I, 100 µg/mL PMSF, 0.5 mM magnesium-ATP and 1 mM DTT. The cell suspension was incubated on ice for 20 min prior to addition of 3 M KCl to a final concentration of 1 M. Cells were disrupted by three passages through a French press (16,000 psi), and cell debris was removed by centrifugation for 30 min at 30,000 ×g and 4 °C. The clarified lysate was applied onto a 5 mL HisTrap HP column (GE Healthcare) equilibrated with buffer A2 (25 mM HEPES/KOH pH 7.4, 450 mM KCl, 50 mM potassium glutamate, 1

mM $MgSO_4$, 1 mM DTT, 100 µM magnesium-ATP) containing 40 mM imidazole. After washing with 10 CV of the same buffer, protein was eluted with a linear imidazole gradient (40–300 mM in buffer A2) at a flow rate of 1 mL/min. Fractions containing high concentrations of His_6-ParA were pooled, dialyzed against 2 L of buffer A4 (25 mM HEPES/KOH, pH 7.4, 100 mM KCl, 200 mM potassium glutamate, 1 mM $MgSO_4$, 1 mM DTT, 100 µM magnesium-ATP, 20% (v/v) glycerol), snap-frozen, and stored at −80 °C until further use.

$BacP_C$

To purify $BacP_C$ (His_6-$BacP_{\Delta 1\text{-}115}$), *E. coli* Rosetta(DE3)pLysS was transformed with plasmid pIB154 (Bulyha et al., 2013) and grown at 37 °C in LB medium supplemented with ampicillin (200 µg/mL) and chloramphenicol (34 µg/mL). At an OD_{600} of 0.6, protein overproduction was induced with 1 mM IPTG and the cultures were incubated for 12 h at 18 °C. Cells were harvested by centrifugation, washed twice with buffer B1 (50 mM NaH_2PO_4, 300 mM NaCl, 10 mM imidazole, adjusted to pH 8.0 with NaOH), and stored at −80 °C. Thawed cells were resuspended in buffer B2 (50 mM NaH_2PO_4, 300 mM NaCl, 10 mM imidazole, 1 mM ß-mercaptoethanol, pH 8.0) containing 10 µg/mL DNase I and 100 µg/mL PMSF and disrupted by three passages through a French press (16,000 psi). After the removal of cell debris by centrifugation for 30 min at 30,000 ×g, the cleared lysate was applied to a 5 mL HisTrap HP column (GE Healthcare) equilibrated with buffer B3 (50 mM NaH_2PO_4, 300 mM NaCl, 1 mM β-mercaptoethanol, 20 mM imidazole, pH 8.0). The column was washed with 10 CV of the same buffer, and protein was eluted with a linear imidazole gradient (20–250 mM in buffer B3) at a flow rate of 1 mL/min. Fractions containing high concentrations of protein were pooled and dialyzed against 3 L of buffer P (25 mM HEPES/KOH, pH 7.6, 100 mM KCl, 10% (v/v) glycerol), The solution was then aliquoted, snap-frozen in liquid N_2, and stored at −80 °C until further use.

ParB

For the purification of His_6-ParB, *E. coli* Rosetta(DE3)pLysS cells carrying plasmid pKA52 (Harms et al., 2013) were grown in at 37 °C in 3L of LB medium supplemented with kanamycin sulfate (50 µg/mL) and chloramphenicol (34 µg/mL). At an OD_{600} of 0.6, the culture was chilled to 18 °C and protein synthesis was induced by the addition of 1 mM IPTG prior to incubation of the cells overnight at 18°C. The cultures were harvested by centrifugation at 10,000 ×g for 20 min at 4 °C, washed with buffer ParB1 (25 mM HEPES/NaOH, pH 8.0, 300 mM NaCl, 0.1 mM EDTA, 5 mM $MgCl_2$), and resuspended in buffer ParB2 (25 mM HEPES/NaOH, pH 8.0, 300 mM NaCl, 0.1 mM EDTA, 5 mM $MgCl_2$, 20 mM imidazole) supplemented with 10 µg/mL DNase I and 100 µg/mL PMSF. After three passages through a French press (16,000 psi), the cell lysate was clarified by centrifugation (30,000 ×g, 30 min, 4 °C) and the supernatant was subjected to immobilized-metal affinity chromatography (IMAC) using a 5 mL HisTrap HP column (GE Healthcare) equilibrated with buffer ParB2 (25 mM HEPES/NaOH, pH 8.0, 300 mM NaCl,

0.1 mM EDTA, 5 mM $MgCl_2$, 20 mM imidazole). Protein was eluted with a linear gradient of 20 to 250 mM imidazole at a flow rate of 1 mL/min. Fractions containing high concentrations of ParB were pooled and dialyzed against 3 L of buffer ParB3 (25 mM HEPES, pH 7.6, 150 mM NaCl, 0.1 mM EDTA, 5 mM $MgCl_2$, 10% (v/v) glycerol). After the removal of precipitates by centrifugation at 30,000 ×g for 30 min, ParB was further purified by size exclusion chromatography (SEC) on a HighLoad 16/60 Superdex 200 pg column (GE Healthcare) equilibrated with buffer ParB3. Fractions containing pure protein were pooled and concentrated. After the removal of precipitates by centrifugation at 30,000 x g, the protein solution was snap-frozen in liquid N_2 and stored at −80 °C until further use. Mutant ParB variants were purified essentially as described for the wild-type protein, using plasmids pMO108 (E126A), pMO109 (R95A), pMO110 (N127A), pMO111 (R130A).

Crystallization and structure determination

The crystallization of PadC as performed with the sitting-drop method at 20 °C in 0.5 µL drops consisting of equal parts of protein and precipitation solution. PadC crystallized in 100 mM NaCl and 25 % (w/v) PEG 3350 at a protein concentration of 170 mg/mL after two weeks of incubation. Prior to data collection, crystals were cryoprotected with the respective mother liquor supplemented with 20 % (v/v) glycerol. Datasets were collected under cryogenic conditions at the European Synchrotron Radiation Facility (ESRF) at beamlines ID23-2 and ID23-1 (Flot et al., 2010; Nurizzo et al., 2006). Phase determination was achieved by single-wavelength anomalous dispersion (Se-SAD) using crystals of selenomethionine-labeled protein. The data were processed with XDS and scaled with XSCALE (Kabsch, 2010). Native crystals diffracted to 1.7 Å resolution, while data of derivative crystals were obtained at 2.2 Å resolution. Both shared a primitive P1 symmetry with the cell constants a=36.85 b=42.44 c=49.53 α=108.54 β=99.15 γ=89.28 (Table S1). The substructure was determined with PHENIX-implemented Autosol and refined with PHENIX-refine prior to manual model building with coot (Adams et al., 2010; Emsley and Cowtan, 2004). Protein structures were visualized with PyMOL 2.1 (www.pymol.org). LIGPLOT (Wallace et al., 1995) was used to generate protein-ligand interaction 2D maps. Amino acid conservation was analyzed with the Consurf server (Ashkenazy et al., 2016). Protein domains were predicted using the PFAM database (El-Gebali et al., 2019).

Bio-layer interferometry

Bio-layer interferometric analyses were conducted using a BLItz system equipped with High Precision Streptavidin (SAX) Biosensors (ForteBio). Proteins were biotinylated with EZ-Link NHS-PEG4-Biotin (Thermo Scientific) as recommended by the manufacturer. After the immobilization of biotinylated proteins or double-stranded DNA oligonucleotides (*parS*-Mxan-wt) on the biosensors and establishment of a stable baseline, association reactions were monitored at various analyte

concentrations. At the end of each binding step, the sensor was transferred into analyte-free buffer to follow the dissociation kinetics. The extent of non-specific binding was assessed by monitoring the interaction of analyte with unmodified sensors. All analyses were performed in BLItz binding buffer (25 mM HEPES/KOH pH 7.6, 100 mM KCl, 10 mM $MgSO_4$, 1 mM DTT, 10 µM BSA, 0.01% Tween), supplemented with nucleotides when indicated. Reactions involving ParA were additionally supplemented with 150 mM potassium glutamate, 5 % glycerol and 1 mM ATP.

Isothermal titration calorimetry (ITC)

Nucleotide binding to ParB was measured using a MicroCal PEAQ-ITC system (Malvern Panalytical). ParB and its mutant derivatives were dialyzed extensively against ITC buffer (25 mM HEPES/NaOH, pH 7.6, 150 mM NaCl, 0.1 mM EDTA, 5 mM $MgCl_2$). Nucleotides (CDP and CTPγS) were dissolved in the same buffer. Proteins (150 µM) were titrated with 13-19 consecutive injections (3 µL) of CDP (5 mM) or CTPγS (at the indicated concentrations) at 25 °C and 150 s intervals, with a duration of each injection of 4 s. The mean enthalpies of dilution were subtracted from the raw titration data before analysis. Titration curves were fitted to a one-set-of-sites model using the MicroCal PAEQ-ITC analysis software (Malvern Panalytical).

Nucleotide hydrolysis assays

Nucleotide hydrolysis was measured using a coupled enzyme assay (Ingerman and Nunnari, 2005; Kiianitsa et al., 2003). Reactions contained 4 µM PadC or ParB variants, 20 U/mL pyruvate kinase (Sigma Aldrich), 20 U/mL L-lactate dehydrogenase (Sigma Aldrich), 800 µg/mL NADH and 3 mM PEP in 200 µL reaction buffer (25 mM HEPES/KOH pH 7.4, 10 mM $MgSO_4$, 1 mM DTT, 100 mM KCl). ParA (1 µM), the C-terminal PadC-binding domain of BacP (1 µM) or a double-stranded DNA oligonucleotide (54 bp) containing a wild-type (*parS*-Mxan-wt) or mutated (*parS*-Mxan-mut) *parS* site (250 nM) were added when indicated. After incubation for 10 min at 30°C, 150 µL of the reaction mixture were transferred into a 96-well microtiter plate and supplemented with the indicated nucleotide (ATP, GTP, CTP, UTP or CTPγS) to a final concentration of 1 mM to start the reactions. The reaction was followed by measuring the decrease in NADH absorbance at 350 nm at 2 min intervals. Initial velocities were calculated by linear regression analysis of each time course and corrected for spontaneous CTP hydrolysis and NADH oxidation.

Circular dichroism (CD) spectroscopy

Far-UV CD spectra (195–260 nm) of PadC variants (25 µM) were recorded in a 0.1 cm path-length cell at a temperature of 25 °C using a Jasco J-810 spectropolarimeter. Data were acquired with a scan speed of 100 nm/min, a bandwidth of 1 nm and a data pitch of 0.2 nm. Each data point represented the average of three consecutive measurements. The analysis of the spectra was performed with the K2D algorithm as implemented by the DichroWeb server (Whitmore and Wallace, 2004).

Hydrogen-deuterium exchange (HDX) mass spectrometry

To analyze the interaction between $BacP_c$ and $PadC_{\Delta N}$, the two proteins were mixed at an equimolar ratio and subjected to size-exclusion chromatography (SEC) on a Superdex 200 10/300 GL column (GE Healthcare) equilibrated with SEC buffer (20 mM Tris-HCl pH 7.6, 150 mM KCl). Fractions containing the $BacP_c$·$PadC_{\Delta N}$ complex were pooled, concentrated and analyzed for HDX mass spectrometry.

Samples were prepared using a two-arm robotic autosampler (LEAP technologies). 7.5 µL of $PadC_{\Delta N}$ or the $BacP_c$·$PadC_{\Delta N}$ complex (30 µM) were mixed with 67.5 µL of D_2O-containing buffer (20 mM HEPES/NaOH pH 7.5, 20 mM $MgCl_2$, 20 mM KCl, 200 mM NaCl) to start the exchange reaction. After 30, 120 and 600 s of incubation at 25 °C, samples (55 µL) were taken from the reaction and mixed with an equal volume of quench buffer (400 mM KH_2PO_4/H_3PO_4, 2 M guanidine-HCl, pH 2.2) kept at 1 °C. 95 µL of the resulting mixture were immediately injected into an ACQUITY UPLC M-class system with HDX technology (Waters) (Wales et al., 2008). Undeuterated samples of $PadC_N$ and the $BacP_c$-$PadC_N$ complex were prepared similarly by 10-fold dilution into H_2O-containing buffer. Proteins were digested online on an Enzymate BEH Pepsin column (300 Å, 5 µm, 2.1 mm × 30 mm; Waters) at 12 °C with a constant flow (100 µL/min) of water + 0.1 % (v/v) formic acid, and the resulting peptic peptides were collected on a trap column (2 mm × 2 cm) that was filled with POROS 20 R2 material (Thermo Scientific) and kept at 0.5 °C. After 3 min, the trap column was placed in line with an ACQUITY UPLC BEH C18 1.7 µm 1.0 × 100 mm column (Waters), and the peptides were eluted at 0.5 °C using a gradient of water + 0.1 % (v/v) formic acid (A) and acetonitrile + 0.1 % (v/v) formic acid (B) at a flow rate of 30 µL/min as follows: 0-7 min/95-65 % A, 7-8 min/65-15 % A, 8-10 min/15 % A, 10-11 min/5 % A, 11-16 min/95 % A. Peptides were ionized with an electrospray ionization source operated at 250 °C capillary temperature and a spray voltage of 3.0 kV. Mass spectra were acquired over a range of 50 to 2000 *m/z* on a G2-Si HDMS mass spectrometer with ion mobility separation (Waters) in $HDMS^E$ or HDMS mode for undeuterated and deuterated samples, respectively (Geromanos et al., 2009; Li et al., 2009). [Glu1]-Fibrinopeptide B standard (Waters) was employed for lock mass correction. After each run, the pepsin column was washed three times with 80 µL of 4 % (v/v) acetonitrile and 0.5 M guanidine hydrochloride, and blanks were performed between each sample. All measurements were carried out in triplicate.

Peptides from the non-deuterated samples (aquired with $HDMS^E$) were identified with ProteinLynx Global SERVER (PLGS, Waters), employing low energy, elevated energy and intensity thresholds of 300, 100 and 1,000 counts, respectively. Peptides were matched using a database containing the amino acid sequences of the proteins of interest, pepsin and their reversed sequences. The search parameters were as follows: peptide tolerance = automatic; fragment tolerance = automatic; min

fragment ion matches per peptide = 1; min fragment ion matches per protein = 7; min peptide matches per protein = 3; maximum hits to return = 20; maximum protein mass = 250,000; primary digest reagent = non-specific; missed cleavages = 0; false discovery rate = 100. Deuterium incorporation was quantified with DynamX 3.0 (Waters), using peptides that fulfilled the following criteria: minimum intensity = 10,000 counts; maximum length = 30 amino acids; minimum number of products = 3; minimum number of products per amino acid = 0.05; maximum mass error = 25 ppm; retention time tolerance = 0.5 min. After automated data processing with DynamX, all spectra were manually inspected and, if necessary, peptides were omitted (e.g. in case of a low signal-to-noise ratio or the presence of overlapping peptides).

$PadC_{\Delta N}$ variants were analyzed as described above, with the exception that H/D exchange was allowed to proceed for 10, 30, 95, 1,000 and 10,000 s in a buffer containing 25 mM HEPES/NaOH, pH 7.6, 10 mM $MgCl_2$, 100 mM NaCl and 0.1 mM β-mercaptoethanol. To study the interaction behavior of ParB, *M. xanthus* ParB (15 µM) was mixed with 4 mM CTPγS or a *parS*-containing double-stranded DNA oligonucleotide (*parS*-Mxan-wt; at a 2:1 molar ratio) in a D_2O-containing buffer (25 mM HEPES/NaOH, pH 7.2, 50 mM NaCl, 5 mM $MgCl_2$, 0.1 mM EDTA) and incubated at 25 °C. Samples were taken after 10, 30 and 95 s of incubation and processed as described above. The HDX raw data are provided in Data S1.

CTP content analysis

Proteins were denatured by mixing 50 µL of protein solution (at a typical concentration of 80-100 µM, as measured with a Bradford assay) with 100 µL $CHCl_3$. The mixture was agitated vigorously for 15 s, incubated for 15 s at 95 °C and then flash-frozen in liquid nitrogen. After removal from the liquid nitrogen, the samples were thawed while being subjected to centrifugation (17,300 ×g, 30 min, 4 °C). Subsequently, the aqueous phase was removed and analyzed by hydrophilic interaction liquid chromatography (HILIC) at neutral to high pH and subsequent high-resolution full-scan mass spectrometry in negative ionisation mode. The chromatographic separation was performed on an Agilent Infinity II 1290 HPLC system using a SeQuant ZIC-pHILIC column (150 x 2.1mm; 3.5 µm, 100 Å) equipped with a 20 x 2.1 mm guard column of similar specificity at a flow rate of 0.25 ml/min and 45 °C with mobile phase A (10 mM ammonium bicarbonate in water) and phase B (methanol) The injection volume was 10 µl. The mobile phase profile comprised the following steps and linear gradients: 2 min constant at 70% B, 2 min – 10 min from 70 % B to 30 % B; 10 min – 12 min constant at 30 % B, 12 min – 12.1 min from 30% to 70 % B; 12.1 min – 15 min constant at 70 % B. A mix of ATP, GTP, CTP and UTP (1 mM each) was used as standard to determine the nucleotide separation efficiency. An Agilent 6560 ion funnel QTOF mass spectrometer was used in negative mode with an electrospray ionization source

and the following conditions: ESI spray voltage 4500 V, sheath gas 200° C at 12 l/min, nebulizer pressure 20 psig and drying gas 170° C at 13 l/min. Compounds were identified based on accurate mass and retention time by comparison with suitable standards. Extracted ion chromatograms of the compound specific accurate mass were integrated using MassHunter software (Agilent). The molarity of CTP bound to PadC was quantified using a CTP standard with a known concentration as a reference.

Quantification and statistical analysis

Details on the number of replicates, the sample sizes as well as the value and meaning of n are included in the figure legends. Standard deviations were calculated in Microsoft Excel 2016. Unless indicated otherwise, all experiments were performed at least twice.

DATA AND CODE AVAILABILITY

The coordinates and structure factors for the PadC structure were deposited at the Protein Data Base (PDB) with the accession code 6RYK. All other data supporting the findings of this study are available in the main text or available from the authors upon reasonable request.

SUPPLEMENTAL FIGURES

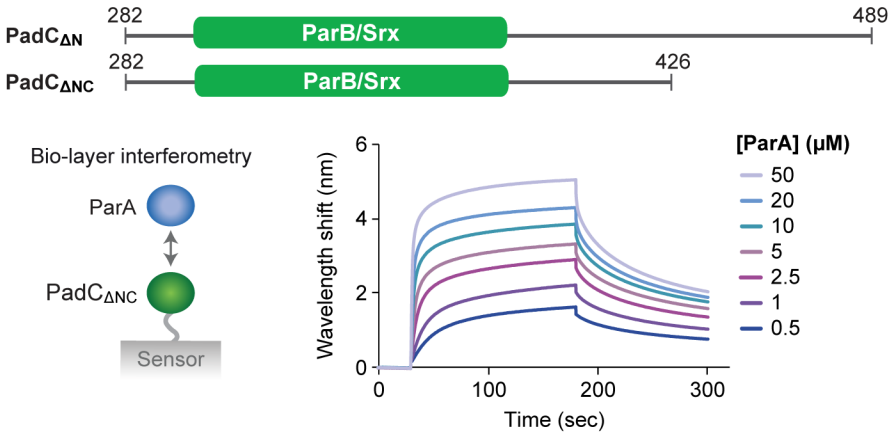

Figure S1. The ParB/sulfiredoxin domain of PadC is sufficient for the interaction with ParA. Related to Figure 1. The interaction of ParA with a truncated variant of PadC lacking the C-terminal bactofilin-binding domain (PadC$_{\Delta NC}$) was analyzed by bio-layer interferometry. Sensors were loaded with biotinylated PadC$_{\Delta NC}$ and probed with the indicated concentrations of ParA (K_D = 1.4 μM). The scheme on top compares the domain organization of PadC$_{\Delta N}$ and PadC$_{\Delta NC}$.

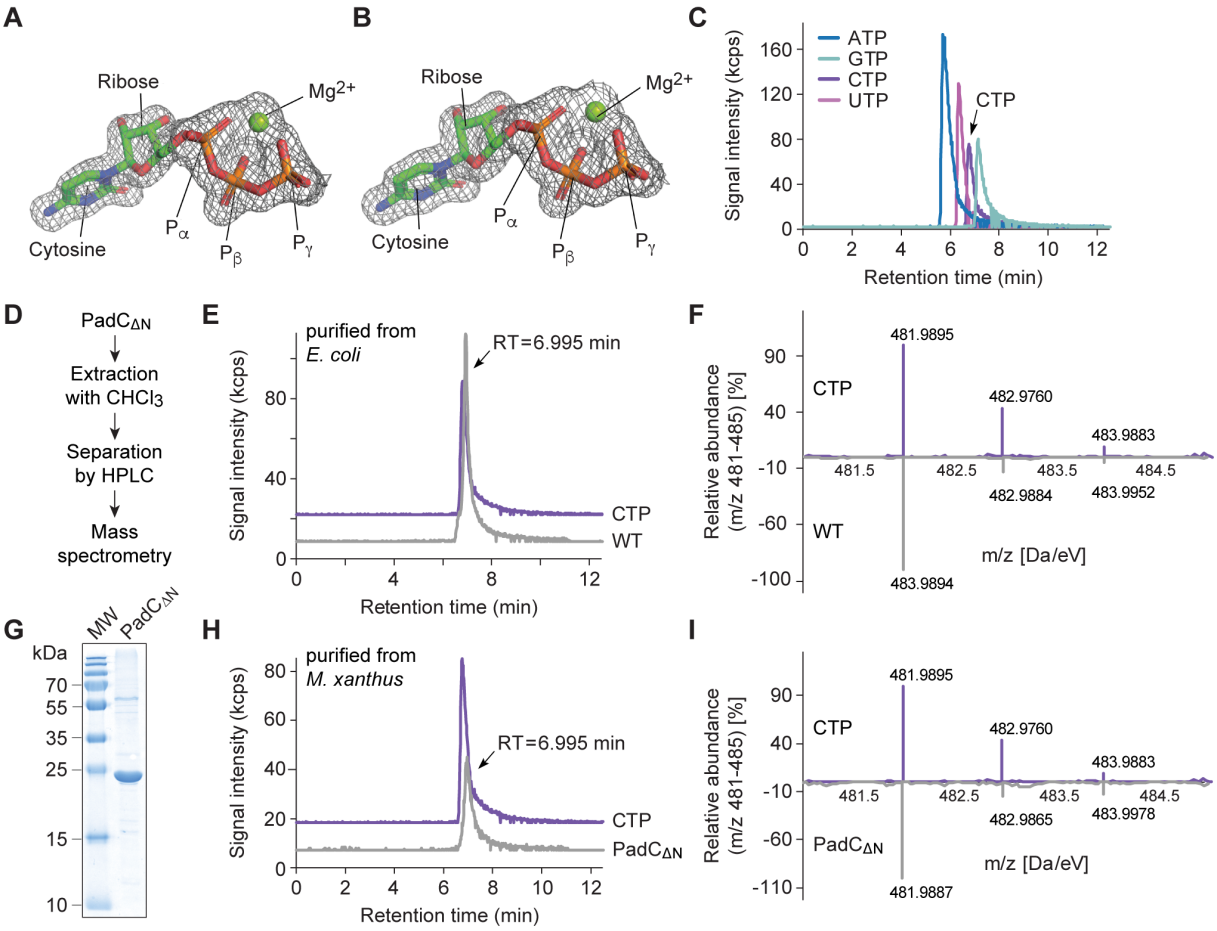

Figure S2. Unambiguous identification of PadC-bound CTP. Related to Figure 1. (A) Unbiased F_{obs}–F_{calc} difference electron density of CTP contoured at 2.5 σ and depicted as a grey mesh. Note that the CTP molecule (represented as sticks) was not present during refinement and is placed only for illustration purposes. **(B)** $2F_{obs}$–F_{calc} electron density of CTP (represented as sticks) after final refinement contoured at 1.0 σ and depicted as a grey mesh. **(C)** Separation of nucleotides by hydrophilic interaction liquid chromatography (HILIC). Standard solutions of ATP, GTP, CTP and UTP (1 mM each) were applied to a HILIC column. The elution of nucleotides was monitored at a wavelength of 260 nm (kcps, kilocounts per second). **(D)** Analysis pipeline used to identify the nucleotide bound to PadC. **(E)** Verification of CTP in $PadC_{\Delta N}$ purified from *Escherichia coli*. $PadC_{\Delta N}$ (80 µM) from the preparation used for crystallization (WT) was precipitated with $CHCl_3$ and the liquid phase was applied to a HILIC column. The elution of nucleotides was detected at a wavelength of 260 nm. A CTP standard was analyzed as a reference. **(F)** Electrospray ionisation mass spectra obtained for a CTP standard (top) and for the peak fraction of the HILIC analysis shown in panel C (retention time: 6.955 min) (bottom). The fraction only contained a single compound, whose spectrum was identical to that of CTP (M_W = 483.1653 g/mol) **(G)** Coomassie blue-stained SDS gel showing StrepII-tagged $PadC_{\Delta N}$ (24.1 kDa) purified from the native host *M. xanthus*. **(H)** Verification of CTP in $PadC_{\Delta N}$ isolated from *M. xanthus*. Strep-tagged $PadC_{\Delta N}$ was purified from *M. xanthus* MO11 cells by affinity chromatography. The protein (40 µM) was precipitated with $CHCl_3$ and analyzed by HILIC as described in (C). **(F)** Electrospray ionisation mass spectra obtained for a CTP standard (top) and for the peak fraction of the HILIC analysis shown in panel H (retention time: 6.955 min) (bottom). The fraction only contained a single compound, whose spectrum was identical to that of CTP.

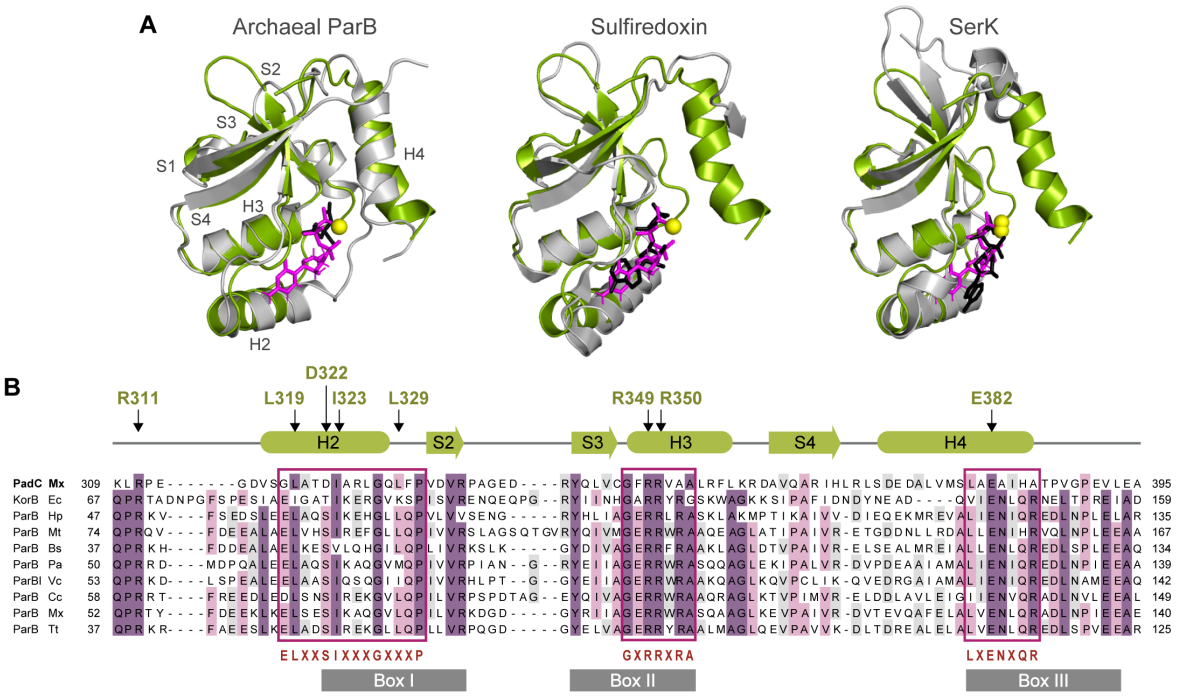

Figure S3. Conservation of the CTP-binding pocket in the ParB/Srx superfamily. Related to Figure 1. (A) Structural comparison of PadC with other members of the ParB/Srx superfamily. Shown are overlays of the ParB/Srx domain of PadC with the corresponding domains of a ParB homologue from the archaeon *Saccharolobus solfataricus* (PDB 5K5D) (Schumacher *et al.*, 2015) with an RMSD of 0.961 Å for 52 paired C_α atoms, human sulfiredoxin (Srx) in complex with ATP (PDB 3CYI) (Jönsson *et al.*, 2008) with an RMSD of 0.798 Å for 43 paired C_α atoms and serine kinase (SerK) from the archaeon *Thermococcus kodakarensis* in complex with ADP (PDB 5X0G) (Nagata *et al*., 2017) with an RMSD of 0.905 Å for 46 paired C_α atoms. **(B)** Amino acid sequence alignment of the CTP-binding domain of PadC and the N-terminal domains of some well-studied plasmidic and chromosomal ParB homologs. The scheme on top of the alignment shows the secondary structure of PadC. Arrows point to selected residues that mediate the interaction of PadC with CTP (compare Figure 1D). Magenta frames indicate conserved regions that constitute the CTP-binding pocket. The respective consensus motifs are given in red letters at the bottom. The previously described conserved regions Box I, Box II and Box III (also known as Region II) (Yamaichi *et al.*, 2000; Bartosik *et al.*, 2004) are indicated in dark gray. The UniProt accession numbers of the sequences used in the alignment are as follows: P07674 (KorB_Ec, *Escherichia coli*), Q1D3H3 (PadC_Mx, *Myxococcus xanthus*), P26497 (ParB_Bs, *Bacillus subtilis*), O25758 (ParB_Hp, *Helicobacter pylori*), P9WIJ9 (ParB_Mt, *Mycobacterium tuberculosis*, Q9HT12 (ParB_Pa, *Pseudomonas aeruginosa*), Q9KNG7 (ParBI Vc, *Vibrio cholerae*), P0CAV8 (ParB_Cc, *Caulobacter crescentus*), Q1CVJ4 (ParB_Mx, *Myxococcus xanthus*), Q72H91 (ParB_Tt, *Thermus thermophilus*). The numbers at the beginning and end of each line indicate the position of the first and last amino acid of the respective protein shown in the primary sequence.

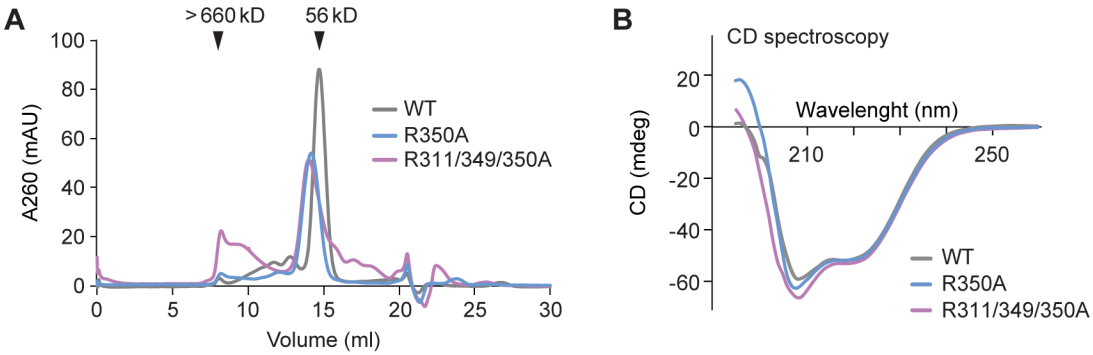

Figure S4. Functional analysis of nucleotide-free PadC variants. Related to Figure 3. (A) Size exclusion chromatography (SEC) analysis of PadC variants. Equal amounts of protein (3 mg/mL) were loaded onto a Superdex 200 10/300 GL column (GE Healthcare), and their elution was monitored at a wavelength of 280 nm. The calculated mass of the main peak and the void volume are indicated at the top of the chromatograms. **(B)** Circular dichroism spectra of wild-type $PadC_{\Delta N}$ and mutant variants with exchanges in the nucleotide-binding pocket.

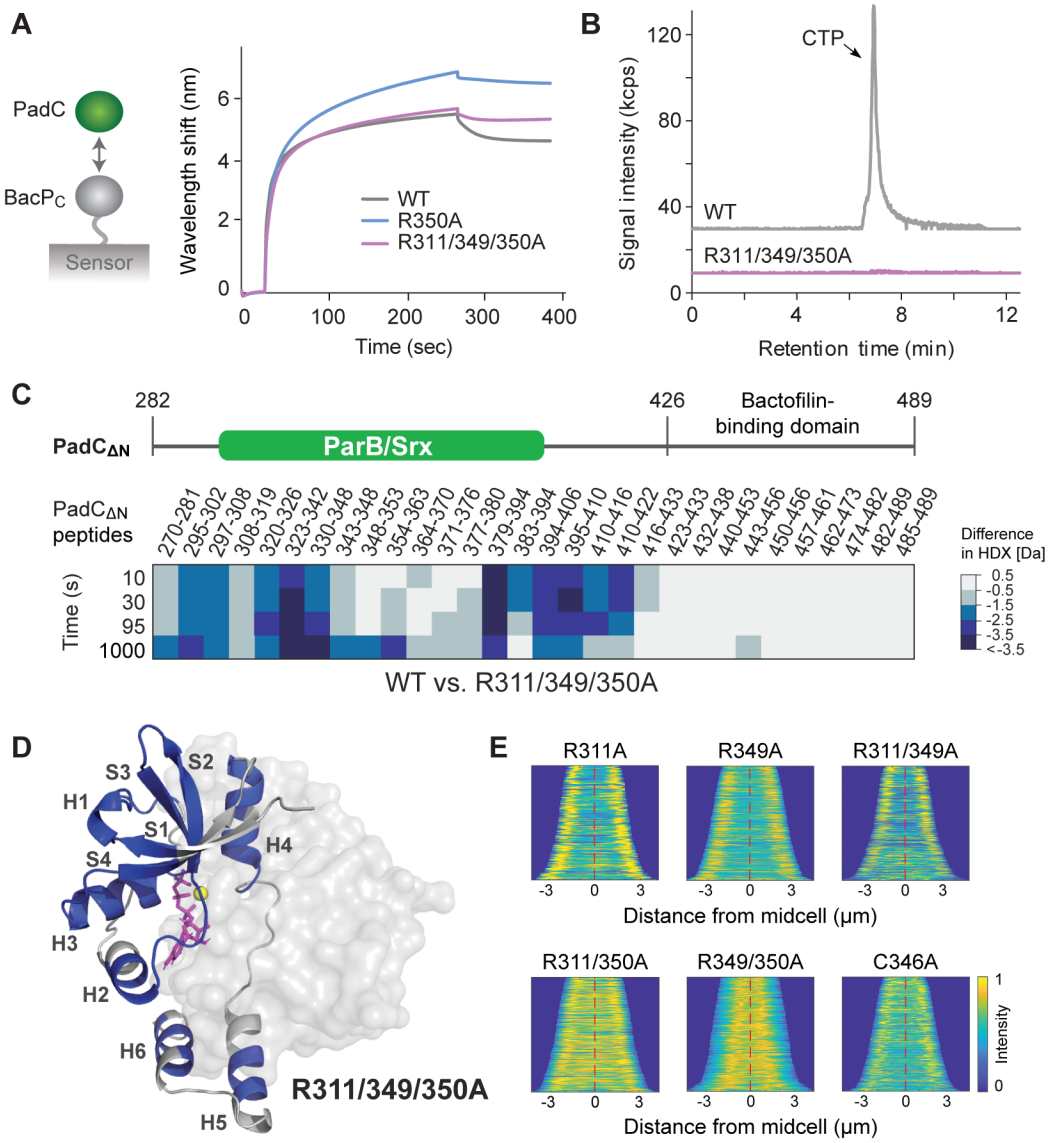

Figure S5. Localization of ParA-mCherry in cells producing different mutant PadC variants. Related to Figures 3 and 4. (A) Biolayer interferometric analysis of the interaction between the C-terminal domain of BacP ($BacP_C$) and nucleotide-free PadC. Sensors were loaded with a fixed amount of biotinylated $BacP_C$ and incubated with the indicated PadC variants (10 µM). **(B)** Loss of CTP from the PadC R311/349/350A variant. Proteins (80 µM) were precipitated with $CHCl_3$ and the liquid phase was separated by hydrophilic interaction liquid chromatography. CTP elution was detected at a wavelength of 260 nm. **(C)** Hydrogen/deuterium exchange (HDX) analysis of the PadC R311/349/350A variant. The heat plots show the differences in deuterium uptake between wild-type (WT) $PadC_{\Delta N}$ and its R350A variant at different incubation times for a series of representative peptides (see Data S1 for the full list of peptides). The color code is given on the right. The scheme on top depicts the domain organization of $PadC_{\Delta N}$. **(D)** Mapping of the changes in HDX observed for the CTP-free $PadC_{\Delta N}$ R350A variant onto the structure of $PadC_{\Delta N}$ (t=1000 s). The color code is identical to the one used in panel A. Note that the structure does not include the C-terminal bactofilin-binding domain. **(E)** Effect of mutations in the nucleotide-binding pocket on the interaction of PadC with ParA. *M. xanthus* strains (Δ*padC* P_{parA}-*parA-mCherry*) carrying the indicated *padC* alleles under the control of a vanillate-inducible promoter (MO60, MO63, MO65, MO66, MO67, MO62) were cultivated for 2 h with 5 µM vanillate before imaging. Fluorescence profiles of individual cells were sorted according to cell length and stacked on top of each other, with the shortest cell shown at the top and the longest cell shown at the bottom. n=142 (R311A), 290 (R349A), 175 (R311/349A), 290 (R311/350A), 175 (R349/350A) and 377 (C346A) cells.

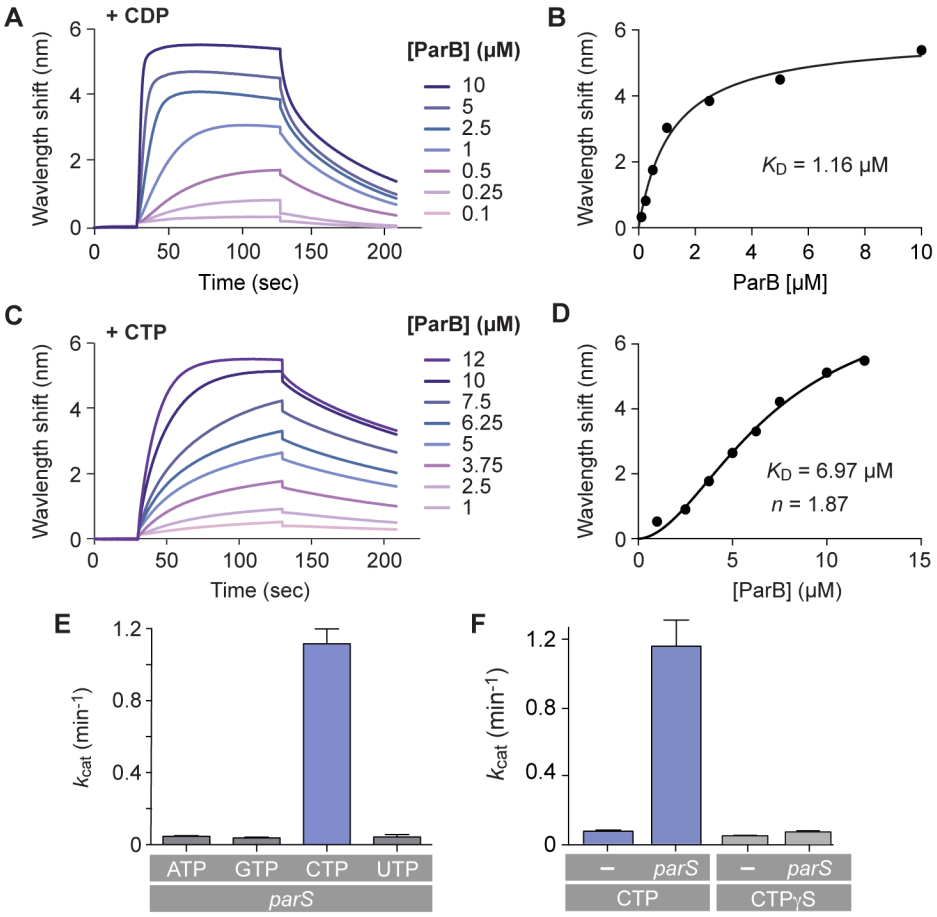

Figure S6. Functional interaction between the CTP- and DNA-binding domains of ParB. Related to Figure 6. (A) Biolayer interferometric analysis of the interaction between ParB and *parS* in the presence of 2 mM CDP. Sensors carrying a double-stranded DNA oligonucleotide with a consensus *parS* motif were incubated with the indicated concentrations of *M. xanthus* ParB. **(B)** Analysis of the binding data shown in panel A. The plot shows the equilibrium levels measured at the different ParB concentrations. The data were fitted to a non-cooperative one-site specific-binding model. The resulting K_D value is given in the graph. **(C)** Biolayer interferometric analysis of the interaction between ParB and *parS* in the presence of 1 mM CTP, performed as described in (A). **(D)** Analysis of the binding data shown in panel C, performed as described in (B). **(E)** Analysis of the nucleotide specificity of ParB. ParB (4 µM) was incubated with 1 mM ATP, GTP, CTP or UTP in the presence of a double-stranded DNA oligonucleotide (54 bp) containing a consensus *parS* site (250 nM). The reaction rates were determined with a coupled enzyme assay. Data represent the mean of three experiments (± SD). **(F)** Comparison of the hydrolytic activity of ParB with CTP and CTPγS. ParB (4 µM) was incubated with 1 mM CTP or CTPγS in the absence or presence (250 nM) of a double-stranded DNA oligonucleotide containing a consensus *parS* site. Reaction rates were determined as described in (C).

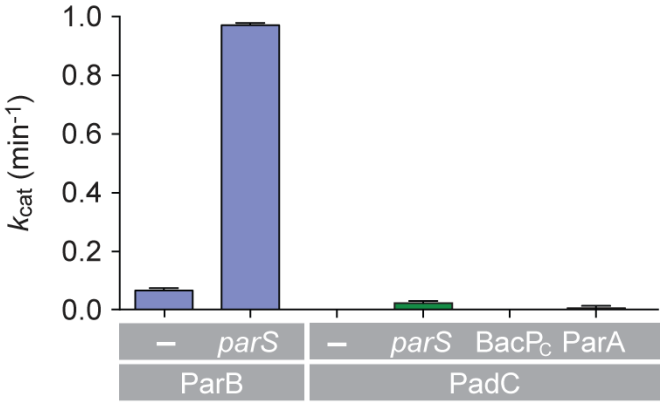

Figure S7. Comparison of the CTPase activities of ParB and PadC. Related to Figure 6. ParB or PadC (4 µM) were incubated alone (-) or with a double-stranded DNA oligonucleotide (54 bp) containing a consensus *parS* site (250 nM), a C-terminal fragment of BacP (BacP$_C$) (1 µM) or *M. xanthus* ParA (1 µM). The reaction rates were determined with a coupled enzyme assay. Data represent the mean of three experiments (± SD).

KEY RESOURCES TABLE

REAGENT or RESOURCE	SOURCE	IDENTIFIER
Antibodies		
anti-GFP	Sigma-Aldrich	Cat. #: G1544
Bacterial strains		
Escherichia coli TOP10	Thermo Fisher Scientific	Cat. #: C404010
Escherichia coli Rosetta(DE3)pLysS	Merck	Cat. #: 70956
Myxococcus xanthus DK1622	Kaiser, 1979	
DK1622 Δ*padC*	Lin et al., 2017	LL101
DK1622 Δ*padC attB*::P_{parA}-*parA-mCherry*	Lin et al., 2017	LL154
DK1622 Δ*padC attB*::P_{parA}-*parA-mCherry MXAN18/19*::P_{van}-*padC*	Lin et al., 2017	LL192
DK1622 Δ*padC attB*::P_{parA}-*parA-mCherry MXAN18/19*::P_{van}-$padC_{\Delta C}$-*eyfp*	This study	MO4
DK1622 Δ*padC* P_{pilA}- *strepII-padC*Δ1-281	This study	MO11
DK1622 Δ*padC attB*::P_{parA}-*parA-mCherry MXAN18/19*::P_{van}-*padC-eyfp*	This study	SU1
DK1622 Δ*padC attB*::P_{parA}-*parA-mCherry MXAN18/19*::P_{van}-$padC_{R350A}$-*eyfp*	This study	SU20
DK1622 Δ*padC attB*::P_{parA}-*parA-mCherry MXAN18/19*::P_{van}-$padC_{R311,349,350A}$-*eyfp*	This study	MO33
DK1622 Δ*padC attB*::P_{parA}-*parA-mCherry MXAN18/19*::P_{van}-$padC_{R311A}$	This study	MO60
DK1622 Δ*padC attB*::P_{parA}-*parA-mCherry MXAN18/19*::P_{van}-$padC_{C346A}$	This study	MO62
DK1622 Δ*padC attB*::P_{parA}-*parA-mCherry MXAN18/19*::P_{van}-$padC_{R349A}$	This study	MO63
DK1622 Δ*padC attB*::P_{parA}-*parA-mCherry MXAN18/19*::P_{van}-$padC_{R350A}$	This study	MO64
DK1622 Δ*padC attB*::P_{parA}-*parA-mCherry MXAN18/19*::P_{van}-$padC_{R311,349A}$	This study	MO65
DK1622 Δ*padC attB*::P_{parA}-*parA-mCherry MXAN18/19*::P_{van}-$padC_{R311,350A}$	This study	MO66
DK1622 Δ*padC attB*::P_{parA}-*parA-mCherry MXAN18/19*::P_{van}-$padC_{R349,350A}$	This study	MO67
DK1622 Δ*padC attB*::P_{parA}-*parA-mCherry MXAN18/19*::P_{van}-$padC_{R311,349,350A}$	This study	MO68
DK1622 Δ*parB* P_{cuoA}-*parB* P_{van}-*sfmTurq2ox-parB*	This study	MO72
DK1622 Δ*parB* P_{cuoA}-*parB* P_{van}-*sfmTurq2ox-*$parB_{R95A}$	This study	MO73
DK1622 Δ*parB* P_{cuoA}-*parB* P_{van}-*sfmTurq2ox-*$parB_{E126A}$	This study	MO75
DK1622 Δ*parB* P_{cuoA}-*parB* P_{van}-*sfmTurq2ox-*$parB_{N127A}$	This study	MO76
DK1622 Δ*parB* P_{cuoA}-*parB* P_{van}-*sfmTurq2ox-*$parB_{R130A}$	This study	MO77
DK1622 Δ*parB* P_{cuoA}-*parB*	Harms et al., 2013	SA4269
Chemicals and Recombinant Proteins		
Acetonitrile Chromasolv LC-MS ultra	Honeywell Riedel-de-Haën	Cat. #: 14261-2l
Ammonium carbonate	Honeywell Riedel-de-Haën	Cat. #: 379999-50
ATP	Jena Bioscience	Cat. #: NU-1010
CDP	Sigma Aldrich	Cat. #: C9755-25MG
CTP	Jena Bioscience	Cat. #: NU-1011
CTPγS	Jena Bioscience	Custom synthesis
Deuterium oxide	Deutero	Cat. #: 00506
EZ-Link NHS-PEG4-Biotin	Thermo Fisher Scientific	Cat. #: 21330
GTP	Jena Bioscience	Cat. #: NU-1012

L-Lactic dehydrogenase	Sigma Aldrich	Cat. #: L2500
NADH	Sigma Aldrich	Cat. #: 10107735001
Phosphoenolpyruvate	Sigma Aldrich	Cat. #: 10108294001
Pyruvate kinase	Sigma Aldrich	Cat. #: P1506
UTP	Jena Bioscience	Cat. #: NU-1013
Deposited Data		
Crystal structure of $PadC_{\Delta N}$	RCSB	6RYK
Oligonucleotides		
For PCR primers, see **Table S4**.	This study	Custom synthesis
parS-Mxan-wt GAGGCTTGTTCCACGTGGAACGTCGGTTTTTCGGACGTTCCACGTG GAACAAGC	This study	Custom synthesis
parS-Mxan-mut GAGGCTTGCCCCACGTGGCCCGTCGGTTTTTCGGACGGGCCACGT GGGGCAAGC	This study	Custom synthesis
Recombinant DNA		
pET-45b(+) carrying *parA*	Harms et al., 2013	pAH17
pSWU30 carrying P_{parA}-*parA-mCherry*	Harms et al., 2013	pAH59
pET-28a(+) Vector for overexpression of N-terminally His_6-tagged proteins , Kan^R	Merck Millipore	Cat. #: 69864
pET-45b(+) Vector for overexpression of N-terminally His_6-tagged proteins, Amp^R	Novagen	Cat. #: 71327
pET-45b(+) carrying $bacP_{116-240}$	Bulyha et al., 2013	pIB154
pET-45b(+) carrying *parB*	Harms et al., 2013	pKA52
pMR3690 carrying *padC*	Lin et al., 2017	pLL126
pMR3690 carrying *padC-eyfp*	Lin et al., 2017	pLL143
pET-28a(+) carrying $padC_{\Delta 1-281}$	Lin et al., 2017	pMO2
pMR3690 Vector for the expression of a gene under the control of the *vanA* promoter, integrating at the *M. xanthus* Mxan18_19 chromosomal locus, Kan^R	Iniesta et al., 2012	N/A
pSW105 Vector for genes ligated to *pilA* promoter integrating at *M. xanthus* chromosomal Mx8 *attB* site, Kan^R	Jakovljevic et al., 2008	N/A
pXYFPC-2 Integration plasmid to fuse 3' end of a target gene to *eyfp* under the control of P_{xyl}, Kan^R	Thanbichler et al., 2007	N/A
pET-28a(+) bearing $padC\Delta 1\text{-}281_{R350A}$	This study	pMO12
pET-28a(+) bearing $padC_{282-426}$	This study	pMO17
pMR3690 bearing StrepII-padCΔ1-281	This study	pMO18
pMR3690 bearing *padC*ΔC-*eyfp*	This study	pMO19
pSW105 bearing StrepII-p*adC*Δ1-281	This study	pMO28

pMR3690 bearing *padC-eyfp*	This study	pSU1
pMR3690 bearing *padC* $_{R350A}$ *-eyfp*	This study	pSU5
pET-28a(+) bearing *padC*Δ1-281$_{R311/349/350A}$	This study	pMO53
pMR3690 bearing *padC* $_{R311/349/350A}$ *-eyfp*	This study	pMO60
pMR3690 bearing *padC*$_{R311A}$	This study	pMO78
pMR3690 bearing *padC*$_{C346A}$	This study	pMO80
pMR3690 bearing *padC*$_{R349A}$	This study	pMO81
pMR3690 bearing *padC*$_{R350A}$	This study	pMO82
pMR3690 bearing *padC*$_{R311/349A}$	This study	pMO83
pMR3690 bearing *padC*$_{R311/350A}$	This study	pMO84
pMR3690 bearing *padC*$_{R349/350A}$	This study	pMO85
pMR3690 bearing *padC*$_{R311/349/350A}$	This study	pMO86
pET-45b(+) bearing *parB*$_{E126A}$	This study	pMO108
pET-45b(+) bearing *parB*$_{R95A}$	This study	pMO109
pET-45b(+) bearing *parB*$_{N127A}$	This study	pMO110
pET-45b(+) bearing *parB*$_{R130A}$	This study	pMO111
pMR3690 bearing *sfmTurq2ox-parB*	This study	pMO115
pMR3690 bearing *sfmTurq*2ox-*parB*$_{R95A}$	This study	pMO118
pMR3690 bearing *sfmTurq*2ox-*parB*$_{E126A}$	This study	pMO120
pMR3690 bearing *sfmTurq*2ox-*parB*$_{N127A}$	This study	pMO121
pMR3690 bearing *sfmTurq*2ox-*parB*$_{R130A}$	This study	pMO122
Software and Algorithms		
Adobe Illustrator CS6	Adobe Systems	https://www.adobe.com/products/illustrator.html
BacStalk	Hartmann et al., 2018	https://drescherlab.org/data/bacstalk
CCP4 7.0	Winn et al., 2011	http://www.ccp4.ac.uk/index.php
Chimera 1.12	UCSF	https://www.cgl.ucsf.edu/chimera
Clustal Omega	Sievers and Higgins, 2018	http://www.clustal.org/omega
Consurf	Ashkenazy et al., 2016	http://consurf.tau.ac.il/index_proteins.php
DynamX 3.0.0	Waters	https://www.waters.com/waters/library.htm?cid=511436&lid=134832928&locale=en_US
Excel 2016	Microsoft	https://products.office.com
Jalview2.10.0	Waterhouse et al., 2009	http://www.jalview.org/development/release-history/Version-2100

Jasco Spectra Manager	Jasco	https://jascoinc.com/products/spectroscopy/circular-dichroism/software/spectra-manager
LigPlot+ 2.1	Wallace et al., 1995	https://www.ebi.ac.uk/thornton-srv/software/LigPlus
Mascot 2.5	Matrix Science	http://www.matrixscience.com/help/june2014.html
MassHunter	Agilent	https://www.agilent.com/en/products/software-informatics/masshunter-suite/masshunter/masshunter-software
Metamorph 7.7.5	Molecular Devices	https://www.moleculardevices.com/products/cellular-imaging-systems/acquisition-and-analysis-software/metamorph-microscopy
PHENIX 1.16	Liebschner et al., 2019	https://www.phenix-online.org
PLGS 3.0.1	Waters	https://www.waters.com/waters/en_US/ProteinLynx-Global-SERVER-(PLGS)/nav.htm?cid=513821&locale=en_US
Prism 6.0	GraphPad	https://www.graphpad.com/scientific-software/prism
PyMOL 1.5.0.5	Schrödinger	https://pymol.org/2
XDS	Kabsch, 2010	http://xds.mpimf-heidelberg.mpg.de
Other		
Crystallization screening plates NeXtal Tubes JCSG Core Suite I	Qiagen	Cat. #: 130724

SUPPLEMENTAL DATA

Table S1. Crystallographic data collection and refinement statistics. Related to Figure 1.

	PadC (Se-Met SAD)	PadC
Data collection		
Space group	*P*1	*P1*
Cell dimensions		
a, *b*, *c* (Å)	36.33 42.09 49.12	36.85 42.44 49.53
α, β, γ (°)	108.080 99.624 89.038	108.539 99.146 89.281
Wavelength (Å)	Peak 0.9791	0.8729
Resolution (Å)	46.01 – 2.07	36.74 - 1.70 (1.76 - 1.70)
R_{merge}	0.066 (0.49)	0.058 (0.98)
I / σI	10.3 (2.0)	11.03 (1.11)
Completeness (%)	95.09 (77.68)	97.07 (96.07)
Redundancy	3.82 (3.31)	3.5 (3.5)
CC1/2	0.99 (0.86)	0.99 (0.52)
Refinement		
Resolution (Å)		36.74 - 1.70
No. reflections		29970 (2956)
R_{work} / R_{free}		18.5 / 22.65
No. atoms		2375
Protein		2067
Ligand/ion		66
Water		242
B-factors		
Protein		39.13
Ligand/ion		30.53
Water		45.50
R.m.s. deviations		
Bond lengths (Å)		0.010
Bond angles (°)		1.46

Values in parentheses are for highest-resolution shell.

Table S2. Strains used in this study. Related to the STAR Methods.

Strain	Genotype/description	Construction	Reference/Source
M. xanthus			
DK1622	*M. xanthus* wild-type strain		Kaiser, 1979
LL101	DK1622 Δ*padC*	In-frame deletion of *padC* in DK1622 using pLL38	Lin *et al.*, 2017
LL154	DK1622 Δ*padC attB*::P_{parA}-*parA-mCherry*	Integration of pAH59 in LL101	Lin *et al.*, 2017
LL192	DK1622 Δ*padC attB*::P_{parA}-*parA-mCherry MXAN18/19*::P_{van}-*padC*	Integration of pLL126 in LL154	Lin *et al.*, 2017
MO4	DK1622 Δ*padC attB*::P_{parA}-*parA-mCherry MXAN18/19*::P_{van}-$padC_{\Delta C}$-*eyfp*	Integration of pMO19 in LL154	This study
MO11	DK1622 Δ*padC* P_{pilA}- *strepII-padC*Δ1-281	Integration of pMO28 in LL101	This study
SU1	DK1622 Δ*padC attB*::P_{parA}-*parA-mCherry MXAN18/19*::P_{van}-*padC-eyfp*	Integration of pLL143 in LL154	This study
SU20	DK1622 Δ*padC attB*::P_{parA}-*parA-mCherry MXAN18/19*::P_{van}-$padC_{R350A}$-*eyfp*	Integration of pSU5 in LL154	This study
MO33	DK1622 Δ*padC attB*::P_{parA}-*parA-mCherry MXAN18/19*::P_{van}-$padC_{R311,349,350A}$-*eyfp*	Integration of pMO60 in LL154	This study
MO60	DK1622 Δ*padC attB*::P_{parA}-*parA-mCherry MXAN18/19*::P_{van}-$padC_{R311A}$	Integration of pMO78 in LL154	This study
MO62	DK1622 Δ*padC attB*::P_{parA}-*parA-mCherry MXAN18/19*::P_{van}-$padC_{C346A}$	Integration of pMO80 in LL154	This study
MO63	DK1622 Δ*padC attB*::P_{parA}-*parA-mCherry MXAN18/19*::P_{van}-$padC_{R349A}$	Integration of pMO81 in LL154	This study
MO64	DK1622 Δ*padC attB*::P_{parA}-*parA-mCherry MXAN18/19*::P_{van}-$padC_{R350A}$	Integration of pMO82 in LL154	This study
MO65	DK1622 Δ*padC attB*::P_{parA}-*parA-mCherry MXAN18/19*::P_{van}-$padC_{R311,349A}$	Integration of pMO83 in LL154	This study
MO66	DK1622 Δ*padC attB*::P_{parA}-*parA-mCherry MXAN18/19*::P_{van}-$padC_{R311,350A}$	Integration of pMO84 in LL154	This study
MO67	DK1622 Δ*padC attB*::P_{parA}-*parA-mCherry MXAN18/19*::P_{van}-$padC_{R349,350A}$	Integration of pMO85 in LL154	This study
MO68	DK1622 Δ*padC attB*::P_{parA}-*parA-mCherry MXAN18/19*::P_{van}-$padC_{R311,349,350A}$	Integration of pMO86 in LL154	This study
MO72	DK1622 Δ*parB* P_{cuoA}-*parB* P_{van}-*sfmTurq2ox-parB*	Integration of pMO115 in SA4269	This study
MO73	DK1622 Δ*parB* P_{cuoA}-*parB* P_{van}-*sfmTurq2ox-*$parB_{R95A}$	Integration of pMO118 in SA4269	This study
MO75	DK1622 Δ*parB* P_{cuoA}-*parB* P_{van}-*sfmTurq2ox-*$parB_{E126A}$	Integration of pMO120 in SA4269	This study
MO76	DK1622 Δ*parB* P_{cuoA}-*parB* P_{van}-*sfmTurq2ox-*$parB_{N127A}$	Integration of pMO121 in SA4269	This study
MO77	DK1622 Δ*parB* P_{cuoA}-*parB* P_{van}-*sfmTurq2ox-*$parB_{R130A}$	Integration of pMO122 in SA4269	This study
SA4269	DK1622 Δ*parB* P_{cuoA}-*parB*	Integration of pAH57 in DK1622, subsequent deletion of *parB* with pAH18	Harms et al., 2013
E. coli			
TOP10	F^- *mcr*A Δ(*mrr-hsd*RMS-*mcr*BC) Φ80*lacZ*ΔM15 Δ*lac*X74 *rec*A1 *ara*D139 Δ(*ara leu*) 7697 *gal*U *gal*K *rps*L (Str^R) *end*A1 *nup*G		Invitrogen
Rosetta(DE3) pLysS	F^- *ompT* $hsdS_B$(r_B^- m_B^-) *gal dcm* (DE3) pLysSRARE (Cam^R)		Merck Millipore

Table S3. Plasmids generated in this work. Related to the STAR Methods.

Plasmid	Description	Construction
pMO12	pET28a(+) bearing *padC*Δ1-281$_{R350A}$	Site-directed mutagenesis of pMO2 with primers *padC*(D322A)-for and *padC*(D322A)-rev
pMO17	pET28a(+) bearing *padC*$_{282-426}$	a) PCR amplification of *padC*$_{282-426}$ with primers padCΔ1-281-for and *padC*ΔC-rev b) Digestion of the product with NdeI and EcoRI c) Ligation of the fragment into pET28a(+) cut with NdeI and EcoRI
pMO18	pMR3690 bearing StrepII-*padC*Δ1-281	a) PCR amplification of *padC*Δ1-281 from pMO2 with primers StrepII-*padC*-for and *padC*-rev b) Ligation of the fragment into pMR3690 cut with NdeI and EcoRI
pMO19	pMR3690 bearing *padC*ΔC-*eyfp*	a) PCR amplification of *padC*$_{1-426}$ with primers *padC*ΔC-for and *padC*ΔC -rev b) PCR amplification of linker-*eyfp* with primers linker-eYFP-for and eYFP-rev c) Insertion of the fragments into pMR3690 cut with NdeI and NheI by Gibson assembly
pMO28	pSW105 bearing StrepII-*padC*Δ1-281	a) PCR amplification of StrepII-*padC*Δ1-281 from pMO38 using primers *padC*-pMR3690-for and padC-pMR3690-rev b) Insertion of the fragment into pMT325 cut with EcoRI and NdeI
pSU1	pMR3690 bearing *padC*-*eyfp*	Site-directed mutagenesis of pLL143 with primers *padC*(R311A)-for and *padC*(R311A)-rev
pSU5	pMR3690 bearing *padC*$_{R350A}$-*eyfp*	Site-directed mutagenesis of pLL143 with primers *padC*(R350A)-for and *padC*(R350A)-rev
pMO53	pET28a(+) bearing *padC*Δ1-281$_{R311/349/350A}$	Site-directed mutagenesis of pMO5 with primers *padC*(R349/350A)-for and *padC*(R349,350A)-rev
pMO60	pMR3690 bearing *padC*$_{R311/349/350A}$-*eyfp*	Site-directed mutagenesis of pSU1 with primers *padC*(R349/350A)-for and *padC*(R349,350A)-rev
pMO78	pMR3690 bearing *padC*$_{R311A}$	Site-directed mutagenesis of pLL126 with primers *padC*(R311A)-for and *padC*(R311A)-rev
pMO80	pMR3690 bearing *padC*$_{C346A}$	Site-directed mutagenesis of pLL126 with primers *padC*(C346A)-for and *padC*(C346)-rev
pMO81	pMR3690 bearing *padC*$_{R349A}$	Site-directed mutagenesis of pLL126 with primers *padC*(R349A)-for and *padC*(R349A)-rev
pMO82	pMR3690 bearing *padC*$_{R350A}$	Site-directed mutagenesis of pLL126 with primers *padC*(R350A)-for and *padC*(R350A)-rev
pMO83	pMR3690 bearing *padC*$_{R311/349A}$	Site-directed mutagenesis of pMO78 with primers *padC*(R349A)-for and *padC*(R349A)-rev
pMO84	pMR3690 bearing *padC*$_{R311/350A}$	Site-directed mutagenesis of pMO78 with primers *padC*(R350A)-for and *padC*(R350A)-rev
pMO85	pMR3690 bearing *padC*$_{R349/350A}$	Site-directed mutagenesis of pLL143 with primers *padC*(R349/350A)-for and *padC*(R349/350A)-rev
pMO86	pMR3690 bearing *padC*$_{R311/349/350A}$	Site-directed mutagenesis of pMO78 with primers *padC*(R349,350A)-for and *padC*(R349/350A)-rev
pMO108	pET45b(+) bearing *parB*$_{E126A}$	Site-directed mutagenesis of pKA52 with primers *parB*(E126A)-for and *parB*(E126A)-rev
pMO109	pET45b(+) bearing *parB*$_{R95A}$	Site-directed mutagenesis of pKA52 with primers *parB*(R95A)-for and *parB*(R95A)-rev
pMO110	pET45b(+) bearing *parB*$_{N127A}$	Site-directed mutagenesis of pKA52 with primers *parB*(N127A)-for and *parB*(N127A)-rev
pMO111	pET45b(+) bearing *parB*$_{R130A}$	Site-directed mutagenesis of pKA52 with primers *parB*(R130A)-for and *parB*(R130A)-rev
pMO115	pMR3690 bearing *sfmTurq2-parB*	a) PCR amplification of *sfmTurq2* with primers *sfmTurq2*L1-for and *sfmTurq2*L1-rev b) PCR amplification of *sfmTurq2*L1 with primers pMR-*sfmTurq2*-for and pMR-*sfmTurq2*-rev c) PCR amplification of *parB* with primers pMR-*parB*-for and pMR-*parB*-rev d) Insertion of the *sfmTurq2*L1 and *parB* fragments into pMR3690 cut with NdeI and NheI by Gibson assembly
pMO118	pMR3690 bearing *sfmTurq2ox-parB*$_{R95A}$	a) PCR amplification of *sfmTurq2*L1 with primers pMR-*sfmTurq2*-for and pMR-*sfmTurq2*-rev b) PCR amplification of *parB*$_{R95A}$ with primers pMR-*parB*-for and pMR-*parB*-rev c) Insertion of the *sfmTurq2*L1 and *parB*$_{R95A}$ fragments into pMR3690 cut with NdeI and NheI by Gibson assembly
pMO120	pMR3690 bearing *sfmTurq2ox-parB*$_{E126A}$	a) PCR amplification of *sfmTurq2*L1 with primers pMR-*sfmTurq2*-for and pMR-*sfmTurq2*-rev b) PCR amplification of *parB*$_{E126A}$ with primers pMR-*parB*-for and pMR-*parB*-rev c) Insertion of the *sfmTurq2*L1 and *parB*$_{E126A}$ fragments into pMR3690 cut with NdeI and NheI by Gibson assembly
pMO121	pMR3690 bearing *sfmTurq2ox-parB*$_{N127A}$	a) PCR amplification of *sfmTurq2*L1 with primers pMR-*sfmTurq2*-for and pMR-*sfmTurq2*-rev b) PCR amplification of *parB*$_{N127A}$ with primers pMR-*parB*-for and pMR-*parB*-rev c) Insertion of the *sfmTurq2*L1 and *parB*$_{N127A}$ fragments into pMR3690 cut with NdeI and NheI by Gibson assembly
pMO122	pMR3690 bearing *sfmTurq2ox-parB*$_{R130A}$	a) PCR amplification of *sfmTurq2*L1 with primers pMR-*sfmTurq2*-for and pMR-*sfmTurq2*-rev b) PCR amplification of *parB*$_{R130A}$ with primers pMR-*parB*-for and pMR-*parB*-rev c) Insertion of the *sfmTurq2*L1 and *parB*$_{R130A}$ fragments into pMR3690 cut with NdeI and NheI by Gibson assembly

Table S4. PCR primers used in this work. Related to the STAR Methods.

Oligonucleotide	Sequence
padC(R311A)-for	GCCTTCCGGGGCAAGCTTGAACGCGCTTTCG
padC(R311A)-rev	CGAAAGCGCGTTCAAGCTTGCCCCGGAAGGC
padC(R350A)-for	CAGCGCAGCGACCGCCCGGAAGCCACAG
padC(R350A)-rev	CTGTGGCTTCCGGGCGGTCGCTGCGCTGC
*padC*Δ1-281-for	AATTCATATGCCCGAACCCGAGCAGCGGC
padC$_{282-426}$rev	CCGGTCGAATTCTTACGCCAGTGTGTCCTC
*padC*ΔC-for	CCGAACCACGATGCGAGGAAACGCATATGCGGGCGCGTGGGCTTT
*padC*ΔC-rev	GCGTAACGTTCGAATTCGACGCCAGTGTGTCCTCAGTGGCGA
linker-eYFP-for	GCCACTGAGGACACACTGGCGTCGAATTCGAACGTTACGCGTCA
eYFP-rev	GATCCCCCGGGCTGCAGCTAGCTTACTTGTACAGCTCGTCCATGC
StrepII-*padC*-for	AATTCATATGTGGAGCCACCCGCAGTTCGAAAAGCCCGAACCCGA
padC-rev	AGTCGAATTCTTACAGCCCCTCCAGATAGG
StrepII-*padC*-pSW105-for	TCTGAGGACCCCCATGTCTAGAATGTGGAGCCACCCGCAGTTC
StrepII-*padC*-pSW105-rev	AACGACGGCCAGTGCCAAGCTTTTACAGCCCCTCCAGATAGGTG
padC(R349/350A)-for	GCGCAGCGCAGCGACCGCCGCGAAGCCACAGACGAGTT
padC(R349/350A)-rev	CAACTCGTCTGTGGCTTCGCGGCGGTCGCTGCGCTGCG
padC(C346A)-for	GCTACCAACTCGTCGCTGGCTTCCGGCGGG
padC(C346A)-rev	CCCGCCGGAAGCCAGCGACGAGTTGGTAGCGG
padC(R349A)-for	CGCAGCGACCCGCGCGAAGCCACAGACG
padC(R349A)-rev	CGTCTGTGGCTTCGCGCGGGTCGCTGCG
padC-pMR3690-for	ATGCGAGGAAACGCATATGGTGCGGGCGCGTG
padC-pMR3690-rev	TACGCGTAACGTTCGAATTCTTACAGCCCCTCCAGATAGGTG
parB(R95A)-for	GGCGAGCGCGCCTGGCGCGCCT
parB(R95A)-rev	GAGGCGCGCCAGGCGCGCTCGCCCGCG
parB(E126A)-for	CTGGCCCTGGTGGCGAACCTCCAGCGC
parB(E126A)-rev	GCGCTGGAGGTTCGCCACCAGGGCCAG
parB(R95A2)-rev	AGGCGCGCCAGGCGCGCTCGCCC
parB(N127A)-for	GGCCCTGGTGGAGGCCCTCCAGCGCGCG
parB(N127A)-rev	CGCGCGCTGGAGGGCCTCCACCAGGGC
parB(R130A)-for	GGAGAACCTCCAGGCCGCGGACCTGAA
parB(R130A)-rev	TTCAGGTCCGCGGCCTGGAGGTTCTCCA
*sfmTurq*2L1-for	ATGGTGAGCAAGGGCGAGGAG
*sfmTurq*2L1-rev	CGTTCCGCCTCCGGATCCGCCTCCCTTGTACAGCTCGTCCATGCC
pMR-*sfmTurq*2-for	CACGATGCGAGGAAACGCATATGGTGAGCAAGGGCGAGGAGC
pMR-*sfmTurq*2-rev	GCATGTCTGCTTTCACCACCGTTCCGCCTCCGGATCCGCCT
pMR-*parB*-for	GGATCCGGAGGCGGAACGGTGGTGAAAGCAGACATGCAGAAG
pMR-*parB*-rev	TACGCGTAACGTTCGAATTCCTACTCCTTCCTGAGAAGCTTCAAG

REFERENCES

Adams, P.D., Afonine, P.V., Bunkoczi, G., Chen, V.B., Davis, I.W., Echols, N., Headd, J.J., Hung, L.W., Kapral, G.J., Grosse-Kunstleve, R.W., et al. (2010). PHENIX: a comprehensive Python-based system for macromolecular structure solution. Acta Crystallogr. D Biol. Crystallogr. *66*, 213-221.

Ashkenazy, H., Abadi, S., Martz, E., Chay, O., Mayrose, I., Pupko, T., and Ben-Tal, N. (2016). ConSurf 2016: an improved methodology to estimate and visualize evolutionary conservation in macromolecules. Nucleic Acids Res. *44*, W344-350.

Autret, S., Nair, R., and Errington, J. (2001). Genetic analysis of the chromosome segregation protein Spo0J of *Bacillus subtilis*: evidence for separate domains involved in DNA binding and interactions with Soj protein. Mol. Microbiol. *41*, 743-755.

Badrinarayanan, A., Le, T.B., and Laub, M.T. (2015). Bacterial chromosome organization and segregation. Annu. Rev. Cell Dev. Biol. *31*, 171-199.

Bange, G., and Sinning, I. (2013). SIMIBI twins in protein targeting and localization. Nat. Struct. Mol. Biol. *20*, 776-780.

Bartosik, A.A., Lasocki, K., Mierzejewska, J., Thomas, C.M., and Jagura-Burdzy, G. (2004). ParB of *Pseudomonas aeruginosa*: interactions with its partner ParA and its target *parS* and specific effects on bacterial growth. J. Bacteriol. *186*, 6983-6998.

Basu, M.K., and Koonin, E.V. (2005). Evolution of eukaryotic cysteine sulfinic acid reductase, sulfiredoxin (Srx), from bacterial chromosome partitioning protein ParB. Cell Cycle *4*, 947-952.

Bouet, J.Y., and Funnell, B.E. (1999). P1 ParA interacts with the P1 partition complex at parS and an ATP-ADP switch controls ParA activities. EMBO J. *18*, 1415-1424.

Bourne, H.R., Sanders, D.A., and McCormick, F. (1990). The GTPase superfamily: a conserved switch for diverse cell functions. Nature *348*, 125-132.

Breier, A.M., and Grossman, A.D. (2007). Whole-genome analysis of the chromosome partitioning and sporulation protein Spo0J (ParB) reveals spreading and origin-distal sites on the *Bacillus subtilis* chromosome. Mol. Microbiol. *64*, 703-718.

Broedersz, C.P., Wang, X., Meir, Y., Loparo, J.J., Rudner, D.Z., and Wingreen, N.S. (2014). Condensation and localization of the partitioning protein ParB on the bacterial chromosome. Proc. Natl. Acad. Sci. U S A *111*, 8809-8814.

Buckstein, M.H., He, J., and Rubin, H. (2008). Characterization of nucleotide pools as a function of physiological state in *Escherichia coli*. J. Bacteriol. *190*, 718-726.

Bulyha, I., Lindow, S., Lin, L., Bolte, K., Wuichet, K., Kahnt, J., van der Does, C., Thanbichler, M., and Søgaard-Andersen, L. (2013). Two small GTPases act in concert with the bactofilin cytoskeleton to regulate dynamic bacterial cell polarity. Dev. Cell *25*, 119-131.

Chang, T.S., Jeong, W., Woo, H.A., Lee, S.M., Park, S., and Rhee, S.G. (2004). Characterization of mammalian sulfiredoxin and its reactivation of hyperoxidized peroxiredoxin through reduction of cysteine sulfinic acid in the active site to cysteine. J. Biol. Chem. *279*, 50994-51001.

Chen, B.W., Lin, M.H., Chu, C.H., Hsu, C.E., and Sun, Y.J. (2015). Insights into ParB spreading from the complex structure of Spo0J and *parS*. Proc. Natl. Acad. Sci. U S A *112*, 6613-6618.

Debaugny, R.E., Sanchez, A., Rech, J., Labourdette, D., Dorignac, J., Geniet, F., Palmeri, J., Parmeggiani, A., Boudsocq, F., Anton Leberre, V., et al. (2018). A conserved mechanism drives partition complex assembly on bacterial chromosomes and plasmids. Mol. Syst. Biol. *14*, e8516.

El-Gebali, S., Mistry, J., Bateman, A., Eddy, S.R., Luciani, A., Potter, S.C., Qureshi, M., Richardson, L.J., Salazar, G.A., Smart, A., et al. (2019). The Pfam protein families database in 2019. Nucleic Acids Res. *47*, D427-D432.

Emsley, P., and Cowtan, K. (2004). Coot: model-building tools for molecular graphics. Acta Crystallogr. D Biol. Crystallogr. *60*, 2126-2132.

Figge, R.M., Easter, J., and Gober, J.W. (2003). Productive interaction between the chromosome partitioning proteins, ParA and ParB, is required for the progression of the cell cycle in *Caulobacter crescentus*. Mol. Microbiol. *47*, 1225-1237.

Fisher, G.L., Pastrana, C.L., Higman, V.A., Koh, A., Taylor, J.A., Butterer, A., Craggs, T., Sobott, F., Murray, H., Crump, M.P., et al. (2017). The structural basis for dynamic DNA binding and bridging interactions which condense the bacterial centromere. Elife *6*, e28086.

Flot, D., Mairs, T., Giraud, T., Guijarro, M., Lesourd, M., Rey, V., van Brussel, D., Morawe, C., Borel, C., Hignette, O., et al. (2010). The ID23-2 structural biology microfocus beamline at the ESRF. J. Synchrotron Radiat. *17*, 107-118.

Fogel, M.A., and Waldor, M.K. (2006). A dynamic, mitotic-like mechanism for bacterial chromosome segregation. Genes Dev. *20*, 3269-3282.

Funnell, B.E. (2016). ParB partition proteins: complex formation and spreading at bacterial and plasmid centromeres. Front Mol. Biosci. *3*, 44.

Gasper, R., Meyer, S., Gotthardt, K., Sirajuddin, M., and Wittinghofer, A. (2009). It takes two to tango: regulation of G proteins by dimerization. Nat. Rev. Mol. Cell Biol. *10*, 423-429.

Geromanos, S.J., Vissers, J.P., Silva, J.C., Dorschel, C.A., Li, G.Z., Gorenstein, M.V., Bateman, R.H., and Langridge, J.I. (2009). The detection, correlation, and comparison of peptide precursor and product ions from data independent LC-MS with data dependant LC-MS/MS. Proteomics *9*, 1683-1695.

Gómez-Santos, N., Treuner-Lange, A., Moraleda-Muñoz, A., García-Bravo, E., García-Hernández, R., Martínez-Cayuela, M., Pérez, J., Søgaard-Andersen, L., and Muñoz-Dorado, J. (2012) Comprehensive set of integrative plasmid vectors for copper-inducible gene expression in *Myxococcus xanthus*. Appl. Environ. Microbiol. *78*, 2515-2521.

Graham, T.G., Wang, X., Song, D., Etson, C.M., van Oijen, A.M., Rudner, D.Z., and Loparo, J.J. (2014). ParB spreading requires DNA bridging. Genes Dev. *28*, 1228-1238.

Gruber, S., and Errington, J. (2009). Recruitment of condensin to replication origin regions by ParB/Spo0J promotes chromosome segregation in *B. subtilis*. Cell *137*, 685-696.

Hanai, R., Liu, R., Benedetti, P., Caron, P.R., Lynch, A.S., and Wang, J.C. (1996). Molecular dissection of a protein SopB essential for *Escherichia coli* F plasmid partition. J. Biol. Chem. *271*, 17469-17475.

Harms, A., Treuner-Lange, A., Schumacher, D., and Søgaard-Andersen, L. (2013). Tracking of chromosome and replisome dynamics in *Myxococcus xanthus* reveals a novel chromosome arrangement. PLoS Genet. *9*, e1003802.

Hartmann, R., van Teeseling, M.C.S., Thanbichler, M., and Drescher, K. (2018). BacStalk: a comprehensive and interactive image analysis software tool for bacterial cell biology. bioarXiv, doi: 10.1101/360230.

Hodgkin, J., and Kaiser, D. (1977). Cell-to-cell stimulation of movement in nonmotile mutants of *Myxococcus*. Proc. Natl. Acad. Sci. U S A *74*, 2938-2942.

Ingerman, E., and Nunnari, J. (2005). A continuous, regenerative coupled GTPase assay for dynamin-related proteins. Methods Enzymol. *404*, 611-619.

Iniesta, A.A., Garcia-Heras, F., Abellon-Ruiz, J., Gallego-Garcia, A., and Elias-Arnanz, M. (2012). Two systems for conditional gene expression in *Myxococcus xanthus* inducible by isopropyl-b-D-thiogalactopyranoside or vanillate. J. Bacteriol. *194*, 5875-5885.

Jakovljevic, V., Leonardy, S., Hoppert, M., and Søgaard-Andersen, L. (2008). PilB and PilT are ATPases acting antagonistically in type IV pilus function in *Myxococcus xanthus*. J. Bacteriol. *190*, 2411-2421.

Jönsson, T.J., Murray, M.S., Johnson, L.C., and Lowther, W.T. (2008). Reduction of cysteine sulfinic acid in peroxiredoxin by sulfiredoxin proceeds directly through a sulfinic phosphoryl ester intermediate. J. Biol. Chem. *283*, 23846-23851.

Kabsch, W. (2010). XDS. Acta Crystallogr. D Biol. Crystallogr. *66*, 125-132.

Kaiser, D. (1979) Social gliding is correlated with the presence of pili in *Myxococcus xanthus*. Proc. Natl. Acad. Sci. U S A *76*, 5952-5956.

Kashefi, K., and Hartzell, P.L. (1995). Genetic suppression and phenotypic masking of a *Myxococcus xanthus frzF*$^-$ defect. Mol. Microbiol. *15*, 483-494.

Kiianitsa, K., Solinger, J.A., and Heyer, W.D. (2003). NADH-coupled microplate photometric assay for kinetic studies of ATP-hydrolyzing enzymes with low and high specific activities. Anal. Biochem *321*, 266-271.

Konermann, L., Pan, J., and Liu, Y.H. (2011). Hydrogen exchange mass spectrometry for studying protein structure and dynamics. Chem. Soc. Rev. *40*, 1224-1234.

Kusiak, M., Gapczynska, A., Plochocka, D., Thomas, C.M., and Jagura-Burdzy, G. (2011). Binding and spreading of ParB on DNA determine its biological function in *Pseudomonas aeruginosa*. J. Bacteriol. *193*, 3342-3355.

Leonard, T.A., Butler, P.J., and Löwe, J. (2004). Structural analysis of the chromosome segregation protein Spo0J from *Thermus thermophilus*. Mol. Microbiol. *53*, 419-432.

Li, G.Z., Vissers, J.P., Silva, J.C., Golick, D., Gorenstein, M.V., and Geromanos, S.J. (2009). Database searching and accounting of multiplexed precursor and product ion spectra from the data independent analysis of simple and complex peptide mixtures. Proteomics *9*, 1696-1719.

Liebschner, D., Afonine, P.V., Baker, M.L., Bunkóczi, G., Chen, V.B., Croll, T.I., Hintze, B., Hung, L.W., Jain, S., McCoy, A.J., Moriarty, N.W., Oeffner, R.D., Poon, B.K., Prisant, M.G., Read, R.J., Richardson, J.S., Richardson, D.C., Sammito, M.D., Sobolev, O.V., Stockwell, D.H., Terwilliger, T.C., Urzhumtsev, A.G., Videau, L.L., Williams, C.J., and Adams, P.D. (2019). Macromolecular structure determination using X-rays, neutrons and electrons: recent developments in Phenix. Acta Crystallogr. D Struct. Biol. *75*, 861-877.

Lim, H.C., Surovtsev, I.V., Beltran, B.G., Huang, F., Bewersdorf, J., and Jacobs-Wagner, C. (2014). Evidence for a DNA-relay mechanism in ParABS-mediated chromosome segregation. Elife *3*, e02758.

Lin, D.C., and Grossman, A.D. (1998). Identification and characterization of a bacterial chromosome partitioning site. Cell *92*, 675-685.

Lin, L., Osorio Valeriano, M., Harms, A., Søgaard-Andersen, L., and Thanbichler, M. (2017). Bactofilin-mediated organization of the ParABS chromosome segregation system in *Myxococcus xanthus*. Nat. Commun. *8*, 1817.

Lynch, A.S., and Wang, J.C. (1995). SopB protein-mediated silencing of genes linked to the *sopC* locus of *Escherichia coli* F plasmid. Proc. Natl. Acad. Sci. U S A *92*, 1896-1900.

Magrini, V., Creighton, C., and Youderian, P. (1999). Site-specific recombination of temperate *Myxococcus xanthus* phage Mx8: genetic elements required for integration. J. Bacteriol. *181*, 4050-4061.

Maindola, P., Raina, R., Goyal, P., Atmakuri, K., Ojha, A., Gupta, S., Christie, P.J., Iyer, L.M., Aravind, L., and Arockiasamy, A. (2014). Multiple enzymatic activities of ParB/Srx superfamily mediate sexual conflict among conjugative plasmids. Nat. Commun. *5*, 5322.

Makino, Y., Sato, T., Kawamura, H., Hachisuka, S.I., Takeno, R., Imanaka, T., and Atomi, H. (2016). An archaeal ADP-dependent serine kinase involved in cysteine biosynthesis and serine metabolism. Nat. Commun. *7*, 13446.

Meiresonne, N.Y., Consoli, E., Mertens, L.M.Y., Chertkova, A.O., Goedhart, J., and den Blaauwen, T. (2019) Superfolder mTurquoise2^{ox} optimized for the bacterial periplasm allows high efficiency *in vivo* FRET of cell division antibiotic targets. Mol. Microbiol. *111*, 1025-1038.

Minnen, A., Attaiech, L., Thon, M., Gruber, S., and Veening, J.W. (2011). SMC is recruited to *oriC* by ParB and promotes chromosome segregation in *Streptococcus pneumoniae*. Mol. Microbiol. *81*, 676-688.

Mohl, D.A., and Gober, J.W. (1997). Cell cycle-dependent polar localization of chromosome partitioning proteins in *Caulobacter crescentus*. Cell *88*, 675-684.

Murray, H., Ferreira, H., and Errington, J. (2006). The bacterial chromosome segregation protein Spo0J spreads along DNA from *parS* nucleation sites. Mol. Microbiol. *61*, 1352-1361.

Nagata, R., Fujihashi, M., Kawamura, H., Sato, T., Fujita, T., Atomi, H., and Miki, K. (2017). Structural study on the reaction mechanism of a free serine kinase involved in cysteine biosynthesis. ACS Chem. Biol. *12*, 1514-1523.

Nurizzo, D., Mairs, T., Guijarro, M., Rey, V., Meyer, J., Fajardo, P., Chavanne, J., Biasci, J.C., McSweeney, S., and Mitchell, E. (2006). The ID23-1 structural biology beamline at the ESRF. J. Synchrotron Radiat. *13*, 227-238.

Pausch, P., Singh, U., Ahmed, Y.L., Pillet, B., Murat, G., Altegoer, F., Stier, G., Thoms, M., Hurt, E., Sinning, I., et al. (2015). Co-translational capturing of nascent ribosomal proteins by their dedicated chaperones. Nat. Commun. *6*, 7494.

Radnedge, L., Youngren, B., Davis, M., and Austin, S. (1998). Probing the structure of complex macromolecular interactions by homolog specificity scanning: the P1 and P7 plasmid partition systems. EMBO J. *17*, 6076-6085.

Rhee, S.G., Woo, H.A., Kil, I.S., and Bae, S.H. (2012). Peroxiredoxin functions as a peroxidase and a regulator and sensor of local peroxides. J. Biol. Chem. *287*, 4403-4410.

Ringgaard, S., van Zon, J., Howard, M., and Gerdes, K. (2009). Movement and equipositioning of plasmids by ParA filament disassembly. Proc. Natl. Acad. Sci. U S A *106*, 19369-19374.

Rodionov, O., Lobocka, M., and Yarmolinsky, M. (1999). Silencing of genes flanking the P1 plasmid centromere. Science *283*, 546-549.

Sanchez, A., Cattoni, D.I., Walter, J.C., Rech, J., Parmeggiani, A., Nollmann, M., and Bouet, J.Y. (2015). Stochastic self-assembly of ParB proteins builds the bacterial DNA segregation apparatus. Cell Syst. *1*, 163-173.

Schumacher, D., and Søgaard-Andersen, L. (2018). Fluorescence live-cell imaging of the complete vegetative cell cycle of the slow-growing social bacterium *Myxococcus xanthus*. J. Vis. Exp. *136*, e57860.

Schumacher, M.A., Piro, K.M., and Xu, W. (2010). Insight into F plasmid DNA segregation revealed by structures of SopB and SopB-DNA complexes. Nucleic Acids Res. *38*, 4514-4526.

Schumacher, M.A., Tonthat, N.K., Lee, J., Rodriguez-Castaneda, F.A., Chinnam, N.B., Kalliomaa-Sanford, A.K., Ng, I.W., Barge, M.T., Shaw, P.L., and Barilla, D. (2015). Structures of archaeal DNA segregation machinery reveal bacterial and eukaryotic linkages. Science *349*, 1120-1124.

Shaw, N., Tempel, W., Chang, J., Yang, H., Cheng, C., Ng, J., Rose, J., Rao, Z., Wang, B.C., and Liu, Z.J. (2008). Crystal structure solution of a ParB-like nuclease at atomic resolution. Proteins *70*, 263-267.

Sievers, F., and Higgins, D.G. (2018). Clustal Omega for making accurate alignments of many protein sequences. Protein Sci *27*, 135-145.

Song, D., Rodrigues, K., Graham, T.G.W., and Loparo, J.J. (2017). A network of *cis* and *trans* interactions is required for ParB spreading. Nucleic Acids Res. *45*, 7106-7117.

Sullivan, N.L., Marquis, K.A., and Rudner, D.Z. (2009). Recruitment of SMC by ParB-*parS* organizes the origin region and promotes efficient chromosome segregation. Cell *137*, 697-707.

Surtees, J.A., and Funnell, B.E. (1999). P1 ParB domain structure includes two independent multimerization domains. J. Bacteriol. *181*, 5898-5908.

Surtees, J.A., and Funnell, B.E. (2001). The DNA binding domains of P1 ParB and the architecture of the P1 plasmid partition complex. J. Biol. Chem. *276*, 12385-12394.

Taylor, J.A., Pastrana, C.L., Butterer, A., Pernstich, C., Gwynn, E.J., Sobott, F., Moreno-Herrero, F., and Dillingham, M.S. (2015). Specific and non-specific interactions of ParB with DNA: implications for chromosome segregation. Nucleic Acids Res. *43*, 719-731.

Thanbichler, M., Iniesta, A.A., and Shapiro, L. (2007). A comprehensive set of plasmids for vanillate- and xylose-inducible gene expression in *Caulobacter crescentus*. Nucleic Acids Res. *35*, e137.

Tran, N.T., Laub, M.T., and Le, T.B.K. (2017) SMC progressively aligns chromosomal arms in *Caulobacter crescentus* but Is antagonized by convergent transcription. Cell Rep. *20*, 2057-2071.

Tran, N.T., Stevenson, C.E., Som, N.F., Thanapipatsiri, A., Jalal, A.S.B., and Le, T.B.K. (2018). Permissive zones for the centromere-binding protein ParB on the *Caulobacter crescentus* chromosome. Nucleic Acids Res. *46*, 1196-1209.

Ueki, T., Inouye, S., and Inouye, M. (1996). Positive-negative KG cassettes for construction of multi-gene deletions using a single drug marker. Gene *183*, 153-157.

Vecchiarelli, A.G., Neuman, K.C., and Mizuuchi, K. (2014). A propagating ATPase gradient drives transport of surface-confined cellular cargo. Proc. Natl. Acad. Sci. U S A *111*, 4880-4885.

Volante, A., and Alonso, J.C. (2015). Molecular anatomy of ParA-ParA and ParA-ParB interactions during plasmid partitioning. J. Biol. Chem. *290*, 18782-18795.

Volkov, A., Mascarenhas, J., Andrei-Selmer, C., Ulrich, H.D., and Graumann, P.L. (2003). A prokaryotic condensin/cohesin-like complex can actively compact chromosomes from a single position on the nucleoid and binds to DNA as a ring-like structure. Mol. Cell Biol. *23*, 5638-5650.

Wales, T.E., Fadgen, K.E., Gerhardt, G.C., and Engen, J.R. (2008). High-speed and high-resolution UPLC separation at zero degrees Celsius. Anal. Chem. *80*, 6815-6820.

Wallace, A.C., Laskowski, R.A., and Thornton, J.M. (1995). LIGPLOT: a program to generate schematic diagrams of protein-ligand interactions. Protein Eng. *8*, 127-134.

Wang, X., Brandao, H.B., Le, T.B., Laub, M.T., and Rudner, D.Z. (2017). *Bacillus subtilis* SMC complexes juxtapose chromosome arms as they travel from origin to terminus. Science *355*, 524-527.

Waterhouse, A.M., Procter, J.B., Martin, D.M., Clamp, M., and Barton, G.J. (2009) Jalview Version 2 – a multiple sequence alignment editor and analysis workbench. Bioinformatics *25*, 1189-1191.

Whitmore, L., and Wallace, B.A. (2004). DICHROWEB, an online server for protein secondary structure analyses from circular dichroism spectroscopic data. Nucleic Acids Res. *32*, W668-673.

Winn, M.D, Ballard, C.C., Cowtan, K.D., Dodson, E.J., Emsley, P., Evans, P.R., Keegan, R.M., Krissinel, E.B., Leslie, A.G., McCoy, A., McNicholas, S.J., Murshudov, G.N., Pannu, N.S., Potterton, E.A., Powell, H.R., Read, R.J., Vagin, A., and Wilson, K.S. (2011). Overview of the CCP4 suite and current developments. Acta Crystallogr. D Biol. Crystallogr. *67*, 235-242.

Yamaichi, Y., and Niki, H. (2000). Active segregation by the *Bacillus subtilis* partitioning system in *Escherichia coli*. Proc. Natl. Acad. Sci. U S A *97*, 14656-14661.

Chapter IV:

A gradient-forming MipZ protein mediating the control of cell division in the magnetotactic bacterium *Magnetospirillum gryphiswaldense*

Mauricio Toro-Nahuelpan[a,b,#,‡], Laura Corrales-Guerrero[c,‡], Theresa Zwiener[a], Manuel Osorio-Valeriano[c,d], Frank-Dietrich Müller[a], Jürgen M. Plitzko[b], Marc Bramkamp[e], Martin Thanbichler[c,d,f,*] and Dirk Schüler[a,*]

This chapter is written in manuscript style and was published in *Molecular Microbiology* in November 2019. My contribution to this work included purifying all the proteins and performing the biochemical experiments together with L.C.-G.

[a] Institute of Microbiology, University of Bayreuth, Bayreuth, Germany
[b] Department of Molecular Structural Biology, Max Planck Institute of Biochemistry, Planegg-Martinsried, Germany
[c] Faculty of Biology, Philipps-Universität, Marburg, Germany
[d] Max Planck Institute for Terrestrial Microbiology, Marburg, Germany
[e] Department of Biology I, Ludwig-Maximilians-Universität München, Planegg-Martinsried, Germany
[f] LOEWE Center for Synthetic Microbiology, Marburg, Germany

[#] Present address: European Molecular Biology Laboratory, Heidelberg, Germany.
[‡] M.T.-N. and L.C.-G. contributed equally to this work.
*Address correspondence to
Dirk Schüler, dirk.schueler@uni-bayreuth.de
Martin Thanbichler, thanbichler@uni-marburg.de

ABSTRACT

Cell division needs to be tightly regulated and closely coordinated with other cellular processes to ensure the generation of fully viable offspring. Here, we investigate division site placement by the cell division regulator MipZ in the alphaproteobacterium *Magnetospirillum gryphiswaldense*, a species that forms linear chains of magnetosomes to navigate within the geomagnetic field. We show that *M. gryphiswaldense* contains two MipZ homologs, termed MipZ1 and MipZ2. MipZ2 localizes to the division site, but its absence does not cause any obvious phenotype. MipZ1, by contrast, forms a dynamic bipolar gradient, and its deletion or overproduction cause cell filamentation, suggesting an important role in cell division. The monomeric form of MipZ1 interacts with the chromosome partitioning protein ParB, whereas its ATP-dependent dimeric form shows non-specific DNA-binding activity. Notably, both the dimeric and, to a lesser extent, the monomeric form inhibit FtsZ polymerization *in vitro*. MipZ1 thus represents a canonical gradient-forming MipZ homolog that critically contributes to the spatiotemporal control of FtsZ ring formation. Collectively, our findings add to the view that the regulatory role of MipZ proteins in cell division is conserved among many alphaproteobacteria. However, their number and biochemical properties may have adapted to the specific needs of the host organism.

ABBREVIATED SUMMARY

MipZ homologs have been identified as regulators of cell division in alphaproteobacteria, but their functional conservation and distribution among species are still poorly investigated. Here, we show that *Magnetosprillum gryphiswaldense* contains two MipZ paralogs with distinct localization patterns and functions. One of them emerges as a gradient-forming protein with a critical role in division site placement, supporting the idea that MipZ-like cell division regulators are widespread in the alpha-proteobacterial lineage, although their modes of action may have diverged.

INTRODUCTION

Magnetotactic bacteria are a diverse group of organisms that have the ability to align along the geomagnetic field lines. This property is mediated by chains of membrane-bounded magnetic crystals, known as magnetosomes, which act as nanoscale compass needles (Uebe *et al.*, 2016). In the alpha-proteobacterium *Magnetospirillum gryphiswaldense* as well as related magnetospirilla, magnetosomes are concatenated into a highly ordered linear array (Uebe *et al.*, 2016). Their formation is mediated by dedicated cytoskeletal elements, termed the "magnetoskeleton", which comprises the actin-like MamK filament, the adapter protein MamJ and the localization factor MamY (Komeili *et al.*, 2006; Scheffel *et al.*, 2006; Toro-Nahuelpan *et al.*, 2016; Toro-Nahuelpan *et al.*, 2019). Throughout the cell cycle of *M. gryphiswaldense*, the magnetosome chain is oriented parallel to the long axis of the spirilloid cell, with the chain center positioned dynamically at midcell (Katzmann *et al.*, 2011; Toro-Nahuelpan *et al.*, 2016; Uebe *et al.*, 2016). During cell division, the magnetosome chain becomes equipartitioned to efficiently pass on the selective advantage of magnetotaxis to both daughter cells (Katzmann *et al.*, 2011). Once cytokinesis is finished, the partitioned chains are repositioned from the new cell poles to the cell center by the pole-to-midcell-directed treadmilling of MamK filaments (Katzmann *et al.*, 2011; Toro-Nahuelpan *et al.*, 2016). The formation and splitting of magnetosome chains need to be closely coordinated with cell division in time and space. However, so far, the mechanisms that control the division process in *M. gryphiswaldense* remain poorly understood.

In most bacteria, the site of cell division is marked by a discontinuous ring-like polymeric assembly of the tubulin homolog FtsZ (Bi and Lutkenhaus, 1991; Ben-Yehuda and Losick, 2002; Li *et al*., 2007). This so-called Z-ring recruits, directly and indirectly, all other components of the cell division apparatus and plays a central regulatory role in the constriction process (Erickson *et al.*, 2010; Bisson-Filho *et al.*, 2017; Yang *et al.*, 2017). Unlike most other bacteria, *M. gryphiswaldense* possesses two FtsZ homologs: a canonical FtsZ and a C-terminally truncated variant termed FtsZm. Previous studies have shown that the canonical FtsZ homolog plays an essential role in cell division (Ding *et al.*, 2010; Müller *et al.*, 2014). Furthermore, cryo-electron tomography (cryo-ET) analysis of the cell division site of *M. gryphiswaldense* revealed arc-like structures that may represent a discontinuous Z-ring driving the typical asymmetric constriction of this species (Katzmann *et al.*, 2011; Yao *et al.*, 2017). Similar to the canonical FtsZ protein, its paralog FtsZm shows GTPase activity, and it is able to form homo- and heteropolymers with FtsZ *in vitro*. However, FtsZm does not appear to be involved in cell division but rather has a role in magnetosome biomineralization, consistent with the fact that its gene is located within a magnetosome-related operon (Ding *et al.*, 2010; Müller *et al.*, 2014).

To ensure proper cell division, Z-ring formation needs to be tightly regulated in time and space. In many bacteria, this task is achieved by the prototypical Min and nucleoid occlusion systems, which prevent the polymerization of FtsZ at the cell poles or over the nucleoid, respectively (Marston *et al.*, 1998; Raskin and de Boer, 1999; Wu and Errington, 2004; Bernhardt and de Boer, 2005; Lutkenhaus, 2007; Wu and Errington, 2011). However, these systems are poorly conserved among the *Alpha-proteobacteria*. Min proteins, for instance, are only found in some members of the orders *Rhizobiales*, *Rhodobacterales* and *Rhodospirillales* (Flores *et al.*, 2018), suggesting the existence of other mechanisms to control cell division in the alphaproteobacterial lineage.

An alternative cell division regulator identified in the *Alphaproteobacteria* is the protein MipZ from *Caulobacter crescentus*. MipZ is a P-loop ATPase that forms a bipolar gradient, with concentration maxima at the cell poles and a minimum at the cell center (Thanbichler and Shapiro, 2006). It acts as an inhibitor of FtsZ polymerization and thus prevents Z-ring assembly in the polar regions of the cell, thereby limiting cell division to the cell center. Loss of MipZ triggers the formation of multiple mispositioned FtsZ assemblies that initiate acentric cell division events, producing a mixture of elongated and mini cells (Thanbichler and Shapiro, 2006). The function of MipZ relies on its interaction with the nucleoid and the DNA partitioning protein ParB, which recognizes a cluster of specific binding sites (*parS*) in the chromosomal origin region (Thanbichler and Shapiro, 2006; Kiekebusch *et al.*, 2012). After entry of the cells into S-phase, the two sister origin regions of *C. crescentus* re-associate with ParB and then become immobilized at opposite cell poles. The polar ParB•*parS* complexes interact with freely diffusible MipZ monomers and induce their ATP-dependent dimerization. The resulting dimers dissociate from ParB and bind non-specifically to the surrounding chromosomal DNA, where they inhibit Z-ring assembly. Spontaneous ATP hydrolysis then triggers their disassembly into monomers, which leave the DNA and finally re-associate with ParB at the cell poles, starting a new localization cycle (Thanbichler and Shapiro, 2006; Kiekebusch *et al.*, 2012).

Remarkably, in the alphaproteobacterium *Rhodobacter sphaeroides*, MipZ shows a very different behavior. While its monomeric form dynamically interacts with the cell pole-associated ParB•*parS* complexes, dimers consistently colocalize with FtsZ, forming an annular structure that lines the inner side of the Z-ring throughout the constriction process. The recruitment of the protein to midcell depends on the presence of FtsZ, and its overproduction leads to cell filamentation and the formation of mini cells. These findings suggest that *R. sphaeroides* MipZ represents a second class of MipZ proteins that may control the stability or dynamics rather than the subcellular localization of the Z-ring. Although MipZ proteins are conserved in the majority of alphaproteobacteria, it is currently unknown whether they belong to any of the two previously identified classes or have adopted different roles in cell division.

In this study, we identify two MipZ homologs in *M. gryphiswaldense*. We show that the loss or over-production of MipZ1 lead to a severe impairment of cell division. Live-cell imaging and photokinetic analyses reveal that MipZ1 uses ATP binding and hydrolysis to establish a highly dynamic, bipolar gradient. Gradient formation depends on the interaction of MipZ1 with ParB and its non-specific association with chromosomal DNA. Importantly, MipZ1 stimulates the GTPase activity of FtsZ and abolishes FtsZ polymerization *in vitro*. It therefore appears to act as a critical negative regulator of cell division that coordinates cell division with chromosome segregation in *M. gryphiswaldense*. MipZ2, by contrast, colocalizes with FtsZ throughout the course of the cell cycle, but its inactivation does not cause any obvious phenotype, suggesting an accessory role in the division process. Collectively, our results demonstrate that *M. gryphiswaldense* employs two functional MipZ homologs. Moreover, they support the idea that the regulatory role of MipZ proteins in cell division is conserved among alphaproteobacteria, although their mechanism of action and importance may vary between species.

RESULTS

MipZ1, but not MipZ2, is critical for proper cell division in *M. gryphiswaldense*

Searching the genomic sequence of *M. gryphiswaldense* for potential cell division regulators, we were unable to detect a Min system or homologs of known nucleoid occlusion proteins. However, we identified two *mipZ*-like genes (locus tags MGR_4222 and MGR_0570), which encode genuine members of the MipZ subfamily of the Mrp/MinD ATPases (Figure S1A). MipZ1 (MGR_4222) and MipZ2 (MGR_0570) exhibit 46% and 43% sequence identity (65% and 64% similarity), respectively, to MipZ from *C. crescentus* ($MipZ_{Cc}$) (Figure S1B). Moreover, the two proteins share 45% identity (63% similarity) with each other. Modeling studies with the crystal structure of $MipZ_{Cc}$ (Kiekebusch *et al.*, 2012) as a template suggested a high structural similarity of the MipZ homologs from *M. gryphiswaldense* to $MipZ_{Cc}$, with root-mean-square deviation (rmsd) values of 0.62 Å (239 atoms) for MipZ1 and 0.62 Å (225 atoms) for MipZ2 (Figure S1C). The predicted structures of MipZ1 and MipZ2 were almost superimposable, with a rmsd of 0.43 Å (224 atoms).

To address the role of the two MipZ homologs, we first generated an *M. gryphiswaldense* strain bearing an in-frame deletion of the *mipZ1* gene. Reminiscent of the Δ*mipZ* phenotype observed for *C. crescentus* (Thanbichler and Shapiro, 2006) and *Brevundimonas subvibrioides* (Curtis and Brun, 2014), the mutation lead to the formation of highly elongated cells (Figure 1Ai-iii and B), indicating that MipZ1 is required for the correct timing and/or spatial regulation of cell division. In both filamentous and normal-sized Δ*mipZ1* cells, magnetosome chains appeared to be properly positioned at midcell (Figure 1Ai-ii) and evenly partitioned to the daughter cells (Figure 1Aiii). Time-lapse analysis confirmed that the mutant formed elongated cells that divided only sporadically and in a highly asymmetric fashion, producing filamentous cells of variable length (Figure 1C). In the wild type, by contrast, cell division consistently occurred around midcell and thus resulted in daughter cells of approximately equal size (Figure 1D), in agreement with previous results (Katzmann *et al.*, 2011). Notably, the cell division defect of the Δ*mipZ1* mutant was accompanied by a significant increase in its doubling time (5.4 ± 0.3 h as compared to 4.1 ± 0.1 h for the wild-type strain; average of three growth curves; ± SD). To further characterize the mutant phenotype, we imaged the constriction site of dividing Δ*mipZ1* filaments by cryo-electron tomography. 3D rendering of specific subcellular structures revealed the characteristic unidirectional invagination of the cell envelope described previously for *M. gryphiswaldense* (Katzmann *et al.*, 2011; Toro-Nahuelpan *et al.*, 2016), with the magnetosome chain centered at midcell (Figures 1E and S2A-E, Movie S1). Thus, the cell division defect observed is likely due to an abnormal spatiotemporal regulation of divisome assembly rather than a block in the division process itself.

To determine how MipZ1 can affect the regulation of cell division, we tagged the protein with the red fluorescent protein mCherry and determined its subcellular localization by fluorescence microscopy. Interestingly, in pre-divisional cells, the fusion formed a bipolar gradient, with the signal intensities peaking at the cell poles and gradually decreasing towards the cell center (Figure 1F), reminiscent of the pattern observed for the *C. crescentus* MipZ homolog (Thanbichler and Shapiro, 2006). Upon overproduction of the fusion protein, gradient formation was abolished and mCherry-MipZ1 was evenly distributed throughout the cell (Figure 1G). Under these conditions, the cells were markedly elongated (Figure 1H) and failed to form constrictions. However, the recruitment of the magnetosome chain to midcell remained unaffected. These findings suggest that MipZ1 has a negative regulatory effect on cell division.

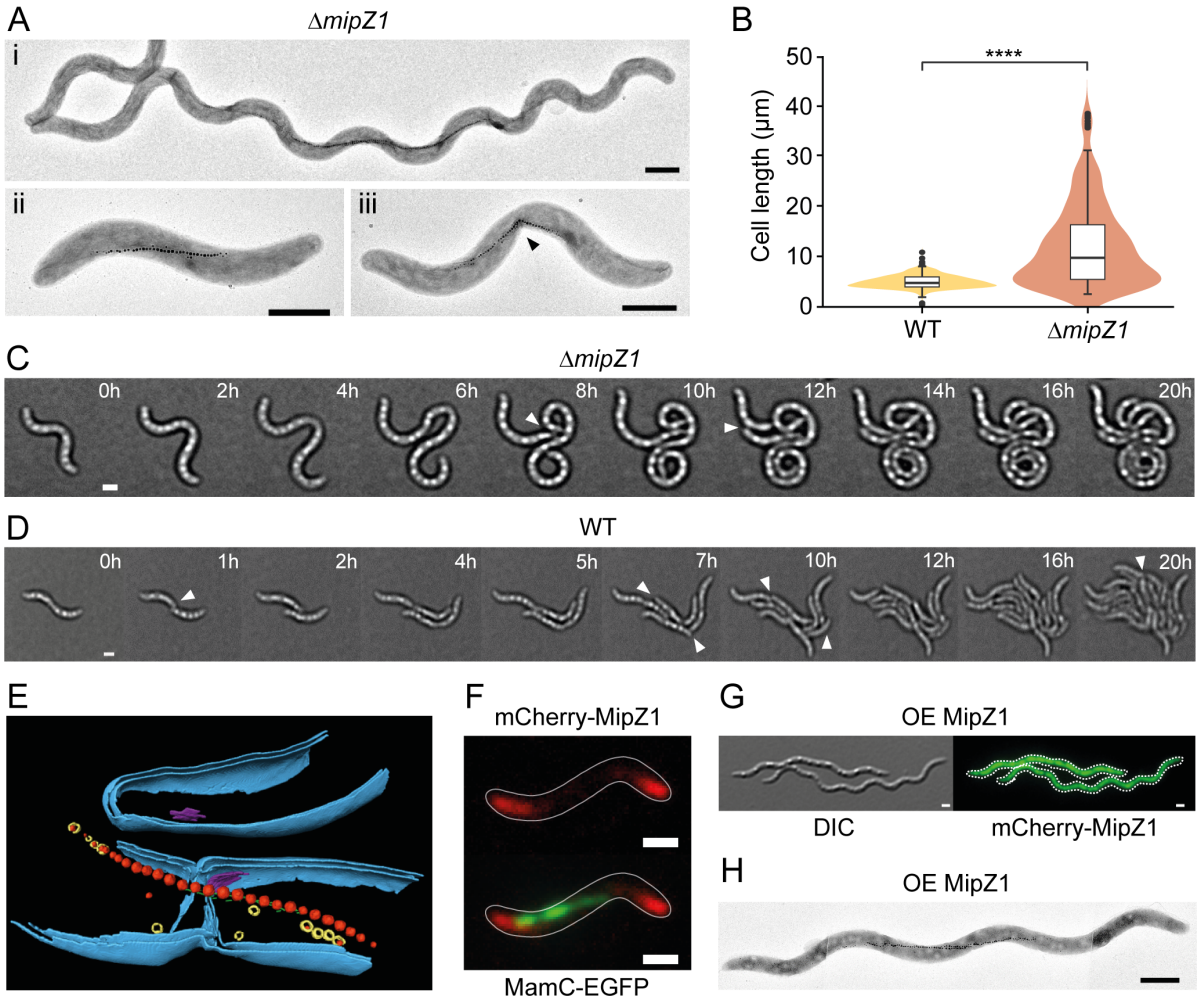

Figure 1. The absence or mislocalization of MipZ1 impairs cell division. (**A**) Transmission electron micrographs of the Δ*mipZ1* mutant (TZ001) showing elongated cells with medial (i-ii) and equally partitioned (iii-black arrowhead) magnetosome chains. (**B**) Cell length distribution of the WT and Δ*mipZ1* strains. The data are represented as box plots, with the thick horizontal line indicating the median, the box the interquartile range, and the whiskers extending to the lowest and highest value within 1.5 times the interquartile range from the hinges, respectively. In addition, rotated kernel density plots (orange) are given for each dataset to indicate the distribution of the data (**** $p < 0.0001$; Student's t-test). n = 522 cells (WT) and 340 cells

(Δ*mipZ1*). (**C,D**) Time-lapse microscopic analysis of the Δ*mipZ1* (C) and WT (D) strains (white arrowheads indicate divided cells). (**E**) 3D surface rendering of cryo-electron tomograms depicting the cell division site in a Δ*mipZ1* cell. Magnetite crystals: red; magnetosome membrane vesicles: yellow; actin-like MamK filament: green; chemoreceptor arrays: purple; inner and outer membrane: blue. (**F**) Subcellular localization of mCherry-MipZ1 and the magnetosome chain (MamC-EGFP) by fluorescence microscopy in strain eMTN023. (**G**) DIC and fluorescence images of a strain (eMTN025) overexpressing the *mipZ1* gene. mCherry fluorescence is depicted in green. (**H**) Transmission electron micrograph of an elongated cell over-producing MipZ1 (composed of 3 stitched micrographs). Scale bars: 1 µm.

Next, we set out to characterize the function of the second MipZ homolog of *M. gryphiswaldense*. Unlike the Δ*mipZ1* mutant, a strain carrying an in-frame deletion of the *mipZ2* gene produced normal-sized cells (Figure 2Ai and B) with a generation time similar to that of the wild type strain (3.9 ± 0.03 h; average of three growth curves). Moreover, time-lapse imaging and TEM analysis did not reveal any apparent defect in cell division or in the positioning and segregation of magnetosome chains (Figure 2Ai-ii, B, and C). Finally, cryo-ET revealed that Δ*mipZ2* cells still displayed the characteristic asymmetric constriction as they underwent cytokinesis (Figures S2F-K and Movie S2), indicating that cell division proceeded normally in this background. Similarly, overproduction of MipZ2 did not affect cell length (4.2 ± 0.9 µm for the wild-type strain compared to 4.4 ± 0.9 µm for a *mipZ2*-overexpressing strain; n=33 cells) or cause any other obvious morphological defects, supporting the notion that this protein has no or only a minor role in the regulation of the division process.

To test whether MipZ1 and MipZ2 have redundant functions, we constructed a strain carrying in-frame deletions in both *mipZ*-like genes. Whole genome sequencing and single nucleotide polymorphism (SNP) analyses verified the absence of suppressor mutations in coding regions. The double mutant formed elongated cells of variable length, essentially phenocopying the Δ*mipZ1* single mutant (Figure 2D). Again, the magnetosome chain was properly localized at the cell center and appeared to be partitioned equally to the daughter cells. Time-lapse imaging showed that filamentous cells formed by the double mutant underwent only sporadic asymmetric division events (Figure 2E), reminiscent of the phenotype observed for Δ*mipZ1* cells. Collectively, these results suggest that only MipZ1 has a critical role in *M. gryphiswaldense* cell division.

To evaluate the subcellular distribution of MipZ2 and correlate its behavior to that of MipZ1, we generated a strain producing both an mCherry-MipZ2 and an eGFP-MipZ1 fusion. We then analyzed the localization patterns of the two proteins in cells at different stages of the cell cycle. In newborn cells, MipZ1 localized to one of the cell poles, whereas MipZ2 was detected at the opposite end of the cell. Intriguingly, MipZ2 also displayed a gradient pattern (Figure 2F). Later in the cell cycle, the MipZ1 focus duplicated and one of the copies moved in direction of the pole occupied by MipZ2 (compare also Figure 5A). Concomitant with the arrival of MipZ1, which now formed a bipolar gradient, most of the MipZ2 population was displaced from its original polar position and localized to midcell, where it

remained until cytokinesis took place. However, in pre-divisional cells, a small fraction of the protein was also detected at the two cell poles (Figure 2F). Thus, both MipZ homologs of *M. gryphiswaldense* show cell cycle-dependent localization dynamics, but their distribution patterns are strikingly different.

We next compared the positioning of MipZ2 to that of FtsZ, using eGFP-MipZ2 and FtsZ-mCherry fusions. In new-born (short) cells, MipZ2 co-localized with FtsZ at one of the poles (Figure 2G). Early in the cell cycle, FtsZ relocated to the cell center where it initially remained poorly focused. This step was followed by the gradual redistribution of MipZ2 to the division site. Notably, a stable FtsZ focus was only detected once MipZ2 has accumulated at midcell, which opens the possibility that MipZ2 could have a stabilizing effect on Z-ring formation. A similar sequence of events was observed when the two fusions were produced in the Δ*mipZ1* Δ*mipZ2* background (Figure S3). However, the Z-ring appeared to form much later in the cell cycle compared to the wild-type strain (Figure S3), likely due to the absence of regulatory effect of MipZ1. Moreover, FtsZ-mCherry fluorescence was rather faint at all stages of the cell cycle. These results further support the notion that MipZ1 is essential for the proper FtsZ localization in *M. gryphiswaldense*.

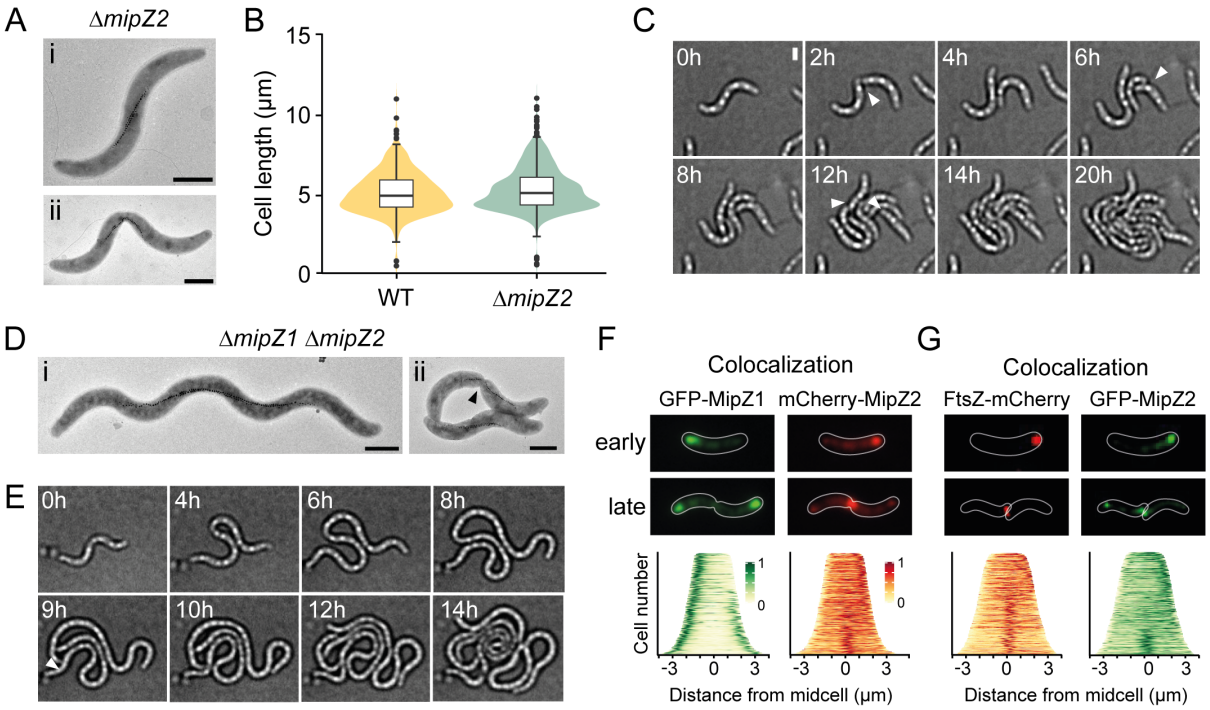

Figure 2. Phenotypes of the Δ*mipZ2* and Δ*mipZ1* Δ*mipZ2* mutants. (**A**) Transmission electron micrographs of the Δ*mipZ2* mutant (MT024) showing WT-like cells with medial magnetosome chains (i) that are evenly segregated upon division (ii). (**B**) Cell length distribution of the WT and Δ*mipZ2* strains. The data are represented as box plots and rotated kernel density plots,

as described in **Figure 1B**. n = 522 cells (WT) and 1021 cells (Δ*mipZ2*). (**C**) Time-lapse microscopic analysis of the Δ*mipZ2* strain (white arrowheads indicate divided cells). (**D**) TEM images of the Δ*mipZ1* Δ*mipZ2* double deletion mutant (TZ003) displaying filamentous and WT-like cells with medial magnetosome chains that are evenly segregated upon division (ii, black arrowhead). (**E**) Time-lapse microscopic analysis of the Δ*mipZ1* Δ*mipZ2* strain (white arrowheads indicate divided cells). Scale bars: 1 µm. (**F**) Subcellular localization of eGFP-MipZ1 and mCherry-MipZ2 (strain FM98). Shown are representative cells at an early and late stage of the cell cycle. The graphs show a demographic analysis of the cells. To generate it, fluorescence intensity profiles obtained from a representative subpopulation of cells (n=251 cells) were normalized, sorted according to cell length, and stacked on top of each other. (**G**) Subcellular localization of eGFP-MipZ2 and FtsZ-mCherry (strain FM100). Shown are representative cells at an early and late stage of the cell cycle. The graphs show a demographic analysis of the cells, generated as described in (F) (n=286 cells).

MipZ1 forms a dynamic gradient that depends on its ATPase activity

The gradient-like pattern observed for mCherry-MipZ1 is likely to be the result of a dynamic process. To obtain insight into the underlying mechanism, we studied the mobility of the fusion protein in the wild-type background using fluorescence-recovery-after-photobleaching (FRAP) analysis. When one of the polar signals was bleached in cells showing a bipolar MipZ1 gradient, fluorescence was recovered with a half-time ($t_{½}$) of ~13 sec (Figure 3A and B), while the intensity of the signal at the opposite pole decreased proportionally. After equilibration, both poles displayed similar signal intensities. The complete equilibration of the fluorescence signal indicates that all MipZ1 molecules were mobile, and rapidly exchanged between the two polar populations. The same dynamics were observed when MipZ1 was produced in a Δ*mipZ1* mutant background, validating the functionality of the mCherry-tagged protein (Figure S4A).

To test for a functional interaction between the two MipZ homologs from *M. gryphiswaldense*, we examined the dynamics of mCherry-MipZ1 in the Δ*mipZ2* mutant background. The behavior of the fusion protein was essentially unchanged under this condition ($t_{½}$ ~11 sec), supporting the notion that MipZ1 and MipZ2 act independently of each other (Figure S4B). To directly visualize and further confirm the rapid exchange of MipZ1 between the two cell poles, we tagged the protein with the green-to-red photoconvertible fluorescent protein Dendra2. Subsequently, one of the cell poles was illuminated with a laser to induce photoconversion, and the redistribution of the newly generated red fluorescent Dendra2-MipZ1 molecules was monitored over time. The photoconverted fusion protein was detected at the opposite pole within only a few seconds after application of the laser pulse. At ~1 min post-photoconversion, the signal intensities at the two poles had reached equilibrium (Figure 3C). This result is in agreement with the kinetics of fluorescence recovery observed in the FRAP experiment and provides direct evidence of an exchange of MipZ1 molecules between the two cell poles.

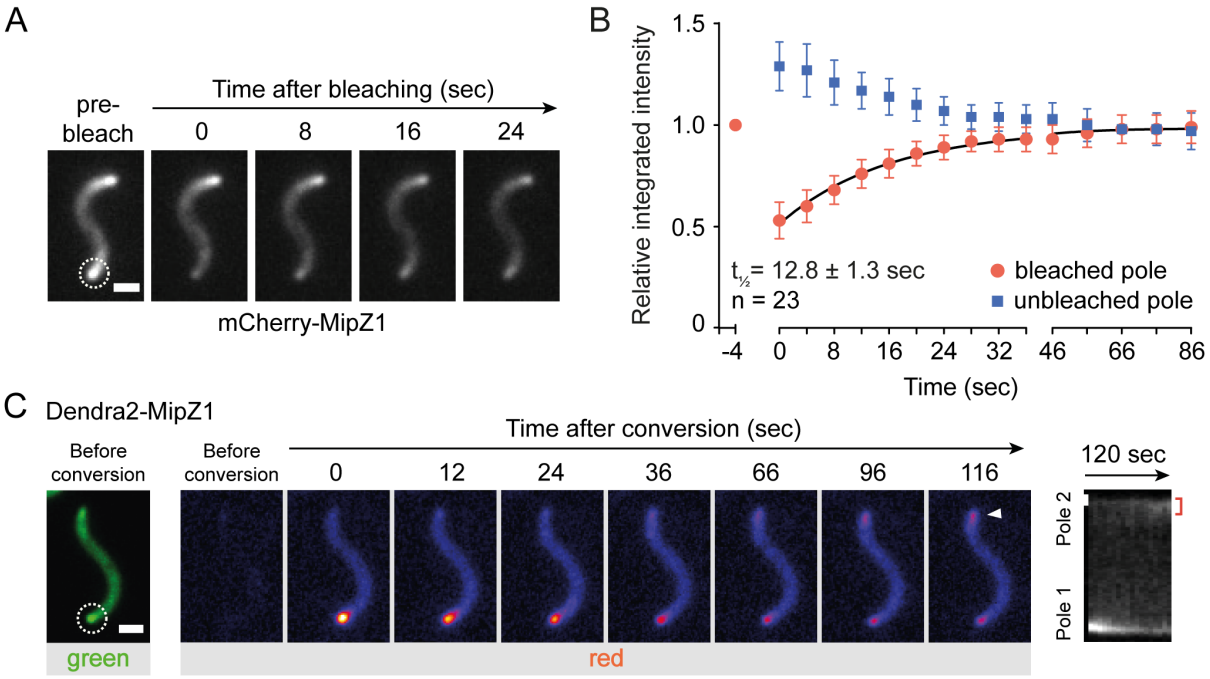

Figure 3. Photokinetic analysis of MipZ1 dynamics. (**A**) FRAP analysis of mCherry-MipZ1 (strain eMTN025). Shown are images of a representative cell taken before and at the indicated time points after photobleaching. White dashed circle: bleached area. (**B**) Quantification of the fluorescence signals in (A). The first image (t=0 sec) was taken immediately after the laser pulse. Error bars: SD. $t_{½}$: fluorescence recovery half-time. A similar recovery half-time (13.8 ± 1.2 sec; n=18 cells) was obtained with the alternative strain eMTN032. (**C**) Photoconversion of Dendra2-MipZ1 in the WT background (strain eMTN030). Green channel: before photoconversion (white dashed circle: laser-illuminated area). Red channel: photoconverted protein after a 405 nm laser pulse. White arrowhead: presence of Dendra2-MipZ1 signal at the opposite non-photoconverted pole. The kymograph on the right shows the signal intensity (red channel) of photoconverted molecules along the cellular long axis (y-axis) over time (x-axis). The Dendra2-MipZ1 signal at the non-illuminated pole are indicated by a red bracket. Scale bars: 1 µm (micrographs) and 500 nm (kymograph).

The ATPase activity of $MipZ_{Cc}$ has previously been shown to be essential for MipZ gradient formation in *C. crescentus*. When the protein was locked in the ATP-bound (dimeric) state by mutation of a conserved aspartic acid residue involved in nucleotide hydrolysis, it no longer accumulated near the cell poles but became tightly associated with the nucleoid, preventing FtsZ assembly throughout the entire cell (Thanbichler and Shapiro, 2006; Kiekebusch *et al.*, 2012). Introduction of an equivalent amino acid exchange (D43A) into MipZ1 from *M. gryphiswaldense* also abolished gradient formation, even when analyzed in the presence of native MipZ1, and led to a significant increase in cell length (Figure 4A, 4E and 4F). To determine whether the delocalized mutant protein was freely diffusible or attached to the nucleoid, we assessed its mobility by FRAP analysis. The mCherry-$MipZ1^{D43A}$ fusion displayed a recovery half-time of ~43 sec (Figure 4B), indicating a significant ($p < 0.001$) decrease in its mobility compared to the wild-type protein (see Figure 3B), consistent with nucleoid binding.

To further investigate the ATPase cycle of MipZ1, we aimed to determine the functional properties of MipZ1 in its monomeric state. Previous work has shown that the substitution of a highly conserved glycine residue in the dimer interface with valine prevented $MipZ_{Cc}$ dimerization, producing an exclusively monomeric variant of the protein (Thanbichler and Shapiro, 2006; Kiekebusch *et al.*, 2012). Cells producing a variant of *M. gryphiswaldense* MipZ1 carrying an equivalent mutation (mCherry-$MipZ1^{G15V}$) lacked the typical bipolar gradient. Instead, they displayed an elevated level of background fluorescence and distinct polar foci, likely reflecting the positions of ParB (see below) (Figure 4C, 4E and 4F). These polar assemblies were highly dynamic and exchanged molecules with a half-time of only 0.7 sec, as determined by FRAP analysis (Figure 4D).

Together, these data demonstrate that ATP binding and hydrolysis are required for proper gradient formation. Moreover, they suggest that the inhibitory effect on cell division may be exerted by the dimeric form of MipZ1 *in vivo*.

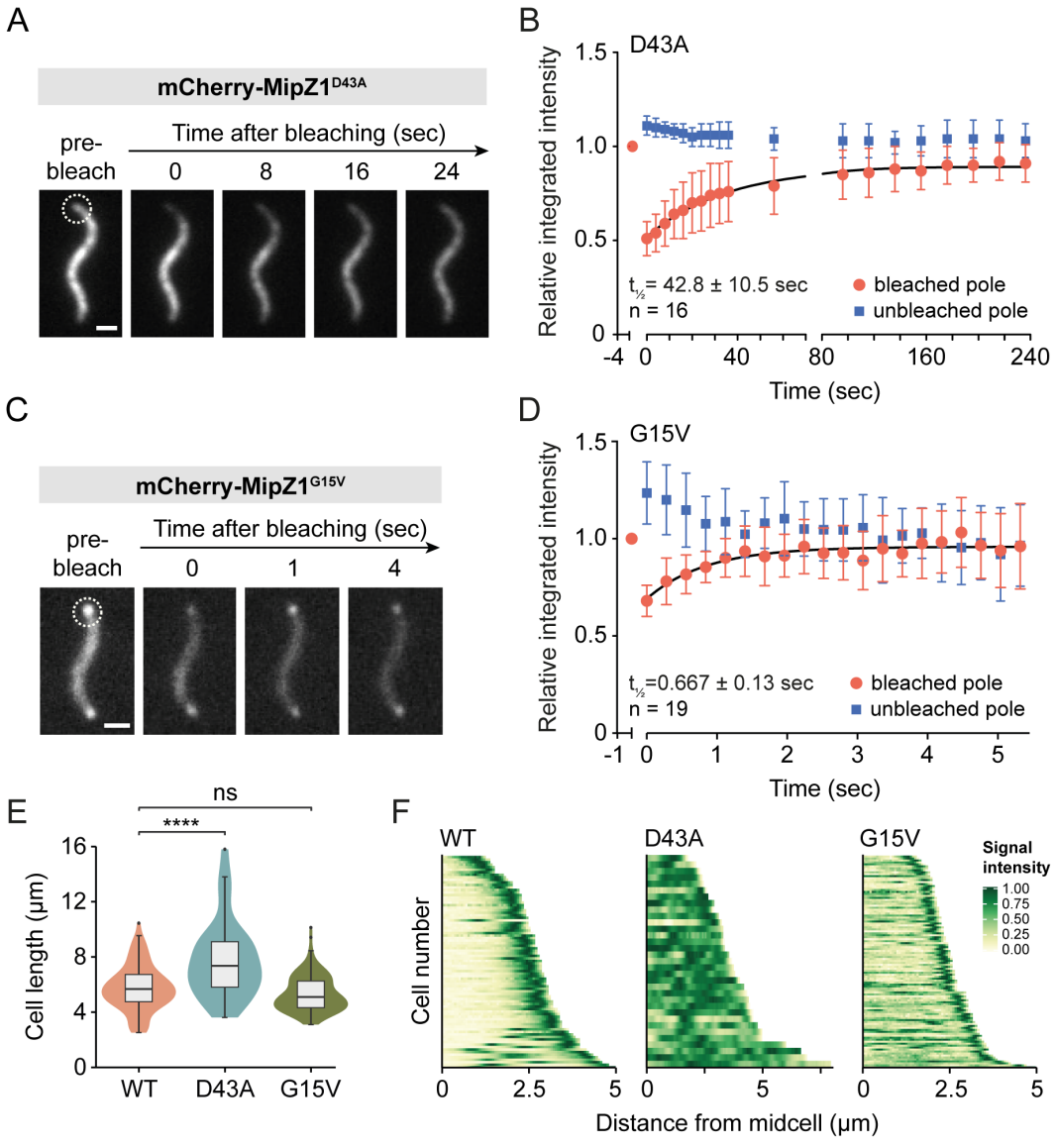

Figure 4. Photobleaching analysis of MipZ1^{D43A} and MipZ1^{G15V}. (**A**) FRAP analysis of mCherry-MipZ1^{D43A} (strain eMTN028). Shown are images of a representative cell taken before and at the indicated time points after photobleaching. White dashed circle: bleached area. Scale bar: 1 µm. (**B**) Quantification of the fluorescence signals in (A). The first image (t=0 sec) was taken immediately after the laser pulse. Error bars: SD. $t_{½}$: fluorescence recovery half-time. (**C**) FRAP analysis of mCherry-MipZ1^{G15V}, performed as described for (A). Scale bar: 1 µm. (**D**) Quantification of the fluorescence signals in (C). The first image (t=0 sec) was taken immediately after the laser pulse. Error bars: SD. $t_{½}$: fluorescence recovery half-time. (**E**) Cell length distribution of strains producing wild-type (WT) mCherry-MipZ1 (eMTN032) or the indicated mutant derivatives (eMTN028 and eMTN029). The data are represented as box plots and rotated kernel density plots, as described in **Figure 1B**. n = 84 cells (WT), 33 cells (D43A) and 108 cells (G15V). (**G**) Subcellular localization of mCherry-MipZ1 (WT) and the indicated mutant derivatives. The graph shows a demographic analysis of the cells measured in (E), generated as described in the legend to **Figure 2F** (**** $p < 0.0005$; ns: not significant). Only the portion corresponding from midcell to the cell pole is shown for every cell.

MipZ1 interacts with ParB

In *C. crescentus*, ParB plays a central role in MipZ$_{Cc}$ gradient formation, likely by stimulating the dimerization of MipZ$_{Cc}$ at the cell poles (Thanbichler and Shapiro, 2006; Kiekebusch *et al.*, 2012). We therefore aimed to determine whether this protein also contributed to the localization of MipZ1 in *M. gryphiswaldense*. To this end, we followed the localization of mCherry-MipZ1 and eCFP-ParB over the course of the cell cycle. In shorter (younger) cells, MipZ1 was only detected at one of the cell poles (Figure 5A). At later stages, cells displayed a second mCherry-MipZ1 focus, which appeared to move gradually to the opposite pole, finally yielding the typical bipolar gradient. Importantly, eCFP-ParB showed a similar transition from a unipolar to a bipolar pattern, suggesting a correlation between the movement of MipZ1 and ParB.

To determine whether MipZ1 binds to ParB directly, we purified the two proteins and conducted *in vitro* interaction analyses using bio-layer interferometry. For this purpose, biotinylated MipZ1 was immobilized on a streptavidin-coated sensor and probed with increasing concentrations of ParB (Figure 5B). Analysis of the resulting binding curves revealed that the two proteins are able to interact efficiently in the absence of any cofactors, as reflected by an apparent equilibrium dissociation constant (K_d) of 4.7 µM (Figure 5C). Notably, a similar behavior has previously been observed for the MipZ and ParB homologs of *C. crescentus* (K_d ~ 2 µM), suggesting the conservation of this interaction across species (Thanbichler and Shapiro, 2006).

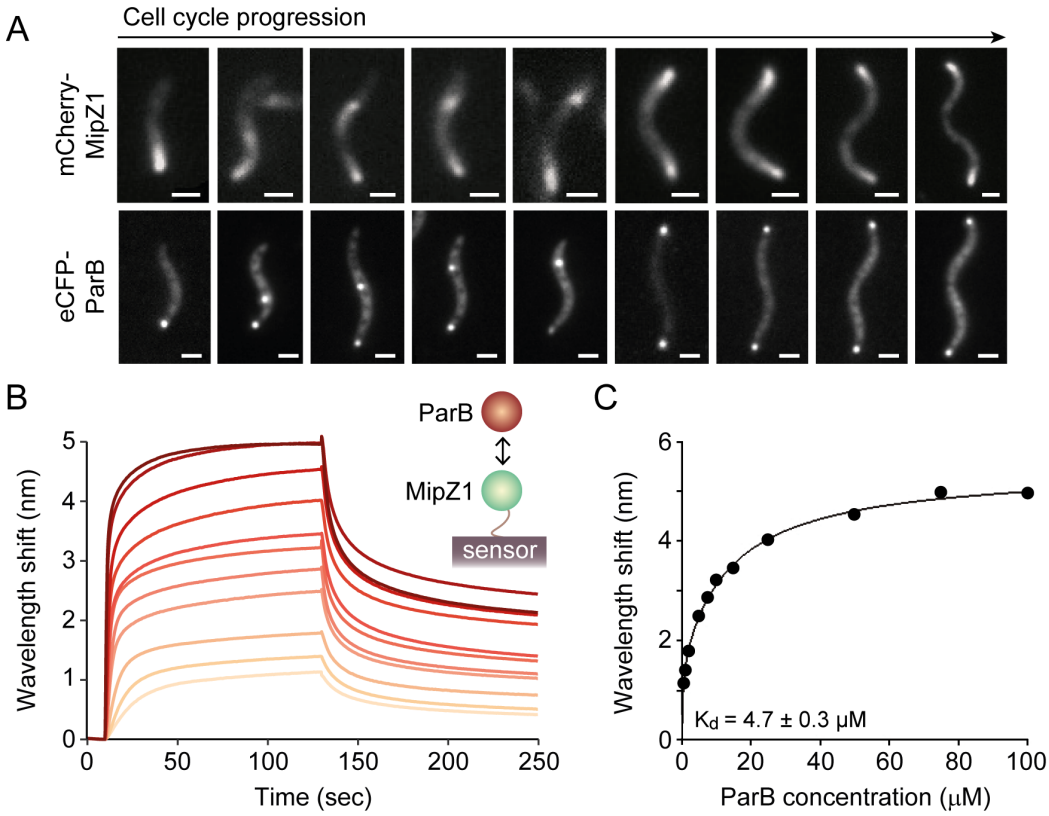

Figure 5. Interaction of MipZ1 with ParB. (**A**) Fluorescence micrographs of *M. gryphiswaldense* cells producing mCherry-MipZ1 (strain eMTN025) or eCFP-ParB (strain eMTN031). Cells are arranged from left to right according to their putative cell cycle state. Note that the fusion proteins are produced in different strains. Scale bars: 1 µm. (**B**) Bio-layer interferometric analysis of the interaction between MipZ1 and ParB. Biotinylated MipZ1 was immobilized on a streptavidin-coated biosensor and probed with increasing concentrations of ParB (from 0.5 to 100 µM). (**C**) Binding analysis of the interaction between MipZ1 and ParB. The wavelength shifts measured at the end of the association phase (Bmax) were plotted against the protein concentration. The apparent equilibrium dissociation constant (K_d) of the MipZ1·ParB complex was obtained by fitting the data to a one-site saturation ligand binding model. The value indicates the average of two independent experiments (± SE).

MipZ1 binds to DNA in a non-specific and ATP-dependent manner

Our results indicated that dimerization drastically reduces the diffusion rate of MipZ1. To determine whether this effect was indeed mediated through association with the nucleoid, we analyzed the interaction of MipZ1 with DNA in an electromobility shift assay. In the presence of ATPγS (a slowly hydrolyzable analog of ATP), MipZ1 and its constitutively dimeric D43A variant drastically reduced the mobility of a linearized plasmid during electrophoresis, whereas no retardation was observed for monomeric MipZ1^{G15V} or nucleotide-free wild-type protein (Figure 6A). These results indicate that MipZ1 indeed gains the ability to interact with non-specific DNA upon dimerization. To corroborate this finding, we performed localization studies in *Escherichia coli*, a species lacking MipZ homologs and a P*ar*AB*S* chromosome partitioning system. A wild-type mCherry-MipZ1 fusion was found to be largely

dispersed throughout the cell (Figure 6B), reminiscent of the results obtained for MipZ$_{Cc}$ (Kiekebusch *et al.*, 2012). The MipZ1^{D43A} variant, by contrast, strictly colocalized with the DAPI-stained nucleoid (Figure 6B). Notably, similar results were obtained when we used this system to analyze the localization behavior of MipZ2 and its putatively dimeric MipZ2^{D43A} variant (Figure S5). Thus, both MipZ homologs of *M. gryphiswaldense* appear to associate with the nucleoid in their dimeric form, a property that likely provides the basis for gradient formation (Figures 1F and 2D).

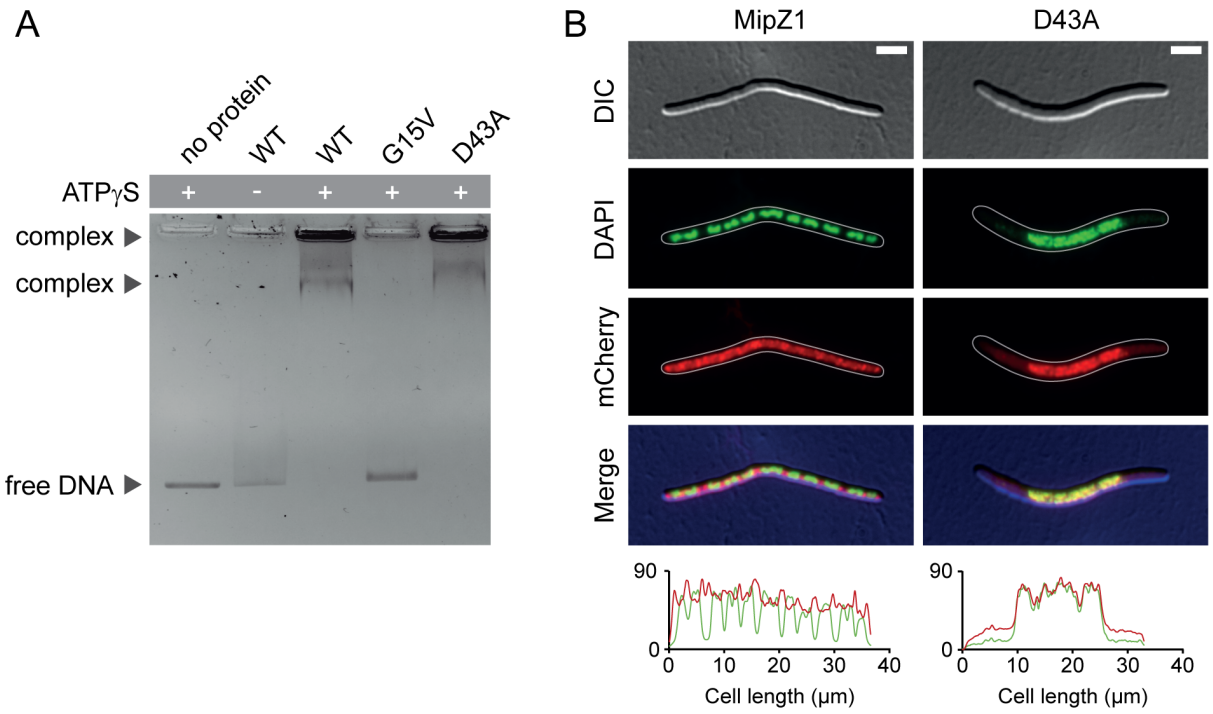

Figure 6. Interaction of MipZ1 with DNA. (**A**) Gel mobility shift assay showing the DNA-binding activity of MipZ1. A non-specific DNA fragment was incubated with wild-type MipZ1 or its mutant derivatives in the presence or absence of ATPγS and subjected to gel electrophoresis. (**B**) *In vivo* interaction of MipZ1 with chromosomal DNA. *E. coli* cells producing mCherry-MipZ1 (strain eMTN036) or mCherry-MipZ1^{D43A} (strain eMTN038) were treated with cephalexin and chloramphenicol to inhibit cell division and condense the nucleoids, respectively, facilitating the interpretation of the data. Nucleic acids were stained with DAPI. Scale bars: 5 μm. The graph at the bottom shows a comparison of the mCherry (red) and DAPI (green) fluorescence intensity profiles.

To investigate the effect of ParB and DNA on the ATPase cycle of MipZ1, we performed *in vitro* nucleotide hydrolysis assays using purified proteins. Wild-type MipZ1 was able to hydrolyze ATP with a turnover number (k_{cat}) of 0.23 min^{-1} (Figure 7), a value similar to that measured for MipZ$_{Cc}$ (Figure 7; Thanbichler and Shapiro, 2006). In contrast, its mutant derivative MipZ1^{D43A} essentially lacked catalytic activity (k_{cat} = 0.0014 min^{-1}), supporting the notion that it is locked in an ATP-bound state. The activity of the putatively monomeric variant, MipZ1^{G15V}, was severely impaired as well (k_{cat} = 0.024 min^{-1}), consistent with the idea that dimerization of MipZ1 is a prerequisite for nucleotide hydrolysis. Notably,

the ATPase activity of MipZ1 was barely affected by the presence of a plasmid or single-stranded DNA (Figures 7). Similarly, ParB alone did not have a stimulatory effect on the catalytic activity of MipZ1. However, when both plasmid or single-stranded DNA and ParB were included in the reaction, nucleotide hydrolysis was slightly accelerated (Figures 7). The presence of *parS* sites did not have any additional stimulatory effect, despite the fact that ParB binds tightly to *parS*-containing DNA under the conditions used (Figure S6). Collectively, these results resemble those obtained in *C. crescentus* (Thanbichler and Shapiro, 2006; Kiekebusch *et al.*, 2012), suggesting the conservation of the MipZ ATPase cycle.

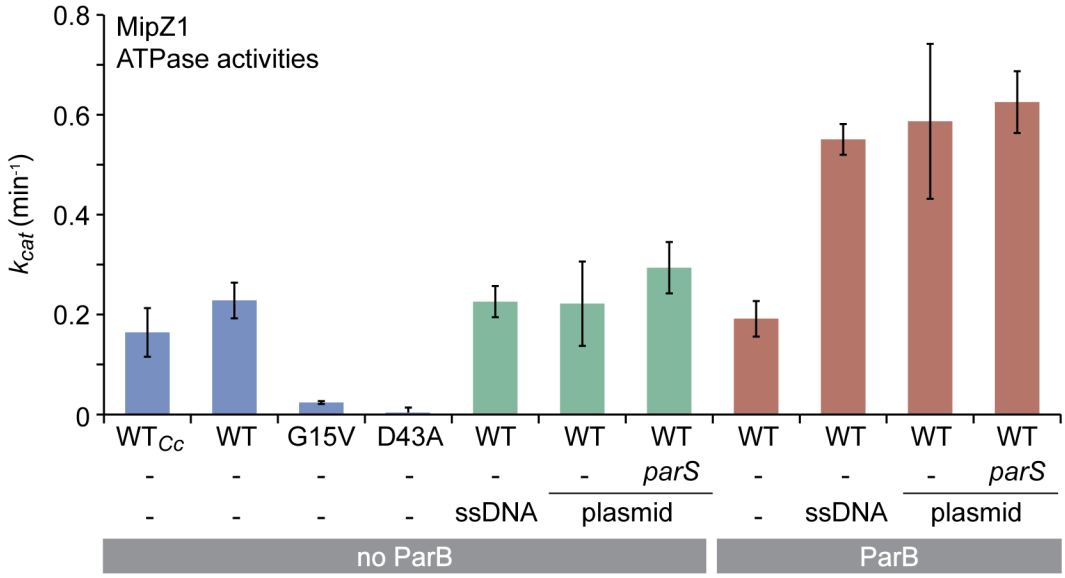

Figure 7. ATPase activities of wild-type MipZ1 and its mutant derivatives. The indicated proteins were incubated in the absence or presence of ParB and/or DNA containing or not the *parS* sites from *C. crescentus*. MipZ$_{Cc}$ was analyzed as a reference. The turnover numbers (k_{cat}) shown represent the the average of 2-8 independent experiments (± SE).

MipZ1 inhibits FtsZ polymerization *in vitro*

The results obtained so far suggested that Z-ring assembly in *M. gryphiswaldense* is regulated by a gradient of nucleoid-associated MipZ1 dimers. To further investigate the regulatory role of MipZ1 in FtsZ polymerization, we first examined its effect on the GTPase activity of FtsZ *in vitro* (Figure 8A). When analyzed in the absence of other proteins, purified FtsZ from *M. gryphiswaldense* hydrolyzed GTP with a turnover number of 2.5 min^{-1}. Notably, addition of MipZ1 in complex with ATPγS led to an ~3.5-fold increase in its hydrolytic activity (k_{cat} = 8.8 min^{-1}). A similar result was obtained upon incubation of FtsZ with the constitutively dimeric MipZ1^{D43A} variant (k_{cat} = 5.8 min^{-1}), suggesting that the MipZ1 dimer interacts with FtsZ, thereby affecting its GTPase cycle. Interestingly, unlike in the

C. crescentus system (Thanbichler and Shapiro, 2006), the putatively monomeric MipZ1^{G15V} variant also induced a moderate (~1.7-fold) increase in the FtsZ GTPase activity.

To determine whether the polymerization behavior of FtsZ was affected by its interaction with MipZ1, we performed sedimentation assays (Figure 8B). In the presence of ATPγS, both MipZ or MipZ1^{D43A} indeed caused a considerable decrease in the amount of FtsZ that was recovered from the pellet after centrifugation, indicating a reduction in the amount and/or length of FtsZ polymers. In line with the results of the GTPase assay, monomeric forms of MipZ1 (either MipZ1^{G15V} or nucleotide-free MipZ1) were also able to inhibit FtsZ assembly, albeit to a lesser extent. Collectively, these results demonstrate that MipZ1 interacts with FtsZ, thereby altering its polymerization properties.

In order to visualize the changes in FtsZ assembly caused by MipZ1, we subjected protein samples to transmission electron microscopy. When incubated alone, *M. gryphiswaldense* FtsZ showed robust GTP-dependent polymerization, forming dense aggregates of straight or slightly bent filaments (Figure 8C). These results are in agreement with previous work reporting the GTP-dependent assembly of this protein by dynamic light scattering (Müller *et al.*, 2014). Importantly, polymeric structures were no longer detectable after addition of MipZ1 or MipZ1^{D43A} in complex with ATPγS (Figure 8C), confirming the inhibitory effect of MipZ1 dimers on FtsZ assembly. Again, nucleotide-free MipZ1 or the constitutively monomeric MipZ1^{G15V} variant also had a noticeable effect on FtsZ polymerization, giving rise to shorter filaments that were no longer straight but rather curved (Figure 8C). This observation may explain the inhibitory effect on cell division induced by overproduction of MipZ1^{G15V} *in vivo* (see Figure 4E).

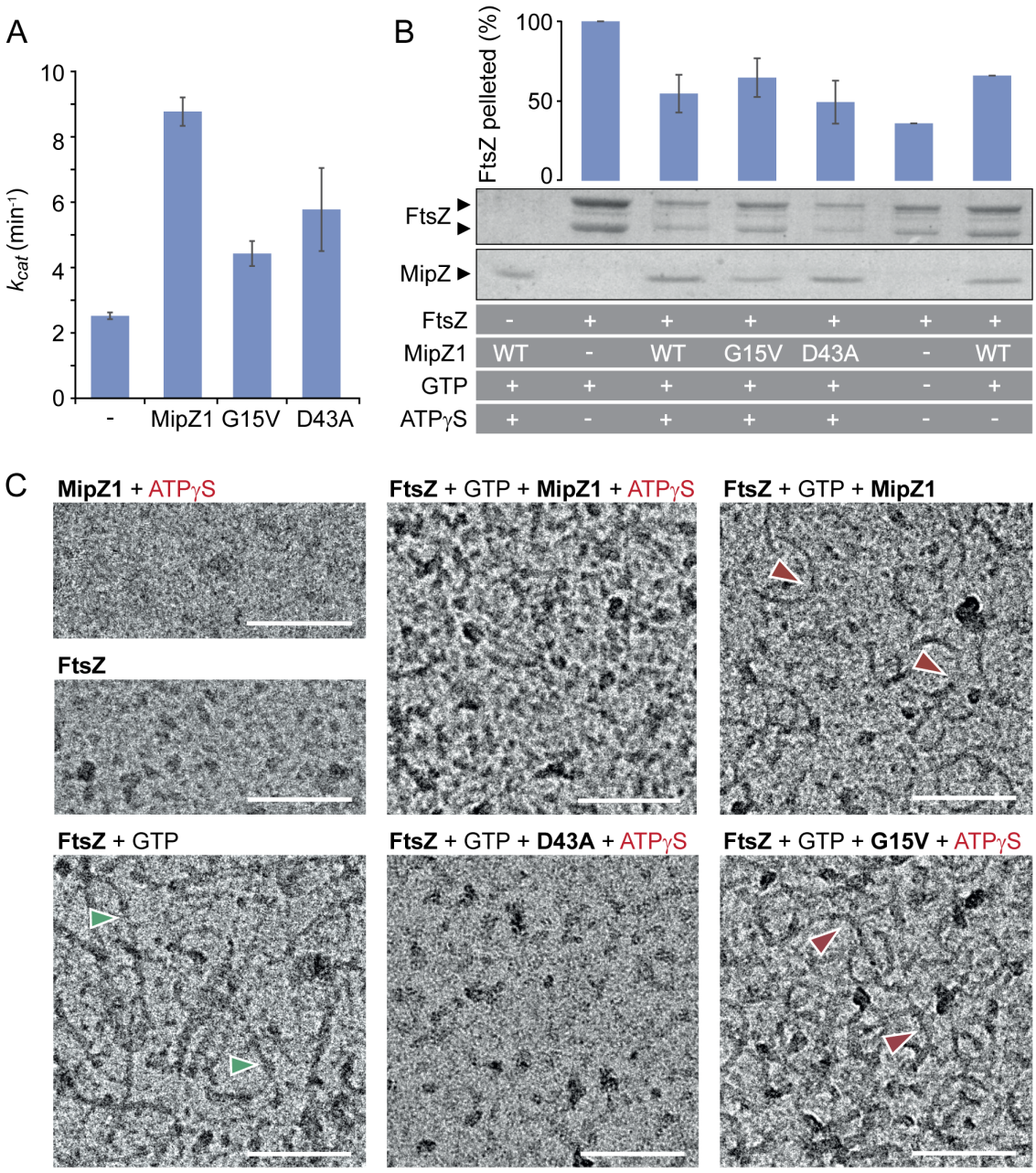

Figure 8. Interaction of MipZ1 with FtsZ. (**A**) Effect of MipZ1 on the GTPase activity of FtsZ. FtsZ was incubated in the presence or absence of wild-type MipZ1 or its mutant derivatives. The turnover numbers (k_{cat}) shown represent the average of three independent experiments (± SE). (**B**) Effect of MipZ1 on the sedimentation of FtsZ. FtsZ was incubated in the presence or absence of MipZ1, ATPγS and/or GTP and subjected to ultracentrifugation. Shown is a representative SDS-gel loaded with the pellet fractions. The values plotted in the graph represent the average of 2-3 independent experiments. (**C**) Effect of MipZ on the structure of FtsZ polymers. FtsZ was incubated in the presence or absence of MipZ1, ATPγS and/or GTP, stained with uranyl acetate and visualized by transmission electron microscopy. Green arrowheads denote straight filaments, whereas red arrowheads indicate curved FtsZ filaments. Scale bars: 100 nm.

DISCUSSION

The molecular mechanisms controlling bacterial division site placement have so far only been investigated in a few selected model species and appear to be highly diverse among different evolutionary lineages. In this study, we dissected the function of two MipZ homologs in the spiral-shaped alphaproteobacterium *M. gryphiswaldense* and show that the prototypical MipZ system of *C. crescentus* is partially conserved in this species. Although the two MipZ homologs of *M. gryphiswaldense* share high sequence similarity, their functions appear to differ significantly. Our results demonstrate that MipZ1 is critical for proper cell division (Figure 1A-B) and represents a *bona fide* homolog of *C. crescentus* MipZ. The function of MipZ2, by contrast, still remains elusive, because in spite of its similarity to $MipZ_{Cc}$ and MipZ1, its absence did not cause any obvious phenotype (Figures 2A-C). Interestingly, the localization patterns of MipZ1 and MipZ2 are diametrically different. Whereas MipZ1 consistently localized to the cell poles, likely driven by its interaction with the polar ParB•*parS* complexes (Pfeiffer *et al.*, 2019), its paralogue MipZ2 shows a unipolar localization in new-born cells and later relocates to the site of cell division, following FtsZ (Figure 2F). This behavior is reminiscent of MipZ from *Rhodobacter sphaeroides*, which represents a functionally divergent class of MipZ proteins (Dubarry *et al.*, 2019) that are recruited to the cell division site and form a ring-like assembly at the inner face of the constricting Z-ring.

The need for a second MipZ system may be explained by the fact that cells of *M. gryphiswaldense* grow significantly longer (2–10 µm) than those of *C. crescentus* (1–2 µm). Considering the limited length of the bipolar MipZ1 gradient, MipZ1 alone may not be sufficient to ensure proper FtsZ assembly at midcell at later stages of the cell cycle. Interestingly, in *M. gryphiswaldense*, FtsZ remains mobile and poorly focused until MipZ2 accumulates at the division site (Figure 2G). MipZ2 could therefore be an accessory factor that serves to stabilize the Z-ring. Alternatively, it may constitute a novel class of MipZ homologs that use the switch-like properties of MipZ to control the positioning or assembly of a protein other than FtsZ. A test of these hypotheses will require in-depth biochemical studies of MipZ2, which are, however, complicated by the fact that the protein is insoluble in purified form (data not shown). Apart from the biological role of MipZ2, it will be interesting to determine the factors mediating its localization to midcell or the cell poles.

An analysis of the conservation of MipZ in the alphaproteobacterial order *Rhodospirillales* shows that MipZ homologs are largely limited to the family *Rhodospirillaceae*, which includes *M. gryphiswaldense* as well as a variety of other spiral-shaped or curved species (Figure 9). The rod-shaped or ovococcoid members of the other families, by contrast, mostly lack MipZ homologs and possess the Min system instead. This differential phylogenetic distribution may indicate that the gradient-forming MipZ

homologs are better suited to control division site placement in cells with spirilloid morphologies, potentially because the oscillatory behavior of the Min system may be more difficult to maintain in these conditions. Notably, some members of the *Rhodospirillales* possess both a MipZ homolog and the MinCDE proteins. It will be interesting to investigate the selective advantage conferred by the combination of these independent regulatory systems.

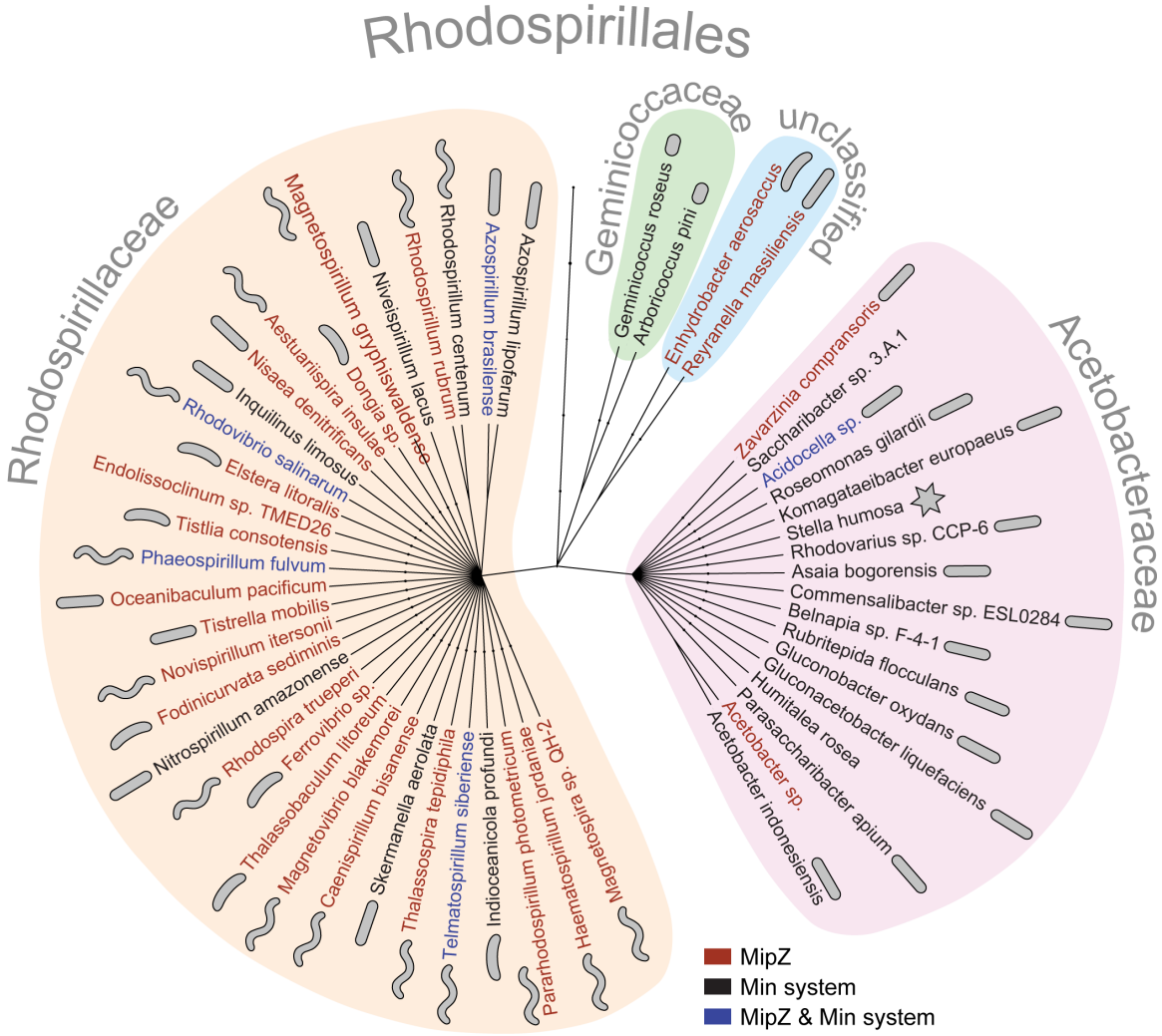

Figure 9. Phylogenetic distribution of the MipZ and Min systems in the order *Rhodospirillales*. Genome sequences from the order *Rhodospirillales* were searched for homologs of *C. crescentus* MipZ (GenBank ACL95711.1) and *E. coli* MinC (GenBank AAC74260.1) using the BLASTp server (https://blast.ncbi.nlm.nih.gov). The phylogenetic relationship of positive species was then determined with phyloT (https://phylot.biobyte.de) and plotted with iTOL. Only one representative species is shown for each genus.

Consistent with its functional similarity, MipZ1 displays biochemical properties that are comparable to those of its homolog in *C. crescentus*. Like other ParA-like ATPases (Scholefield *et al.*, 2011; Ringgaard *et al.*, 2011; Kiekebusch *et al.*, 2012), MipZ1 can exist in a monomeric and a dimeric form with distinct localization patterns and diffusion rates. Continuous oscillation between these two states, driven by ATP binding and hydrolysis, is required to establish the typical bipolar concentration gradient (Figures 3 and 4). As observed for $MipZ_{Cc}$, MipZ1 dimers have non-specific DNA-binding activity and thus associate with the nucleoid, leading to a considerable decrease in their diffusion rate (Figures 4 and 6). Once they hydrolyze ATP, they dissociate into monomers, which are released from the DNA (Figures 4 and 6). Monomeric MipZ1 diffuses rapidly within the cell and interacts with ParB at the cell poles (Figures 4 and 5), thereby transitioning to the dimeric state again. After dissociation from the polar ParB•*parS* complex, MipZ1 dimers re-associate with pole-proximal regions of the nucleoid, where they remain tethered until ATP hydrolysis initiates the next localization cycle. A recent report showed that, in *M. gryphiswaldense*, inactivation of PopZ causes various cellular defects, including cell filamentation and acentric cell division (Pfeiffer *et al.*, 2019). These phenotypes may, at least in part, be explained by the failure of the mutant cells to recruit ParB to the cell poles and thus to establish a symmetric MipZ1 gradient, which further underscores the importance of MipZ1 for division site placement in this species.

Interestingly, unlike in the *C. crescentus* system, monomeric MipZ1 also had a noticeable effect on FtsZ, in particular on its GTPase activity (Figure 8). However, the functional significance of this observation remains unclear, because *in vivo* most MipZ1 monomers interact with the polar ParB•*parS* complex and are therefore unable to affect the positioning of FtsZ at midcell. Nevertheless, it is conceivable that changes in the level of MipZ1 monomers, as potentially induced by duplication of the ParB•*parS* complex upon entry of the cells into S-phase, or the fast-diffusive cytoplasmic population of monomers could help to modulate the kinetics of Z-ring assembly.

M. gryphiswaldense has a second FtsZ gene, named FtsZm, which shares the core region of its canonical paralog but lacks the C-terminal linker and peptide (Müller *et al.*, 2014). It therefore retains the ability to polymerize but may have lost the capacity to bind to FtsZ tethers or stabilizers. FtsZm localizes at midcell, likely through interaction with FtsZ. However, it does not play a role in cell division but rather in magnetosome biomineralization (Müller *et al.*, 2014). It remains unclear whether MipZ1 or MipZ2 can interact with FtsZm. However, MipZ1 is likely to affect FtsZm polymerization at least indirectly through its regulatory effect on the canonical FtsZ homolog, thereby potentially coordinating cell division with the formation and cleavage of the magnetosome chain.

Taken together, our findings show that *M. gryphiswaldense* uses two functionally distinct MipZ systems to ensure robust cell division. Gradient-forming MipZ systems may be widespread among the

Alphaproteobacteria, especially in their spiral-shaped representatives, even though their cellular roles may have adapted to the specific needs of their host species.

EXPERIMENTAL PROCEDURES

Bacterial strains, plasmids and culture conditions

The bacterial strains, plasmids and oligonucleotides generated and used in this work are listed in **Tables S1-S3**. The construction of plasmids is detailed in the Supplemental Material. Strains of *M. gryphiswaldense* MSR-1 were grown under microoxic conditions in 2% oxygen-aerated modified flask standard medium (Heyen and Schüler, 2003) (FSM) containing 50 µM ferric citrate at 30 °C and moderate agitation (120 rpm). Media were supplemented with kanamycin (5 µg ml^{-1}) when appropriate. The expression of genes placed under the control of the P_{tet} promoter was induced by addition of 50 ng ml^{-1} anhydrotetracycline. For localization studies, cells were analyzed in the early induction phase (3-5 h post induction), whereas longer induction times (> 12 h) were used for overexpression studies. FtsZ-mCherry localization was analyzed in the absence of inducer. *E. coli* strains DH5α, TOP10, Rosetta2(DE3)pLysS (Novagen) and WM3064 (W. Metcalf, unpublished) were grown in LB medium at 37 °C. In the case of *E. coli* strain WM3064, which was used for the conjugative transfer of plasmids into *M. gryphiswaldense*, media were supplemented with 1 mM DL-α,ε-diaminopimelic acid (DAP). *E. coli* strains carrying recombinant plasmids were grown in media containing additives at the following concentrations (µg ml^{-1}; liquid/solid medium) when required: kanamycin (25/50), ampicillin (50/200), chloramphenicol (20/30) or 2 % (w/v) glucose.

Epifluorescence microscopy

Images were acquired with (i) an Olympus BX81 microscope equipped with a 100x/1.40 Oil UPLSAPO100XO objective and an Orca-ER camera (Hamamatsu), (ii) an Axio Observer.Z1 (Zeiss) microscope equipped with a Plan Apochromat 100x/1.45 Oil DIC and a pco.edge sCMOS camera (PCO) or (iiI) a DeltaVision Elite (GE Healthcare, Applied Precision) Olympus IX71 microscope equipped with a 100x/1.40 Oil PSF objective (U-PLAN S-APO 100x Oil, 0.12 WD), a CoolSnap HQ2 CCD camera (Photometrics) and a four-color standard set Insight SSITM illumination module. *M. gryphiswaldense* cells were spotted onto a 1% of the "MSR agarose pad" as described previously (Toro-Nahuelpan *et al.*, 2016). Snap-shot images were taken at room temperature (25 °C; for the Olympus BX81 microscope) or at 30 °C (for the Delta Vision Elite microscope). Time-lapse series were recorded at 30 °C using the DeltaVision Elite microscope. The fluorescence-recovery-after-photobleaching (FRAP) and photoconversion assays are detailed in the Supplemental Material.

Transmission electron microscopy

To visualize cell morphology by conventional bright-field TEM analysis, cells were grown at 28 °C under microaerobic conditions, fixed with formaldehyde (1%), concentrated tenfold and adsorbed to carbon-coated copper mesh grids (Plano, Germany). For the analysis of FtsZ polymerization, 5 µM FtsZ

was incubated for 15 min at room temperature in buffer P (50 mM Hepes/NaOH, pH 7.2, 50 mM KCl, 5 mM $MgCl_2$) containing 2 mM GTP and/or 1 mM ATPγS in the presence or absence of 7.5 µM MipZ1 or its mutant derivatives. Glycerol concentrations were adjusted to the same values by compensating different volumes of protein solutions with storage buffer. Samples were incubated on glow-discharged carbon-coated grids for 2 min, treated for 1 min with 2% uranyl acetate, and then washed twice with water. Micrographs were taken with a FEI CM200 (FEI, Netherlands) transmission electron microscope at an acceleration voltage of 160 kV. Images were captured with an Eagle 4k CCD camera using EMMenu 4.0 (TVIPS, Germany) and FEI software. Fiji software (Schindelin *et al.*, 2012) was used for data analysis.

Plunge-freezing vitrification

5 µL of *M. gryphiswaldense* culture were mixed with 2 µL of (two-fold concentrated) BSA-coated 15 nm colloidal gold clusters (Sigma-Aldrich, USA) to facilitate subsequent image alignment. The mixture was added onto glow-discharged Quantifoil R 2/1 holey carbon molybdenum grids (Quantifoil Micro Tools GmbH, Germany), manually blotted for 4 s, and embedded in vitreous ice by plunge-freezing in liquid ethane (< −170 °C). The grids were stored in sealed boxes in liquid nitrogen until further use.

Cryo-electron tomography

Tomography was performed under low-dose conditions using a FEI Tecnai F30 G^2 Polara microscope equipped with a 300 kV field emission gun and a Gatan GIF 2002 post-column energy filter. A 3838 x 3710 Gatan K2 Summit Direct Detection Camera, operated in counting and dose-fractionation mode, was used for imaging. Data collection was performed at 300 kV, with the energy filter operated in the zero-loss mode (slit width of 20 eV). Tilt series were acquired using Serial EM software (Mastronarde, 2005). The specimen was tilted about one axis with 1.5° increments over a typical total angular range of ± 60°. The cumulative electron dose applied during each tilt series was kept below 150 e^- $Å^{-2}$. To account for the increased specimen thickness at high tilt angles, the exposure time was multiplied by a factor of 1/cos α. The pixel sizes at the specimen level were 5.22 Å at an EFTEM magnification of 22,500x. Images were recorded at a nominal 5 to 8 µm defocus.

Tomogram reconstruction and segmentation

Tomograms were reconstructed with the IMOD package (Kremer *et al.*, 1996). Tomographic reconstructions from tilt series were performed with the weighted back-projection approach using particles as fiducial markers. Aligned images were binned to the final pixel size of 31.32 Å. For tomographic reconstruction, the radial filter options were cut off: 0.5 and fall off: 0.05. The datasets using in this study comprised 10 tomograms for the Δ*mipZ1* strain and 9 tomograms for Δ*mipZ2* strain. Tomograms were treated with an anisotropic nonlinear diffusion denoising algorithm to improve the signal-to-

noise ratio. Segmentation of the tomogram was achieved with Amira software on binned volumes with a voxel size of 31.32 Å. Membrane segmentation was performed using the Matlab-based segmentation tool termed TomoSegMemTV and the complementary package SynapSegTools (Martínez-Sánchez A, 2014). Tomogram slices were obtained using 3dmod software from the IMOD package.

Protein overproduction and purification

To purify native MipZ1 protein or its mutant derivatives, Rosetta2(DE3)pLysS (Merck Millipore, Germany) was transformed with the appropriate plasmid and grown to an OD_{600} of 0.6. IPTG was added to a final concentration of 0.5 mM to induce protein synthesis. After 3 h of incubation, the culture was harvested by centrifugation and frozen at -80 °C until further use. The cells were suspended in buffer B3 (2 ml per gramm of cells) (50 mM NaH_2PO_4, 300 mM NaCl, 20 mM imidazole, adjusted to pH 8.0 with NaOH) containing 100 µg ml^{-1} PMSF and 10 U ml^{-1} DNase I, and lysed by three passages through a French press (16,000 psi). After centrifugation of the lysate for 60 min at 38,400 × *g*, the supernatant was passed through a membrane filter (0.45 µm pore size) and applied to a HisTrap HP 5 mL column (GE Healthcare) equilibrated with B3 buffer. Protein was eluted with B4 buffer (50 mM NaH_2PO_4, 300 mM NaCl, 250 mM imidazole, adjusted to pH 8.0 with NaOH). Pooled fractions containing the protein of interest were dialysed against B3 buffer lacking imidazole in two steps (18 h and 4 h). The His-SUMO tag was cleaved by incubation of the protein with Ulp1-His protease in the presence of 1 mM DTT at 4 °C for 2 h. Subsequently, untagged MipZ1 protein, Ulp1-His protease and His-SUMO were separated by chromatography on a HisTrap HP 5 mL column and elution with B4 buffer. The fractions containing pure MipZ1 protein were pooled, dialysed against PG buffer (50 mM Hepes/NaOH, pH 7.2, 50 mM KCl, 5 mM $MgCl_2$, 10% (v/v) glycerol) in two steps (18 h and 4 h), aliquoted, and stored at -80 °C.

Native FtsZ and ParB were purified essentially as described for MipZ1 but using different buffers. In this case, cells were suspended in BZ3 buffer (50 mM Tris-HCl, 300 mM KCl, 20 mM imidazole, 10% (v/v) glycerol), the His-SUMO fusions were eluted from the column with BZ4 buffer (50 mM Tris-HCl, 300 mM KCl, 250 mM imidazole, 10% (v/v) glycerol), and dialyzed against CB buffer (50 mM Tris-HCl, 300 mM KCl, 10% (v/v) glycerol). After cleavage of the His-SUMO tag and further chromatographic purification, the native proteins were dialysed against PG buffer.

Protein concentrations were determined using the Roti-Nanoquant reagent (Carl Roth, Germany) with BSA as a standard.

Nucleotide hydrolysis assays

GTPase and ATPase activity was measured using a continuous, regenerative coupled-enzyme assay (Ingerman and Nunnari, 2005). All assays (total volume 150 µL) were performed at 25 °C in P buffer (50 mM Hepes/NaOH, pH 7.2, 50 mM KCl, 5 mM $MgCl_2$) containing 20 U ml^{-1} pyruvate kinase (Sigma-

Aldrich), 20 U ml^{-1} L-lactate dehydrogenase (Sigma-Aldrich), 600 µg ml^{-1} NADH and 3 mM phospho-enolpyruvate. GTPase reactions contained 3 µM FtsZ, 2 mM GTP, 1 mM ATPγS and 6 µM MipZ (when appropriate). ATPase reactions contained 6 µM MipZ, 1 mM ATP and 0.2 µM DNA and/or 12 µM ParB (when appropriate). Glycerol concentrations were adjusted to the same values by compensating varying volumes of protein solution with storage buffer. The linear decrease in the absorbance of NADH at 334 nm was monitored for 40 min in an Epoch 2 microplate reader (BioTek Instruments, USA). Activity values were calculated using the extinction coefficient for NADH (6220 M^{-1} cm^{-1}) and an experimentally determined path length of 0.367 cm.

Bio-layer interferometry

Bio-layer interferometry was conducted using the BLItz system (Fortebio, USA) with Dip and Read Streptavidin Biosensors. For biotinylation, MipZ was incubated with a four-fold molar excess of wEZ-Link NHS-PEG4-Biotin (Thermo Fisher Scientific, USA) for 1 h at 4 °C, followed by 15 min at room temperature. After the reaction, the protein was dialysed extensively against PG buffer. All assays were performed at room temperature in PG buffer containing 0.01% Triton X-100 and 0.01 mM BSA, with agitation at 2,200 rpm. Pre-equilibrated biosensors were incubated for 45 sec with 4 µL of biotinylated MipZ1 and then washed for 30 sec. The immobilized protein was then probed with various concentrations of ParB in a reaction volume of 4 µl. After an association phase of 90 sec, the biosensor was transferred into protein-free reaction buffer to monitor the dissociation reaction. To determine the equilibrium dissociation constant (K_d), the maximal wavelength shifts measured at the end of the association phases were plotted against the corresponding protein concentrations. The data were then subjected to curve fitting using a one-site saturation ligand binding model in SigmaPlot version (Systat Software, USA).

Electrophoretic mobility shift assays

Assays were performed in PG buffer in the presence or absence of ATPγS. Glycerol concentrations were adjusted to the same values by compensating varying volumes of protein solution with storage buffer. MipZ1 protein or its mutant derivatives (10 µM) were incubated with 10 nM of linearized plasmid pMCS-2 (Thanbichler *et al.*, 2007) as a source of double-stranded DNA for 15 min at room temperature. Subsequently, 5 µL of sample were applied for standard DNA agarose gel electrophoresis.

Sedimentation assays

FtsZ (3 µM) was incubated for 15 min at room temperature with 3 µM MipZ1 or its mutant derivatives, 2 mM GTP and/or 1 mM ATPγS in buffer P. Glycerol concentrations were adjusted to the same values by compensating varying volumes of protein solution with storage buffer. The mixture was then centrifuged for 15 min at 385,900 x *g* at 25 °C using a Beckman MLA-130 rotor in a Beckman TL-100

ultracentrifuge. After immediate removal of the supernatants, the pellets were dissolved in 250 µL SDS sample buffer and incubated at 95 °C for 5 min. Samples (5 µl) were loaded on a 10% SDS-polyacrylamide gel, and proteins were visualized with Coomassie brilliant blue after electrophoresis. For the quantification of protein bands, gels were imaged with a ChemiDoc MP imaging system (Bio-Rad, USA) and analyzed using Image Lab 5.0 (Bio-Rad).

Bioinformatic tools

Protein sequences were aligned with MAFFT v6 (Katoh *et al.*, 2002). Phylogenetic relationships were determined using the maximum likelihood method as implemented in RaxML (Stamatakis *et al.*, 2008) and visualized with the help of iTOL (Letunic and Bork, 2007; https://itol.embl.de) as described previously (Kiekebusch *et al.*, 2012). Structural models of proteins were generated with I-TASSER (Zhang, 2008) using $MipZ_{Cc}$ as a template and analyzed with the UCSF Chimera package (Pettersen *et al.*, 2004). Cell length measurements were performed with Fiji (Schindelin *et al.*, 2012) or BacStalk (Hartmann *et al.*, 2018). Boxplots were generated using R version 3.5.1 (http://www.r-project.org).

ACKNOWLEDGEMENTS

We thank Julia Rosum (Philipps-Universität Marburg) for excellent technical assistance. This work was supported by the German Research Foundation (DFG) (grant Schu 1080/9-2; to D.S.) and the European Research Council (AdG *Syntomagx*; to D.S.). Additional funding was provided by the DFG-funded Transregio Collaborative Research Center TRR 174 (project 269423233; to M.T. and M.B.) and a Max Planck Fellowship from the Max Planck Society (to M.T.). M.O.-V. was a fellow of the International Max Planck Research School for Environmental, Cellular and Molecular Microbiology (IMPRS-Mic).

DATA AVAILABILITY STATEMENT

The data that support the findings of this study are included in the paper or available from the corresponding authors upon reasonable request.

CONFLICT OF INTEREST STATEMENT

The authors declare that there are no conflicts of interest.

AUTHOR CONTRIBUTIONS

M.T.-N. and D.S. conceived the study. M.T.-N., L.C.-G., M.T. and D.S. designed the study. M.T.-N. and F.-D.M. performed the *in vivo* experiments. M.T.-N. and L.C.-G. analyzed the data. M.T.-N., T.Z. and F.-D.M. generated strains. T.Z. performed the growth experiments and quantified the TEM data. L.C.-G. and M.O.-V. purified proteins and performed the biochemical analyses. J.M.P., M.B., M.T. and D.S. supervised the work. M.T.-N., L.C.-G., M.T. and D.S. wrote the manuscript, with input from all other authors.

REFERENCES

Ben-Yehuda, S., and Losick, R. (2002) Asymmetric cell division in *B. subtilis* involves a spiral-like intermediate of the cytokinetic protein FtsZ. *Cell* **109:** 257-266.

Bernhardt, T.G., and de Boer, P.A. (2005) SlmA, a nucleoid-associated, FtsZ binding protein required for blocking septal ring assembly over chromosomes in *E. coli*. *Mol Cell* **18:** 555-564.

Bertani, G. **(**1951) Studies on lysogenesis I: the mode of phage liberation by lysogenic *Escherichia coli*. *J Bacteriol* **62:** 293-300.

Bi, E.F., and Lutkenhaus, J. (1991) FtsZ ring structure associated with division in *Escherichia coli*. *Nature* **354:** 161-164.

Bisson-Filho, A.W., Hsu, Y.P., Squyres, G.R., Kuru, E., Wu, F., Jukes, C., Sun, Y., Dekker, C., Holden, S., VanNieuwenhze, M.S., Brun, Y.V., and Garner, E.C. (2017) Treadmilling by FtsZ filaments drives peptidoglycan synthesis and bacterial cell division. *Science* **355:** 739-743.

Borg, S., Hofmann, J., Pollithy, A., Lang, C., and Schüler, D. (2014) New vectors for chromosomal integration enable high-level constitutive or inducible magnetosome expression of fusion proteins in *Magnetospirillum gryphiswaldense*. *Appl Environ Microbiol* **80:** 2609-2616.

Curtis, P.D. and Brun, Y.V. (2014) Identification of essential alphaproteobacterial genes reveals operational variability in conserved developmental and cell cycle systems. *Mol Microbiol* **93:** 713-735.

Ding, Y., Li, J., Liu, J., Yang, J., Jiang, W., Tian, J., Li, Y., Pan, Y., and Li, J. (2010) Deletion of the *ftsZ*-like gene results in the production of superparamagnetic magnetite magnetosomes in *Magnetospirillum gryphiswaldense*. *J Bacteriol* **192:** 1097-1105.

Dubarry, N., Willis, C.R., Ball, G., Lesterlin, C., and Armitage, J.P. (2019) In vivo imaging of the segregation of the 2 chromosomes and the cell division proteins of *Rhodobacter sphaeroides* reveals an unexpected role for MipZ. *MBio* **10:** e02515-18.

Erickson, H.P., Anderson, D.E., and Osawa, M. (2010) FtsZ in bacterial cytokinesis: cytoskeleton and force generator all in one. *Microbiol Mol Biol Rev* **74:** 504-528.

Flores, S.A., Howell, M., Daniel, J.J., Piccolo, R., and Brown, P.J.B. (2018) Absence of the Min system does not cause major cell division defects in *Agrobacterium tumefaciens*. *Front Microbiol* **9:** 681.

Hartmann, R., van Teeseling, M.C.F., Thanbichler, M., and Drescher, K. (2018) BacStalk: a comprehensive and interactive image analysis software tool for bacterial cell biology. *bioRxiv* 360230 (doi: 10.1101/360230).

Heyen, U., and Schüler, D. (2003) Growth and magnetosome formation by microaerophilic *Magnetospirillum* strains in an oxygen-controlled fermentor. *Appl Microbiol Biotechnol* **61:** 536-544.

Ingerman, E., and Nunnari, J. (2005) A continuous, regenerative coupled GTPase assay for dynamin-related proteins. *Methods Enzymol* **404:** 611-619.

Katoh, K., Misawa, K., Kuma, K., and Miyata, T. (2002) MAFFT: a novel method for rapid multiple sequence alignment based on fast Fourier transform. *Nucleic Acids Res* **30:** 3059-3066.

Katzmann, E., Müller, F.D., Lang, C., Messerer, M., Winklhofer, M., Plitzko, J.M., and Schüler, D. (2011) Magnetosome chains are recruited to cellular division sites and split by asymmetric septation. *Mol Microbiol* **82:** 1316-1329.

Kiekebusch, D., Michie, K.A., Essen, L.O., Löwe, J., and Thanbichler, M. (2012) Localized dimerization and nucleoid binding drive gradient formation by the bacterial cell division inhibitor MipZ. *Mol Cell* **46:** 245-259.

Komeili, A., Li, Z., Newman, D., and Jensen, G. (2006) Magnetosomes are cell membrane invaginations organized by the actin-like protein MamK. *Science* **311:** 242-245.

Kremer, J.R., Mastronarde, D.N., and McIntosh, J.R. (1996) Computer visualization of three-dimensional image data using IMOD. *J Struct Biol* **116:** 71-76.

Letunic, I., and Bork, P. (2007) Interactive Tree Of Life (iTOL): an online tool for phylogenetic tree display and annotation. *Bioinformatics* **23:** 127-128.

Li, Z., Trimble, M.J., Brun, Y.V., and Jensen, G.J. (2007) The structure of FtsZ filaments in vivo suggests a force-generating role in cell division. *EMBO J* **26**: 4694-4708.

Lutkenhaus, J. (2007) Assembly dynamics of the bacterial MinCDE system and spatial regulation of the Z ring. *Annu Rev Biochem* **76:** 539-562.

Marston, A.L., Thomaides, H.B., Edwards, D.H., Sharpe, M.E., and Errington, J. (1998) Polar localization of the MinD protein of Bacillus subtilis and its role in selection of the mid-cell division site. *Genes Dev* **12:** 3419-3430.

Martínez-Sánchez, A., García, I., Asano, S., Lucic, V., and Fernández, J.J. (2014) Robust membrane detection based on tensor voting for electron tomography. *J Struct Biol* **186:** 49-61.

Mastronarde, D.N. (2005) Automated electron microscope tomography using robust prediction of specimen movements. *J Struct Biol* **152:** 36-51.

Müller, F.D., Raschdorf, O., Nudelman, H., Messerer, M., Katzmann, E., Plitzko, J.M., Zarivach, R., and Schüler, D. (2014) The FtsZ-like protein FtsZm of *Magnetospirillum gryphiswaldense* likely interacts with its generic homolog and is required for biomineralization under nitrate deprivation. *J Bacteriol* **196:** 650-659.

Pettersen, E.F., Goddard, T.D., Huang, C.C., Couch, G.S., Greenblatt, D.M., Meng, E.C., and Ferrin, T.E. (2004) UCSF Chimera – a visualization system for exploratory research and analysis. *J Comput Chem* **25:** 1605-1612.

Pfeiffer, D., Toro-Nahuelpan, M., Bramkamp, M., Plitzko, J.M., and Schüler, D. (2019) The polar organizing protein PopZ is fundamental for proper cell division and segregation of cellular content in *Magnetospirillum gryphiswaldense*. *MBio* (in press).

Radhakrishnan, S.K., Pritchard, S., and Viollier, P.H. (2010) Coupling prokaryotic cell fate and division control with a bifunctional and oscillating oxidoreductase homolog. *Dev Cell* **18:** 90-101.

Raskin, D.M., and de Boer, P.A. (1999) Rapid pole-to-pole oscillation of a protein required for directing division to the middle of *Escherichia coli*. *Proc Natl Acad Sci U S A* **96:** 4971-4976.

Ringgaard, S., Schirner, K., Davis, B.M., and Waldor, M.K. (2011) A family of ParA-like ATPases promotes cell pole maturation by facilitating polar localization of chemotaxis proteins. *Genes Dev* **25:** 1544-1555.

Scheffel, A., Gruska, M., Faivre, D., Linaroudis, A., Plitzko, J.M., and Schüler, D. (2006) An acidic protein aligns magnetosomes along a filamentous structure in magnetotactic bacteria. *Nature* **440:** 110-114.

Schindelin, J., Arganda-Carreras, I., Frise, E., Kaynig, V., Longair, M., Pietzsch, T., Preibisch, S., Rueden, C., Saalfeld, S., Schmid, B., Tinevez, J.Y., White, D.J., Hartenstein, V., Eliceiri, K., Tomancak, P., and Cardona, A. (2012) Fiji: an open-source platform for biological-image analysis. *Nat Methods* **9:** 676-682.

Scholefield, G., Whiting, R., Errington, J., and Murray, H. (2011) Spo0J regulates the oligomeric state of Soj to trigger its switch from an activator to an inhibitor of DNA replication initiation. *Mol Microbiol* **79:** 1089-1100.

Stamatakis, A., Hoover, P., and Rougemont, J. (2008) A rapid bootstrap algorithm for the RAxML Web servers. *Syst Biol* **57:** 758-771.

Thanbichler, M., Iniesta, A.A., and Shapiro, L. (2007) A comprehensive set of plasmids for vanillate- and xylose-inducible gene expression in *Caulobacter crescentus*. *Nucleic Acids Res* **35:** e137.

Thanbichler, M., and Shapiro, L. (2006) MipZ, a spatial regulator coordinating chromosome segregation with cell division in *Caulobacter*. *Cell* **126:** 147-162.

Toro-Nahuelpan, M., Giacomelli, G., Raschdorf, O., Borg, S., Plitzko, J.M., Bramkamp, M., Schüler, D., Müller, F. (2019) MamY is a membrane-bound protein that aligns magnetosomes and the motility axis of helical magnetotactic bacteria. *Nat Microbiol* (in press; doi: 10.1038/s41564-019-0512-8).

Toro-Nahuelpan, M., Müller, F.D., Klumpp, S., Plitzko, J.M., Bramkamp, M., and Schüler, D. (2016) Segregation of prokaryotic magnetosomes organelles is driven by treadmilling of a dynamic actin-like MamK filament. *BMC Biol* **14:** 88.

Uebe, R., and Schüler, D. (2016) Magnetosome biogenesis in magnetotactic bacteria. *Nat Rev Microbiol* **14:** 621-637.

Wu, L.J., and Errington, J. (2004) Coordination of cell division and chromosome segregation by a nucleoid occlusion protein in *Bacillus subtilis*. *Cell* **117:** 915-925.

Wu, L.J., and Errington, J. (2011) Nucleoid occlusion and bacterial cell division. *Nat Rev Microbiol* **10:** 8-12.

Yang, X., Lyu, Z., Miguel, A., McQuillen, R., Huang, K.C., and Xiao, J. (2017) GTPase activity-coupled treadmilling of the bacterial tubulin FtsZ organizes septal cell wall synthesis. *Science* **355:** 744-747.

Yao, Q., Jewett, A.I., Chang, Y.W., Oikonomou, C.M., Beeby, M., Iancu, C.V., Briegel, A., Ghosal, D., and Jensen, G.J. (2017) Short FtsZ filaments can drive asymmetric cell envelope constriction at **355:** the onset of bacterial cytokinesis. *EMBO J* **36:** 1577-1589.

Zhang, Y. (2008) I-TASSER server for protein 3D structure prediction. *BMC Bioinformatics* **9:** 40.

SUPPLEMENTAL FIGURES

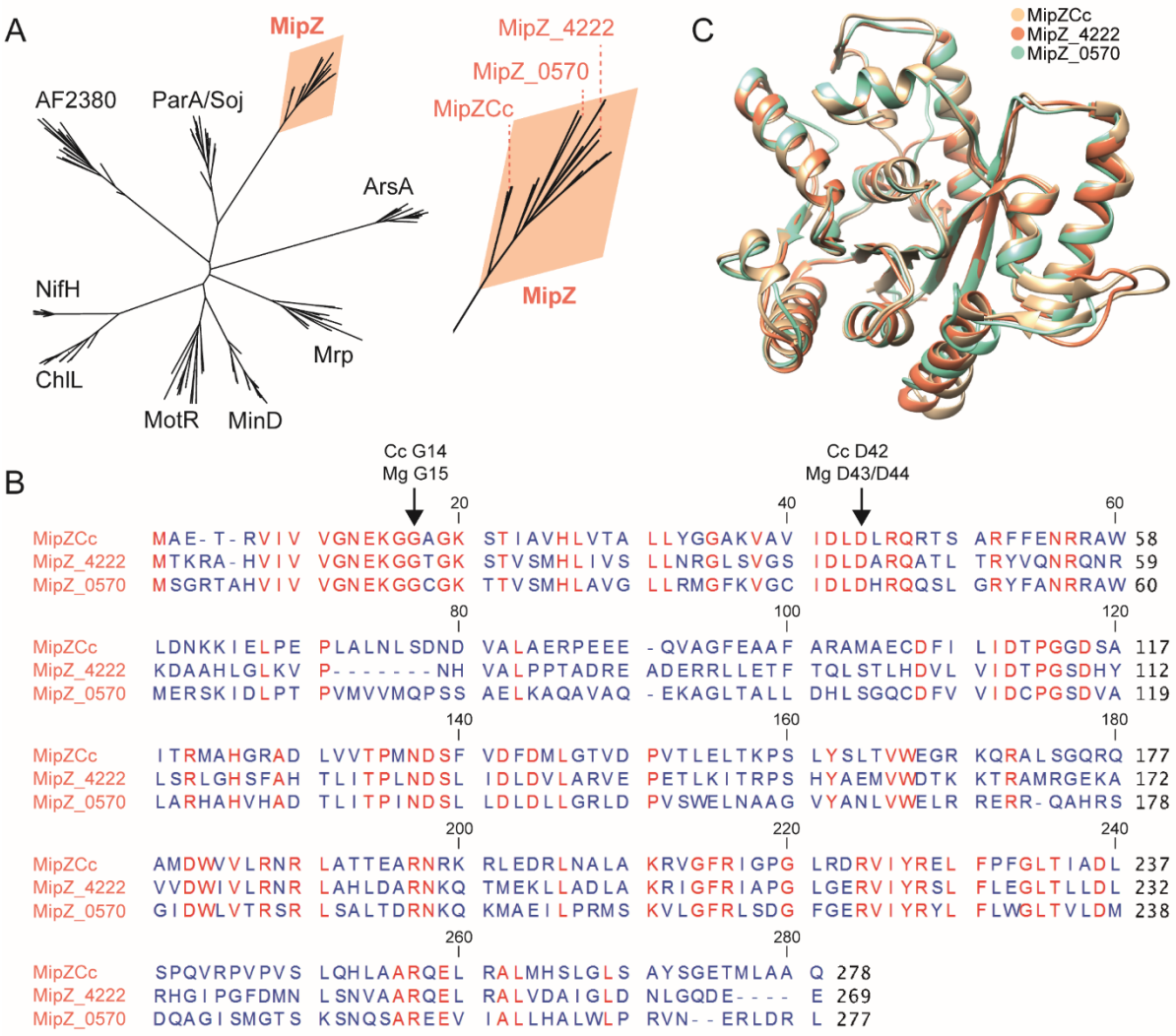

Figure S1. *Magnetospirillum gryphiswaldense* possesses two MipZ homologs. (**A**) Phylogenetic tree of the ParA-like P-loop ATPases. Amino acid sequences of 15 representative members from each of the indicated subfamilies were aligned and analyzed for their phylogenetic relationship using the maximum likelihood method. (**B**) Alignment of the amino acid sequences of MipZ_4222 and MipZ_0570 to that of *Caulobacter crescentus* MipZ. Amino acids conserved in all species are shown in red. Amino acids mutated in this study are indicated by arrows. (**C**) Superposition of the crystal structure of $MipZ_{Cc}$ (PDB ID 2XJ4) with structural models of MipZ_4222 and MipZ_0570, generated on the basis of the $MipZ_{Cc}$ structure.

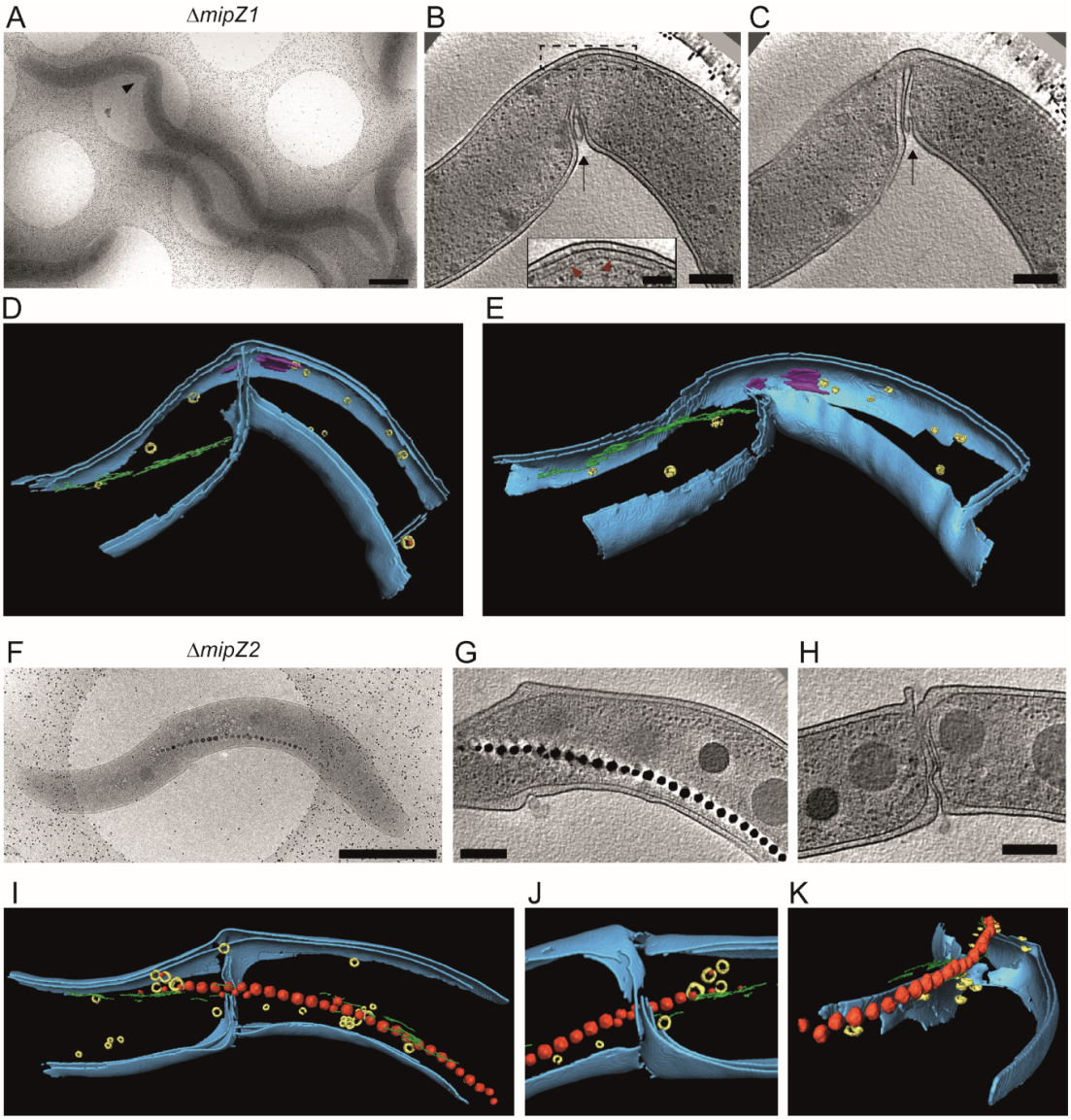

Figure S2. Cryo-electron tomographic analysis of Δ*mipZ1* and Δ*mipZ2* cells. (**A**) Cryo-electron micrograph of a Δ*mipZ1* cell (strain TZ001) undergoing asymmetric cell division (indicated by the arrowhead). (**B,C**) Central slices through the tomogram displaying the unidirectional constriction of the cell envelope (black arrows). The dashed rectangle in (B) indicates the area magnified in the inset. The red arrowheads in the inset point to the base plates of chemoreceptor. (**D,E**) 3D surface rendering of the cell division site shown in (A) and (B). Magnetite crystals: red; magnetosome membrane vesicles: yellow; actin-like MamK filament: green; chemoreceptor arrays: purple. The inner and outer membranes are depicted in blue. (**F**) Cryo-electron micrograph of a Δ*mipZ2* cell (strain MT024). (**G,H**) Central slices through the tomogram displaying (G) the magnetosome chain and the (H) unidirectional constriction of the cell envelope. (**I-K**). 3D surface rendering of the cell division site shown in (G) and (H), showing the characteristic membrane invagination at the septum. The colors are as described above. Scale bars: 1 µm (A,F), 200 nm (B-C,G-H), 100 nm (B inset).

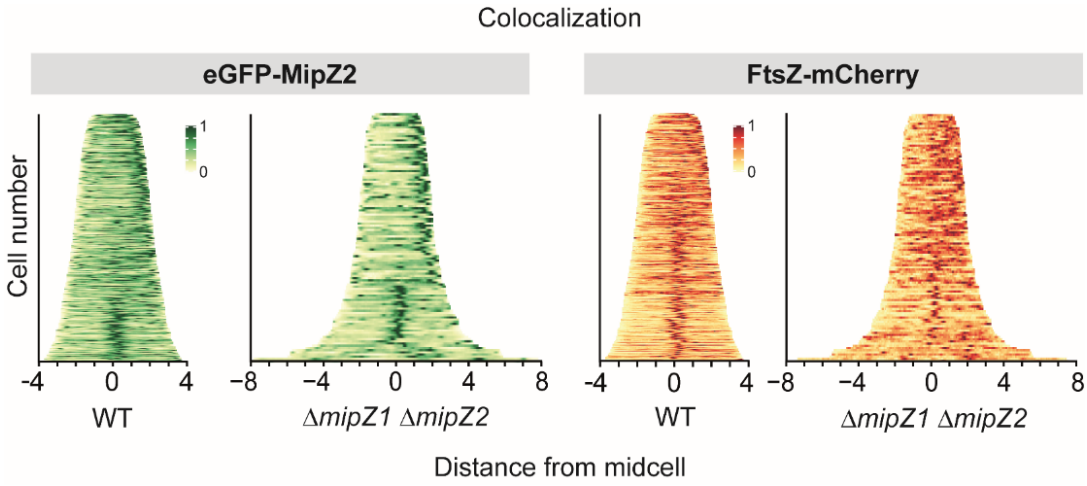

Figure S3. Subcellular localization of eGFP-MipZ2 and FtsZ-mCherry. The graphs show a demographic analysis of the localization patterns of the indicated proteins in the wild-type (strain FM100) and Δ*mipZ1* Δ*mipZ2* (strain FM101) backgrounds. To generate them, fluorescence intensity profiles obtained from a representative subpopulation of cells (n=114) were normalized, sorted according to cell length, and stacked on top of each other.

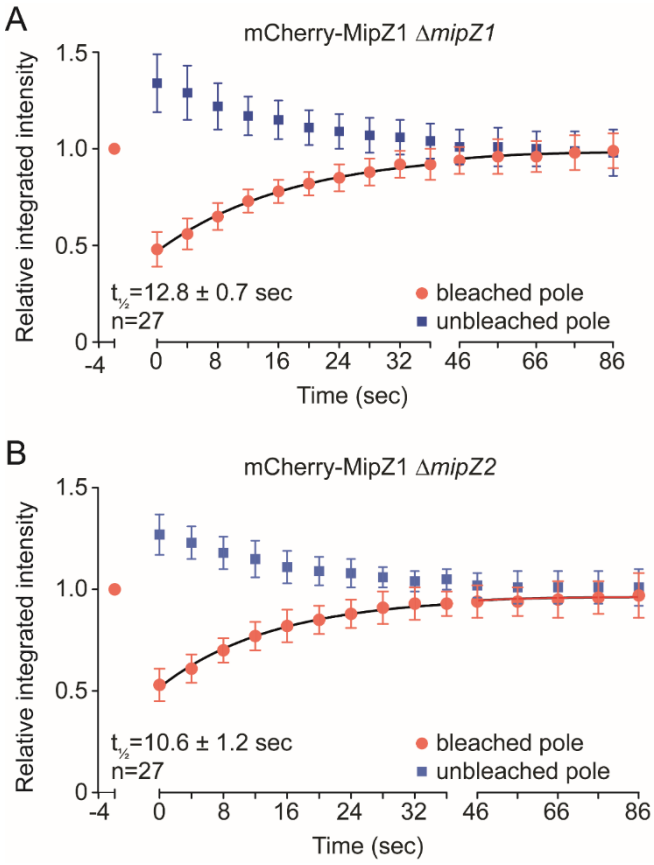

Figure S4. FRAP analysis of mCherry-MipZ1 in the Δ*mipZ1* and Δ*mipZ2* backgrounds. (**A**) FRAP analysis of mCherry-MipZ1 in the Δ*mipZ1* background (strain eMT026). Photobleaching and imaging were performed as described in the legend to Figure 4. Shown are the integrated fluorescence intensities of the bleached polar region before and at various time points after the laser pulse. Error bars: SD. $t_{½}$: fluorescence recovery half-time. (**B**) FRAP analysis of mCherry-MipZ1 in the Δ*mipZ2* background (strain eMT027). The experiment was performed as described in (A).

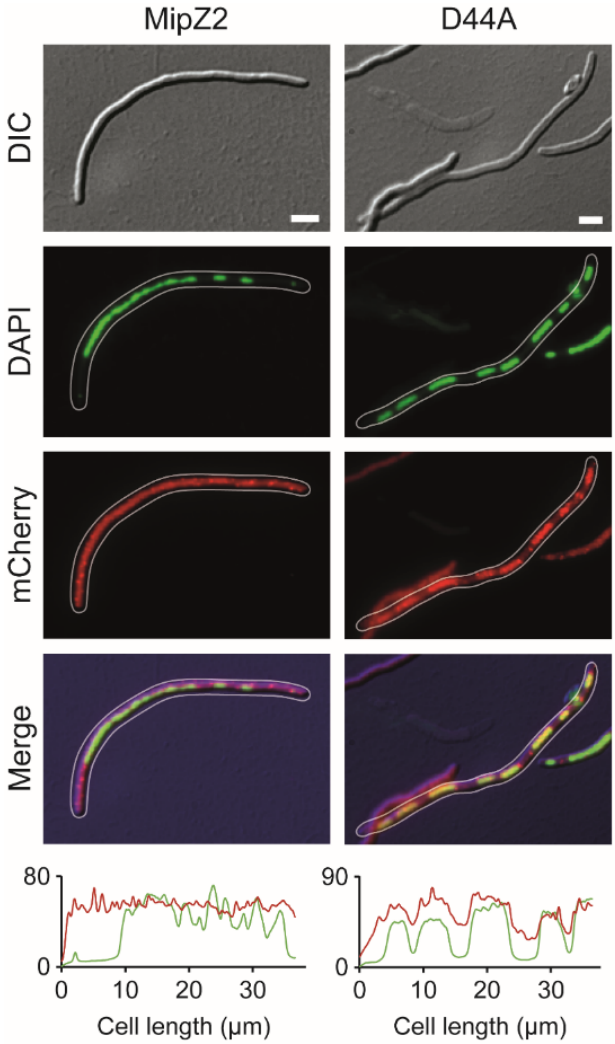

Figure S5. Interaction of MipZ2 with DNA. *E. coli* cells producing mCherry-MipZ2 (strain eMTN037) or mCherry-MipZ2$_{D44A}$ (strain eMTN039) were treated with cephalexin and chloramphenicol to inhibit cell division and condense the nucleoids, respectively, facilitating the interpretation of the data. Nucleic acids were stained with DAPI. Scale bars: 5 µm. The graphs show the intensity of mCherry (red) and DAPI (green) fluorescence along the long axis of the indicated cells.

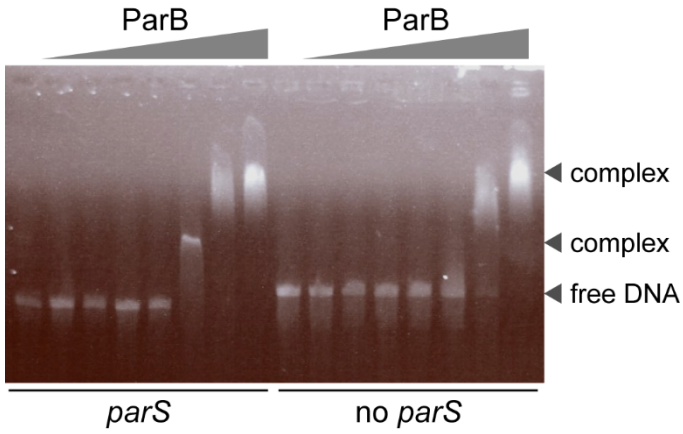

Figure S6. Interaction of MipZ1 with DNA and ParB. Gel mobility shift assay in the presence of ParB. A *parS*-containig and a *parS*-free plasmid were incubated with increasing concentrations of ParB (0.1-12 µM) and subjected to gel electrophoresis. Note that ParB binds non-specifically to DNA, but the presence of *parS* sites increases its DNA-binding affinity by stimulating the formation of a specific ParB•*parS* complex.

SUPPLEMENTAL TABLE

Table S1. Bacterial strains created and used in this work.

Strain*	Description	Reference
M. gryphiswaldense		
MSR WT	Wild-type MSR-1 R3/S1 (Rif^R, Sm^R)	Schultheiss and Schüler, 2003
FM021	*mamC-egfp*	Raschdorf *et al.*, 2014
FM98	*egfp-mipZ1 mCherry-mipZ2*, Km^R	This work
FM100	*egfp-mipZ2 ftsZ-mCherry*, Km^R	This work
FM101	Δ*mipZ1* Δ*mipZ2 egfp-mipZ2 ftsZ-mCherry*, Km^R	This work
MT024	Δ*mipZ2*	This work
TZ001	Δ*mipZ1*	This work
TZ003	Δ*mipZ1* Δ*mipZ2*	This work
eFM098	MSR WT, transformed with pFM292a, Km^R	This work
eMTN023	FM021, transformed with pMT017, Km^R	This work
eMTN025	MSR WT, transformed with pMT017, Km^R	This work
eMTN026	TZ001, transformed with pMT017, Km^R	This work
eMTN027	MT024, transformed with pMT017, Km^R	This work
eMTN028	MSR WT, transformed with pMT020, Km^R	This work
eMTN029	MSR WT, transformed with pTZ019, Km^R	This work
eMTN030	MSR WT, transformed with pMT097, Km^R	This work
eMTN031	MSR WT, transformed with pMT029, Km^R	This work
eMTN032	MSR WT, transformed with pTZ023, Km^R	This work
E. coli		
DH5α	F$^-$ ϕ80*lac*ZΔM15 Δ(*lac*ZYA-*arg*F) U169 *rec*A1 *end*A1 *hsd*R17 (rK$^-$, mK$^+$) *pho*A *sup*E44 λ$^-$ *thi*-1 *gyr*A96 *rel*A1	Invitrogen
WM3064	*thrB1004 pro thi rpsL hsdS lacZ*ΔM15 *RP4-1360* Δ(*araBAD*)*567* Δ*dapA1341*::[*erm pir* (*wt*)]	W. Metcalf (unpublished)
Rosetta 2(DE3)pLysS	F$^-$ *ompT hsdS*$_B$(r$_B^-$ m$_B^-$) *gal dcm* (DE3) pLysSRARE2 (Cm^R)	Merck Millipore
eMTN036	DH5α, transformed with pMT017, Km^R	This work
eMTN037	DH5α, transformed with pMT018, Km^R	This work
eMTN038	DH5α, transformed with pMT020, Km^R	This work
eMTN039	DH5α, transformed with pMT021, Km^R	This work

* MT and TZ strains carry stable in-frame deletions. eMTN strains are transformed with a replicative pBBR1-derived or an integrative pBAM1-derived plasmid.

** Rif^R, rifampicin resistance; Sm^R, spectinomycin resistance; Km^R, kanamycin resistance; Cm^R, chloramphenicol resistance.

Table S2. Plasmids used in this study.

Plasmid	Description	Reference
pORFM-GalK-MCS	Integrative backbone vector for in-frame gene deletion *ori*T, P_{tet}-*galK*, Km^R, Tc^R	Raschdorf *et al.*, 2014
pBBR1MCS2	Replicative backbone vector for *in trans* gene expression in MSR. *ori*T, *mob*, Km^R	Kovach *et al.*, 1994
pMT009	pBBR1MCS2 based vector. P_{mamAB}-*mCherry-mamK*; Km^R	Toro-Nahuelpan *et al.*, 2016
pMT065	pBBR1MCS2, P_{tet}-*dendra2-mamK,* terminator-fragment, P_{Neo}-TetR; Km^R	Toro-Nahuelpan *et al.*, 2016
pJH2	pBAM1 *ori*R6K, with P_{tet}-*mamC-magegfp*, terminator, P_{Neo}-TetR; Km^R, Ap^R	Borg *et al.*, 2014
pTB146	ColE1 *bla lacI*^{q} PT7::*his-sumo*, Ap^R	Bendezu *et al.*, 2009
pFM287	pBBR1-based vector, with tetracycline-inducible promoter	This work
pFM292a	pFM287 derivative, P_{tet}-*egfp-mipZ1 mCherry-mipZ2*	This work
pFM293a	pBAM-based plasmid, P_{tet}-*egfp-mipZ2 ftsZ-mCherry*	This work
pLC026	pTB146 bearing *mipZ1*	This work
pLC028	pTB146 bearing *parB*	This work
pLC029	pTB146 bearing *mipZ1* G15V	This work
pLC030	pTB146 bearing *mipZ1* D43A	This work
pLC031	pTB146 bearing *ftsZ*	This work
pMT017	pMT009 derivative, P_{tet}-*mCherry-mipZ1*	This work
pMT018	pMT009 derivative, P_{tet}-*mCherry-mipZ2*	This work
pMT020	pMT009 derivative, P_{tet}-*mCherry-mipZ1* D43A	This work
pMT021	pMT009 derivative, P_{tet}-*mCherry-mipZ2 D44A*	This work
pMT024	pORFM-GalK derivative, for *mipZ2* deletion	This work
pMT029	pJH2 derivative, P_{tet}-*ecfp-parB*	This work
pMT097	pMT065 derivative, P_{tet}-*dendra2-mipZ1*	This work
pTZ012	pORFM-GalK derivative, for *mipZ1* deletion	This work
pTZ019	pJH2 derivative, P_{tet}-*mCherry-mipZ1* G15V	This work
pTZ023	pJH2 derivative, P_{tet}-*mCherry-mipZ1*	This work

* Km^R, kanamycin resistance; Tc^R, tetracyclin resistance; Ap^R, ampicillin resistance.

Table S3. Oligonucleotides used in this study.

Name	Sequence	Restriction site
oFM620	cctgcagggcgagccgatgaccaaacgggcccatgtcatcgtcg	
oFM621	agactaTCTAGActattcttcgtcctggcccagattgtcc	*Xba*I
oFM622	agactaATGCATgtgtcgaagggcgaggaactgttcacc	*Nsi*I
oFM623	gccctgcaggcacagcggcttatacagctcgtccatgcccaggg	
oFM624	ccgctgtgcctgcagggcgagccgtccgggcgcaccgcccatgtc	
oFM625	agactaCTCGAGctaaagccggtccaaccgttcattcacc	*Xho*I
oFM626	agactaCATATGgtgagcaagggcgaggaggataacatg	*Nde*I
oFM627	cggctcgccctgcaggcacagcggcttgtacagctcgtccatgccgcc	
oFM634	cacgtg tttaaa ccgctgtgcctgcagggcg	
oFM635	agacgtaCCGCGGtcgatcggtctagactaaagccggtccaaccgttcattcacc	*Sac*II
oFM638	agactaATGCATgtgtcgaagggcgaggaactg	*Nsi*I
oFM639	tttaaa cacgtg cttatacagctcgtccatgcccaggg	
oMTN044	agactaCATATGgtgagcaagggcgaggaggataac	*Bam*HI
oMTN054	agactaGGATCCctattcttcgtcctggcccagatt	BamHI
oMTN055	gactaGCTAGCatgtccgggcgcaccgcccat	NheI
oMTN056	agactaGGATCCctaaagccggtccaaccgttcatt	BamHI
oMTN059	tccatcgacctggccgcccgtcaggcc	
oMTN060	tgtatcgatctggcccatcgtcagcaa	
oMTN062	ggtaccttaagatctcgagctccggagaattcggcggccgccgatcct	
oMTN068	ggcccgtttggtcatGCTAGCaggatcggcggccgccgaatt	*Nhe*I
oMTN073	agactaCGGCCGCgctggcgccacccggaaatggggtt	*Not*I
oMTN077	agactaCTGCAGcatgccaacatctgatcgccatggc	*Pst*I
oMTN078	GGATCCtagtctGTTAACCatagcgtgatcccgttgttgttcgct	*Bam*HI, *Hpa*I
oMTN079	GTTAACagactaGGATCCtagcggtgtgttaggcgagtccac	*Hpa*I, *Bam*HI
oMTN080	agactaGCGGCCGCtgagaaactgatcgtcgaggaagccat	*Not*I
oMTN101	agactaCATATGgtgagcaagggcgaggagctgttc	*Nde*I
oMTN102	agctcgagatcttaaggtacccttgtacagctcgtccatgccgag	*Nhe*I
oMTN103	cggcggccgccgatcctGCTAGCgtggcggaagacaagcgtcgcaag	*Nhe*I
oMTN104	agactaGGATCCtcagatacccgagcgcgacaggcg	*Bam*HI
oMTN142	agactaGTCGACcggtgggcgaggctaggtccaacc	*Sal*I
oMTN232	agactaGAATTCcttgtacagctcgtccatgccgc	*EcoR*I
oMTN260	gctaGGATCCtagtctGTTAACggtcatgcgttttcccctgscgcgttg	*Bam*HI, *Hpa*I
oMTN261	gaccGTTAACagactaGGATCCtagctgttcggggaaaagtacaccggc	*Hpa*I, *Bam*HI
oTZ002	agactaGCTAGCatgaccaaacgggcccatgtcatcgtcgtcggcaacgaaaaggtcggtaccggc	*Nhe*I
mipZMg-1	taGCTCTTCgggtatgaccaaacgggcc	SapI
mipZMg-2	actagtggatccctattcttcgtcctg	BamHI
parBMg-1	taGCTCTTCgggtatgcttgagcaagggagtgtaaggacagtggcggaagacaagcgt	SapI
parBMg-2	actagtGGATCCtcagatacccgagcg	BamHI
ftsZMg-1	taGCTCTTCgggtatgcttaactttcttccg	SapI
ftsZMg-rev-1	acgttcCTCGAGttaattggcctgacggcg	XhoI

* Introduced restriction sites are indicated by capital letters.

SUPPLEMENTAL METHODS

Construction of plasmids

pFM292a was constructed to simultaneously produce fluorescently tagged MipZ1 and MipZ2. The mipZ1 and egfp genes were amplified with the primer pairs oFM620/ oFM621 and oFM622/ oFM623, respectively, and fused by overlap PCR with primers oFM621 and oFM622. The resulting PCR product was then inserted between the NsiI and XbaI restriction sites of pFM287 (a pBBR-based vector containing a tetracycline-inducible promoter). Subsequently, mipZ2 and mCherry were amplified with the primer pairs oFM624/oFM625 and oFM626/oFM627, respectively, and fused by overlap PCR. The PCR product was then cloned downstream of egfp-mipZ1 between the NdeI and XhoI restriction sites. pFM293a was generated to simultaneously express fluorescently tagged MipZ2 and FtsZ from a random chromosomal locus. To this end, mipZ2 was amplified with primers oFM634/oFM635 and egfp was amplified with primers oFM638/ oFM639. The two fragments were fused by overlap PCR and cloned into pFM290a, a pBAM-based backbone vector containing Ptet, ftsZ-mCherry and tetR.

Plasmids pLC26, pLC30, pLC31 and pLC28 bear His-SUMO fusions of mipZ, mipZG15V, mipZD43A and parB genes. To construct them, the different mipZ alleles were PCR-amplified from pMT017, pTZ019 and pMT020 using primers mipZMg-1 and mipZMg-2, whereas parB was PCR-amplified from pMT029 using primers parBMg-1 and parBMg-2. The PCR products were digested with SapI and BamHI and ligated into pTB146 (1) cut with the same enzymes.

To construct pLC29, containing a gene encoding His-SUMO-FtsZ, the ftsZ gene was PCR-amplified from pMT026 using primers ftsZMg-1 and ftsZMg-rev-1. The product was cut with SapI and XhoI and ligated into pTB146 (Bandezu et al., 2009) cut with the same enzymes.

To create plasmids pMT017 and pMT018, fragments containing mipZ1 and mipZ2 were amplified from genomic DNA using the primer pairs oMTN054/oMTN068 and oMT055/oMT056, respectively, and cloned between the NheI and BamHI restriction sites of vector pMT009.

For the generation of pMT020, primers oMTN054, oMTN059 and oMTN068 were used to amplify the mipZ1-D43A allele, which encodes alanine instead of glutamate at amino acid position 43. The fragment was then cloned between the NheI and BamHI restriction sites of pMT009.

pMT021 was generated using the primers oMTN055, oMTN056 and oMTN060 to amplify the mipZ1-D44A allele, which encodes alanine instead of glutamate at amino acid position 44. The fragment was then cloned between the NheI and BamHI restriction sites of pMT009.

To construct pMT024 (in-frame deletion of mipZ2), 700 bp-fragments comprising the up- and downstream regions of mipZ2 were PCR-amplified from genomic DNA using the primer pairs oMTN077/oMTN078 and oMTN079/oMTN080, respectively. After fusion of the resulting fragments

by an overlap PCR, the reaction product was ligated into vector pORFM-galK using the PstI and NotI restriction sites. This vector was then used to generate ΔmipZ2 and the ΔmipZ1 ΔmipZ2 mutants.

Plasmid pMT029 was constructed by amplification of ecfp with primers oMTN101 and oMTN102 and parB with oMTN103 and oMTN104. A fragment containing an ecfp-parB fusion (with a linker incorporated in the primers) was generated by an overlap PCR using primers oMTN101, oMTN104 and oMTN062 and subsequently cloned into pJH2 using the NdeI and BamHI restriction sites.

To generate plasmid pMT097, mipZ1 was amplified using primers oMTN054 and oMTN068 and ligated into pMT065 using the NheI and BamHI restriction sites.

Plasmid pTZ012 was used to generate an inframe deletion of the mipZ1 gene in the wild-type strain. To construct it, 700 bp-fragments comprising the up- and downstream region of mipZ1 were amplified from wildtype genomic DNA with the primer pairs oMTN142/oMTN260 and oMTN261/oMTN073, respectively. The resulting fragments were fused by overlap PCR and subsequently cloned into pORFM-galK using the SalI and NotI restriction sites.

Plasmid pTZ019 was created to generate the mCherry-MipZ1 G15V fusion. The mCherry gene (plus an α-helix linker) was amplified with primers oMTN044 and oMTN232, digested with NdeI and EcoRI, and ligated into pJH2. Subsequently, primers oTZ02 and oMTN054 were used to mutate mipZ1 to mipZ1-G15V by replacing the codon GGC (encoding glycine 15) with GTC (encoding valine). The mipZ1-G15V gene was then inserted immediately downstream of the mCherry-α-helix fragment contained in the above pJH2 derivative using the NheI and BamHI restriction sites.

To construct pTZ023, the mipZ1 gene was PCR-amplified from pMT017 using the primer pair oMTN054/oMTN068. The product was cut with NheI and BamHI and ligated into pTZ019 cut with the same enzymes.

Photokinetic analysis

Fluorescence recovery after photobleaching (FRAP) and photoconversion analysis was performed on *M. gryphiswaldense* strains expressing different constructs. For genes under the control of the tetracycline-inducible promoter, expression was induced by addition of anhydrotetracycline to a concentration of 50 ng ml. The induction times ranged between 3-5 h. Cells were mounted on “MSR agarose pads” as described previously (Toro-Nahuelpan et al., 2016) and imaged with a Delta Vision Elite system (GE Healthcare) at 30ºC. During the photokinetic experiment, a time-lapse series was acquired at 30 ºC with a hardware-based “Ultimate-Focus” autofocus, and images were collected with a 100x Oil PSF Objective. Cells producing mCherry-MipZ1 and mCherry-MipZ1D43A were analyzed with an mCherry filter set at 10% SSI (Solid State Illumination) with 500 ms exposure. Bleaching was achieved with a single 8 ms laser pulse, using a 561 nm laser line (50 mW) at 10% power with 70% of

the laser in TIRF mode (only to decrease laser power, as TIRF imaging was not performed). Subsequently, images were taken at 4 s intervals for the first 36 s and then every 10 s until the end of the experiment. Cells producing mCherry-MipZ2D44A were imaged with an mCherry filter set at 10% SSI with 150 ms exposure. Bleaching was achieved with a single 4 ms laser pulse, using a 561 nm laser line (50 mW) at 10% power, with 75% of the laser in TIRF mode. Subsequently, images were taken at 15 s intervals. Fluorescence recovery half-times (t½) were calculated independently for each bleached cell and averaged in order to obtain the SEM for the entire cell population analyzed. Moreover, the standard deviation is given for each data point of the recovery curves.

Photoconversion was used to qualitatively assess the localization dynamics of MipZ1 in *M. gryphiswaldense.* Before conversion, Dendra2-MipZ1 was imaged with an FITC filter set, using 2% SSI with 400 ms exposure. Photoconversion was achieved with a 405 nm laser line (100 mW) at 10% power, with 80% of the laser in TIRF mode and a single pulse applied for 4 ms. Subsequently, cells were imaged with a TRITC filter set at 10% SSI with 400 ms exposure. Images were taken every 4 s for 36 s and then every 10 s until the end of the experiment. They were then aligned and further analyzed with Fiji (Schindelin et al., 2012). After sub-traction of the background signal, each region of interest was corrected for bleaching considering the whole cell fluorescence as described previously (Toro-Nahuelpan et al., 2016). Relative values were used to enable the comparison and averaging of data from multiple cells. To control for a spontaneous reversal of Dendra2 to the dark state, cells were fixed with 1% formaldehyde for 1 h at room temperature prior to application of a laser pulse and then subjected to image analysis (Müller et al., 2012). No reversal was observed after prolonged incubation of the cells after photoconversion.

SUPPLEMENTAL REFERENCES

Bendezu, F.O., Hale, C.A., Bernhardt, T.G., and de Boer, P.A. (2009) RodZ (YfgA) is required for proper assembly of the MreB actin cytoskeleton and cell shape in E. coli. EMBO J 28: 193-204.

Borg, S., Hofmann, J., Pollithy, A., Lang, C., and Schüler, D. (2014) New vectors for chromosomal integration enable high level constitutive or inducible magnetosome expression of fusion proteins in Magnetospirillum gryphiswaldense. Appl Environ Microbiol 80: 2609-2616.

Kovach, M., Phillips, R., Elzer, P., Roop, R., and Peterson K. 1994. pBBR1MCS: a broad-host-range cloning vector. BioTechniques 16: 800-802.

Müller, F., Morisakim T., Mazza, D., and McNally, J.G. (2012) Minimizing the impact of photoswitching of fluorescent proteins on FRAP analysis. Biophys J 102: 1656-1665.

Raschdorf, O., Plitzko, J.M., Schüler, D., and Müller, F.D. (2014) A tailored galK counterselection system for efficient marker less gene deletion and chromosomal tagging in Magnetospirillum gryphiswaldense. Appl Environ Microbiol 80: 4323-4330.

Schindelin, J., Arganda-Carreras, I., Frise, E., Kaynig, V., Longair, M., Pietzsch, T., Preibisch, S., Rueden, C., Saalfeld, S., Schmid, B., Tinevez, J.Y., White, D.J., Hartenstein, V., Eliceiri, K., Tomancak, P., and Cardona, A (2012) Fiji: an open-source platform for biological image analysis. Nat Methods 9: 676-682.

Schultheiss, D., and Schüler, D (2003) Development of a genetic system for Magnetospirillum gryphiswaldense. Arch Microbiol 179: 89-94.

Toro-Nahuelpan, M., Müller, F.D., Klumpp, S., Plitzko, J.M., Bramkamp, M., and Schüler, D (2016) Segregation of prokaryotic magnetosomes organelles is driven by treadmilling of a dynamic actin-like MamK filament. BMC Biol 14: 88.

DISCUSSION

Bactofilins as organizers of the chromosome segregation machinery

Cells have evolved various mechanisms to position protein complexes, membrane vesicles and DNA to specific locations within the cell (Thanbichler & Shapiro, 2008). Cytoskeletal elements are key players in the organization of the cellular contents. These polymeric scaffolds often act in concert with the DNA segregation machinery to mediate chromosome organization and ensure faithful segregation of the genetic material during cell division (Gerdes *et al.*, 2010).

Bactofilins are a newly identified class of cytoskeletal proteins widely distributed within bacteria (Kuhn *et al.*, 2010, Deng *et al.*, 2019). These filament-forming proteins are characterized by a central β-helical domain (Vasa *et al.*, 2015, Shi *et al.*, 2015), typically flanked by short unstructured terminal regions (Kühn *et al.*, 2010, Lin & Thanbichler, 2013). Their polymerization is mediated by end-to-end association of the β-helical domains in a nucleotide-independent manner (Deng *et al.*, 2019). Bactofilin polymers associate with the cytoplasmic membrane through weak hydrophobic interactions involving residues at the N-terminal region (Deng *et al.*, 2019, Kühn *et al.*, 2010). Furthermore, some bactofilins possess N-terminal transmembrane helices (Lin & Thanbichler, 2013, Hay *et al.*, 1999), strongly suggesting that membrane association is crucial for bactofilin function.

It has become apparent that bactofilins are involved in a range of cellular processes in different bacterial species. For instance, in *C. crescentus* and *Asticcacaulis biprosthecum* bactofilins are implicated in stalk biogenesis (Kühn *et al.*, 2010, Caccamo *et al.*, 2020). In *Helicobater pylori*, the absence of the single bactofilin homologue *ccmA* completely abolishes its characteristic helical cell shape (Sycuro *et al.*, 2010). CcmA presumably acts in concert with peptidoglycan hydrolytic enzymes to remodel the shape of the cell wall (Blair *et al.*, 2018). Similarly, in the spirochaete *Leptospira biflexa* the bactofilin homologue LbbD influences the helical shape of cells (Jackson *et al.*, 2018). On the other hand, bactofilins BacE and BacF form *B. subtilis* are essential for flagella-mediated motility (El Andari *et al.*, 2015).

In this work, we have uncovered a new role of bactofilins as organizers of the ParAB*S* chromosome segregation machinery in *M. xanthus*. In this bacterium, bactofilins BacN BacO and BacP form polar scaffolds that control the localization of the ParB*S* partition complex and the DNA partition ATPase ParA within the cell (Lin *et al.*, 2017, Osorio-Valeriano *et al.*, 2019). The centromere (*parS*)-binding protein ParB is tethered to the pole-distal ends of the bactofilin filaments, whereas ParA binds along their entire length.

We found that BacNOP polymers localize in a cell cycle-dependent manner. Newborn cells display a mature bactofilin polymer at the old cell pole and a small polymer at the new pole. The nascent

polymer gradually grows until it reaches its full size (~ 1 µM). In pre-divisional cells, a third patch assembles at midcell, which is later split during cytokinesis (Lin *et al.*, 2017).

The recruitment of bactofilins to the division site by a so-far unknown mechanism ensures the establishment of these assemblies at the new cell pole upon cell division and, may be thus responsible for their bipolar localization. Interestingly, modifications of the C-terminal region of BacP result in unipolarly localized polymers (Lin *et al.*, 2017). Therefore, BacP might play an important role in BacNOP positioning.

Polymerization of bactofilins at specific locations within the cell has been reported in other species (Kühn *et al.*, 2010, Taylor *et al.*, 2020, Caccamo *et al.*, 2020). However, the mechanisms controlling the proper positioning of these assemblies have not yet been studied. One possibility is that they recognize geometric cues in the cell. Alternatively, they could be recruited through direct interaction with specific localization determinants.

BacNOP consistently colocalize *in vivo*. Furthermore, inactivation of *bacP* severely impairs BacO localization. Conversely, loss of *bacO* results in fragmented BacP filaments (Lin *et al.*, 2017), suggesting that they assemble into a joint polymeric structure. Nevertheless, each bactofilin can form large filaments on its own *in vitro* (Kühn *et al.*, 2010). Therefore, it remains to be clarified whether the three bactofilins assemble into homopolymeric structures that subsequently bundle to form larger complexes or whether they associate into mixed polymers in the cell. Incorporation of different bactofilin paralogues into a single filamentous structure could confer distinct polymerization properties and facilitate the recruitment of multiple interaction partners.

Interestingly, bactofilin filaments do not grow longer than 1 µm in *M. xanthus* cells. Given that bactofilins polymerize independently of nucleotide cofactors, their polymerization could be influenced by the number of bactofilin subunits available in the cell, intrinsic polymerization properties or protein–protein interactions.

In addition to its role in positioning the ParABS system, BacP also participates in type IV-mediated motility by recruiting the small GTPase SofG, which results in the polar localization of the motor ATPases PilB and PilT (Bulyha *et al.*, 2013). A fourth bactofilin in *M. xanthus*, named BacM, is involved in cell morphology and cell wall stability (Koch *et al.*, 2011). Therefore, bactofilins can regulate and coordinate seemingly unrelated cellular processes.

To date, the biology of the bactofilin cytoskeleton remains largely unexplored. Future studies in different phylogenetic groups might reveal new functions as well as common principles governing the action of this versatile and widely distributed family of cytoskeletal elements.

A ParB-like protein recruits ParA to the bactofilin polymers in a CTP-dependent manner

During active DNA translocation, the ParB*S* partition complex interacts with nucleoid-bound ParA dimers and stimulates the ParA ATPase activity. Upon ATP hydrolysis, ParA monomers are released from the nucleoid and ParB binds to adjacent ParA dimers (Lim *et al.*, 2014). In *C. crescentus*, the polar scaffolding protein PopZ sequesters released ParA monomers (Ptacin *et al.*, 2014). Similarly, in *M. xanthus*, bactofilins recruit ParA monomers to the subpolar regions of the cell, thereby likely preventing their reassembly, and thus, facilitating the progressive directional translocation of the partition complex.

In contrast to PopZ, bactofilins do not interact directly with ParA but they use the newly identified ParB-like protein PadC as an adaptor (Lin *et al.*, 2017, Osorio-Valeriano *et al.*, 2019). Although ParA and ParB are essential in *M. xanthus* (Iniesta, 2014, Harms *et al.*, 2013), inactivation of BacNOP or PadC has only a moderate effect on the overall efficiency of chromosome segregation (Lin *et al.*, 2017). However, simultaneous inactivation of the structural maintenance of chromosome (SMC) complex and BacNOP/PadC scaffold is lethal, demonstrating that both systems act redundantly to enable chromosome segregation in this bacterium (Anand *et al.*, 2020).

Structural studies of PadC revealed that the ParB/Srx domain of this protein constitutes a nucleotide binding module that specifically interacts with the ribonucleotide CTP. We found that PadC binds to ParA through its ParB/Srx domain in a CTP-dependent manner. PadC binding to CTP mediates the dimerization of its ParB/Srx domain and keeps the protein in a closed dimer conformation that is necessary for ParA interaction.

Remarkably, the CTP-binding pocket of PadC is also present in canonical ParB proteins. Residues interacting with CTP correspond to the highly conserved Box I, Box II and Box III (also known as Region II) regions previously identified in the ParB protein family (Yamaichi & Niki, 2000, Bartosik *et al.*, 2004). In particular, the arginine patch in BoxII is engaged in hydrogen bonding interactions with the triphosphate moiety of the nucleotide. In fact, previous studies have shown that mutations in the arginine patch completely abolish ParB function (Autret *et al.*, 2001, Graham *et al.*, 2014, Tran *et al.*, 2018).

PadC is restricted to the deltaproteobacterial suborder *Cystobacterineae* and likely evolved from a ParB ancestor through gene duplication and divergence. In contrast to ParB, PadC lacks CTP hydrolytic activity (see below). It is possible that the evolution of PadC into a ParA-localizing factor went along with the loss of its CTPase activity. Catalytically inactive PadC might thus exist as a constitutive dimer that is targeted to the subpolar regions of the cell through its bactofilin-binding C-terminal domain to mediate the recruitment of ParA monomers to these locations.

CTP: a central component of prokaryotic DNA segregation

In the cell, hundreds of ParB molecules spread over tens of kilobases away from *parS* loading sites, forming a higher-order nucleoprotein complex (Breier & Grossman, 2007, Lynch & Wang, 1995). However, reconstitution of the ParB*S* partition complex *in vitro* has proven challenging, indicating the lack of an essential component (Soh *et al.*, 2019).

ParB has long been regarded exclusively as a DNA-binding protein. However, in this work, we showed that ParB-type DNA segregation proteins can bind and hydrolyze CTP (Osorio-Valeriano *et al.*, 2019). Notably, at the same time, another group reported similar findings for the *B. subtills* ParB homologue Spo0J (Soh *et al.*, 2019). A more recent study showed that the chromosomal ParB protein from *C. crescentus* and other eight distantly related bacteria are able to spread on *parS*-containing DNA fragments in a CTP-dependent manner *in vitro*. The new biochemical approaches used in these studies recapitulate many properties of ParB previously only observed in cells and demonstrate that this is a general property of the ParB protein family (Jalal *et al., 2020)*.

The discovery of CTP as an essential component of the ParAB*S* partition system adds an unforeseen layer of complexity to prokaryotic DNA segregation and opens new perspectives in the investigation of mechanisms underlying this central process. Some of the previously reported biochemical studies conducted on ParB might need to be revisited (Funnell, 2019) and performed in the presence of CTP.

A new model for partition complex formation

Based on the crystal structure of ParB bound to CDP and additional biochemical data, Y. M. Soh and colleagues proposed a new model for partition complex formation which is compatible with the negative effect of roadblocks on ParB spreading. In this model, ParB forms a ring that encircles DNA upon CTP-mediated engagement of its N-terminal domain at *parS* loading sites and slides to adjacent DNA regions (Soh *et al.*, 2019).

Consistent with previous observations (Leonard *et al.*, 2004, Surtees & Funnell, 1999, Fisher *et al.*, 2017), the authors suggest that the C-terminal domain of ParB keeps the protein in a constitutive dimeric conformation. ParB dimers can bind CTP with moderate affinity, with Kd values in the range of 10 to 60 µM (Osorio-Valeriano *et al.*, 2019, Soh *et al.*, 2019), ensuring its saturation at the CTP concentration present in the cytoplasm (~500 µM) (Buckstein *et al.*, 2008). Therefore, freely diffusing CTP-bound ParB dimers exist in a loading-competent nucleotide-bound open state (Figure 1).

In the absence of nucleotide, the N-terminal domain of ParB is flexible (Surtees & Funnell, 1999) and can adopt different conformations (Chen *et al.*, 2015, Leonard *et al.*, 2004, Jalal *et al.*, 2019). However, it dimerizes upon nucleotide binding, as shown by the crystal structure of CDP-bound ParB (Soh *et al.*, 2019). Similarly, the crystal structure of PadC revealed a CTP-dependent dimerization of its ParB/Srx

domain (Osorio-Valeriano *et al.*, 2019). Interestingly, in these studies, ParB crystals were grown in the presence of CTP, thus, the nucleotide must have been hydrolyzed during crystallization (Soh *et al.*, 2019).

Site-specific cross-linking experiments showed that only CTP and not CDP can efficiently support ParB N-terminal (N) engagement in the presence of *parS* (Soh *et al.*, 2019). It has been proposed that binding to *parS* catalyzes CTP-dependent N engagement, restricting the closure of ParB rings around the DNA at *parS* sites (Figure 1).

Our results showed that the CTP-mediated dimerization of ParB reduces its affinity for *parS* sites by ~8-fold. We hypothesized that this effect could be due to conformational changes in the HTH motif induced by nucleotide binding, as shown by our HDX analysis (Osorio-Valeriano *et al.*, 2019). These results were further confirmed by Y. M. Soh and collaborators. While comparing the crystal structure of CDP-bound ParB with a previously reported structure of apo ParB in complex with *parS* (Chen *et al.*, 2015), the authors realized that in nucleotide-bound ParB, one of the HTH motifs clashes with the second, so that the ParB dimer cannot accommodate a full *parS* sequence (Soh *et al.*, 2019).

The reduced affinity of ParB rings for *parS* allows ParB to dissociate from *parS* and slide along flanking DNA. Once the newly formed ParB ring leaves *parS*, the loading site becomes available for the next ParB dimer (Figure 2). This model explains how even a single *parS* site can be sufficient to support the loading of multiple ParB dimers necessary for partition complex *in vivo* (Wang et al., 2017, Böhm et al., 2020).

Interestingly, the nonhydrolyzable CTP analogue CTPγS can promote efficient N engagement even in the absence of *parS*, as shown by HDX (Osorio-Valeriano *et al.*, 2019) and site-specific cross-linking experiments (Soh *et al.*, 2019), suggesting that CTP hydrolysis is dispensable for the loading of ParB rings onto DNA.

It has been hypothesized that CTP hydrolysis could mediate the release of ParB rings from the DNA (Soh *et al.*, 2019). Upon CTP hydrolysis, the hydrolytic product CDP rapidly dissociates from ParB due to its low affinity (K_D= 678 µM) (Osorio-Valeriano *et al.*, 2019), approximately 10-fold lower than CTP, destabilizing the closed ring conformation. The open ParB dimer dissociates from the DNA and is ready to be loaded at *parS* again (Figure 2). CTP hydrolysis might thus be at least partially responsible for the rapid exchange of ParB molecules in the partition complex previously reported by FRAP experiments *in vivo* (Debaugny *et al.*, 2018).

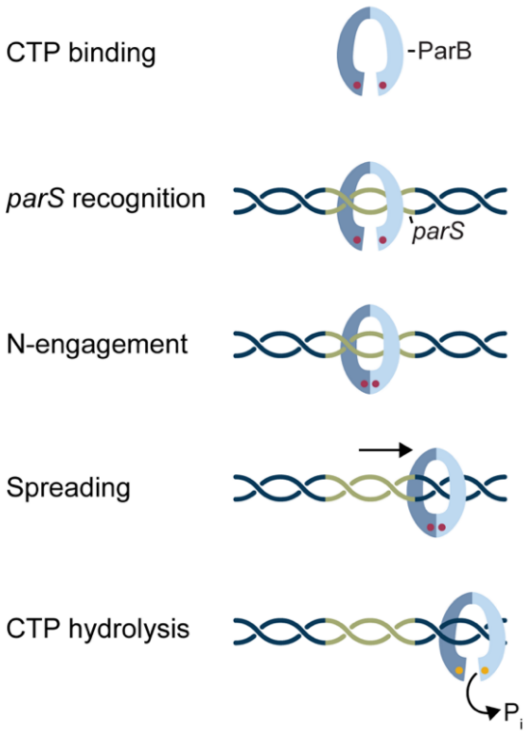

Figure 1. Model for CTP-dependent loading of ParB rings at *parS* sites. CTP-bound ParB dimers interact specifically with *parS*, which catalyzes the engagement of the ParB N-terminal domains. ParB adopts a closed ring conformation that entraps the DNA. ParB rings then dissociate from *parS* and slide along flanking DNA. Centromeric *parS* sites, thus become available for loading new ParB dimers. CTP hydrolysis destabilizes the N-terminal dimerization of ParB, resulting in the dissociation of ParB from the chromosome.

To better understand the role of CTP hydrolysis in partition complex formation it is imperative to generate ParB catalytic mutants able to undergo CTP-mediated dimerization upon *parS* binding. Unfortunately, previously reported catalytic mutants are also impaired in N engagement (Osorio-Valeriano *et al.*, 2019, Soh *et al.*, 2019) and, thus, fail to accumulate on *parS*-containing DNA fragments.

Although this model incorporates the new findings on CTP-mediated loading and lateral sliding of ParB rings (Jalal *et al.*, 2020, Osorio-Valeriano *et al.*, 2019, Soh *et al.*, 2019), it does not take into account a substantial amount of previous work reporting the ability of ParB to condense DNA *in vitro* (Song *et al.*, 2017, Graham *et al.*, 2014, Broedersz *et al.*, 2014). A central question to be addressed is whether the loading and sliding of ParB rings is accompanied by DNA condensation *in vivo*.

DNA condensation by ParB could result from bridging interaction mediated by the non-specific DNA binding activity of the C-terminal domain. Nevertheless, this activity has only been described for some plasmidic ParB proteins and the chromosomally encoded ParB from *B. subtilis* (Fisher *et al.*, 2017, Madariaga-Marcos *et al.*, 2019, Jalal *et al.*, 2019, Schumacher & Funnell, 2005, Schumacher *et al.*, 2010). Alternatively, previously loaded ParB rings could open after CTP hydrolysis and expose their N-terminal domains, making them available for the formation of bridging interactions with other ParB dimers.

Consistent with the later hypothesis, a previous structural study of *H. pylori* ParB in complex with *parS* revealed that the nucleotide-free ParB/Srx domain can act as an additional binding interface that mediates nucleotide-independent head-to-head interactions between adjacent ParB dimers, resulting in the formation of a tetrameric DNA-bridging complex (Chen *et al.*, 2015). This complex is stabilized by interactions involving residues that participate in CTP-binding. In particular, the arginine rich motif in Box II is engaged in ParB oligomerization. Interestingly, mutations in this region abrogate DNA condensation *in vitro* (Graham *et al.*, 2014).

Very recently, a new property of ParB to form liquid-liquid phase separated (LLPS) condensates has been reported (Guilhas *et al.*, 2020). Super-resolution microscopy analysis showed that ParB exists at a high concentration within the partition complex (10 mM) and that ParB condensates can undergo fusion events in the absence of ParA (Guilhas *et al.*, 2020). However, biochemical evidence supporting this finding is still missing.

A better understanding on the precise architecture of the partition complex will shed light on the contribution of the different activities of ParB to the formation of this highly dynamic structure and their role in DNA partition.

It takes two to tango: the coordinated action of two NTPases drives bacterial DNA translocation

The active translocation of the *ori* region relies on the productive interaction between ParB dimers in the partition complex and ParA dimers associated with the nucleoid (Lim *et al.*, 2014) (Figure 2). This interaction has proven challenging to be studied *in vitro*. In many cases, it has only been inferred from a moderate stimulatory effect of ParB on ParA ATPase activity. However, this effect can only be seen when using high concentrations of ParB and in the presence of DNA (Lim *et al.*, 2014, Davis *et al.*, 1992). The recent development of a biochemical approach that allows to monitor the loading of ParB rings on *parS*-containing DNA fragments in real time offers new possibilities to investigate the ParB-ParA interaction (Jalal *et al.*, 2020). Previous studies have suggested that ParB binds to ParA via a highly conserved peptide located within the first 20 amino acids of the protein (Leonard *et al.*, 2005, Ah-Seng *et al.*, 2009, Radnedge *et al.*, 1998). We hypothesize that CTP-mediated dimerization of the ParB N-terminal domain could enhance the interaction with ParA and further stimulate its ATPase activity. It also remains to be investigated whether ParA interaction has an effect on the CTPase activity of ParB and thus influence the dynamics of the partition complex.

Our results on the ParB-like protein PadC strongly support an important role of CTP in the ParA interaction. PadC variants impaired in CTP-binding fail to efficiently recruit ParA. Future studies on the interaction of ParB with ParA in the presence of CTP could provide new insights into ParAB*S*-mediated DNA translocation.

ParAB*S*-mediated DNA segregation can be regarded as the coordinated action of two NTPases with different nucleotide specificities: a CTPase, which is loaded on the chromosome at centromere-like *parS* sites and spreads to adjacent DNA regions to form the partition complex, and an ATPase, which associates with the nucleoid surface and directs the active translocation of the *ori* region (Figure 2).

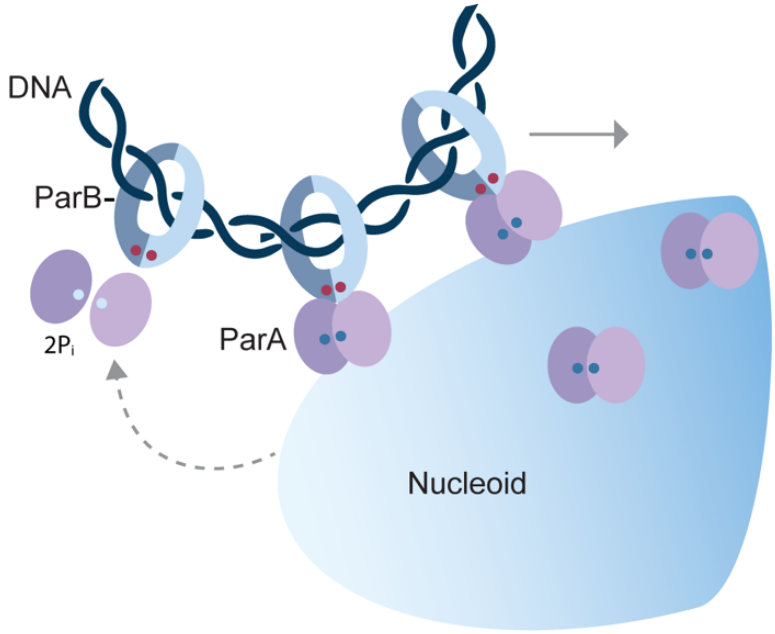

Figure 2. ParA-mediated DNA translocation. ParB proteins at the partition complex interact with nucleoid-bound ParA dimers. ParB interaction stimulates the ATPase activity of ParA. Upon ATP hydrolysis, ParA dimers dissociate and detach from the nucleoid. ParB then interacts with adjacent ParA dimers, directing DNA segregation towards the opposite cell pole.

In addition to its role in ParA-mediated DNA translocation, the ParB*S* partition complex is responsible for SMC loading on the chromosome in several bacterial species (Sullivan *et al.*, 2009, Gruber & Errington, 2009, Minnen *et al.*, 2011, Böhm *et al.*, 2020, Chan *et al.*, 2020, Tran *et al.*, 2017). However, the molecular mechanism underlying this process remains largely unknown. To date, a physical interaction between ParB and the SMC complex has not been observed *in vitro*. CTP could play a role in this interaction directly by keeping ParB in a SMC-interaction competent state or indirectly by supporting partition complex formation, and thus influencing chromosome topology. The overall contribution of CTP on chromosome organization and segregation could expand by modulating the interaction of the partition complex with additional proteins such as ParA and the SMC complex.

ParB coordinates chromosome segregation with cell division in alphaproteobacteria

ParB is a versatile protein that interacts with other proteins to couple chromosome segregation with different cellular processes. In *C. crescentus* ParB coordinates chromosome segregation with cell division by controlling the assembly and placement of the FtsZ cytokinetic ring through the interaction with MipZ, a negative regulator of FtsZ polymerization (Thanbichler & Shapiro, 2006). MipZ interaction with polar ParB*S* complexes results in the formation of a bipolar gradient with the highest

concentration at the tip of the cell and the lowest concentration at the cell center (Kiekebusch *et al.*, 2012, Thanbichler & Shapiro, 2006). As a result, MipZ prevents Z-ring assembly in the polar regions of the cell, limiting cell division to the cell center.

In this work we investigated the function of two MipZ homologues in the magnetotactic alphaproteobacterium *Magnetospirillum gryphiswaldense* (Toro-Nahuelpan *et al.,* 2019*)*. Although both proteins share high sequence similarity, their function and localization patterns differ significantly. Whereas the deletion of *mipZ*1 severely impairs cell division, inactivation of *mipZ*2 has no obvious phenotype. MipZ1 forms a gradient from the cell poles towards midcell, by contrast, MipZ2 shows a unipolar localization in newborn cells and later relocates to the site of cell division, following FtsZ (Toro-Nahuelpan *et al.*, 2019).

MipZ1 thus represents a *bona fide* homologue of the *C. crescentus* protein. On the other hand, MipZ2 behaves similar to the *Rhodobacter sphearoides* MipZ protein which localizes at mid cell, close to the Z-ring and likely regulates FtsZ activity by a so-far unknown mechanism (Dubarry *et al., 2019)*. The need of two MipZ systems in *M. gryphiswaldense* cells could be explained by their relatively larger size compared to *C. crescentus*. The inhibitory effect of the MipZ1 gradient might not be enough to efficiently restrict FtsZ polymerization at midcell. Thus, MipZ2 could play an auxiliary role in Z-ring stabilization. Altogether, our results demonstrate that the regulatory role of MipZ is conserved in many alphaproteobacteria, however their number and biochemical properties may have adapted to the specific needs of the host.

The interaction of MipZ with ParB has been studied *in vitro* (Kiekebusch *et al.*, 2012, Thanbichler & Shapiro, 2006, Toro-Nahuelpan *et al.*, 2019). However, all previous experiments have been performed in the absence of CTP. Given that CTP-bound ParB dimers likely exist as rings in the partition complex, it is possible that the interactions with MipZ and ParA are influenced by this nucleotide.

CTP, a new regulator of protein function

Many proteins are regulated by non-covalent binding of small molecules. Particularly, nucleotide-mediated regulation plays an important role in a range of cellular processes. All previously reported examples use the purine nucleotides ATP and GTP (Shan, 2016, Leipe *et al.*, 2002). In this work we showed for the first time that the pyrimidine nucleotide CTP controls the activity of the DNA-segregation protein ParB, expanding the repertory of nucleotides regulating protein function.

The evolutionary advantage of the different nucleotide specificity in ParB proteins remains to be understood. However, it is tempting to speculate that it could provide a regulatory link to CTP-dependent metabolic pathways such as membrane phospholipids biosynthesis, possibly orchestrating DNA segregation with other cellular processes.

Interestingly, the CTPase domain described in this study, is present in a large variety of protein sequences with diverse domain organizations (PFAM: PF02195), opening the possibility that CTP binding and hydrolysis could also control the activity of other protein families and thus be a more general regulatory principle in biology.

REFERENCES

Ah-Seng, Y., Lopez, F., Pasta, F., Lane, D., and Bouet, J.Y. (2009) Dual role of DNA in regulating ATP hydrolysis by the SopA partition protein. *J Biol Chem* **284**: 30067-30075.

Anand, D., Schumacher, D., and Søgaard-Andersen, L. (2020) SMC and the bactofilin/PadC scaffold have distinct yet redundant functions in chromosome segregation and organization in Myxococcus xanthus. *Mol Microbiol* (in press).

Autret, S., Nair, R., and Errington, J. (2001) Genetic analysis of the chromosome segregation protein Spo0J of Bacillus subtilis: evidence for separate domains involved in DNA binding and interactions with Soj protein. *Mol Microbiol* **41**: 743-755.

Bartosik, A.A., Lasocki, K., Mierzejewska, J., Thomas, C.M., and Jagura-Burdzy, G. (2004) ParB of Pseudomonas aeruginosa: interactions with its partner ParA and its target parS and specific effects on bacterial growth. *J Bacteriol* **186**: 6983-6998.

Blair, K.M., Mears, K.S., Taylor, J.A., Fero, J., Jones, L.A., Gafken, P.R., Whitney, J.C., and Salama, N.R. (2018) The Helicobacter pylori cell shape promoting protein Csd5 interacts with the cell wall, MurF, and the bacterial cytoskeleton. *Mol Microbiol* **110**: 114-127.

Böhm, K., Giacomelli, G., Schmidt, A., Imhof, A., Koszul, R., Marbouty, M., and Bramkamp, M. (2020) Chromosome organization by a conserved condensin-ParB system in the actinobacterium Corynebacterium glutamicum. *Nat Commun* **11**: 1485.

Breier, A.M., and Grossman, A.D. (2007) Whole-genome analysis of the chromosome partitioning and sporulation protein Spo0J (ParB) reveals spreading and origin-distal sites on the Bacillus subtilis chromosome. *Mol Microbiol* **64**: 703-718.

Broedersz, C.P., Wang, X., Meir, Y., Loparo, J.J., Rudner, D.Z., and Wingreen, N.S. (2014) Condensation and localization of the partitioning protein ParB on the bacterial chromosome. *Proc Natl Acad Sci U S A* **111**: 8809-8814.

Buckstein, M.H., He, J., and Rubin, H. (2008) Characterization of nucleotide pools as a function of physiological state in Escherichia coli. *J Bacteriol* **190**: 718-726.

Bulyha, I., Lindow, S., Lin, L., Bolte, K., Wuichet, K., Kahnt, J., van der Does, C., Thanbichler, M., and Søgaard-Andersen, L. (2013) Two small GTPases act in concert with the bactofilin cytoskeleton to regulate dynamic bacterial cell polarity. *Dev Cell* **25**: 119-131.

Caccamo, P.D., Jacq, M., VanNieuwenhze, M.S., and Brun, Y.V. (2020) A Division of labor in the recruitment and topological organization of a bacterial morphogenic Complex. *Curr Biol* (in press).

Chan, H., Söderström, B., and Skoglund, U. (2020) Spo0J and SMC are required for normal chromosome segregation in Staphylococcus aureus. *Microbiologyopen* **9**: e999.

Chen, B.W., Lin, M.H., Chu, C.H., Hsu, C.E., and Sun, Y.J. (2015) Insights into ParB spreading from the complex structure of Spo0J and parS. *Proc Natl Acad Sci U S A* **112**: 6613-6618.

Davis, M.A., Martin, K.A., and Austin, S.J. (1992) Biochemical activities of the parA partition protein of the P1 plasmid. *Mol Microbiol* **6**: 1141-1147.

Debaugny, R.E., Sanchez, A., Rech, J., Labourdette, D., Dorignac, J., Geniet, F., Palmeri, J., Parmeggiani, A., Boudsocq, F., Anton Leberre, V., Walter, J.C., and Bouet, J.Y. (2018) A conserved mechanism drives partition complex assembly on bacterial chromosomes and plasmids. *Mol Syst Biol* **14**: e8516.

Deng, X., Gonzalez Llamazares, A., Wagstaff, J.M., Hale, V.L., Cannone, G., McLaughlin, S.H., Kureisaite-Ciziene, D., and Löwe, J. (2019) The structure of bactofilin filaments reveals their mode of membrane binding and lack of polarity. *Nat Microbiol* (12):2357-2368.

Dubarry, N., Willis, C.R., Ball, G., Lesterlin, C., and Armitage, J.P. (2019) In vivo imaging of the segregation of the 2 chromosomes and the cell division proteins of Rhodobacter sphaeroides reveals an unexpected role for MipZ. *mBio* **10** (1):e02515-18.

El Andari, J., Altegoer, F., Bange, G., and Graumann, P.L. (2015) Bacillus subtilis bactofilins are essential for flagellar hook- and filament assembly and dynamically localize into structures of less than 100 nm diameter underneath the cell membrane. *PLoS One* **10**: e0141546.

Fisher, G.L., Pastrana, C.L., Higman, V.A., Koh, A., Taylor, J.A., Butterer, A., Craggs, T., Sobott, F., Murray, H., Crump, M.P., Moreno-Herrero, F., and Dillingham, M.S. (2017) The structural basis for dynamic DNA binding and bridging interactions which condense the bacterial centromere. *Elife* **6:** e28086.

Funnell, B.E. (2019) An unexpected cofactor. *Science* **366**: 1072-1073.

Gerdes, K., Howard, M., and Szardenings, F. (2010) Pushing and pulling in prokaryotic DNA segregation. *Cell* **141**: 927-942.

Graham, T.G., Wang, X., Song, D., Etson, C.M., van Oijen, A.M., Rudner, D.Z., and Loparo, J.J. (2014) ParB spreading requires DNA bridging. *Genes Dev* **28**: 1228-1238.

Gruber, S., and Errington, J. (2009) Recruitment of condensin to replication origin regions by ParB/SpoOJ promotes chromosome segregation in B. subtilis. *Cell* **137**: 685-696.

Guilhas, B., Walter, J.C., Rech, J., David, G., Walliser, N.O., Palmeri, J., Mathieu-Demaziere, C., Parmeggiani, A., Bouet, J.Y., Le Gall, A., and Nollmann, M. (2020) ATP-Driven Separation of Liquid Phase Condensates in Bacteria. *Mol Cell* **79**: 293-303.e294.

Harms, A., Treuner-Lange, A., Schumacher, D., and Søgaard-Andersen, L. (2013) Tracking of chromosome and replisome dynamics in Myxococcus xanthus reveals a novel chromosome arrangement. *PLoS Genet* **9**: e1003802.

Hay, N.A., Tipper, D.J., Gygi, D., and Hughes, C. (1999) A novel membrane protein influencing cell shape and multicellular swarming of Proteus mirabilis. *J Bacteriol* **181**: 2008-2016.

Iniesta, A.A. (2014) ParABS system in chromosome partitioning in the bacterium Myxococcus xanthus. *PLoS One* **9**: e86897.

Jackson, K.M., Schwartz, C., Wachter, J., Rosa, P.A., and Stewart, P.E. (2018) A widely conserved bacterial cytoskeletal component influences unique helical shape and motility of the spirochete Leptospira biflexa. *Mol Microbiol* **108**: 77-89.

Jalal, A.S., Tran, N.T., and Le, T.B. (2020) ParB spreading on DNA requires cytidine triphosphate in vitro. *Elife* **9.**53515.

Jalal, A.S.B., Pastrana, C.L., Tran, N.T., Stevenson, C.E., Lawson, D.M., Moreno-Herrero, F., and Le, T.B.K. (2019) Structural and biochemical analyses of C*aulobacter crescentus* ParB reveal the role of its N-terminal domain in chromosome segregation. *bioRxive* doi: https://doi.org/10.1101/816959.

Kiekebusch, D., Michie, K.A., Essen, L.O., Löwe, J., and Thanbichler, M. (2012) Localized dimerization and nucleoid binding drive gradient formation by the bacterial cell division inhibitor MipZ. *Mol Cell* **46**: 245-259.

Koch, M.K., McHugh, C.A., and Hoiczyk, E. (2011) BacM, an N-terminally processed bactofilin of Myxococcus xanthus, is crucial for proper cell shape. *Mol Microbiol* **80**: 1031-1051.

Kühn, J., Briegel, A., Mörschel, E., Kahnt, J., Leser, K., Wick, S., Jensen, G.J., and Thanbichler, M. (2010) Bactofilins, a ubiquitous class of cytoskeletal proteins mediating polar localization of a cell wall synthase in Caulobacter crescentus. *EMBO J* **29**: 327-339.

Leipe, D.D., Wolf, Y.I., Koonin, E.V., and Aravind, L. (2002) Classification and evolution of P-loop GTPases and related ATPases. *J Mol Biol* **317**: 41-72.

Leonard, T.A., Butler, P.J., and Lowe, J. (2005) Bacterial chromosome segregation: structure and DNA binding of the Soj dimer--a conserved biological switch. *EMBO J* **24**: 270-282.

Leonard, T.A., Butler, P.J., and Löwe, J. (2004) Structural analysis of the chromosome segregation protein Spo0J from Thermus thermophilus. *Mol Microbiol* **53**: 419-432.

Lim, H.C., Surovtsev, I.V., Beltran, B.G., Huang, F., Bewersdorf, J., and Jacobs-Wagner, C. (2014) Evidence for a DNA-relay mechanism in ParABS-mediated chromosome segregation. *Elife* **3**: e02758.

Lin, L., Osorio Valeriano, M., Harms, A., Søgaard-Andersen, L., and Thanbichler, M. (2017) Bactofilin-mediated organization of the ParABS chromosome segregation system in Myxococcus xanthus. *Nat Commun* **8**: 1817.

Lin, L., and Thanbichler, M. (2013) Nucleotide-independent cytoskeletal scaffolds in bacteria. *Cytoskeleton (Hoboken)* **70**: 409-423.

Lynch, A.S., and Wang, J.C. (1995) SopB protein-mediated silencing of genes linked to the sopC locus of Escherichia coli F plasmid. *Proc Natl Acad Sci U S A* **92**: 1896-1900.

Madariaga-Marcos, J., Pastrana, C.L., Fisher, G.L., Dillingham, M.S., and Moreno-Herrero, F. (2019) ParB dynamics and the critical role of the CTD in DNA condensation unveiled by combined force-fluorescence measurements. *Elife* **8**:e43812.

Minnen, A., Attaiech, L., Thon, M., Gruber, S., and Veening, J.W. (2011) SMC is recruited to oriC by ParB and promotes chromosome segregation in Streptococcus pneumoniae. *Mol Microbiol* **81**: 676-688.

Osorio-Valeriano, M., Altegoer, F., Steinchen, W., Urban, S., Liu, Y., Bange, G., and Thanbichler, M. (2019) ParB-type DNA Segregation Proteins are CTP-dependent molecular switches. *Cell* **179**: 1512-1524.e1515.

Ptacin, J.L., Gahlmann, A., Bowman, G.R., Perez, A.M., von Diezmann, A.R., Eckart, M.R., Moerner, W.E., and Shapiro, L. (2014) Bacterial scaffold directs pole-specific centromere segregation. *Proc Natl Acad Sci U S A* **111**: E2046-2055.

Radnedge, L., Youngren, B., Davis, M., and Austin, S. (1998) Probing the structure of complex macromolecular interactions by homolog specificity scanning: the P1 and P7 plasmid partition systems. *EMBO J* **17**: 6076-6085.

Schumacher, M.A., and Funnell, B.E. (2005) Structures of ParB bound to DNA reveal mechanism of partition complex formation. *Nature* **438**: 516-519.

Schumacher, M.A., Piro, K.M., and Xu, W. (2010) Insight into F plasmid DNA segregation revealed by structures of SopB and SopB-DNA complexes. *Nucleic Acids Res* **38**: 4514-4526.

Shan, S.O. (2016) ATPase and GTPase Tangos Drive Intracellular Protein Transport. *Trends Biochem Sci* **41**: 1050-1060.

Shi, C., Fricke, P., Lin, L., Chevelkov, V., Wegstroth, M., Giller, K., Becker, S., Thanbichler, M., and Lange, A. (2015) Atomic-resolution structure of cytoskeletal bactofilin by solid-state NMR. *Sci Adv* **1**: e1501087.

Soh, Y.M., Davidson, I.F., Zamuner, S., Basquin, J., Bock, F.P., Taschner, M., Veening, J.W., De Los Rios, P., Peters, J.M., and Gruber, S. (2019) Self-organization of parS centromeres by the ParB CTP hydrolase. *Science* **366**: 1129-1133.

Song, D., Rodrigues, K., Graham, T.G.W., and Loparo, J.J. (2017) A network of cis and trans interactions is required for ParB spreading. *Nucleic Acids Res* **45**: 7106-7117.

Sullivan, N.L., Marquis, K.A., and Rudner, D.Z. (2009) Recruitment of SMC by ParB-parS organizes the origin region and promotes efficient chromosome segregation. *Cell* **137**: 697-707.

Surtees, J.A., and Funnell, B.E. (1999) P1 ParB domain structure includes two independent multimerization domains. *J Bacteriol* **181**: 5898-5908.

Sycuro, L.K., Pincus, Z., Gutierrez, K.D., Biboy, J., Stern, C.A., Vollmer, W., and Salama, N.R. (2010) Peptidoglycan crosslinking relaxation promotes Helicobacter pylori's helical shape and stomach colonization. *Cell* **141**: 822-833.

Taylor, J.A., Bratton, B.P., Sichel, S.R., Blair, K.M., Jacobs, H.M., DeMeester, K.E., Kuru, E., Gray, J., Biboy, J., VanNieuwenhze, M.S., Vollmer, W., Grimes, C.L., Shaevitz, J.W., and Salama, N.R. (2020) Distinct cytoskeletal proteins define zones of enhanced cell wall synthesis in. *Elife* **9**: e52482.

Thanbichler, M., and Shapiro, L. (2006) MipZ, a spatial regulator coordinating chromosome segregation with cell division in Caulobacter. *Cell* **126**: 147-162.

Thanbichler, M., and Shapiro, L. (2008) Getting organized--how bacterial cells move proteins and DNA. *Nat Rev Microbiol* **6**: 28-40.

Toro-Nahuelpan, M., Corrales-Guerrero, L., Zwiener, T., Osorio-Valeriano, M., Müller, F.D., Plitzko, J.M., Bramkamp, M., Thanbichler, M., and Schüler, D. (2019) A gradient-forming MipZ protein mediating the control of cell division in the magnetotactic bacterium Magnetospirillum gryphiswaldense. *Mol Microbiol* **112**: 1423-1439.

Tran, N.T., Laub, M.T., and Le, T.B.K. (2017) SMC Progressively aligns chromosomal arms in Caulobacter crescentus but is antagonized by convergent transcription. *Cell Rep* **20**: 2057-2071.

Tran, N.T., Stevenson, C.E., Som, N.F., Thanapipatsiri, A., Jalal, A.S.B., and Le, T.B.K. (2018) Permissive zones for the centromere-binding protein ParB on the Caulobacter crescentus chromosome. *Nucleic Acids Res* **46**: 1196-1209.

Vasa, S., Lin, L., Shi, C., Habenstein, B., Riedel, D., Kühn, J., Thanbichler, M., and Lange, A. (2015) β-Helical architecture of cytoskeletal bactofilin filaments revealed by solid-state NMR. *Proc Natl Acad Sci U S A* **112**: E127-136.

Wang, X., Brandão, H.B., Le, T.B., Laub, M.T., and Rudner, D.Z. (2017) Bacillus subtilis SMC complexes juxtapose chromosome arms as they travel from origin to terminus. *Science* **355**: 524-527.

Yamaichi, Y., and Niki, H. (2000) Active segregation by the Bacillus subtilis partitioning system in Escherichia coli. *Proc Natl Acad Sci U S A* **97**: 14656-14661.

AKNOWLEDGMENTS

First and foremost, I would like to thank Prof. Dr. Martin Thanbichler for giving me the opportunity to join his lab. For always being supportive and giving me the freedom to develop my ideas. For his guidance over the last 5 years and for being an extraordinary supervisor from whom I have learnt a lot. His scientific input was invaluable, not only for the projects in which we have worked together, but also for my professional development. Martin, I will be always very grateful.

I would also like to thank the members of my Thesis Advisor Committee: Prof. Dr. Lotte Søgaard-Andersen and Prof. Dr. Simon Ringgaard for the fruitful discussion and valuable input to my project. Specially, Prof. Dr. Lotte Søgaard-Andersen who was my second supervisor and provided me with a place to work when our laboratory closed due to the fire. And thanks to her working group because they always answer all my doubts about working with M. xanthus.

I have been very lucky to work with the most extraordinary people. The former and present members of the Thanbichler's lab made my everyday life at work very pleasant. I learnt a lot from them, but most importantly they became my friends: Yacine, who I first met when I came to Marburg for the selection symposium, and then, when I moved to Marburg, you were always helpful. Soon I noticed that you were "different", and it did not take me long to realize that you are an extraordinary person. Somehow you became one of my best friends. Olla, for your honest friendship, I have missed you since you moved from Marburg. Maria for always looking after me, I am very happy to have you around. Dani, despite our differences in character and personalities we have built a very special friendship, one that I want to keep after I move from Marburg. Thanks for giving me the chance of sharing with you a bit of my culture and unforgettable moments. Laura, despite the language barriers, we got along really well jajaja. Thanks a lot for the scientific discussions and collaborations but most importantly for your friendship.

Alex, Olli, Wolle, Emöke, Sabine I miss you all. The old times in the Thanbichler's lab will always be special. Adrián, it has been a pleasure working with you for more than 4 years. Celine, I know we had ups and downs, but we like each other in our own way. Ying and Revathi, my two sisters, you are a very important part of my life in Marburg. Julia tanks a lot for being the most efficient technician, the best office mate and a good friend. You always helped me when I needed it and that happened quite often hahaha.

I also want to thank my students: Svenja, Sandra, Lucas and Juri. Your help has been very valuable for my projects and I have learnt a lot from you. Special thanks to Svenja, who somehow decided to do her Bachelor's and Master's thesis under my supervision, I hope you enjoyed it because I had a great time working with you and I am happy we became friends.

Last but not least, I want to thank my family and friends. My family always believed in me and supported me in every step I took. They always made me feel close to home despite the distance. Tere, who became my adoptive mother, you will always be a very special person in my life. Thanks for cheering me on and for all your help. Hanna. Francisco, Marc, Tarryn and Stefano, you became my family in Marburg, I cannot imagine the last 5 years without you. Raymond, you have been my main support over the last 10 years.

Of course, I could not mention everyone who accompanied me and supported me, all my collaborators and colleagues, my friends from Mexico and Germany. I will be always thankful to all of you.